



Universitat Autònoma de Barcelona

**ADVERTIMENT.** L'accés als continguts d'aquesta tesi queda condicionat a l'acceptació de les condicions d'ús establertes per la següent llicència Creative Commons:  [http://cat.creativecommons.org/?page\\_id=184](http://cat.creativecommons.org/?page_id=184)

**ADVERTENCIA.** El acceso a los contenidos de esta tesis queda condicionado a la aceptación de las condiciones de uso establecidas por la siguiente licencia Creative Commons:  <http://es.creativecommons.org/blog/licencias/>

**WARNING.** The access to the contents of this doctoral thesis it is limited to the acceptance of the use conditions set by the following Creative Commons license:  <https://creativecommons.org/licenses/?lang=en>

**Chiral cyclobutane scaffolds:  
their application in the the development  
of new functionalized organogelators,  
organocatalysts and MRI contrast  
agents**

**Oriol Porcar Tost**

**Tesi Doctoral  
Estudi de Doctorat en Química**

**Supervised by:  
Prof. Rosa M<sup>a</sup> Ortuño Mingarro  
Dr. Ona Illa Soler**

**Departament de Química  
Facultat de Ciències**

**2017**



Memòria presentada per aspirar al Grau de Doctor per **Oriol Porcar Tost**

This thesis is presented for Graduation as Doctor by **Oriol Porcar Tost**

Vist i plau,

Read and approved,

Prof. Rosa M<sup>a</sup> Ortuño Mingarro

Dr. Ona Illa Soler

Bellaterra, 27 de setembre de 2017

Bellaterra, 27th of September 2017



## Acknowledgements

This thesis has been carried out in the *Departament de Química* of the *Universitat Autònoma de Barcelona (UAB)* under the direction of Professor Rosa M<sup>a</sup> Ortuño and Doctor Ona Illa. I truly would like to thank Rosa the opportunity to work in her group and participate in several projects that resulted in this thesis. I want to thank both of them, Rosa and Ona, for the scientific and financial support and the confidence placed in me.

Thanks to the *UAB* for the the financial support through a *Personal Investigador en Formació (PIF)* grant, without which the realization of this thesis would have not been possible.

I would like to thank Dr. Eva Jacob Toth for giving me the chance to work in her team in a three-month collaboration in the Centre de Biophysique Moléculaire (CBM) in Orléans, France. Also, I wish to thank Agnès Pallier for teaching me different methodologies and techniques during this collaboration. Thanks again to *UAB* for the financial support to carry out this stay.

Furthermore, I want to thank Professor Vicenç Branchadell for his collaboration in the projects contributing with interesting computational studies. I would like also to mention Dr. Jordi García-Antón for his help in Ru complexes related discussions. I do not forget the help received from Dr. Pau Nolis from *SeRMN* at *UAB* for carrying out structural studies and from Dr. Alba Eustaquio Ruiz for her help in mass spectrometry analysis.

Additionally, I would like to extend my thanks to all labmates I have been working with, Jimena, Bernat, Carme, Thomas, Jose, Chris, Maamar, Patrick and Saida for their useful advices and discussions and all the after-work nice moments we had together. Special mention to thesis mates and good friends, Bernat, Kirian, Albert, Alex, and Ana María, for the laughs, support and useful advices.

I want to thank all my family, specially my parents, my grandfather and my brother for their support and affection. Finally, my candid gratitude to Naroa. Without her affection and encouragement none of this would have been possible.

Moltes gràcies a tots!



*“If we knew what it was we were doing,  
It would not be called research, would it?”*

A. Einstein



Part of the results reported in this thesis have been published in the following scientific article:

- **Stereoselectivity of Proline / Cyclobutane Amino Acid-Containing Peptide Organocatalysts for Asymmetric Aldol Additions: a Rationale.**

Ona Illa, Oriol Porcar-Tost, Carme Robledillo, Carlos Elvira, Pau Nolis, Vicenç Branchadell, Oliver Reiser, Rosa M. Ortuño.

*Submitted to J. Org. Chem. Revised manuscript under preparation*

Other articles with the rest of the results are under preparation.

## Table of contents

1.1 Preface .....	13
1.2 Table of abbreviations .....	15
2. General Introduction.....	17
3. Synthesis and Supramolecular Studies of New Functionalized Organogelators .....	25
3.1 Introduction .....	27
3.1.1 Functional gelators.....	32
3.1.1.1 Functional gels as catalysts.....	34
3.2 Objectives .....	39
3.3 Results and discussion .....	41
3.3.1 Synthesis of new functionalized organogelators .....	41
3.3.1.1 Synthesis of protected <i>cis</i> - $\beta$ -amino acid <b>31</b> .....	43
3.3.1.2 Synthesis of protected <i>trans</i> - $\beta$ -amino acid <b>26</b> .....	44
3.3.1.3 Synthesis of dipeptide <b>DP</b> and <b>terpyDP</b> .....	45
3.3.1.4 Synthesis of hybrid tetrapeptides <b>TP</b> and <b>TPb</b> , and <b>terpyTP</b> .....	47
3.3.2 Gelation study of <b>terpyDP</b> and <b>terpyTP</b> .....	50
3.3.2.1 Scanning electron microscopy.....	52
3.3.2.2 Theoretical calculations .....	54
3.3.2.3 Circular dichroism and UV spectroscopy.....	62
3.3.3 Complexation of <b>terpyDP</b> and <b>terpyTP</b> with $\text{Ru}^{2+}$ and $\text{Pd}^{2+}$ .....	68
3.3.3.1 Preparation and gelation study of $\text{Ru}^{2+}$ and $\text{Pd}^{2+}$ complexes.....	69
3.3.3.3 Electrochemical studies of Ru complexes .....	71
3.3.3.4 Catalyzed reaction studies of $\text{Ru}^{2+}$ complexes.....	73
3.4 Summary and conclusions.....	77

## Table of contents

4. Synthesis of Proline / Cyclobutane Amino Acid-Containing Tripeptides: Organocatalysts for Asymmetric Aldol Additions.....	79
4.1 Introduction .....	81
4.3.1 Short peptides as organocatalysts .....	88
4.2 Objectives .....	93
4.3 Results and discussion .....	95
4.3.1 Synthesis of tripeptides .....	95
4.3.1.1 Synthesis of protected $\beta$ -amino acids <b>34</b> and <b>70</b> .....	97
4.3.1.2 Synthesis of protected $\gamma$ -amino acids <b>71</b> and <b>72</b> .....	98
4.3.1.3 Synthesis of tripeptides <b>A</b> , <b>B</b> , <b>C</b> and <b>D</b> .....	99
4.3.2 Catalyzed reaction studies .....	102
4.3.2.1 Aldol reactions using different aldehydes and ketones. ....	107
4.3.2.2 Michael reaction using <i>trans</i> - $\beta$ -nitrostyrene.....	109
4.3.3 Structural studies of catalyst <b>D</b> .....	110
5.3.4 Theoretical studies .....	116
5.3.4.1 Mechanistic study and stereoselectivity .....	117
4.4 Summary and conclusions.....	121
5. Gd <sup>3+</sup> and Mn <sup>2+</sup> Complexes of Open-chain Ligands as Potential New MRI Contrast Agents: Synthesis, Stability, Inertness, Structure and Relaxation Studies.....	123
5.1 Introduction .....	125
5.1.1 Contrast agents for MRI .....	128
5.1.2 Design of contrast agents .....	131
5.2 Objectives .....	137
5.3 Results and discussion .....	139
5.3.1 Synthesis of Ligands .....	139
5.3.1.1 Synthesis of protected <i>trans</i> -diamine <b>99</b> and <b>L1</b> .....	140
5.3.1.2 Synthesis of ligand <b>L2</b> .....	141

5.3.2 Potentiometric studies .....	142
5.3.3 Kinetic inertness studies .....	151
5.3.4 Luminescence studies for determining $q$ .....	158
5.3.4.1 Anion binding studies .....	162
5.3.5 Relaxivity studies .....	166
5.3.5.1 NMRD Profiles .....	166
5.3.5.2 $^{17}\text{O}$ NMR studies.....	171
5.3.5.3 Physicochemical parameters that rule the relaxivity.....	174
5.4 Summary and conclusions.....	179
6. General Conclusions .....	181
7. Experimental Methodologies .....	185
7.1 $^1\text{H}$ NMR and $^{13}\text{C}$ NMR spectroscopy .....	187
7.2 Infrared spectroscopy (IR) .....	188
7.3 High resolution mass spectrometry (HRMS) .....	188
7.4 UV spectroscopy.....	188
7.5 Circular dichroism spectroscopy (CD) .....	188
7.5.1 CD in solution .....	188
7.5.2 CD in xerogel phase.....	189
7.6 Scanning electron microscopy (SEM).....	190
7.7 Chromatography .....	190
7.7.1 Flash chromatography .....	190
7.7.2 Gas chromatography (GC).....	191
7.7.3 High-performance liquid chromatography (HPLC) .....	191
7.8 Electrochemical studies .....	191
7.9 Gelation studies .....	192
7.10 Sample preparation for metal complexes .....	193

## Table of contents

7.11 Potentiometric studies .....	193
7.12 Kinetic measurements .....	195
7.13 Lifetime measurements .....	195
7.14 Relaxometric measurements .....	196
7.14.1 Equations used for the analysis of the NMRD profiles.....	197
7.15 Temperature-dependent $^{17}\text{O}$ NMR spectroscopy .....	199
7.15.1 Equations used for the analysis of the $^{17}\text{O}$ NMR.....	200
7.16 Other details .....	203
7.17 Computational details .....	204
7.18 Synthetic procedures .....	205
7.19 Details for the catalysis presented in chapter 3 .....	261
7.19.1 General epoxidation for uncatalyzed reactions .....	261
7.19.2 General epoxidation for catalyzed reactions .....	261
7.19.3 Experimental data of the catalyzed reaction products .....	262
7.20 Details for the catalysis presented in chapter 4 .....	264
7.20.1 General procedure for catalytic asymmetric aldol reactions .....	264
7.20.2 General procedure for catalytic asymmetric Michael reactions.....	265
7.20.3 Experimental data of the catalyzed reaction products .....	265
8. Bibliography.....	271

## 1.1 Preface

In this thesis, three different systems containing a cyclobutane-based scaffold were synthesized and studied as gelators, catalysts or contrast agents. The structure of this thesis is organized first with a general introduction (chapter 2) with precedents of our research group. The results of the present thesis are presented in three different chapters (3-5), which are divided in different sections: introduction, objectives, results and discussion and conclusions. Then, the general conclusions of all results are summarized in chapter 6. Finally, the Experimental methodologies are explained in chapter 7.

**Chapter 3.** Two peptide-based low molecular weight gelators previously studied in our group were functionalized with a terpyridine derivative. The influence of this added function was determined in the final gelation behaviour. This study was performed by tube inversion test, scanning electron microscopy, circular dichroism and theoretical calculations. These new gelators were complexed with some metal ions in order to obtain metallogelators. The influence of the metal ion in the gelation ability was also studied.

**Chapter 4.** Different new hybrid tripeptides containing two proline units and a cyclobutane-based amino acid were synthesized and studied as organocatalysts for aldol reactions. The results were rationalized by conformational mechanistic studies using NMR, circular dichroism and theoretical calculations.

**Chapter 5.** Two new linear ligands containing a cyclobutane-based diamine were synthesized and complexed with different paramagnetic metal ions. The thermodynamic stability, kinetic inertness, and the hydration number of these complexes were studied using different techniques. They were studied as potential contrast agents for magnetic resonance imaging (MRI) using different NMR methodologies.



## 1.2 Table of abbreviations

AFM	Atomic force microscopy
Boc	<i>tert</i> -Butyl carbamate
CBAA	Cyclobutane-based amino acid
Cbz	Benzyl carbamate
CD	Circular dichroism
COSY	Correlation spectroscopy
CV	Cyclic voltammetry
DFT	Density functional theory
DiPEA	<i>N,N</i> -Diisopropylethylamine
DMAP	4-Dimethylaminopyridine
DMF	Dimethylformamide
DMSO	Dimethylsulfoxide
DPV	Differential pulse voltammetry
d.r.	Diastereomeric ratio
EDX	Energy dispersive X-ray
e.r.	Enantiomeric ratio
ESI	Electrospray ionization
FDPP	Pentafluorophenyl diphenylphosphinate
GC	Gas chromatography
HMBC	Heteronuclear multiple-bond correlation
HPLC	High-performance liquid chromatography
HRMS	High resolution mass spectrometry
HSQC	Heteronuclear single quantum correlation
IR	Infrared
LMWG	Low molecular weight gelator
<i>mgc</i>	Minimum gelation concentration
NMR	Nuclear magnetic resonance
NOE	Nuclear Overhauser effect
NOESY	Nuclear Overhauser enhancement spectroscopy
PLE	Pig liver esterase
PyBOP	(Benzotriazol-1-yloxy)tripyrrolidinophosphonium hexafluorophosphate
PNBA	<i>p</i> -Nitrobenzoic acid



ROE	Rotating-frame nuclear Overhauser effect
ROESY	Rotating-frame nuclear Overhauser effect correlation spectroscopy
r.t.	Room temperature
s.d.	Standard deviation
SEM	Scanning electron microscopy
TFA	Trifluoroacetic acid
THF	Tetrahydrofurane
TLC	Thin layer chromatography
TS	Transition state
UV	Ultraviolet light
Vis	Visible light

## **2. General Introduction**

---



## 2. General Introduction

In the last decade, our research group *Synthesis, Structure and Chemical Reactivity (SERQ)* has been interested in the use of a disubstituted cyclobutane moiety as conformational restriction element in the synthesis of several chiral new compounds and their use in a wide variety of applications.<sup>1-4</sup> Different enantioselective synthesis and methodologies were developed to achieve these compounds in an enantioselective manner. The presence of the highly constricted four-membered ring in the molecules provides rigidity and two chiral centers of known configuration.

Mainly, two different disubstituted cyclobutane-based compounds have been prepared in our research group; the 1,2- or  $\beta$ -substituted (Figure 1), and the 1,3- or  $\gamma$ -substituted ones (Figure 2). The 1,2-substituted cyclobutane-based compounds can be obtained from a photochemical reaction between ethylene and maleic anhydride and the resulting achiral product can be easily desymmetrised by a chemoenzymatic approach. Then, selective manipulation of the functional groups and introducing epimerization steps allowed to synthesise all possible isomers in an enantiopure form.<sup>5</sup>

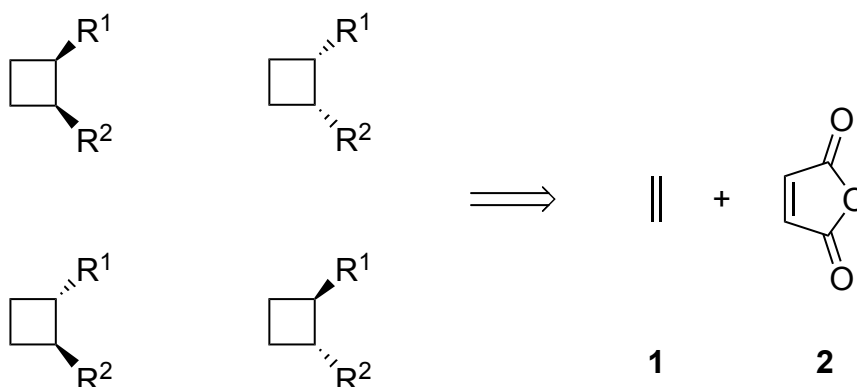


**Figure 1.** Schematic representation of all 1,2-substituted cyclobutane-based isomers and their synthetic precursors.

## 2. General Introduction

The 1,3-substituted cyclobutane based compounds can be obtained from (–)-verbenone (**3**) or from (–)- $\alpha$ -pinene (**4**) (Figure 2). Both compounds can be commercially obtained in a reasonable price in an enantiopure form. (–)-verbenone (**3**) and (–)- $\alpha$ -pinene (**4**) can be oxidized and selective function manipulations can lead to the desired compound.<sup>6</sup> Unlike 1,2-substituted compounds, only *cis* 1,3-disubstituted cyclobutane-based compounds can be easily obtained from the chiral pool.

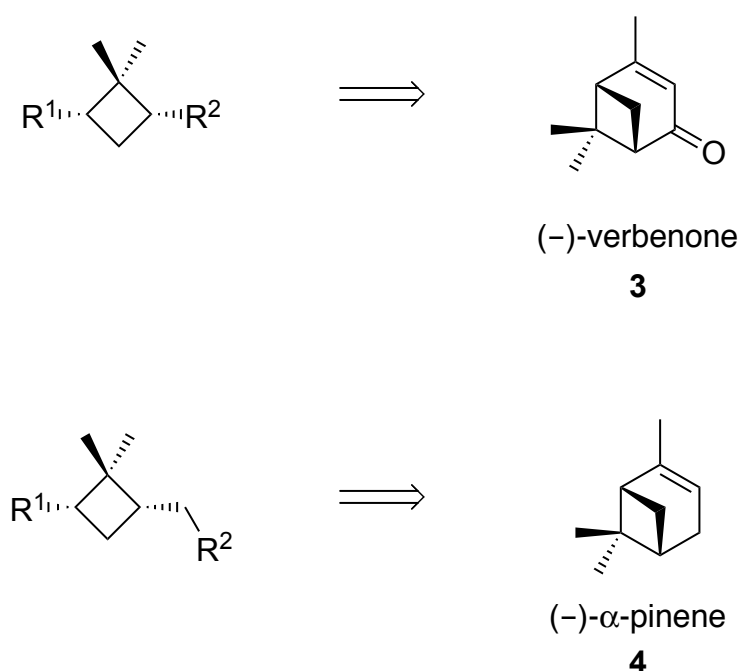


**Figure 2.** Schematic representation of 1,3-substituted cyclobutane-based compounds used in our research group and their synthetic precursors.

Many investigations have proved that the conformational restriction of small molecules with potential biological activity is crucial to guarantee unique interactions with the target receptor and to increase their metabolic stability and activity.<sup>7–10</sup> One of the main topics of our research group is the synthesis of optically active cyclobutane-based amino acids (CBAA) and their incorporation in peptides which could be used in different applications. The rigidity of 1,2-substituted cyclobutane-based scaffold and their relative and absolute stereochemistry have proven to be relevant issues in the stabilization of the well-defined secondary

## 2. General Introduction

structures and to play relevant roles in the properties of various homo or hybrid peptides and other derivatives in which they have been incorporated.<sup>11,12</sup> In general, 1,2-CBAA moiety, as part of a peptide, can give rise to two types of hydrogen-bonded arrangements, either an intra-residue 6-membered ring and inter-residue 8-membered ring (Figure 3).<sup>13</sup> On the other hand, *cis*-cyclobutane  $\gamma$ -amino acids have been incorporated in short peptides with interesting properties and they have been studied as foldamers.<sup>14</sup> In general, the structures adopted of  $\gamma$ -CBAA compounds are extended, and intra-residue 7-membered hydrogen-bonded rings between the carbonyl group substituent of the cyclobutane ring and the amino group are observed.

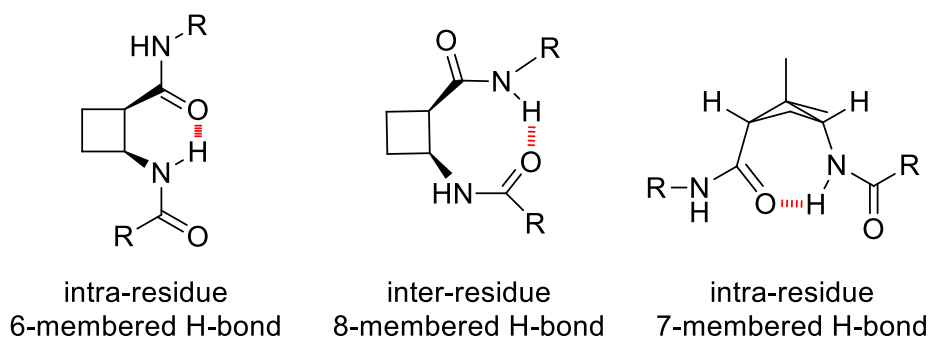


**Figure 3.** Intra- and inter- residue hydrogen bond (remarked in red) in peptides that incorporate either *cis*- $\beta$ -CBAA or *cis*- $\gamma$ -CBAA.

The cyclobutane moiety not only has been used as amino acids in peptide synthesis but also in the synthesis of different compounds. Advantages given by the rigidity and the well-known conformation of these building blocks have been applied in different fields. There are some examples of cyclobutane-based compounds related to the different fields of this thesis. In that case, they are explained in the introduction of each chapter.

Figure 4 shows different examples of  $\beta$ -substituted cyclobutaned-based compounds used in different applications, such as diamine **5** or compound **6** that was screened for the first time as ligand of metalloproteases (MCPs).<sup>2,15</sup> It showed moderate selective inhibitory activity against mammalian MCPs and

## 2. General Introduction

offered a valuable alternative in the design of novel inhibitors for disease-linked metalloproteases. Considering catalytic studies of Takemoto and coworkers,<sup>16</sup> cyclobutane-based thiourea **7** and other related compounds were studied as catalyst in the Michael reaction, resulting in good yields and moderate enantioselectivities.<sup>17</sup> Finally, the cyclobutane scaffold has been applied in the field of materials, like organobridged silsesquioxanes **8** and **9** or conductive material **10**.<sup>18,19</sup>

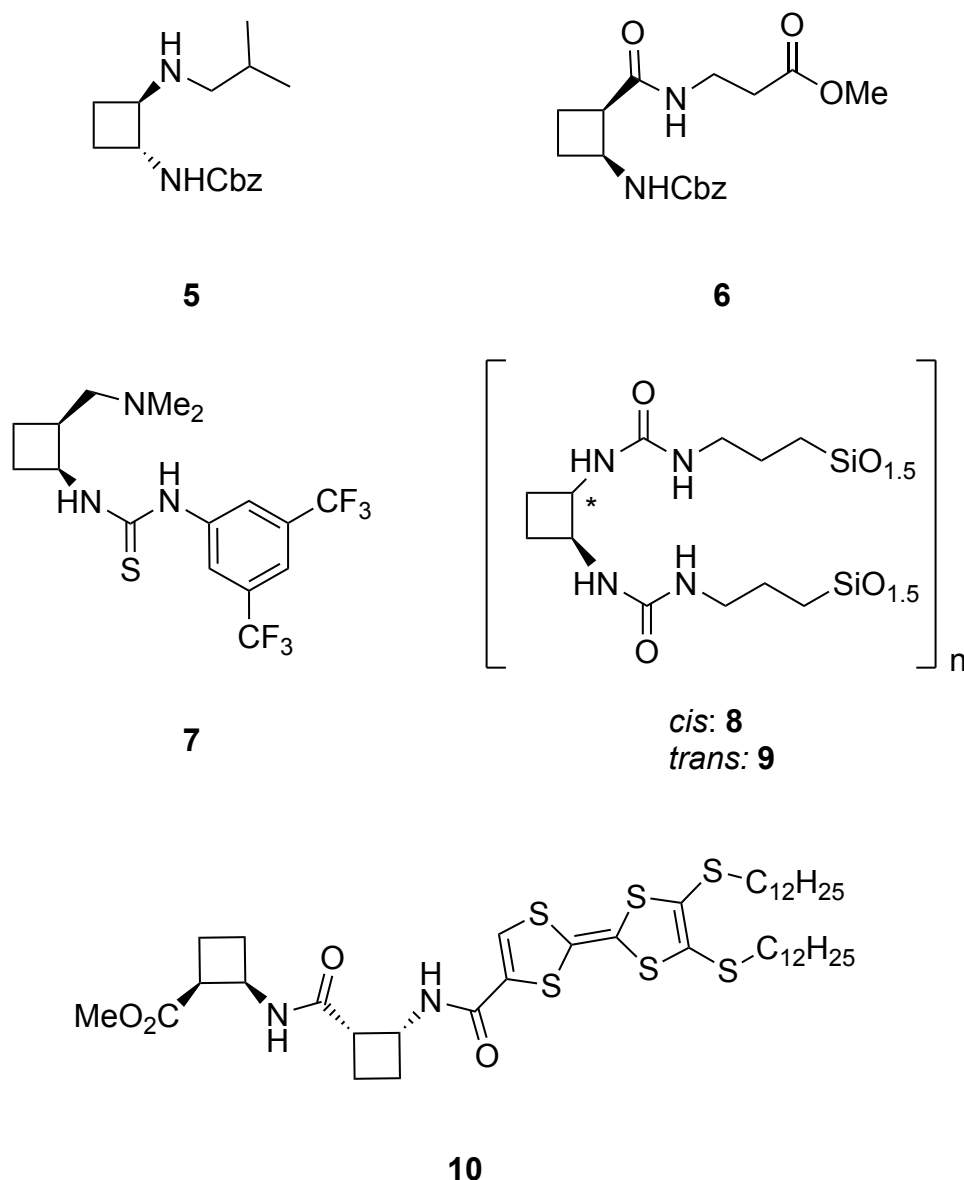


**Figure 4.** Structures of different 1,2-disubstituted cyclobutane-based compounds synthesized in our research group.

## 2. General Introduction

$\gamma$ -Substituted cyclobutane-based compounds have been also applied in different fields (Figure 5). Diamine **11** performed as ruthenium nanoparticles stabilizer with good catalytic properties in the hydrogenation of arenes and nitrobenzenes derivatives,<sup>3</sup> while amino acid **12** is a good example of zwitterionic surfactant.<sup>20</sup> Peptide **13** was evaluated as cell penetrating peptide, resulting in lower toxicity and similar cell-uptake properties when compared with other peptidic agents.<sup>21</sup> The introduction of cyclobutane residues inside the peptidic sequence afforded a good balance between charge and hydrophobicity. The last example is  $C_3$ -symmetric peptide dendrimer **14** which could be further elongated and functionalized for future applications in the field of chiral materials.<sup>22</sup>

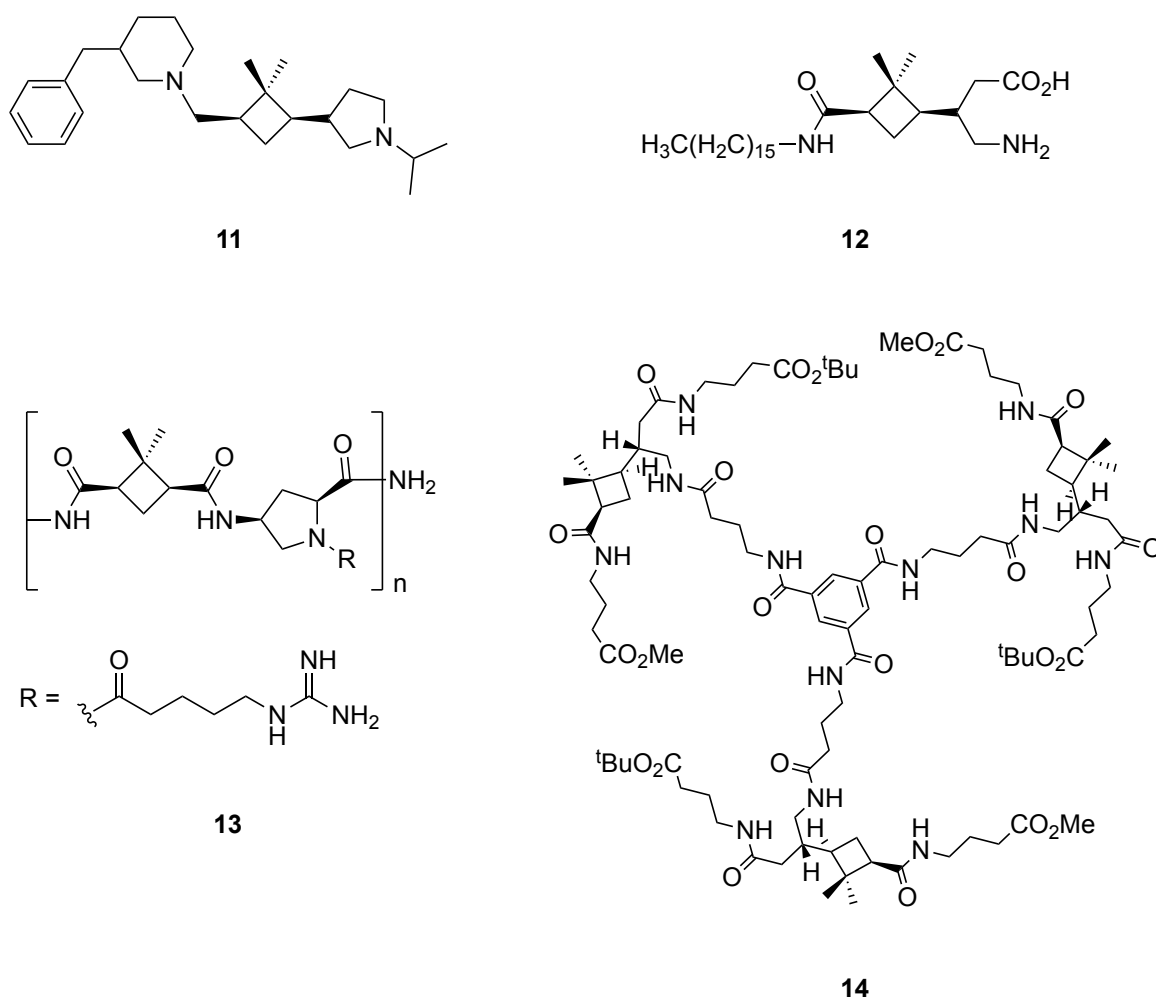


**Figure 5.** Structures of different 1,3-disubstituted cyclobutane-based compounds synthesized in our research group.



## 2. General Introduction

In this thesis, the chiral cyclobutane scaffold is the common motif in various compounds that have found application as: functionalized organogelators, hybrid peptides as organocatalysts, and  $\text{Gd}^{3+}$  and  $\text{Mn}^{2+}$  complexes as contrast agents for MRI.

### **3. Synthesis and Supramolecular Studies of New Functionalized Organogelators**

---



## 3. Synthesis and Supramolecular Studies of New Functionalized Organogelators

### 3.1 Introduction

Gels have been used in different fields such as cosmetics, medicine, and food. We can easily recognize them in our daily lives in shampoos, toothpastes or jellies.<sup>23</sup> Most of these examples are polymer-based hydrogels, because they consist of polymeric compounds in aqueous solvent. Although gels have been broadly used and studied for decades, a definition has been reached with difficulties from the scientific point of view. Lloyd noted about 90 years ago that "... the colloid condition, the gel, is easier to recognize than to define" or "if it looks like a jello it must be a gel".<sup>24</sup> Since then, more definitions were proposed to concrete and define the gel state. Nowadays, it is widely accepted that a liquid system consisting in two or more components becomes a gel when one of these components forms a 3-dimensional entangled solid network within the bulk liquid phase.<sup>25,26</sup> Thus, a gel should contain low concentrations of gelators in a solvent, and macroscopically, it should appear solid-like despite being mostly liquid.

Gels can be classified in two big categories; chemical gels and physical or supramolecular gels. Chemical gels are formed by covalent bonds, such as polymer-based gels, while physical gels are built by non-covalent interactions. Physical gels can be reversible between solution and gel phase by applying a stimulus to the sample, such as temperature, since the supramolecular interactions that build the gel are also tunable. This sol-gel transition process is usually thermoreversible without deterioration for many times.<sup>27,28</sup>

Depending on the nature of the solvent, gels can also be classified as organogelators, based on organic solvents, or hydrogelators, based on aqueous solvent. It should be mentioned that some authors relate the word "organogel" with the nature of the gelator (an organic compound) and not with the solvent.

In the last years, the interest of low molecular-weight gelators (LMWGs) has grown significantly, since they possess very interesting properties and have a huge potential for different applications.<sup>29</sup> These compounds are small organic molecules

## Chapter 3

that are able to gelate organic solvents or water to form physical or supramolecular gels. The structure of LMWGs can be very different, but all of them have in common that their self-assembly into fibrous networks is mainly motivated by supramolecular forces such as hydrogen bonding, van der Waals,  $\pi$ -, or dipolar interactions, or even metal coordination. These fibered structures are interconnected between themselves to create three dimensional networks that can immobilize the solvent molecules. Usually, an organogel is prepared by heating the gelator in the appropriate solvent until a clear isotropic solution is formed, and after, the mixture is cooled down. Since most supramolecular gels are in a metastable state, their formation is governed by kinetics and thermodynamics. From a microscopic point of view, the gelation process was not been deeply elucidated, but most researchers agree that the assembly of the gelators could involve the hierarchical process shown in Figure 6.<sup>25,26,30</sup>

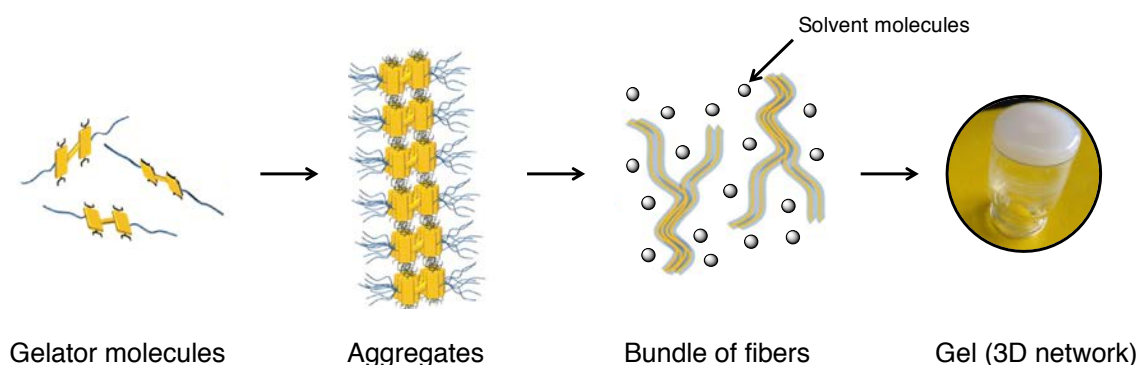


**Figure 6.** Proposed process for the supramolecular gel formation.

First of all, two discrete organic molecules self-assemble forming dimers, that further aggregate, usually in only one dimension, through multiple and complementary intermolecular interactions. Then, these oligomers aggregate into long scale structures, such as rods or fibers, and additional development creates for example bundles of fibers. These elongated structures are able to further interconnect themselves immobilizing the solvent molecules to build 3D networks, forming the gel.

Thus, the design of new gelators should take into account this mechanism. Introducing molecular functions that are able to aggregate might enhance the supramolecular interactions, but other effects have to be taken in consideration. For instance, it was found that solvophobic effects play an important role in the gelation process. Generally, reducing the overall solubility of the gelator contributes positively to the gelating ability. This effect can be modified by introducing functional groups or moieties in the gelator molecule that are poorly soluble in the solvent to be gelled. In Figure 7, the structure of various low molecular weight gelators is shown.

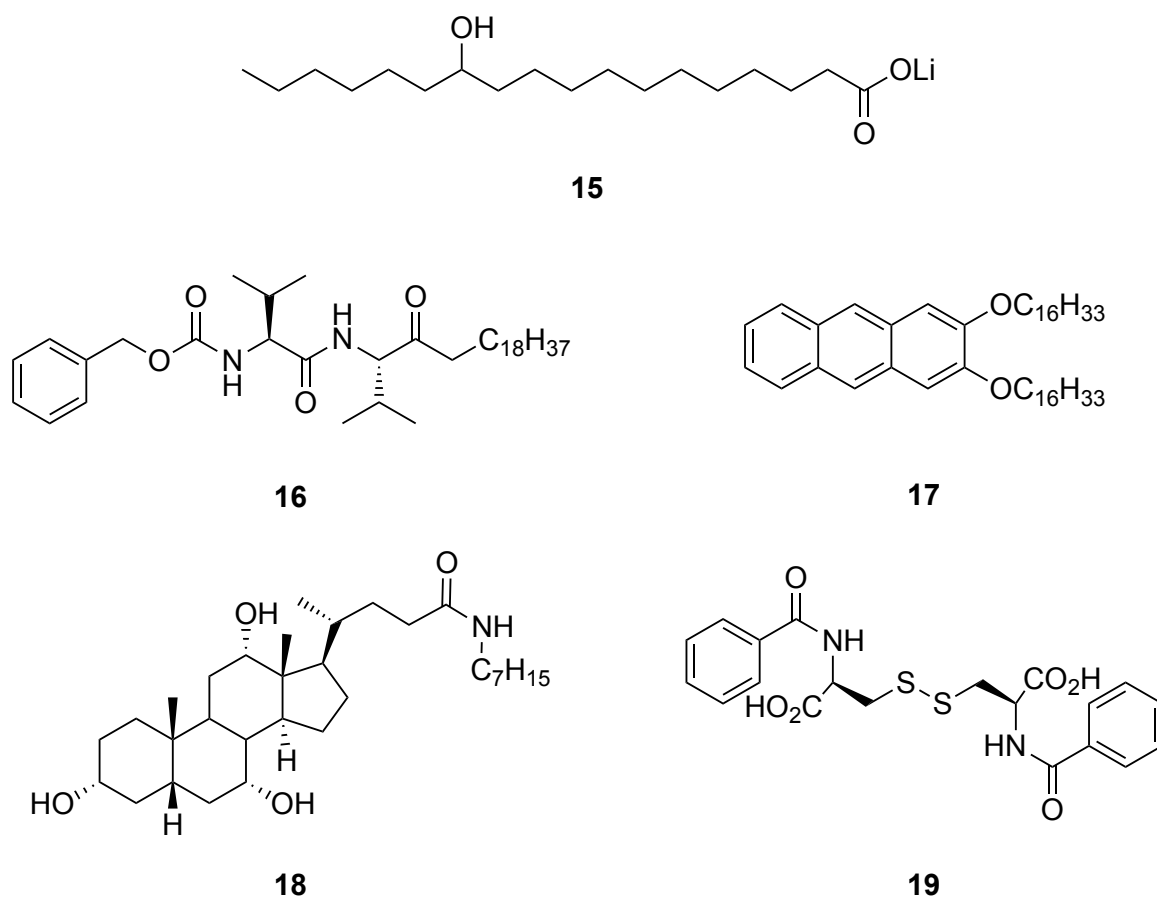


**Figure 7.** Structures of different LMWGs.

Some gelators are related to amphiphiles, like compound **15**, which aggregates with different intermolecular interactions, like ionic interactions, van der Waals interactions between the alkyl chains or hydrogen-bonding interactions

## Chapter 3

between hydroxyl groups. Other gelators are based on aminoacids or peptides (**16** and **19**),<sup>31,32</sup> ethers (**17**)<sup>32</sup> or steroids (**18**).<sup>35</sup> Some functions, like the presence of aromatic groups in **17** and **19**, contribute very positively to the gel formation due to two factors; the  $\pi$ -interactions for the aggregation, as well as the solvophobic effect reducing the solubility. These compounds become even more interesting when the gelators are chiral, like **16**, **18** or **19**. The resulting gel from a chiral gelator should present supramolecular chirality features, making these soft materials very interesting for different applications, such as catalysis or as chiral sensors.<sup>36-39</sup>

Although, it is known that some functions promote the gelation, a rational design of new gelators is not straightforward. A large library of organogelators has been reported, but most of them were discovered by serendipity. Some researchers, have tried to rationalize the relationship between the molecular structure of the gelator with the resulting gel properties. In that context, our research group studied different LMWGs with different regiochemistry and relative configuration in order to clarify this problem (Figure 8).<sup>34</sup>

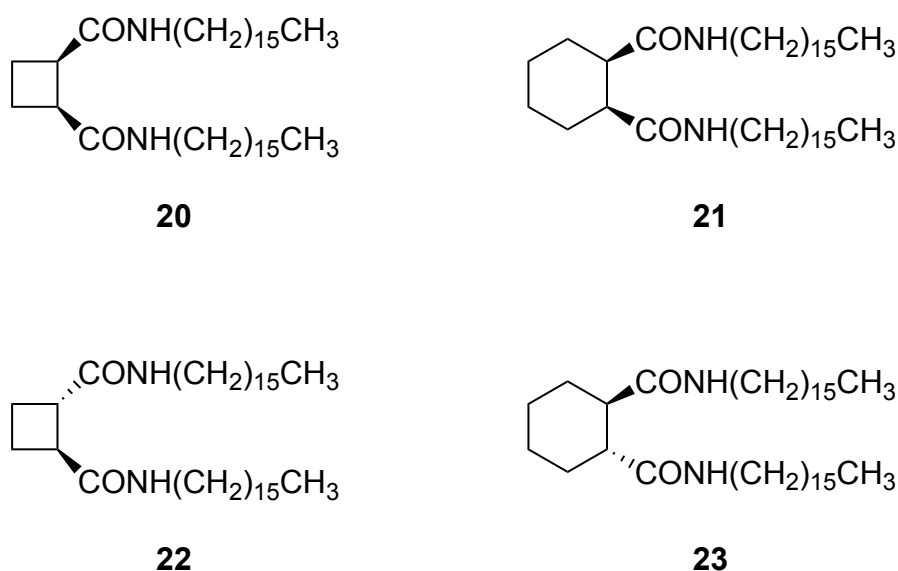


**Figure 8.** Structure of bisamide-based LMWGs studied in our research group.

The morphology and size of the aggregates were investigated. In the case of cyclobutane derivatives, the *cis/trans* stereochemistry was not relevant while it was remarkable for cyclohexane-based derivatives. All studied compounds, chiral **22**

and **23** and, surprisingly, **20** and **21**, that are *meso* achiral molecules formed chiral aggregates. These *meso* organogelators are an example of stochastic symmetry breaking induced by a stimulus (sonication), confirming that the chirality of the supramolecular structure can be different to the chirality of the gelator.

Also, our research group developed LMWGs constituted from small peptides formed by cyclobutane-based  $\beta$ -amino acids (Figure 9). Among all investigated peptides, the *trans*-cyclobutane-containing dipeptide, **DP**, performed as a good organogelator.<sup>40</sup> Later, another family of hybrid peptides presenting a cyclobutane-based  $\beta$ -amino acid joined in alternation with linear amino acids such as glycine (**TP**),  $\beta$ -alanine and  $\gamma$ -aminobutyric acid, were found to be good LMWGs in several solvents.<sup>41</sup>

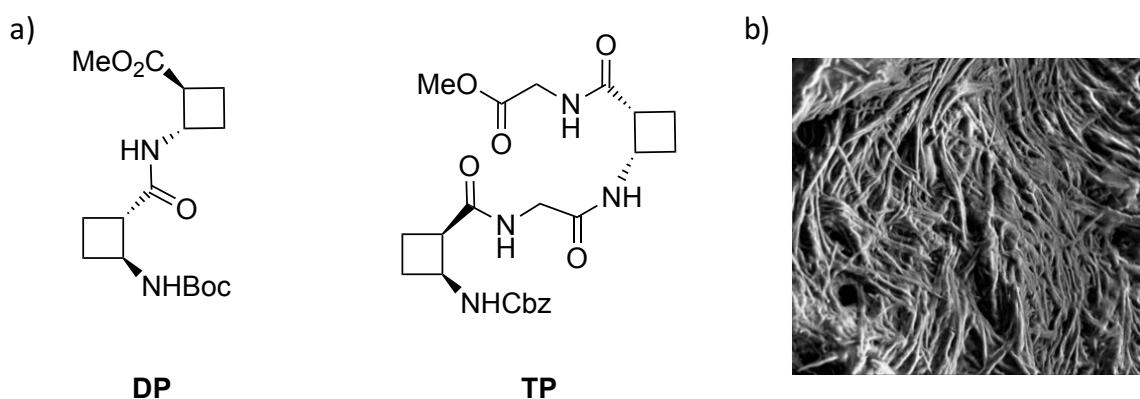


**Figure 9.** a) Peptide-based organogelators developed in our research group. b) SEM image of **TP** in a xerogel form.

The gels were characterized by different techniques, such as the tube inversion test, NMR, circular dichroism or scanning electron microscopy. SEM images of **TP** confirmed the fibers formation and computational calculations were used to explain that the self-assembly process of individual molecules to form the aggregates is mostly governed by H-bonding.



### 3.1.1 Functional gelators.

Although the understanding of the relation between molecular structure and the gel properties is still challenging, new LMWGs with secondary functionalities (in addition to the gelation behaviour) have been developed. For example, organogels have been used as sensors, catalysts, to grow liquid crystals, or as photoresponsive and conductive materials.<sup>16–18</sup> In some cases, this progress has been possible using the named “scaffold or modular approach”, which consists in introducing functional moieties at defined positions of a well known gelator. Unmistakably, the incorporation of new functions can deeply affect the aggregation process due to steric constraints, or even can change the solubility, modifying the overall gelation ability.

The 3D networks of gels are maintained by a subtle equilibrium between the aggregation of gelators and the interactions between the gelators and the solvent. Beside the parameters that influence the formation of the gel, such as concentration or temperature, external forces or stimulus can modify the reversibility or the behaviour of the resulting gel. For example, by introducing photoresponsive or electroactive functions in the gelator (Figure 10), the gel-sol process responded not only to thermal stimuli but also to redox reactions and light irradiation.<sup>45</sup>

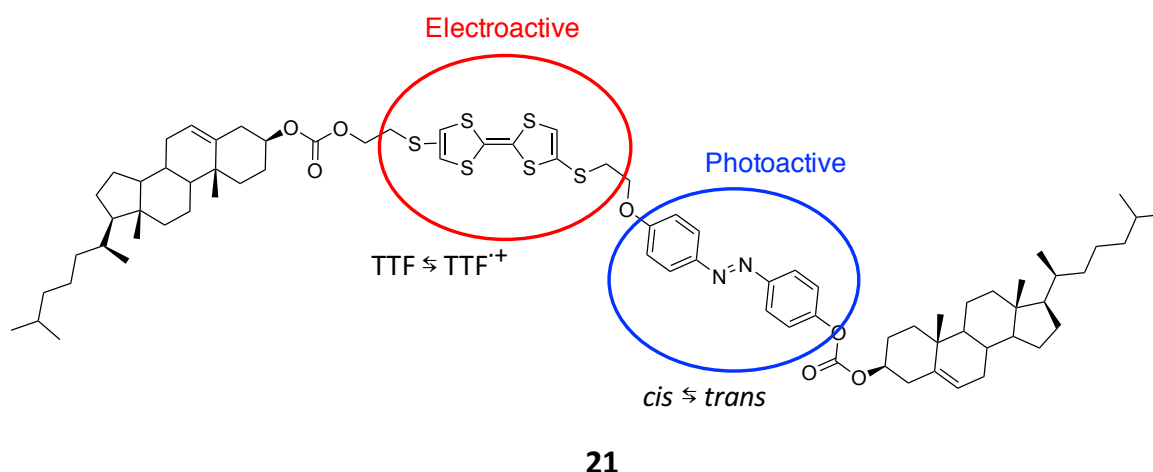


**Figure 10.** Chemical structure of a reversible multistimuli organogelator, **21**.

More recently, metal ions have been incorporated into LMWGs forming compounds called metallogelators.<sup>46–49</sup> These compounds are able to combine the interesting properties of metal complexes with gelator molecules to exhibit very promising optical, magnetic or catalytic applications.<sup>50</sup> Metallogelators could be divided into three categories (Figure 11):

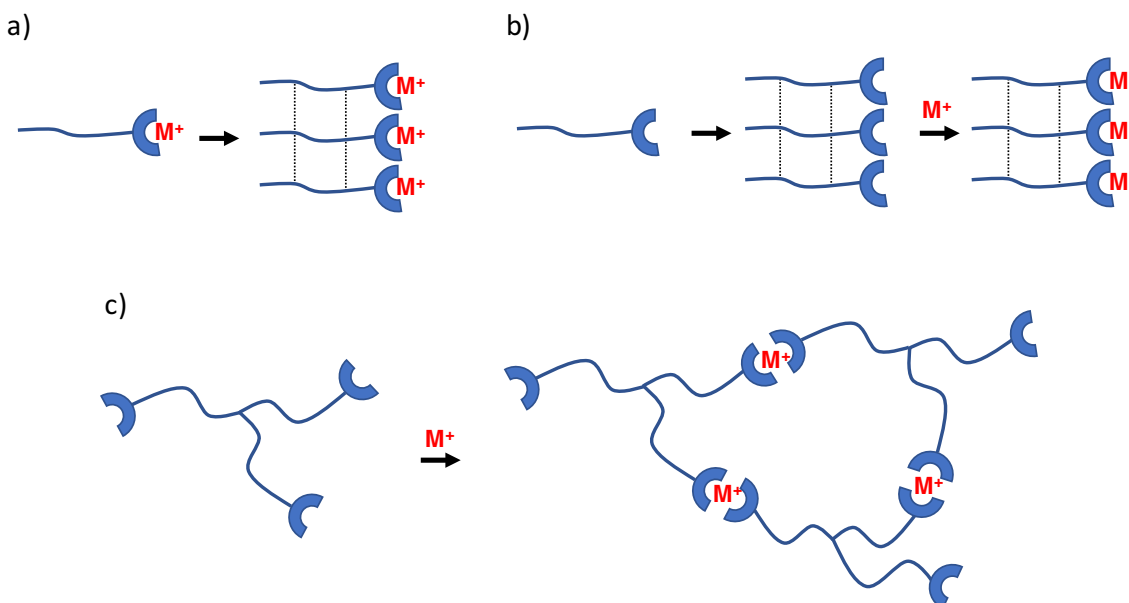


**Figure 11.** Classification of different types of metallogels.

- Discrete metallogelators. A gelator that already contains a metal ion is used to immobilize solvent molecules through non-covalent interactions, such as hydrogen-bonding interactions due to the functions of the ligand, or metal-metal interactions.
- Multitopic ligands. The gel network is built with free ligand sites and after the metal ion is coordinated.
- Coordination polymers. The formation of the metallogel is induced by the metal ligand coordination upon addition of metal ions. The resulting cross-linked coordination polymer traps the solvent molecules and usually do not present thermoreversibility.

Coordination polymer-based metallogelators have been used, for example, for the preparation of luminescent supramolecular gels (Figure 12). Lanthanide

## Chapter 3

directed self-assembly formation generated metallogels that gave a variety of luminescent colors depending on the  $\text{Eu}^{3+}/\text{Tb}^{3+}$  and ligand stoichiometric ratios.<sup>51</sup>

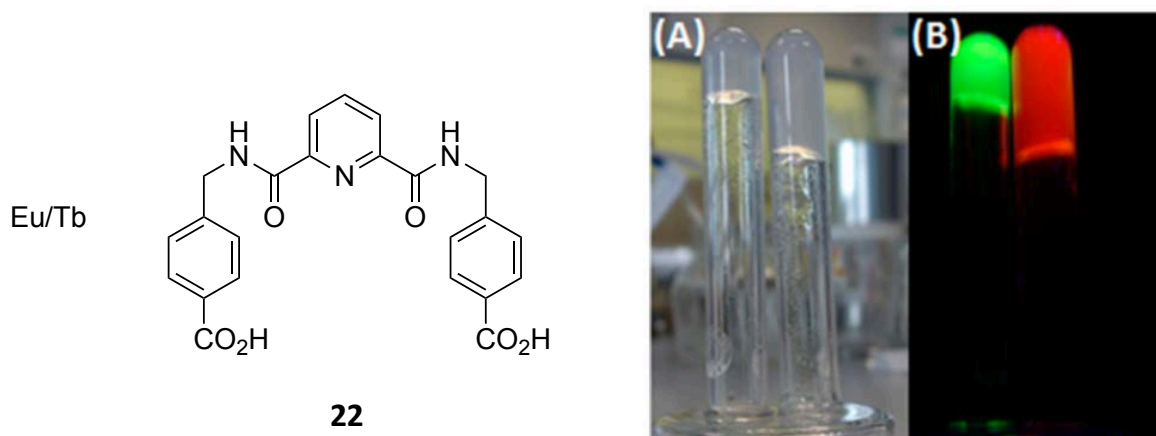


**Figure 12.** Structure of gelator **22** and metallogels formed with **22** and  $\text{Eu}^{3+}$  and  $\text{Tb}^{3+}$  under daily light (A) and under UV light (B).

### 3.1.1.1 Functional gels as catalysts

The interest of studying the reactivity of several organic reactions in organised assemblies has grown significantly. The use of self-assembled microreactors such as micelles, vesicles or nanocapsules in chemical reactivity has been deeply studied during the last decades. Taking into account this approach, the use of functional molecular gels as containers for chemical reactions has been considered, and the few examples found gave promising results.<sup>52</sup> Catalytic gelators can be designed using the “scaffold approach”, by combining assembling fragments with catalytic functions. Using these functional gelators, a supramolecular material with built-in catalytic sites could be formed. The organization of multiple catalytic sites in the fibre structure could originate new catalytic features such as cooperativity, multivalent interactions or neighbouring effects. Furthermore, high ordered chiral supramolecular structures could induce regioselective, or even if they are chiral, stereo or enantioselective transformations (Figure 13).

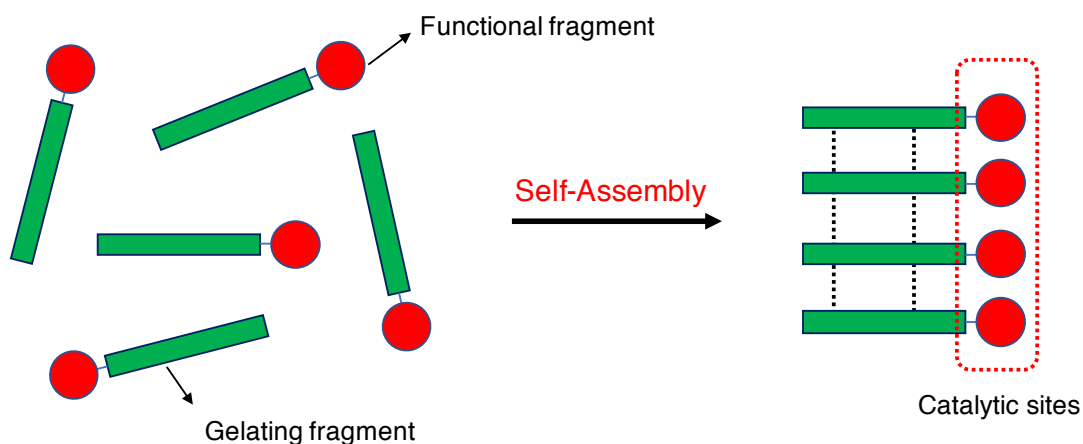


**Figure 13.** Schematic representation of functional gelators used in catalysis.

Considering that idea, Miravet and Escuder designed *L*-valine-based gelators containing *L*-proline moieties as catalytic fragments, like gelator **23**, and studied them as catalyst in gel and in solution for the Henry nitroaldol reaction (Figure 14).<sup>43</sup> For the study of the catalytic activity in gel phase, first of all, the gel was prepared using nitromethane and the reactants were left to diffuse into the gel. After the reaction time, the gel was disassembled by addition of acid and an organic solvent, and the gelator and the products were separated from the aqueous and organic phase. Furthermore, the gelator could be reused without losing efficiency. The results showed that the formation of the catalytic gel was associated to a basicity boost of the *L*-proline. The reaction in gel phase was promoted through an ionic pair type mechanism, while using the same gelator in solution an iminium-based mechanism was responsible for the formation of the dehydrated product. Pitifully, although the gelator was chiral, no enantioselectivity was observed. So, for the first time a big change in the catalytic activity associated with supramolecular gelation was described.

## Chapter 3

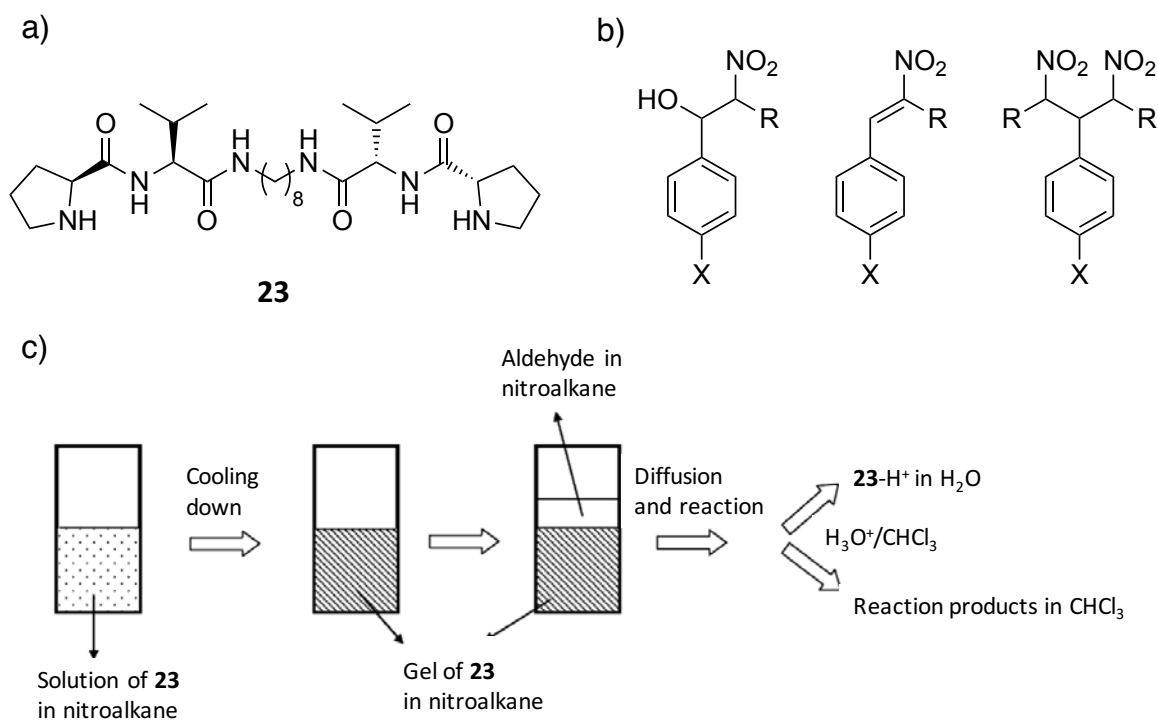


**Figure 14.** a) Chemical structure of gelator **23**. b) Different products for the Henry reaction. c) Scheme of an experimental procedure of catalysis in gel phase.

Metallogels can be also useful for catalytic applications. However, the use of metal complexes as gelators for the construction of gel-supported catalytic systems is still in its infancy. One of the very few examples found in the literature was the use of a palladium biscarbene complex as an air stable organometallic LMWG (Figure 15).<sup>53,54</sup> SEM images of gels of **24** in methanol showed a helical P ribbon morphology, which is rarely observed in gel networks formed by achiral compounds. Different structural studies indicated that the  $\pi$ -stacking of the heteroarene moieties, Van der Waals interactions between the alkyl chains, as well as the metal-metal interactions might be responsible for the aggregation. Catalytic test revealed that these gels were able to catalyse C-C formation reactions in gel state, for example a double Michael addition. Furthermore, their high stability allowed to test the catalytic reactions up to 50 °C without suffering thermal reversibility. Gels formed by different solvents revealed different catalytic activity, probably due to different structures of gel networks. Catalytic tests performed in gel

phase were faster than the observed results in solution, indicating that the supramolecular structure of the metallogel played an important role.

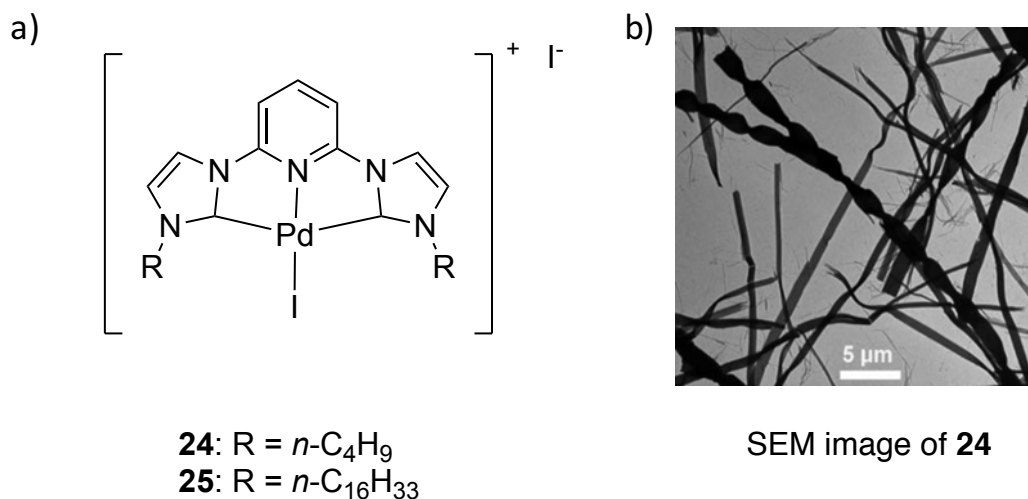


**Figure 15.** a) Structure of gelators **24** and **25** and b) SEM image of a gel formed by **24** in MeOH.

Despite the previous example, the typical problems associated with heterogeneous metal-based catalysts, such as leaching or catalyst inactivation, are also present in catalytic metallogels. Furthermore, additional problems related with the complexation of gel-supported catalyst, such as slow diffusion or disassembly of fragments in solution, make the development of new catalytic metallogels still a challenge nowadays.



## 3.2 Objectives

In this part of the thesis, the synthesis of two new functionalized LMWGs, **terpyDP** and **terpyTP**, was proposed using the “modular approach” to study the effect of the incorporated function in the gelation behaviour. Two well known peptide-based gelators, **TD** and **TP**, were considered to incorporate in their structure a terpyridine-based fragment, which could be precatalytic (Figure 16). Finally, the complexation of these compounds with different metals would give metallogelators that could have new catalytic properties.

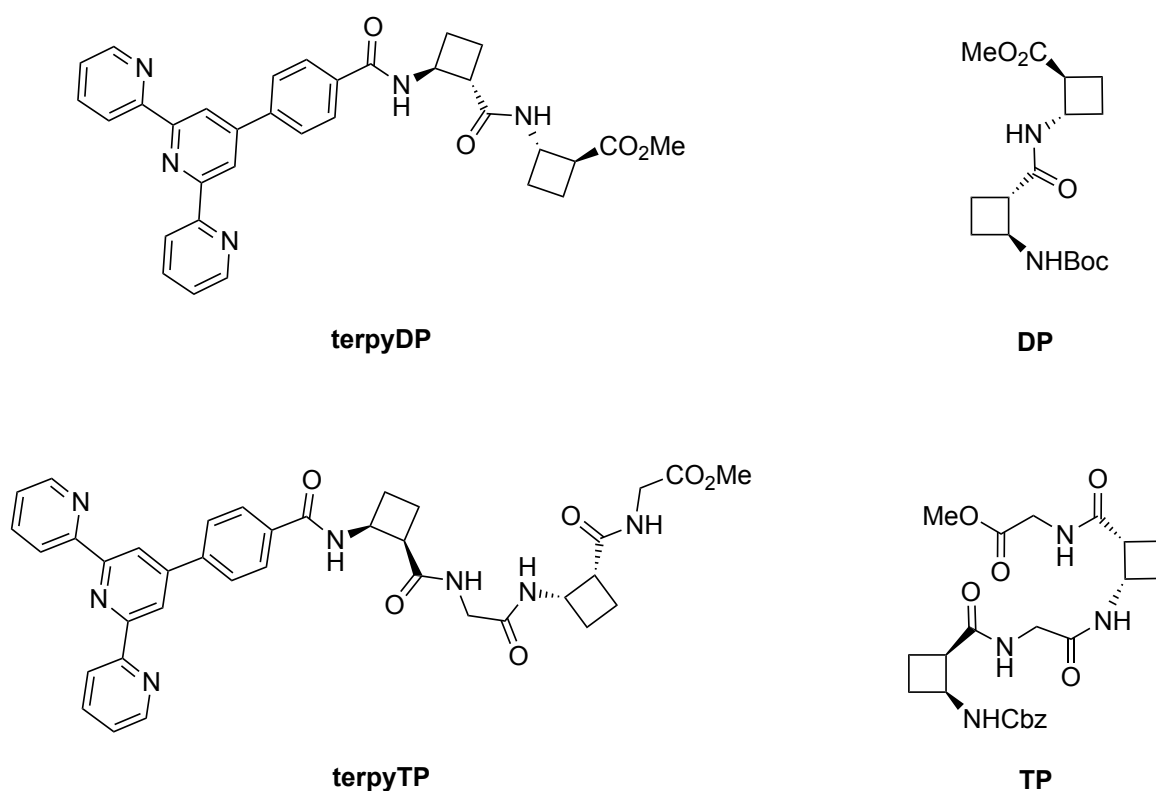


**Figure 16.** Structures of LMWGs **DP** and **TP** and the new **terpyDP** and **terpyTP**.

The objectives of this part are:

- The synthesis of these new possible LMWGs.
- The study of their gelation behaviour, the characterization of the structure of their aggregates by SEM, theoretical calculations and circular dichroism.



### Chapter 3

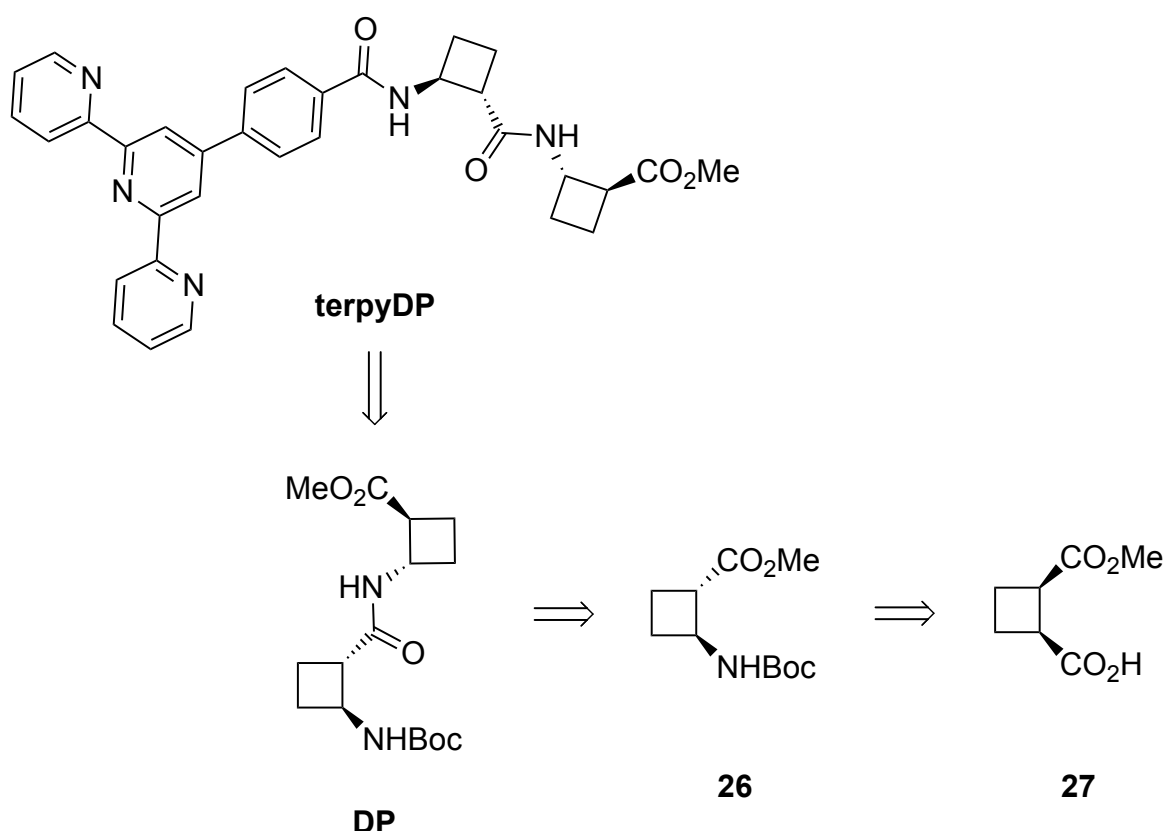
- The complexation of these compounds with  $\text{Ru}^{2+}$  and  $\text{Pd}^{2+}$  to prepare potential metallogels and to study their gelation behaviour.
- The study of the  $\text{Ru}^{2+}$  derivatives as catalytic materials in the epoxidation of alkenes.

### 3.3 Results and discussion

The results of this part of the thesis are presented in three parts. First, the synthesis of the new functionalized organogelators is described (section 3.3.1) After, the gelation study is explained (section 3.3.2) followed by the study of the complexes of these LMWG with different metal ions (section 3.3.3).

#### 3.3.1 Synthesis of new functionalized organogelators

Taking into account the acquired experience in our research group preparing enantiopure compounds,<sup>40,41</sup> the new functionalized organogelators **terpyDP** and **terpyTP** were synthesized through the following general retrosynthetic pathways, shown in Scheme 1 and Scheme 2, respectively.



**Scheme 1.** General retrosynthetic pathway of **terpyDP**.

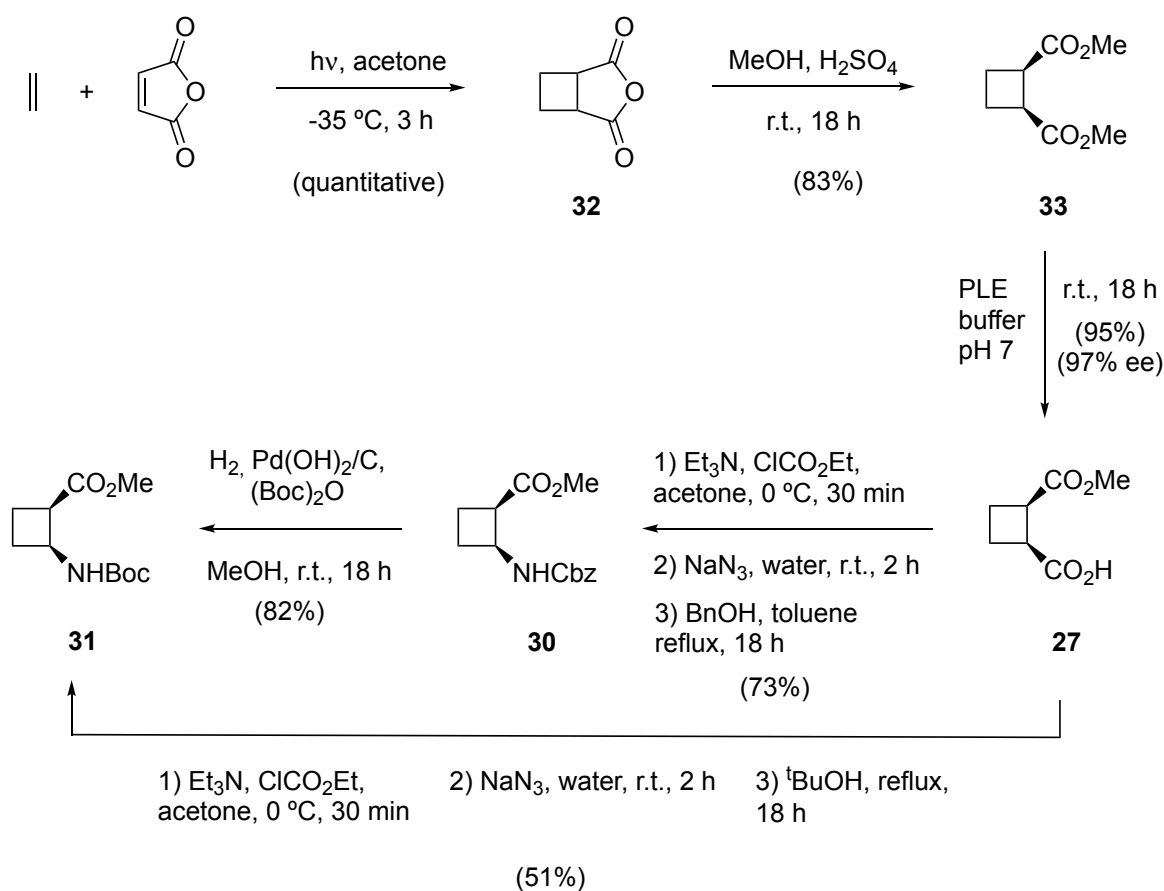


On the other hand, **terpyTP** was achieved by coupling **TPb** with the same terpyridine derivative and the hybrid tetrapeptide **TP** was synthesized from dipeptide **29**, which was synthesized from the coupling of *trans*- $\beta$ -amino acid **31** and a glycine derivative.

The synthetic routes for both compounds and the corresponding intermediates are explained below.

### 3.3.1.1 Synthesis of protected *cis*- $\beta$ -amino acid **31**

The synthetic route towards the protected *cis*- $\beta$ -amino acid **31** can be achieved in 4-5 steps in 47% overall yield. The synthetic route is described in Scheme 3.



**Scheme 3.** Synthetic route for amino acids **30** and **31**

## Chapter 3

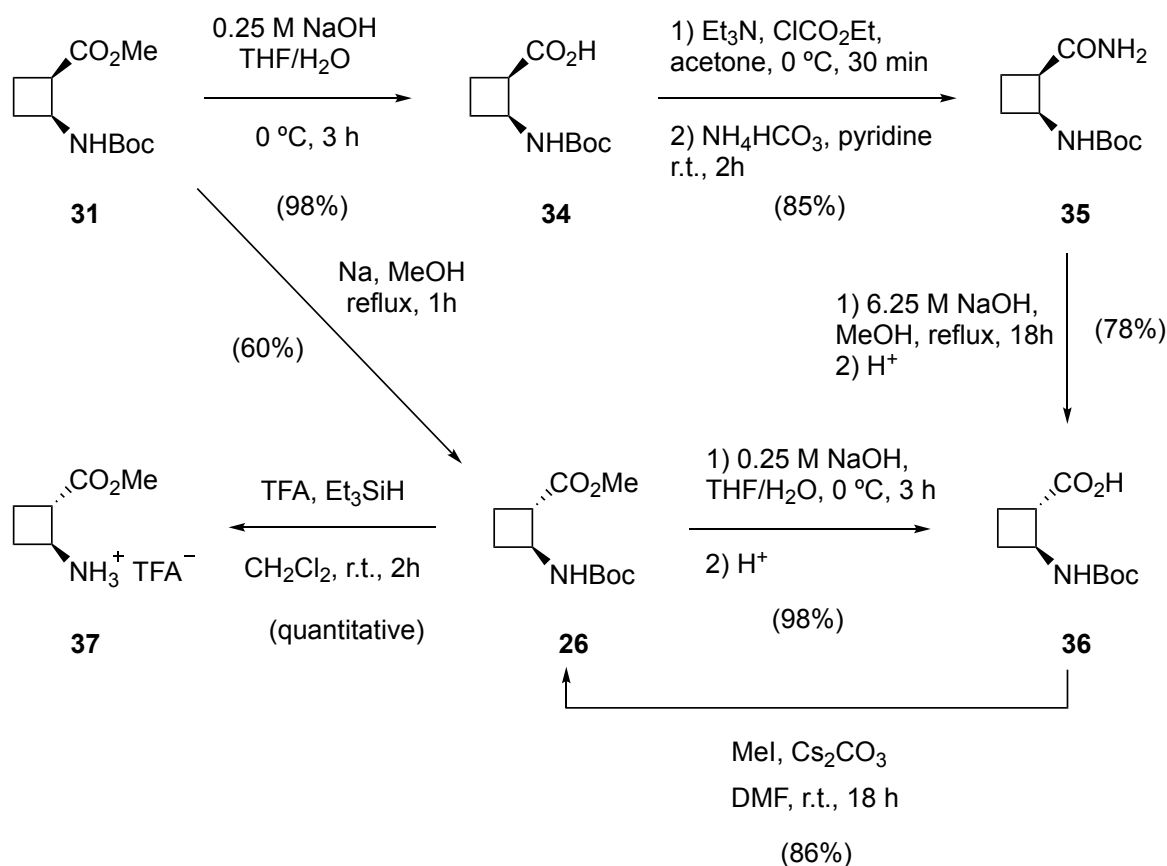
The cyclobutane ring was prepared following a [2+2] photochemical cycloaddition reaction from ethylene and maleic anhydride using acetone as a photosensitizer and as solvent.<sup>56</sup> Then, diester **33** was synthesized through Fischer esterification of the photoadduct **32** in 83% yield. In the next step, the optically active half-ester **27** was obtained through an asymmetric pig liver esterase-catalyzed hydrolysis in 95% yield and 97% ee. The fully protected amino acid **30** was prepared stepwise by treatment of **27** with ethyl chloroformate and triethylamine, followed by reaction with sodium azide. The resultant acyl azide was decomposed by heating to reflux in the presence of benzyl alcohol, affording compound **30** in 73% yield. Finally, Pd-catalyzed hydrogenation in the presence of Boc anhydride, provided the amino group in **31** protected as a *tert*-butyl carbamate.

Compound **31** can also be obtained directly from **27** by a three steps procedure including a Curtius rearrangement in neat *tert*-butanol, however, due to its poor nucleophilic character the yield is 51%.

### 3.3.1.2 Synthesis of protected *trans*- $\beta$ -amino acid **26**

The synthetic route of the protected *trans*- $\beta$ -amino acid **26** can be achieved in 1 or 4 steps in 60% overall yield from amino acid **31**. The synthetic route is described in Scheme 4.

The preparation of the protected *trans*- $\beta$ -amino acid **26** could be easily achieved by the transformation of the methyl ester **31** into amide **35** and subsequent epimerization at the carbonyl  $\alpha$ -position. Afterwards, the basic hydrolysis of the amide allowed the formation of the *trans* carboxylic acid **36** in 78% yield.<sup>57</sup> The protected amino acid **26** was achieved by methylation of **36** using methyl iodide and Cs<sub>2</sub>CO<sub>3</sub> as a base in 86% yield.

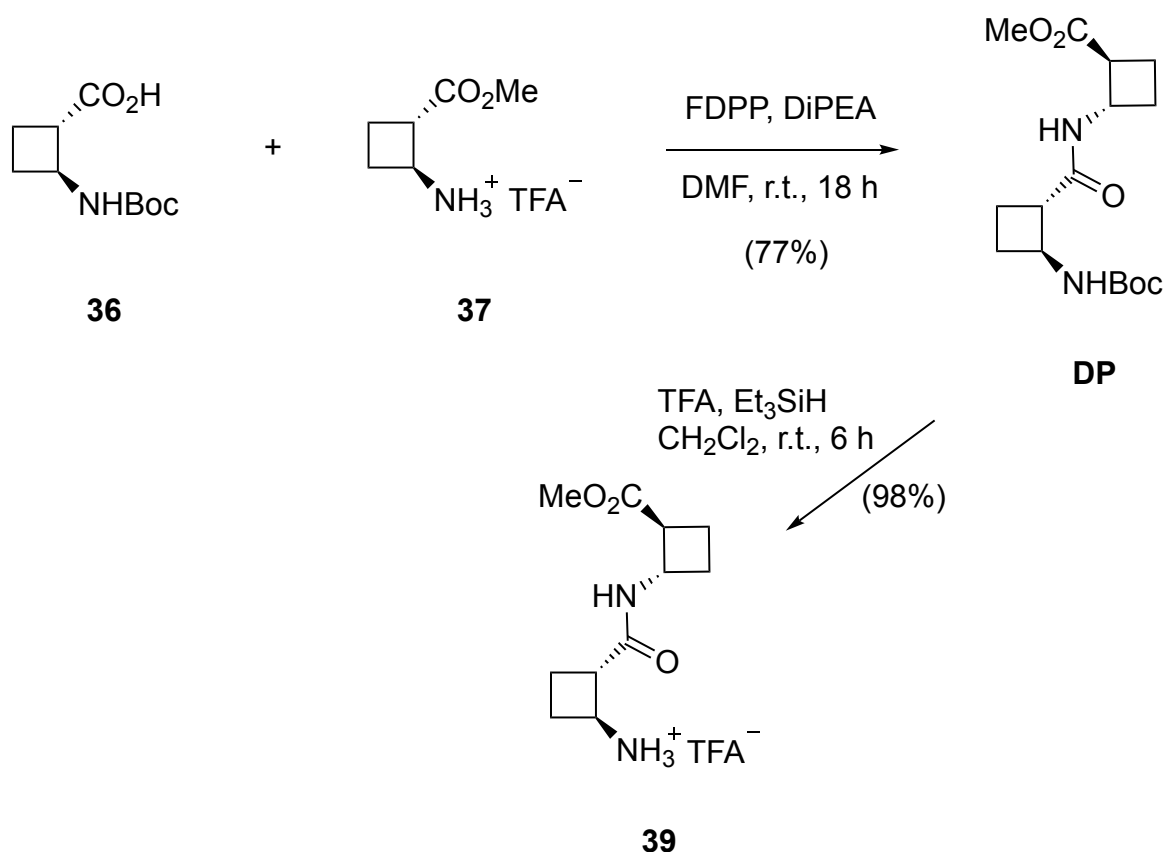


**Scheme 4.** Synthetic route for amino acid **26**.

Furthermore, another methodology to carry out the epimerization of the  $\alpha$ -position to the ester in **31** was carried out by employing sodium methoxide in methanol.<sup>58</sup> In this case, the amino acid **26** was obtained directly in 60% yield. Finally, the orthogonal protection of **26** allowed the selective deprotection of the functional groups obtaining the carboxylic acid **36** by saponification and the amine hydrochloride **37** by acidolysis, both in a high yield.

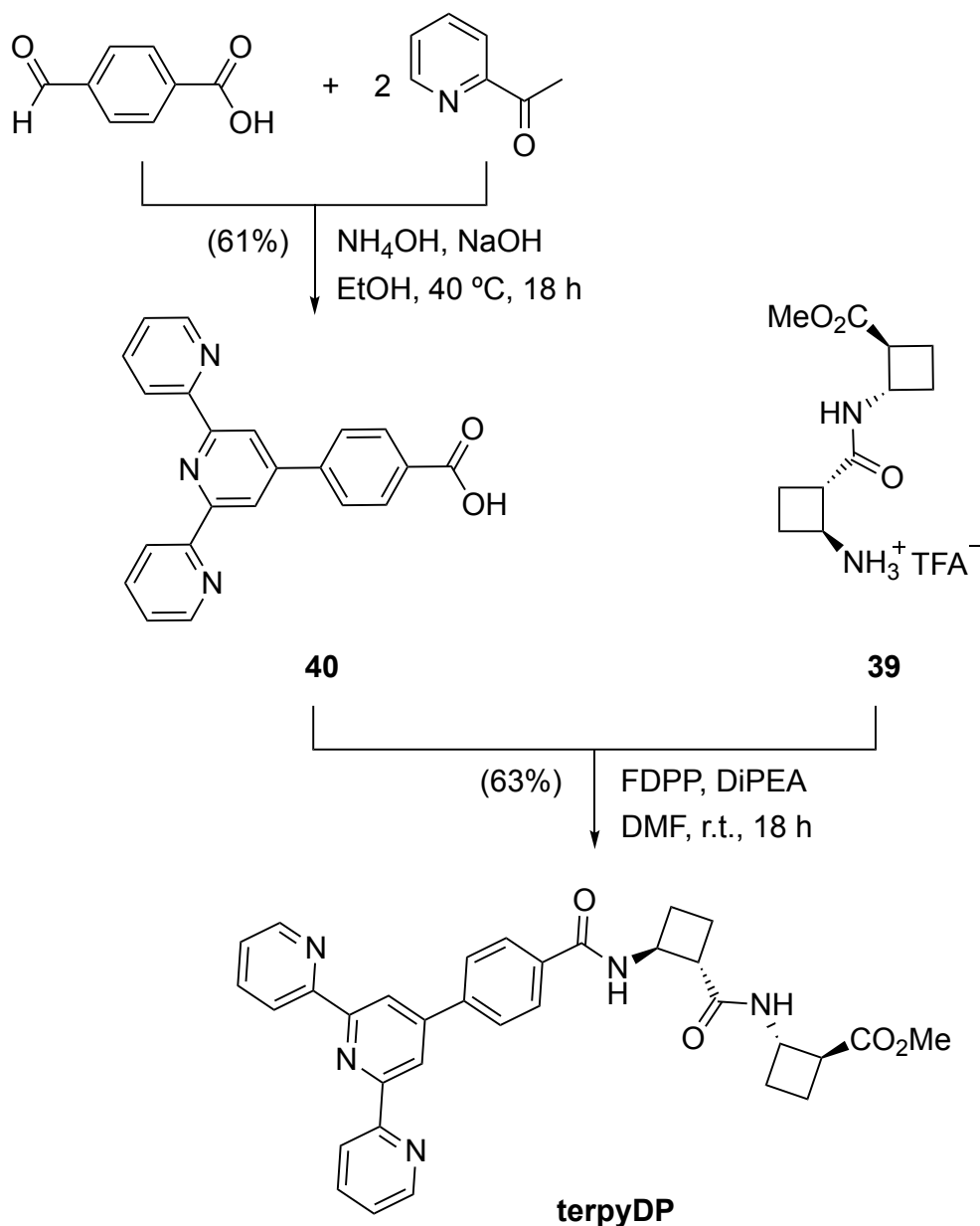
### 3.3.1.3 Synthesis of dipeptide DP and terpyDP

The synthetic route of **terpyDP** can be achieved in 5 steps and in 48% overall yield from amino acids **36** and **37**. The synthetic route is described in Scheme 5 and Scheme 6.



**Scheme 5.** Synthetic route for dipeptide **DP**.

Dipeptide **DP** was prepared in 77% yield under mild conditions by reacting the free carboxylic acid **36** and free amine **37** in the presence of DiPEA and using FDPP as coupling agent.<sup>40</sup> The acidolysis of **DP** achieved the free amine in dipeptide **39**. A convergent synthetic route allowed the efficient preparation of **terpyDP** from the desired dipeptide **DP** and the terpyridine derivative **40**. The terpyridine derivative was synthesized by condensing 4-formylbenzoic acid with 1-(pyridine-2-yl)ethanone in the presence of sodium hydroxide and ammonium hydroxide at 40 °C. It was reacted with the free amino **39** in the presence of DiPEA and using also FDPP as coupling agent, obtaining **terpyDP** in 63% yield.



**Scheme 6.** Synthetic route for **terpyTP**

### 3.3.1.4 Synthesis of hybrid tetrapeptides **TP** and **TPb**, and **terpyTP**

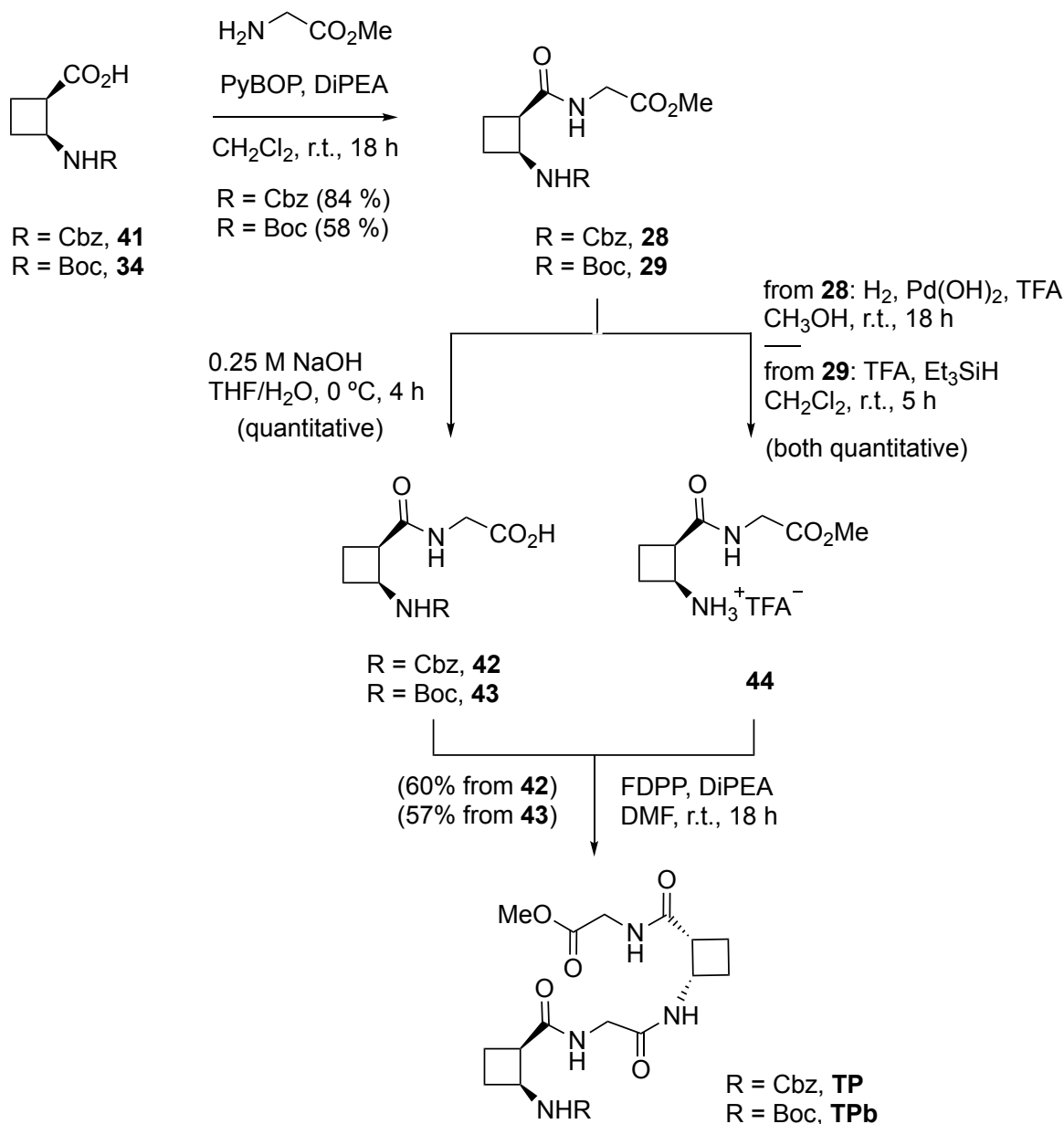
The synthetic route for **terpyTP** can be achieved in 5 steps in an overall yield of 60 % from amino acid **34**. The synthetic routes of the hybrid tetrapeptide **TP** and **terpyTP** are described in Scheme 7 and in Scheme 8, respectively.

Hybrid tetrapeptide **TP** with the amino group protected as benzyl carbamate was prepared following the strategy described by Dr. Sergi Celis.<sup>55</sup> Furthermore, a



## Chapter 3

new tetrapeptide **TPb** with the amino group protected as *tert*-butyl carbamate was also synthesized.

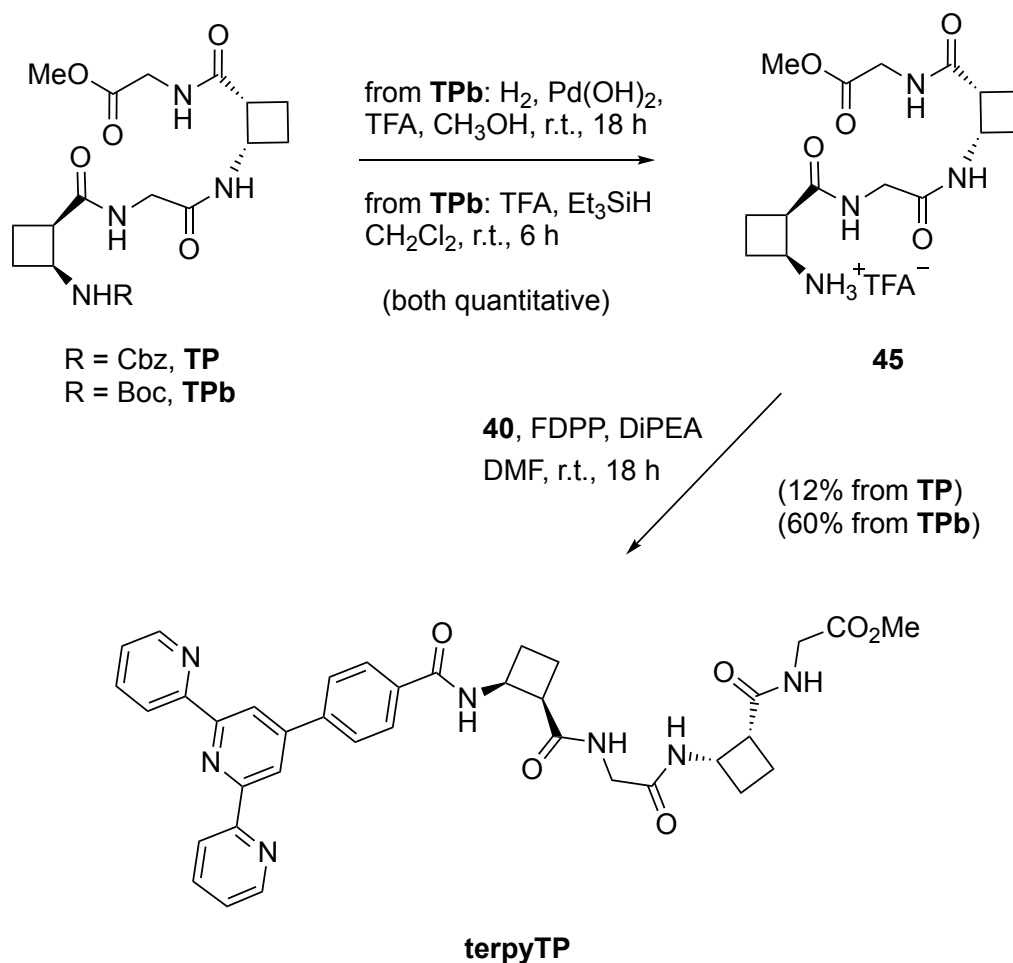


**Scheme 7.** Synthetic route for hybrid tetrapeptides **TP** and **TPb**.

The synthesis started with the reaction of the free carboxylic acids **41** or **34**, respectively, with O-Me protected glycine in the presence of DiPEA and using PyBOP as coupling agent. In this way, hybrid dipeptides **28** and **29** were obtained in 84% and 58% yield, respectively. Then, the ammonium triflate **44** was

quantitatively prepared by submitting **28** to hydrogenation in the presence of TFA, or by acidolysis of **29** with TFA. Following an alternative route, mild saponification of the ester function in **41** and **34**, afforded free acids **42** and **43**, respectively, both in quantitative yields. Subsequently, the coupling of **42** or **43**, respectively, with **44** afforded hybrid tetrapeptides **TP** and **TPb**, in 60% and 57% of yield.

The Cbz-protected hybrid tetrapeptide **TP** and the Boc-protected hybrid tetrapeptide **TPb** were used for the preparation of **terpyTP** (Scheme 8).



**Scheme 8.** Synthetic route for **terpyTP**.

First, the *N*-terminus of **TP** was deprotected by hydrogenation affording **45** in a quantitative yield. Then, the free amino tetrapeptide **45** was coupled with the terpyridine derivative **40**, affording **terpyTP** in poor yield. In the crude product, a purple by-product was observed, which was retained in the column chromatography

## Chapter 3

in the purification step. We hypothesised that this by-product could be a Pd complex with reagents and/or the product. The Pd source could come from the Pd(OH)<sub>2</sub>/C used as catalyst in the previous hydrogenation step. For that reason, when the Boc-protected hybrid tetrapeptide **TPb** was deprotected by acidolysis, and coupled with the terpyridine derivative **40**, **terpyTP** was afforded in 60% of yield. In this case, no purple by-product was observed.

### 3.3.2 Gelation study of terpyDP and terpyTP

The gelation ability of **terpyDP** and **terpyTP** was studied in 13 solvents of different polarity. The tube inversion test was used to determine the formation of a gel, using a procedure described in section 7.9 in the experimental part. The results are quantified by the minimum gelation concentration (mgc), which is the minimum quantity of organogelator required to gelate a volume of a specific solvent (Table 1). In order to compare their gelation ability and the effect of the introduced terpyridine moiety, results obtained for peptides **DP** and **TP** are also shown.<sup>40,41</sup>

**Table 1.** Gelation behaviour of **DP**, **TP**, **terpyDP** and **terpyTP**.

Compound	Pentane	1,4 dioxane	toluene	chloroform	tert-AmOH	AcOEt	THF	DCM	i-PrOH	Acetone	Methanol	Acetonitrile	Water
<b>DP</b>	i	s	6	s	s	33	112	s	s	80	s	57	i
<b>terpyDP</b>	i	s	49	84	123	100	104	100	78	58	59	76	i
<b>TP</b>	i	33	3	122	s	8	100	60	50	50	100	17	i
<b>terpyTP</b>	i	114	63	s	67	92	79	s	43	104	48	i	i

Solvents are ordered by their dielectric constants. mgc values are in mg/mL. i: insoluble, s: soluble.

For an easier visualization, in Table 1 results are highlighted in green when a gel is formed, in blue if the tested compounds are soluble and in red when they

are insoluble. **terpyDP** can gelate all studied solvents, except for being soluble in dioxane and insoluble in pentane and water. Thus, **terpyDP** is not a hydrogelator, since it is insoluble in water. The best (lowest) mgc values found are 49, 58 and 59 mg/mL, corresponding to toluene, acetone and methanol, respectively. Interestingly, toluene is also the solvent in which **DP** performs best. The mgc values for the other solvents are between 76 and 104.

On the other hand, **terpyTP** is insoluble in acetonitrile and it is soluble in chloroform and dichloromethane, and it can gelate the other 8 studied solvents. The best mgc values found are 43 and 48 mg/mL, corresponding to 2-propanol and methanol, respectively. The mgc values for the other solvents are in the range of 63 and 104 mg/mL. Macroscopically, the gels formed by **terpyDP** and **terpyTP** in alcohols are opaque, while the gels formed in the other solvents are translucent. Although the mgc values are not low, they could be interesting for some applications because they can gelate a wide range of solvents.

If we compare the results obtained for **terpyDP** and **terpyTP** with the respective peptides **DP** and **TP**, we can recognize that there are some differences. **DP** can gelate less solvents than **terpyDP**, but **DP**'s mgc values are lower. Thus, the incorporated terpyridine residue reduces the ability of the peptide fragment to gelate large amounts of solvents but favors the gelation of more solvents. **TP** gelates almost the same solvents than **terpyTP**, but its mgc values are better. In this case, the incorporated terpyridine residue does not benefit the gelation ability of the peptide.

Gels from LMWGs are not a thermodynamically stable state, and many of them suffer from long-term instability.<sup>59</sup> The stabilities of gels formed with both compounds were tested. The gels with the lowest mgc value for each organogelator were left to stand at room temperature for at least 1 month. All gels reported were stable at room temperature during that period. Furthermore, their thermoreversibility was tested by heating the gels at a temperature just below the boiling point of the solvent and after, they were allowed to cool down again. In all cases, the gel was formed again, so we can conclude that all gels reported were thermoreversible. As an example, two images of the sol-gel transition of a gel formed by **terpyTP** in methanol are shown in Figure 17.

## Chapter 3

The thermoreversibility is an evidence that gels formed by **terpyDP** and **terpyTP** are physical gels assembled by noncovalent intermolecular bonds. These noncovalent bonds could be disrupted upon heating and reformed during cooling.<sup>60</sup>

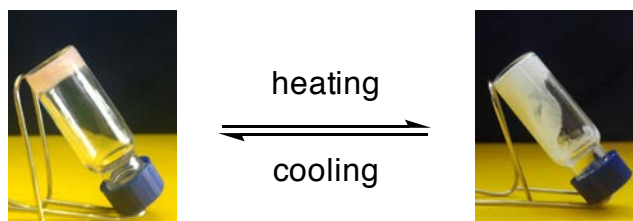


**Figure 17.** Thermoreversibility of a gel formed by **terpyTP** in methanol.

### 3.3.2.1 Scanning electron microscopy

SEM experiments were carried out to investigate the morphology and the supramolecular structure of the gels obtained from **terpyDP** and **terpyTP** in two different solvents. Gels are dried when they are introduced in the microscope chamber due to its vacuum. Usually, the network structure of the gels collapses onto itself during drying to yield a xerogel (if collapse does not occur, the structure is referred as an aerogel). It should be pointed that structural changes (other than collapse) may also occur during the drying process, however, it is often assumed that such effect is minor.<sup>25,61,62</sup>

The studied gels were prepared at their minimum gelation concentration (mgc) for each compound in toluene and methanol (see Table 1). The micrographs obtained are shown in Figure 18 and Figure 19, respectively.

SEM images of the xerogels revealed a remarkable influence of the solvent nature on the morphology of the supramolecular aggregates. The non-conductive behaviour of both compounds hindered good resolutions in high magnifications.<sup>63</sup> Xerogels of **terpyDP** in methanol show undefined structures. In higher magnifications, it looks like squashed fibers. On the other hand, disordered fibers are observed with lengths of 120 to 200 nm when the xerogel was formed in toluene (Figure 18).

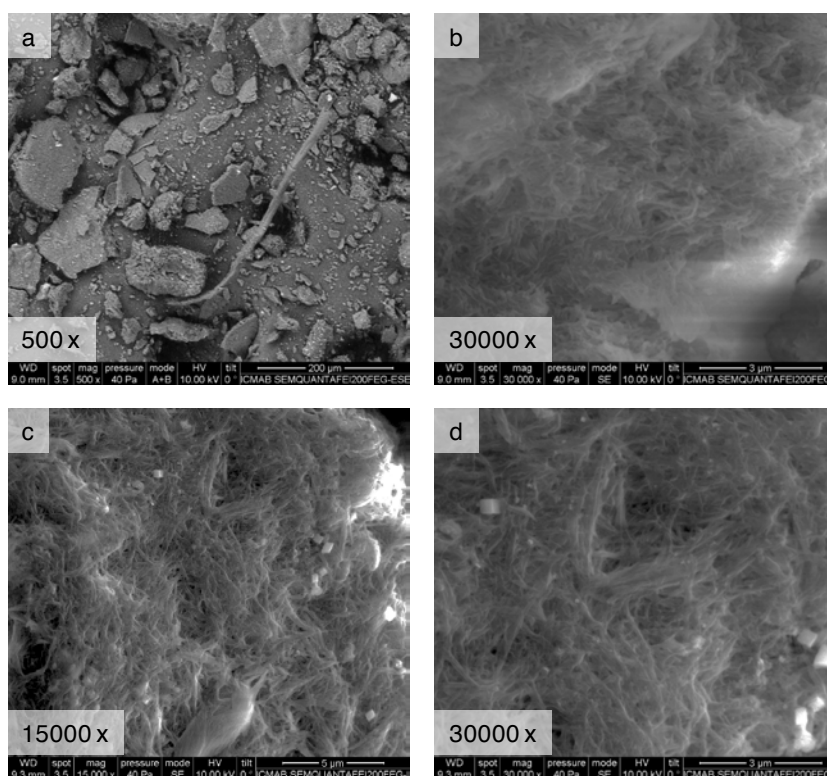


**Figure 18.** SEM images of **terpyDP** in a) and b) from methanol, and c) and d) from toluene at two different magnifications.

On the other hand, xerogels formed by **terpyTP** in methanol exhibit undefined spongy-like structures. In higher magnifications, we can observe that the cavities of this structure are formed by smashed fibers. Besides, xerogels formed by **terpyTP** in toluene present undefined structures. In higher magnifications, we can notice that the walls of this structure are made of regular fibers of around 40 nm (Figure 19). If we compare the obtained micrographs of both compounds with those of the respective peptides (Figure 9), we can conclude that the xerogels from peptides **DP** and **TP** present better defined and more regular structures in the form of fibers. An explanation for this difference could be that both peptides are better organogelators in toluene, or that the presence of the terpyridine disrupts the self assembly of the molecules. Other possibility could be that the networks of **terpyDP** and **terpyTP** could suffer structural changes when the gels collapsed into a xerogel, specially in methanol, since smashed fibers are observed.

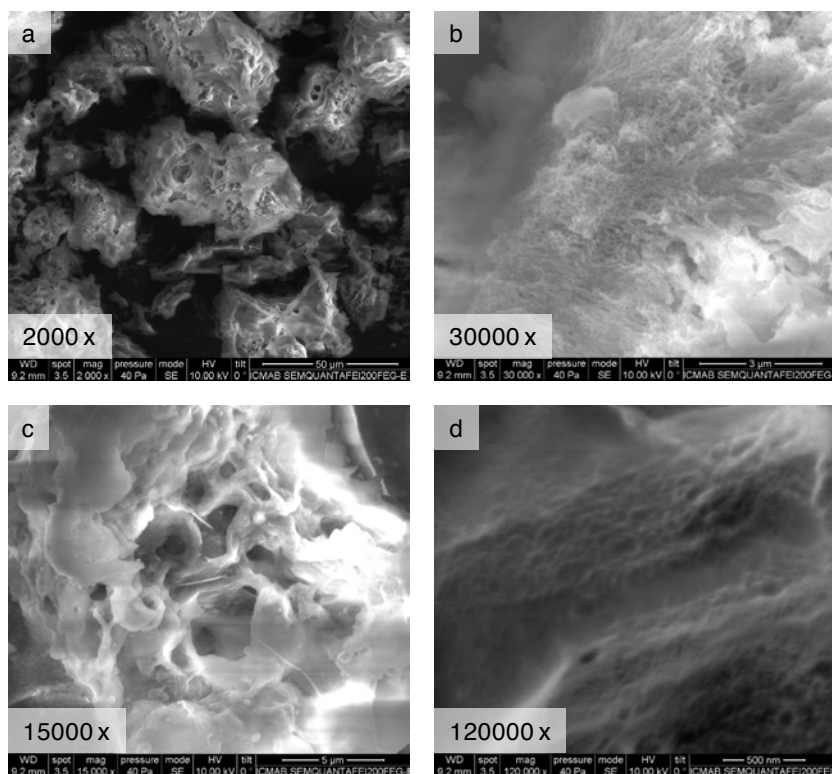


**Figure 19.** SEM images of **terpyTP** in a) and b) from methanol, and c) and d) from toluene at two different magnifications.

In conclusion, the fibrillar nature of the gel networks was evidenced by SEM images of the corresponding xerogels. The length of the observed fibers is from 40 to 200 nm. However, it should be noted that the diameter of fibers is much larger than the molecular diameter. Generally, molecular-scale fibrils bundle together to generate larger nanofibers.<sup>64</sup> SEM images from xerogels obtained from toluene present better defined fibers than the ones acquired from methanol. Macroscopically, for both compounds, gels from toluene are transparent and gels from methanol are opaque. This fact could explain these differences since transparent gels often exhibit nanoscale structuring, while opaque gels, which can scatter light, have larger microscopic arrangements.<sup>65,66</sup>

### 3.3.2.2 Theoretical calculations

Theoretical calculations were carried out to better understand the structure of the gels, their formation process and to establish the main interactions

responsible for the supramolecular arrangement. The theoretical calculations were carried out in collaboration with Dr. Bernat Pi from our research group. Also, their aggregation energies were compared with the aggregation energies of dipeptide **DP** and tetrapeptide **TP**, to understand if the terpyridine residue benefits in energetic terms the aggregation or disfavors it.

First, the structure of **terpyDP** and **terpyTP** of a single molecule of both compounds was studied. A conformational search using molecular mechanics was accomplished for both monomeric **terpyDP** and **terpyTP**, and then, the most stable structures were optimized employing quantum mechanics using M06-2X as DFT functional (Figure 20).

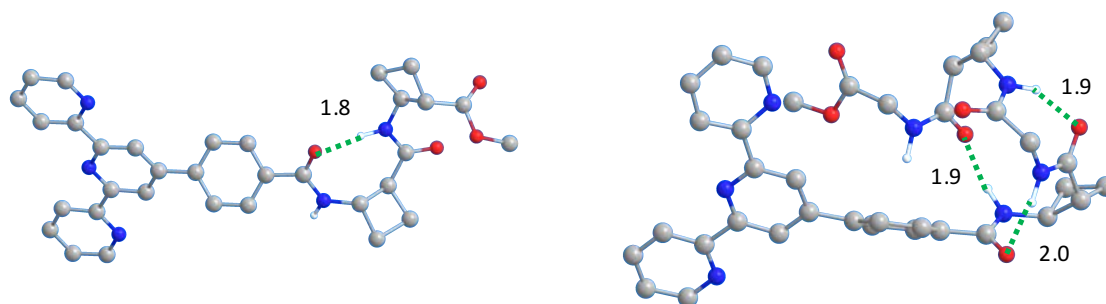


**Figure 20.** Optimized structures of **terpyDP** (left) and **terpyTP** (right). Hydrogen bonds are remarked with green lines. Distances in Å.

In the resulting computed geometries, we can observe that the structure of **terpyDP** is extended and fixed by an 8-membered hydrogen-bonded ring which is typical for *trans*-based cyclobutane moieties.<sup>13</sup> On other hand, the **terpyTP** structure is folded and fixed by three hydrogen bonds between the carbonyl functions and nitrogen atoms of different amide groups. The relative conformation of the peptide moieties in **terpyDP** and **terpyTP** are the same found in previous studies of **DP** and **TP**,<sup>67</sup> so the incorporated terpyridine residue does not play a significant role.

Once the structure of the discrete molecules was computed, small aggregates of both compounds were studied. The conformational search performed for dimeric and tetrameric aggregates of both compounds showed that the most



## Chapter 3

stable structures involved intermolecular hydrogen bonds between the NH groups of one molecule and the CO groups of the other one. These hydrogens bonds may be formed in two different directions, head-to-head (hh) and head-to-tail (ht). The head-to-head arrangement has the advantage that terpyridines from different molecules are close, and it could allow  $\pi$ - $\pi$  stacking and stabilize the energy (Figure 21).

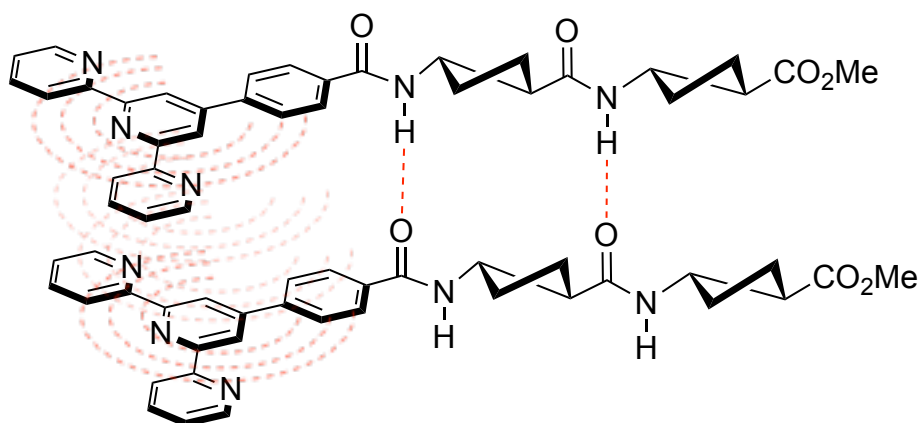


**Figure 21.** Schematic representation of head-to-head arrangement of a dimer of **terpyDP**.  $\pi$ - $\pi$  and H-bonding interactions are remarked in red.

Initially, the structure of tetramers was studied using the same head-to-head or head-to-tail consideration described before. Then, from the structure of the tetramer was extracted the internal dimer and this dimer was optimized again obtaining the aggregation energy ( $\Delta E_{agg}$ ).  $\Delta E_{agg}$  of a dimer is the difference in energy of the dimer and two monomers. Then, if the calculated energy is negative, the aggregation is favourable. Also, the aggregation energy per monomer ( $\Delta E_{agg}/n$ ) gives information about the stabilization due to the introduction of a new molecule in the aggregate.

Following these patterns of interactions, two tetrameric aggregates (head-to-head and head-to-tail) were built for each gelator using the same method. The energy values were calculated using 6-31G(d) basis set. The calculated aggregation energies and the aggregation energies per molecule of **DP**, **TP**, **terpyDP** and **terpyTP** are shown in Table 2.

**Table 2.** Aggregation energies for the formation of dimers and tetramers of **DP**, **TP**, **terpyDP** and **terpyTP**.

Compound	Arrangement	$\Delta E_{\text{agg}}$ (kcal/mol)	$\Delta E_{\text{agg}}/n$
<b>DP</b> <sup>40</sup>	Dimer hh	-13.95	-6.98
	Dimer ht	-11.69	-5.85
	Tetramer hh	-59.37	-14.84
	Tetramer ht	-47.21	-11.80
<b>terpyDP</b>	Dimer hh	-40.97	-20.49
	Dimer ht	-14.22	-7.11
	Tetramer hh	-112.71	-28.18
	Tetramer ht	-90.52	-22.63
<b>TP</b> <sup>67</sup>	Dimer hh	-15.80	-7.90
	Tetramer hh	-50.60	-12.65
<b>terpyTP</b>	Dimer hh	-45.39	-22.70
	Dimer ht	-25.45	-12.73
	Tetramer hh	-136.00	-34.00
	Tetramer ht	-90.02	-22.51

The resulting calculations showed that the aggregation energies are more favourable when the number of monomers increased. Also, the aggregation energy per molecule increases in all cases, and it could mean that the self-assembly of both compounds is promoted by a cooperative effect.<sup>68-71</sup> In both arrangements for **terpyDP** (the dimer and the tetramer), the head-to-head conformation was preferred. If we compare the new gelator with its parent peptide **DP**, the  $\Delta E_{\text{agg}}$  for the **DP** tetramer is -59 kcal/mol while it's -113 kcal/mol for **terpyDP**.

## Chapter 3

Analogous results were obtained for **terpyTP**, being the head-to-head arrangement the preferred. Also, the  $\Delta E_{\text{agg}}$  for the **TP** tetramer is -51 kcal/mol while it is -136 kcal/mol for **terpyDP**. Comparing the values, we can conclude that the terpyridine plays an important role in the aggregation. Noticing the values are almost the double for **terpyDP**, and more than the double for **terpyTP**, we could say in a qualitative way, that the half of the main forces involved in the self-assembly process are the hydrogen bonding of the amides, and the other half, the  $\pi$ - $\pi$  stacking of the terpyridine derivative moieties.

The structures of the calculated geometries head-to-head dimers and tetramers for **terpyDP** and **terpyTP** are shown in Figure 22 and Figure 23, respectively. For an easier visualization, the pictures of each aggregates are oriented in the same way, the terpyridines residues are located on the right, while peptide moieties are on the left part of each drawing.

Optimized structures of the dimeric and tetrameric aggregates show that **terpyDP** and **terpyTP** self-assemble in a preferred monodirectional dimension. In dimeric aggregates, terpyridine moieties are in a parallel disposition while the peptide moiety remains folded, but not in a well-defined structure. When the aggregates grow until a tetramer, the peptide moieties stretch, starting a helical-like structure. This effect is more visible in the tetrameric aggregate of **terpyTP**. It could be explained because the peptide moiety of **terpyTP** is larger, thus more flexible, and it could be easily accommodated in a helical-like aggregate. This explanation is in agreement with the calculated aggregation energies, which are more negative for **terpyTP**.

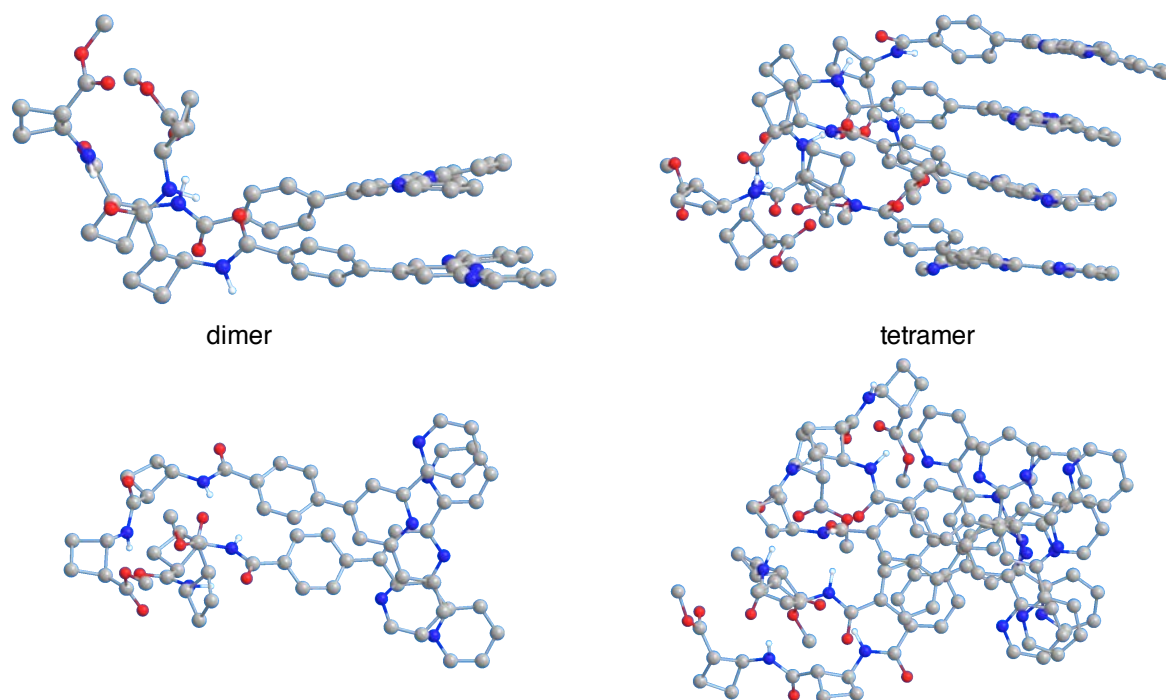


**Figure 22.** Side and top view for the predicted structure of a dimeric (left) and tetrameric (right) aggregate of **terpyDP**. Non-polar H atoms were omitted for clarity

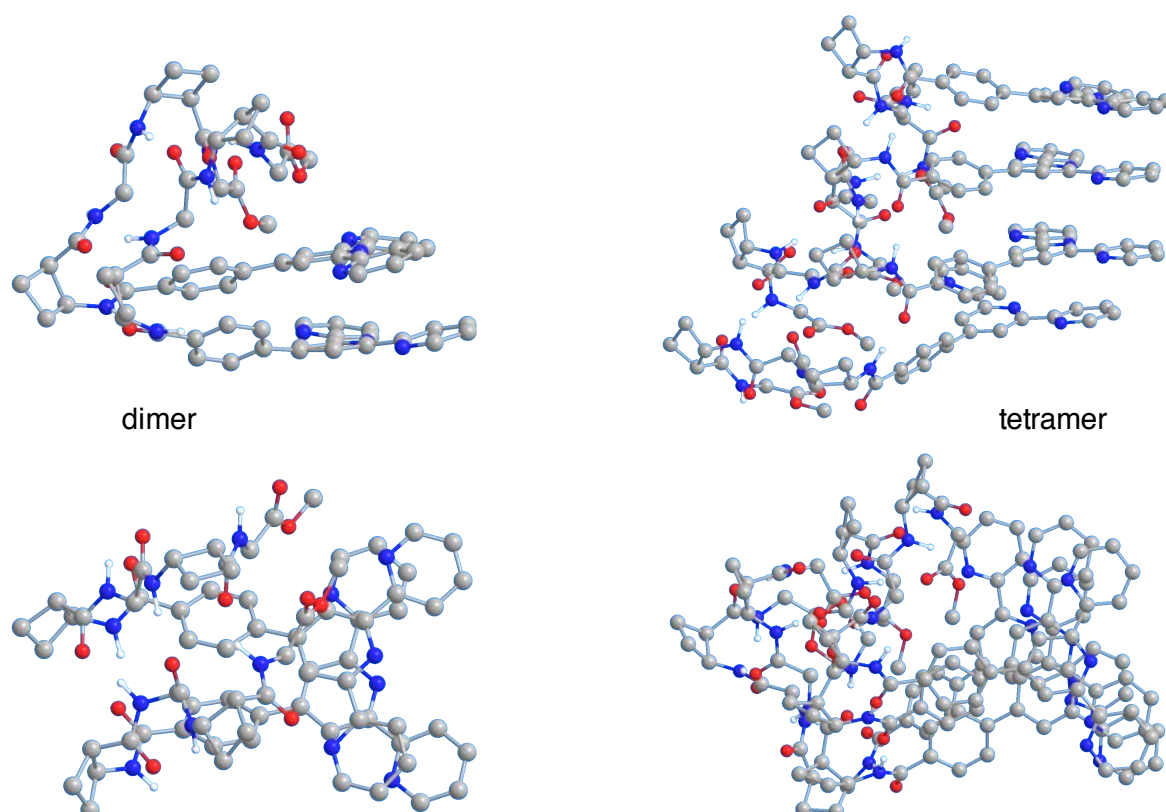


**Figure 23.** Side and top view for the predicted structure of a dimeric (left) and tetrameric (right) aggregate of **terpyTP**. Non-polar H atoms were omitted for clarity.

## Chapter 3

Once tetrameric aggregates were studied, the dodecameric structure of **terpyTP** was constructed using the same methodology described for the dimer and tetramer. After, a minimization of energy was followed by a DFT single point calculation of energy. The structure of the predicted dodecamer of **terpyTP** is shown in Figure 24.

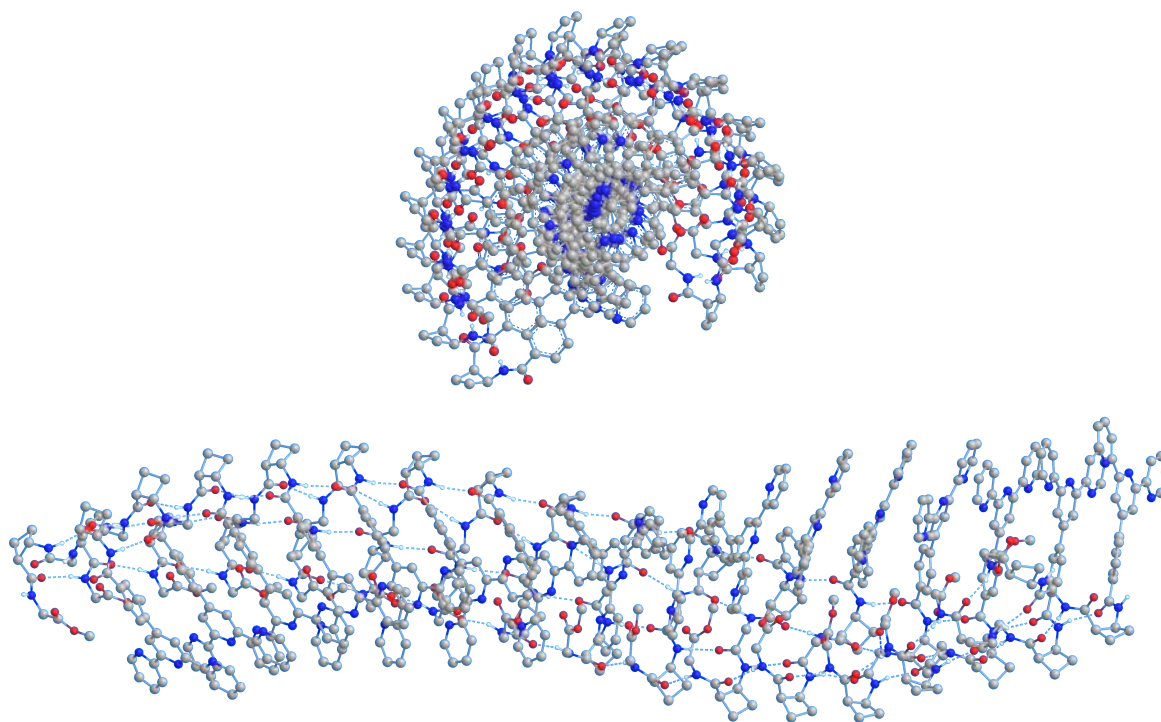


**Figure 24.** Top and side view for the predicted structure of a dodecameric aggregate of **terpyTP**. Non-polar H atoms were omitted for clarity.

The predicted structure of the dodecameric aggregate confirms the helical trend. However, twelve monomers are not enough to complete a turn of the helix, but almost three quarters. The molecules were not completely in parallel, they moved one with respect to the others, in the three dimensions along the fibril. Looking at the aggregate from a top view, we can see the relative position of the terpyridine moieties and the peptide moieties along the fibril. Terpyridine moieties remain in the middle of the fibril, while the peptide part of the molecules spins around. This well-ordered structure could be very interesting for catalytic applications. The arrangement of the multiple precatalytic moieties (terpyridines) in

the fiber structure could give new catalytic features. Additionally, the observed high-ordered supramolecular chirality could induce some selectivity.

To clarify the exact position of each function in the big aggregate, the dodecamer was cut and an internal dimer and monomer were extracted (Figure 25). Knowing the relative position of the functions is crucial to compare our predicted model with structural experimental studies, such as circular dichroism. We can observe that each amide group of the compound forms hydrogen bonds with the equivalent amide group of the next molecule. So, each molecule that participates into the supramolecular aggregate establishes four hydrogen bonds with the next molecule. The same results were obtained when the structure of **TP** hexadecamer was studied.<sup>55</sup>

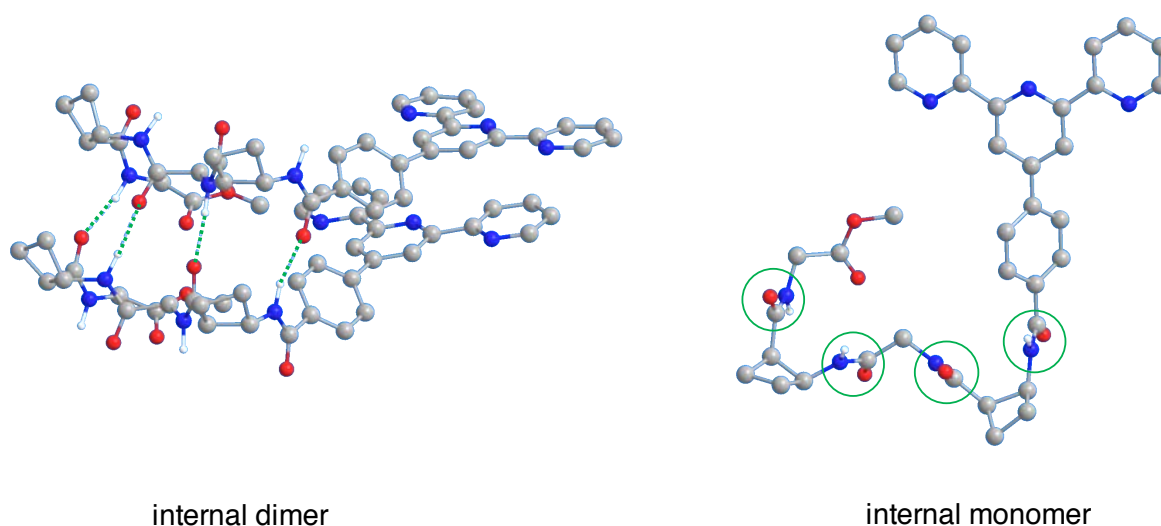


**Figure 25.** Internal dimer and monomer of a dodecamer of **terpyTP**. Hydrogen bonds and amides, respectively, are remarked in green.

So, calculations of big aggregates suggest that the terpyridine moiety does not interfere in the interactions of the peptidic part. Furthermore, each pyridine and the phenyl ring remain in a shifted parallel position due to  $\pi$ -stacking interactions with the same functions of the next and previous molecule.

### 3.3.2.3 Circular dichroism and UV spectroscopy

Circular dichroism spectroscopy (CD) is a usual technique to study the morphology of the supramolecular structures of the gels, and to investigate the chirality transfer and amplification between the monomers and the aggregates. The CD spectrum of a compound in solution gives information about the relative disposition of the chromophores. Besides, in xerogel phase, only chiral aggregates will give signal on the CD, and the shape of the CD spectrum changes depending on the structure of the aggregate.<sup>72</sup> Finally, predicted CD spectra of the calculated structures are usually studied using GaussSum software to compare the calculated with the experimental spectra. Predicted CD spectra have been studied in collaboration with Dr. Bernat Pi from our research group.

First, UV spectroscopy was performed to know the region of the spectra where **terpyDP** and **terpyTP** absorb. The resulting spectra are shown in Figure 26.

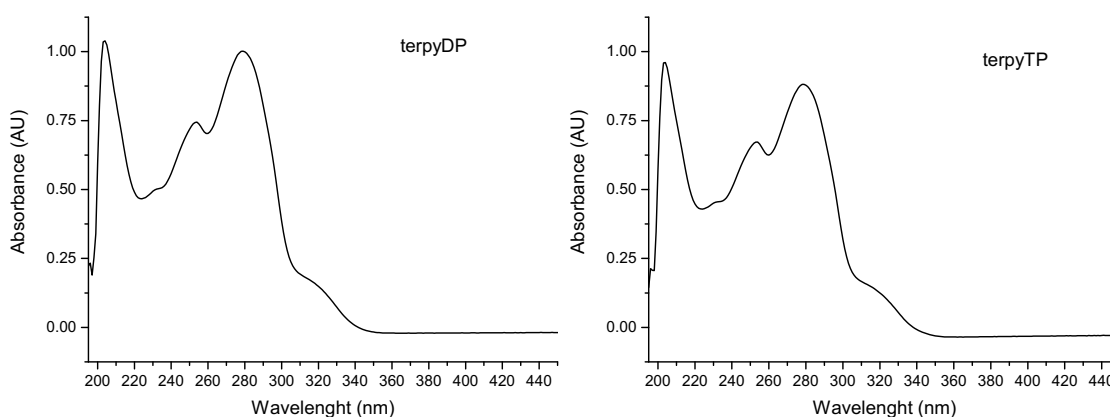


**Figure 26.** UV spectra of **terpyDP** (left) and **terpyTP** (right) in solutions of 0.05 mM in methanol.

Both spectra of **terpyDP** and **terpyTP** were almost equivalent, since both compounds have the same chromophores. Amides absorb at 200-240 nm due to the  $\pi$ - $\pi^*$  and the  $n$ - $\pi^*$  transitions and the aromatic functions absorb at higher wavelengths.<sup>73</sup> The obtained spectra show three intense bands at 200, 250 and 280 nm. Comparing these spectra with the UV spectrum of compound **40**, which

corresponds to the terpyridine residue alone, we could assign some signals. The 250 and 280 nm bands correspond to the aromatic  $\pi$ - $\pi^*$  transitions, while the 200 nm bands are due to the overlap of amides and aromatic transitions. Finally, the broad small band around 320 nm could correspond to the  $n$ - $\pi^*$  transitions of the lone pair of the nitrogen.

To sum up, the left part of the spectra corresponds to the amides functions and the right part to the aromatic functions. Having both chromophores separated in the UV spectra could be important to study the aggregation of the molecules, because we could observe the differences between the H-bonding (between amides) and the  $\pi$ - $\pi$  stacking (aromatic functions).

To study the chirality of the monomers, CD spectra of **terpyDP** and **terpyTP** were performed in methanol solution. To study the aggregates, gels of both compounds were prepared at their minimum gelation concentration in toluene. After, xerogels were prepared by removing the solvent under reduced pressure and the resulting materials were mixed with KBr. Circular disks were made using the procedure described in the experimental part (7.5.2). It should be pointed that the intensity of the bands depends on the thickness of the disk, and it is hard to reproduce. For this reason, solid state CD spectra were normalised, and interpreted qualitatively.

The CD spectra for **terpyDP** in solution and in xerogel are shown in Figure 27. In solution, **terpyDP** presents a complicated CD spectra with different bands. The most intense bands are two non-symmetric bisignate signals at 234 and 316 nm. **terpyDP** has 4 stereogenic centers, two amides, one phenyl group and three pyridines, so a rational of the CD spectra is not achievable since the possible interactions between the chromophores are considerable. However, we tried to interpret the spectra in a simple and qualitative approach. The bisignate Cotton signal on the left could be attributed to the amides and the right could be associated to the aromatic functions.

The shape of the obtained signals is bisignate, indicating that the relative position of the chromophores (their orbitals) responsible for that signal are not symmetric (antiparallel). In the case of the amides it is easy to understand that they



## Chapter 3

are not in a parallel position. Regarding the aromatic rings, it should indicate that, at least some of the rings are not in the same plane as the others. This explanation is in agreement with the calculated structure shown in Figure 20. In that structure, the phenyl group is not in a parallel position with the terpyridine.

In xerogel phase, **terpyDP** presents an easier spectrum. It shows a bisignate signal with a crossing at 217 nm and a broad signal at 347 nm. Interpreting that the bisignate signal is due to the amides, we can observe that it has shifted to smaller wavelengths with respect to the same signal in solution. This blue shift is related to the difference between the intramolecular hydrogens bonds of the amide groups and the intermolecular hydrogen bonds that are formed between molecules of the aggregate. Moreover, the shape of the signal is bisignate, indicating that the relative position of the amides in the aggregate is not symmetrical. This behaviour is typically described for helical aggregates.

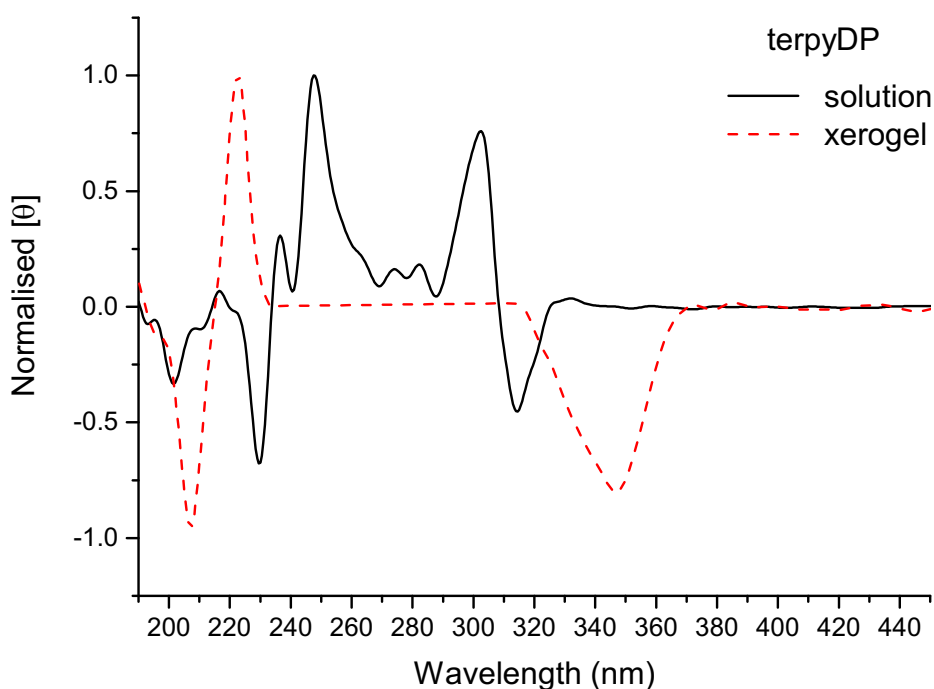


**Figure 27.** Normalised CD spectra of compound **terpyDP**. 0.048 mM solution in methanol and in xerogel phase at 0.019 mmol/g KBr.

Concerning the signal of the aromatic functions, in xerogel phase it has shifted to higher wavelength and its chirality has changed from a bisignate signal to a broad band. The single band could be explained because in the aggregate, the relative position of the aromatic functions is parallel between them, as it is showed in the calculated structure (Figure 22). The red shift of the band of the aromatic functions could be related to partial overlapping of them, performing a kind of staircase aggregation, like it is observed in many examples of aggregates of aromatic compounds, such as porphyrins.<sup>74,75</sup>

The CD spectra for **terpyTP** are shown in **Figure 28**. In solution, it shows a more complicated spectrum compared with **terpyDP**. **terpyTP** presents more chromophores, so there are more interactions between them. In this case, a similar general interpretation can be used, relating the lower wavelength signals to the amides and the higher wavelength signals to the aromatic functions.

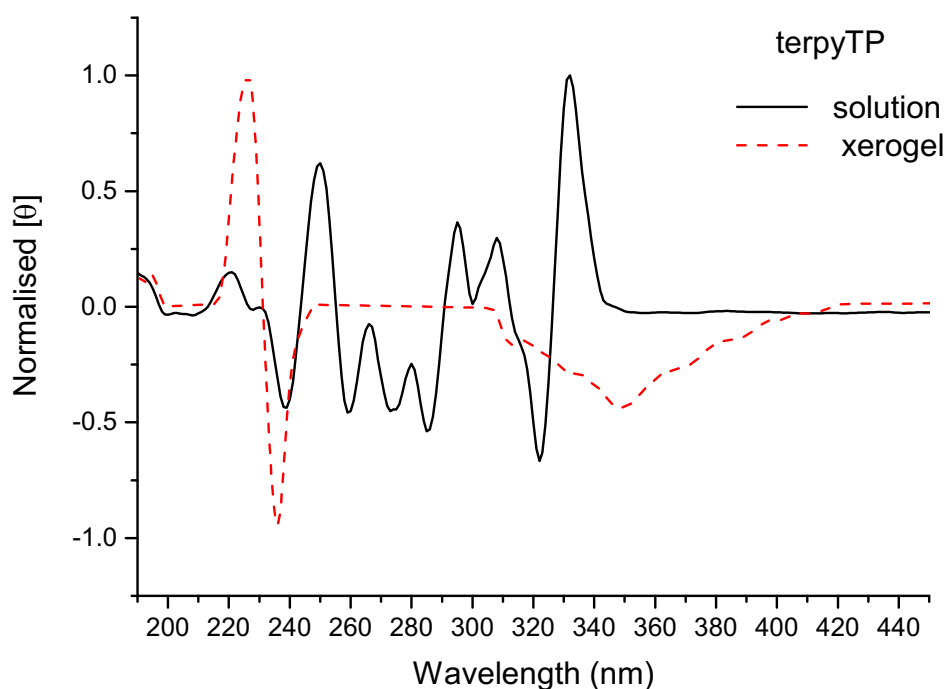


**Figure 28.** Normalised CD spectra of compound **terpyTP**. 0.051 mM solution in methanol and in xerogel phase at 0.021 mmol/g KBr.

## Chapter 3

Again, the spectrum of **terpyTP** is simplified in the xerogel. It shows a bisignate signal with a crossing at 225 nm and a broad and non-symmetric signal at 352 nm. It is similar with the xerogel spectra of **terpyDP**, both compounds present analogous spectra. For an easier and simple interpretation of the CD spectra of the xerogels, in Figure 29, the relative position of the chromophores is remarked, using the calculated tetramer of **terpyTP**. In the aggregates, the relative position of the amides between the molecules are non-parallel, generating helicity, while the aromatic groups remain in a shifted parallel plane. These interpretations are another evidence of the helical-like structure of the aggregates found in the calculations. Also, bigger aggregates of these compounds could form fibers, which is in concordance with the SEM experiments.

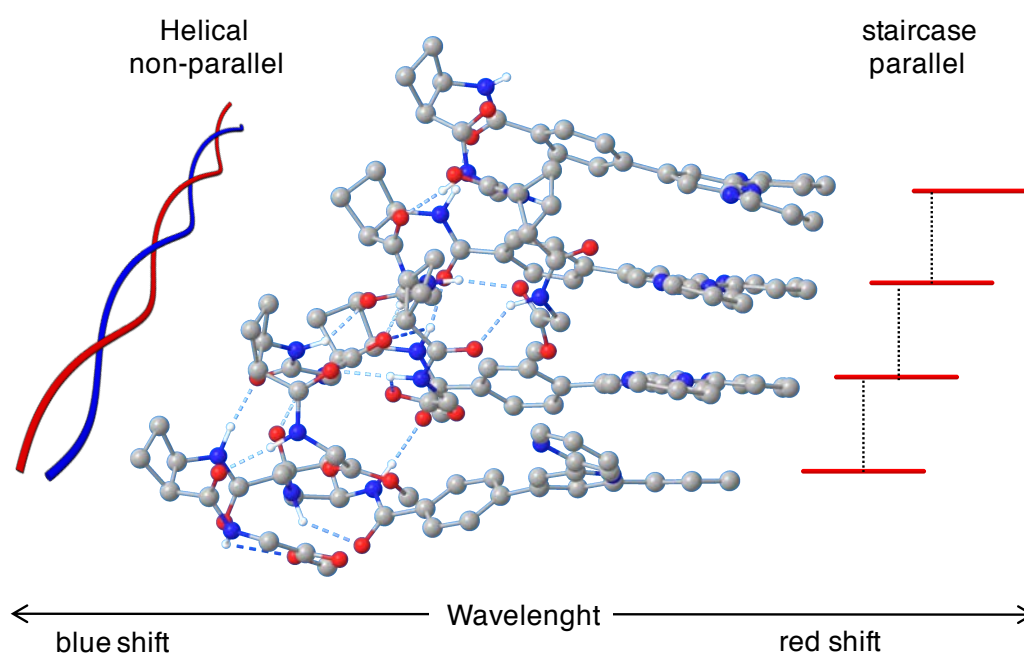


**Figure 29.** Calculated structure of a tetramer of **terpyTP**. The relative position and shifts in the CD of the chromophores is represented.

Our structural model of the aggregate is in agreement in a qualitative approach with the experimental CD spectra. Moreover, the CD spectra can be also calculated taking into account the optimized structures with a software named GaussSum. We hypothesized that if we simulate the CD spectra of a single

molecule, we will obtain the CD spectrum of the compound in solution. Otherwise, if we calculate the CD spectrum of an aggregate, for example a tetramer or an octamer, we could obtain the CD spectrum of the xerogel. The CD spectra of both compounds in solution were calculated taking into account 30 excited states following the methodology described in the literature.<sup>76–80</sup> The calculated CD spectra for single molecules of **terpyDP** and **terpyTP** are shown in Figure 30.

Predictions are in good agreement with the experimental spectra (Figure 27 and Figure 28). The shape of the predicted spectra is almost equal of the experimental curves, but the relative intensity presents small differences. These differences could be related with the limited excited states used in the calculation.

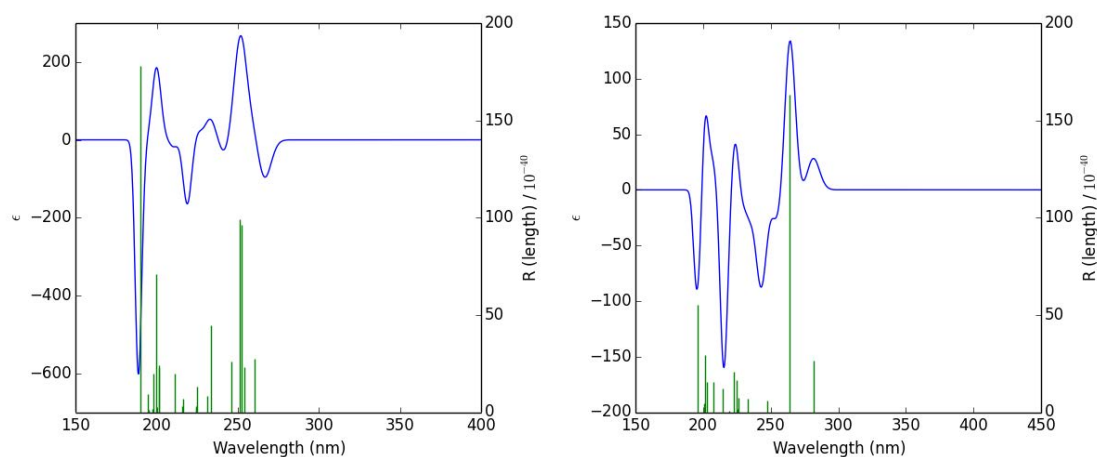


**Figure 30.** Predicted CD spectra of **terpyDP** (left) and **terpyTP** (right).

Due to calculation limitations, it was not possible to predict the spectra of the xerogels. To predict a CD spectrum in xerogel phase, a high number of excited states of the molecular orbitals using a good level of theory are needed. Unfortunately, calculations were only possible using a high number of excited states with a small basis set, or using a few excited states with a larger basis set. The CD spectra of a dimer of **terpyDP** and **terpyTP** were predicted using CAM-B3LYP/6.31G(d,p) level of theory (10 excited states). Due to the low number of excited states, the predicted spectra did not fit with the experimental. Also, using a

small aggregate (dimer), the predicted CD spectra will not only consider the intermolecular interactions but also the intramolecular ones.

### 3.3.3 Complexation of terpyDP and terpyTP with Ru<sup>2+</sup> and Pd<sup>2+</sup>

Once both gelators **terpyDP** and **terpyTP** were studied and characterized, they were complexed with metals ions. Both compounds have the same three coordinating points, which corresponds to the three nitrogen atoms of the pyridine moieties. Coordinating **terpyDP** and **terpyTP** with a metal ion, respectively, we could expect that the gelation ability of this ligands would be transferred to the final metal-complex.

The metals were chosen taking into account the following considerations. Looking forward to the final application we needed some metal-complexes which could be used in catalysis. To perform catalysis in gel phase, the reaction conditions are very important. Since the catalyst is supported in a gel phase, if the reaction to catalyse needs high temperature it should be discarded, because the gel would be destroyed at high temperatures. Another handicap is that the metal-complex should be stable enough to isolate it and not be formed "*in situ*" in the catalysed reaction. The metal complex should be formed, isolated and studied, and after, it should be mixed with the solvent to form the metallo-gel and finally the reagents would be added.

Taking into account the previous discussion, Ru<sup>2+</sup> was chosen as metal. Ru<sup>2+</sup> complexes are octahedral with 6 coordinating sites. Since terpyridines have 3 nitrogen atoms to coordinate, there are still 3 free positions. One possibility is use two **terpyDP** or **terpyTP** to form the complex, but this was not considered because Ru(terpy)<sub>2</sub> complexes are quite inert and usually do not have applications in catalysis.<sup>81</sup> For that reason, pyridine-2,6-dicarboxylate (**pydic**) was used as the second ligand in the complex. Furthermore, a palladium complex using **terpyTP** was prepared and studied to compare the results of the Ru complexes. Pd<sup>2+</sup> – terpyridine complexes usually adopt a square planar geometry, and this could favour the supramolecular aggregation.

### 3.3.3.1 Preparation and gelation study of Ru<sup>2+</sup> and Pd<sup>2+</sup> complexes

The synthesis of the ruthenium complexes **Ru(pydic)(terpyDP)** and **Ru(pydic)(terpyTP)** were achieved in one step in 54-60% yield (Figure 31).

The complexation was achieved by reacting one equivalent of **terpyDP** or **terpyTP** with one equivalent of **pydic** ligand and one equivalent of a ruthenium dimer, Ru(*p*-cymene)Cl<sub>2</sub>, in methanol/water under reflux conditions. Due to their high stability, both complexes were purified by column chromatography and characterized using the common techniques (<sup>1</sup>H NMR, <sup>13</sup>C NMR, IR and HRMS).

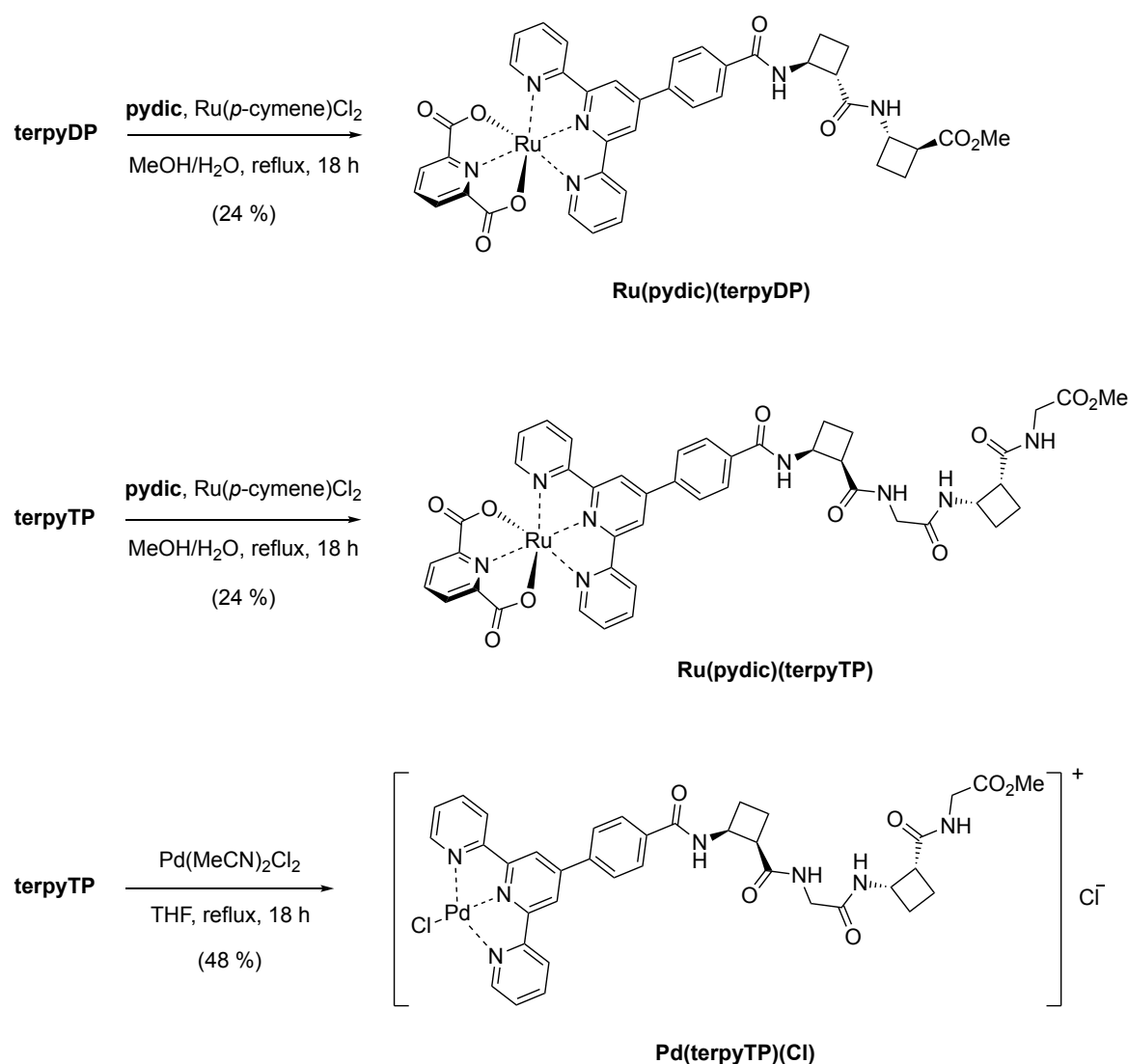


**Figure 31.** Structures of the complexes **Ru(pydic)(terpyDP)**, **Ru(pydic)(terpyTP)** and **Pd(terpyTP)(Cl)**.

## Chapter 3

The synthesis of the palladium complex **Pd(terpyTP)(Cl)** is achieved in one step in 78% yield (Figure 31). With this aim, one equivalent of **terpyTP** was reacted with one equivalent of Pd(MeCN)<sub>2</sub>Cl<sub>2</sub> in THF under reflux. Due to its poor solubility, this complex was not purified, but it was characterized using the same techniques employed for Ru<sup>2+</sup> complexes.

The gelation ability of **Ru(pydic)(terpyDP)**, **Ru(pydic)(terpyTP)** and **Pd(terpyTP)(Cl)** was studied in 18 common solvents of different polarity. The tube inversion test was used to determine the presence of a gel. Summarized results are shown in Table 3.

**Table 3.** Gelation behaviour of **Ru(pydic)(terpyDP)**, **Ru(pydic)(terpyTP)** and **Pd(terpyTP)(Cl)** using polar solvents.

	<i>i</i> -PrOH	<i>n</i> -BuOH	Acetone	Ethanol	Methanol	Acetonitrile	DMF	DMSO	Water
<b>Ru(pydic)(terpyDP)</b>	i	i	i	i	s	i	s	s	i
<b>Ru(diPic)(terpyTP)</b>	i	i	i	i	s	i	s	s	i
<b>Pd(terpyTP)(Cl)</b>	i	i	i	i	i	i	s	s	i

Solvents are ordered by their dielectric constants. i: insoluble, s: soluble.

In Table 3, only results with polar solvents are described. Complexes were insoluble in nine common solvents with less polarity. All three complexes are not able to gelate any solvent; thus, these complexes are not metallogelators. Ruthenium complexes are insoluble in most of the studied solvents, they are only soluble in *iso*-propanol, methanol, DMF and DMSO. The palladium complex is insoluble in almost all the solvents and it is only soluble in DMF and DMSO.

Unfortunately, the gelation ability of **terpyDP** and **terpyTP** is not transferred to the resulting complexes. Furthermore, they are insoluble in most of the studied solvents, limiting their applicability in catalysis. Comparing the results of the gelators with their corresponding metal complexes is easy to observe the huge differences between them (Table 1). So, the incorporated metal ion has a high

impact in the gelation and solubility behaviour. Also, the palladium complex was studied to compare the influence of the metal geometry, since palladium complexes are usually square planar while ruthenium complexes are octahedral. None of them can gelate, so the geometry and the metal do not influence in this ability, but they could influence in the solubility, being the palladium complex less soluble in the studied solvents.

The obtained results are a clear example of the fact that a rational structural design of gelators, and especially metallogelators, is still challenging. Incorporating different functionalities in a gelator can influence their gelation ability and often it is not possible to predict.

### 3.3.3.3 Electrochemical studies of Ru complexes

Electrochemical studies of Ru complexes were undertaken to comprehend the redox properties of these compounds. These results are interesting for catalytic applications where an oxidation or reduction step is required. This study was carried out in collaboration with Dr. Jordi García-Antón. The methodologies used were cyclic voltammetry (CV) and differential pulse voltammetry (DPV) in methanol. Methanol is not often used as solvent in electrochemistry because its electrochemical window is not wide. Nevertheless, we studied the oxidation potential of the complexes, and methanol was not electroactive in the studied potential range. Furthermore, TBABF<sub>4</sub> was used as supporting electrolyte.

Oxidation voltammograms for **Ru(pydic)(terpyDP)** and **Ru(pydic)(terpyTP)** using CV and DPV are shown in Figure 32.

Both complexes were redox active. The CV voltammograms exhibit one reversible oxidation wave associated to the electron transfer of Ru<sup>2+</sup> to Ru<sup>3+</sup>. The wave of **Ru(pydic)(terpyDP)** presents an oxidation peak at 0.64 V/SCE and a reduction peak at 0.56 V/SCE, while these values are 0.63V/SCE and 0.56V/SCE for **Ru(pydic)(terpyTP)**. DPV voltammograms show one oxidation peak at 0.58 V/SCE and 0.56 V/SCE for **Ru(pydic)(terpyDP)** and **Ru(pydic)(terpyTP)**, respectively.



## Chapter 3

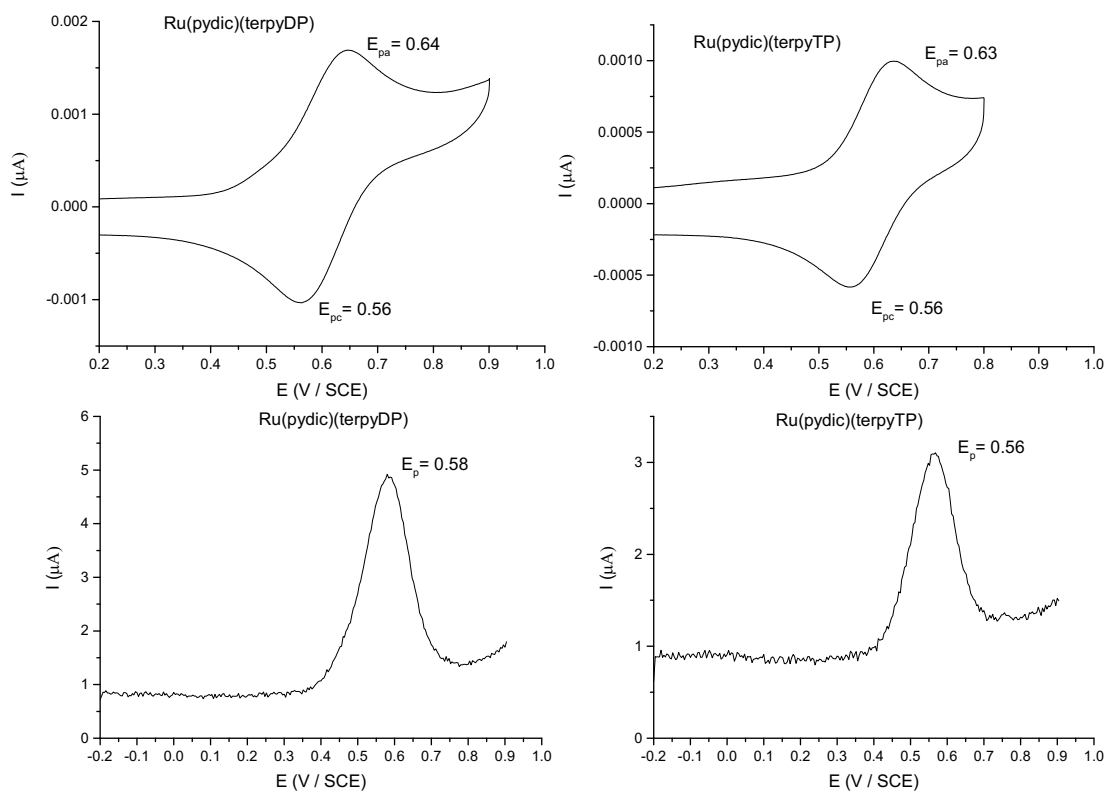


**Figure 32.** CV (top) and DPV (bottom) voltammograms for 7 mM **Ru(pydic)(terpyDP)** and **Ru(pydic)(terpyTP)** + 0.1 M TBABF<sub>4</sub> in methanol. Glassy Carbon working electrode, Pt counter electrode and SCE reference electrode.  $v = 0.1$  V/s in CV and  $\Delta E = 10$  mV in DPV.

It is possible to calculate the value of  $E_{1/2}$  (half-wave potential) because the system is completely reversible using both methods. The equations used are described in the experimental section 7.8 and the resulting  $E_{1/2}$  values are shown in Table 4. In the table, the  $E_{1/2}$  value of the related complex **Ru(pydic)(terpy)** studied in the literature is also shown (Figure 33).<sup>82</sup>

The observed  $E_{1/2}$  value is due to the oxidation of the  $\text{Ru}^{2+}$ . The values are almost equal using both techniques, but they are slightly lower using DPV. Both studied complexes and the analogous **Ru(pydic)(terpy)** have similar values of  $E_{1/2}$ . The presence of the peptide moiety in our complexes does not alter the oxidation of the metal ion because it is located at a considerably distant position. However, half-wave potential of **Ru(pydic)(terpyTP)** is lower than **Ru(pydic)(terpyDP)**. Thus, it means that **Ru(pydic)(terpyTP)** can be oxidized slightly more easily than

**Ru(pydic)(terpyDP)**. In a catalyzed reaction in which an oxidation step is required, that fact is very important. The lower standard potential of the catalyst is, the better the reactivity.<sup>82-86</sup> Our complexes have a similar  $E_{1/2}$  value to **Ru(pydic)(terpy)**, so we expected a similar reactivity using them.

**Table 4.**  $E_{1/2}$  values for **Ru(pydic)(terpyDP)** and **Ru(pydic)(terpyTP)** using CV and DPV.

Complex	$E_{1/2}$ (CV)	$E_{1/2}$ (DPV)
<b>Ru(pydic)(terpyDP)</b>	0.600 V	0.585 V
<b>Ru(pydic)(terpyTP)</b>	0.595 V	0.565 V
<b>Ru(pydic)(terpy)</b> <sup>82</sup>	0.60 V	-

### 3.3.3.4 Catalyzed reaction studies of $Ru^{2+}$ complexes

Some catalytic studies using **Ru(pydic)(terpyDP)** and **Ru(pydic)(terpyTP)** in the epoxidation of alkenes were carried out. Since both complexes are not metallogelators, we could not study them as catalysts in reactions in gel phase. Nevertheless, to prove that they are suitable for catalysis, we studied them in solution. Several efficient catalysts have been reported in the literature for the epoxidation of alkenes. Beller and coworkers studied the epoxidation of different branched aliphatic and aromatic alkenes using **Ru(pydic)(terpy)** and derivatives as catalysts.<sup>82,84,87</sup> They followed a mild procedure (room temperature and using  $H_2O_2$  as oxidant) for the epoxidation, achieving good to excellent yields. Their mechanistic studies showed that the use of protic solvents makes the oxidation of Ru center faster. Furthermore, different Ru species in higher oxidation were found to be possible intermediates in the reaction pathway (Figure 33).<sup>82</sup>

## Chapter 3

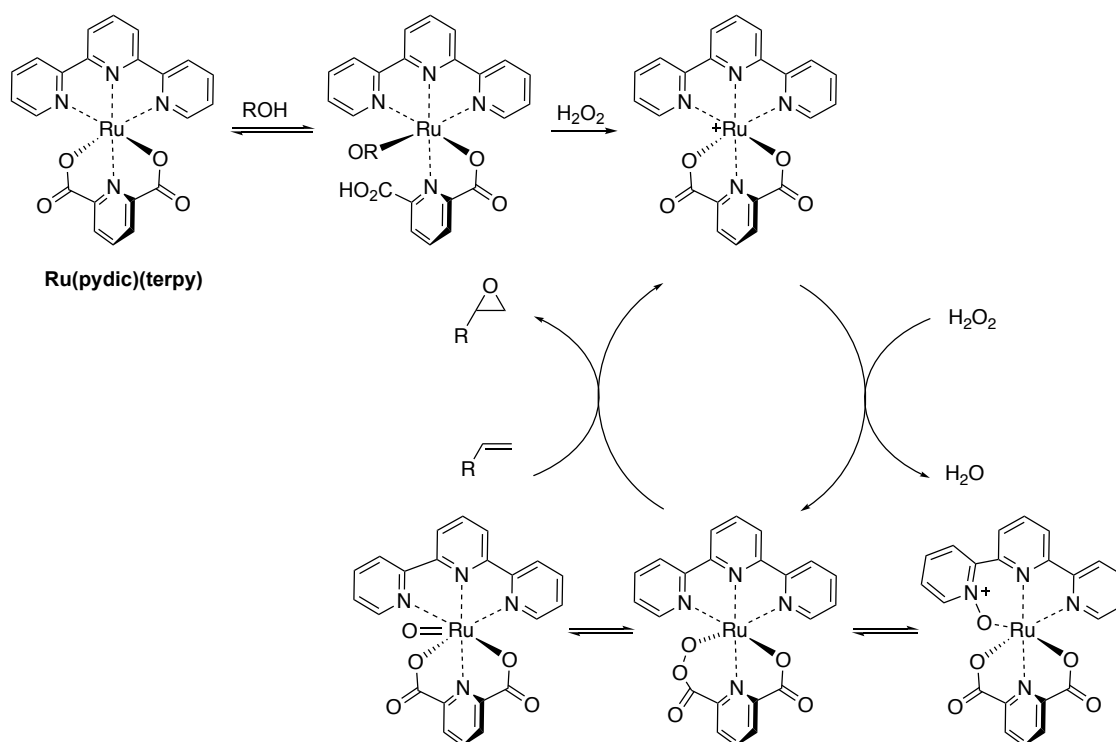


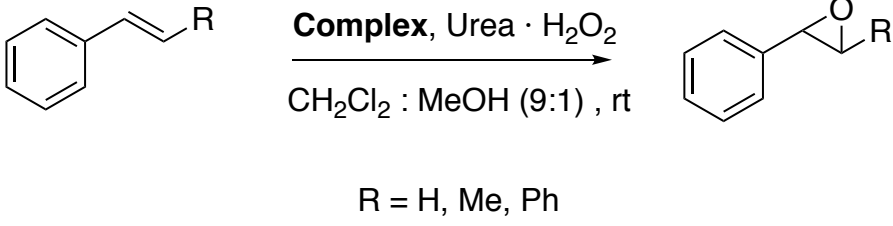
**Figure 33.** Epoxidation of alkenes mechanism catalysed by **Ru(pydic)(terpy)**.

Using the same conditions that Beller and coworkers, **Ru(pydic)(terpyDP)** and **Ru(pydic)(terpyTP)** were tested as catalysts in the epoxidation of different aromatic alkenes. Only 0.5 mol% of catalyst was used in the reaction test and UHP (urea hydrogen peroxide) was used as oxidant at room temperature. Since the solubility of these complexes is limited, in our first trials we used methanol as solvent. Unfortunately, methanol solvolysis (attack to the epoxide) products were obtained. After, we tested the reaction in dichloromethane/methanol, 9:1 mixture as solvent, and the obtained results are shown in Table 5.

Results showed that both complexes catalyse the formation of the epoxide product in moderate yields in the case of styrene, and excellent yields using other substituted substrates. **Ru(pydic)(terpyDP)** gave slightly better yields and faster reaction times than **Ru(pydic)(terpyTP)** in the case of styrene and *trans*-stilbene. This result can be justified by the fact that with long reaction times, solvolysis of epoxide can still occur since methanol is used as co-solvent. Beller's catalyst gave similar yields but faster reaction times in the case of *trans*-stilbene and  $\beta$ -methyl styrene, but lower yield in the case of styrene comparing it with our complexes.

These results are in agreement with the electrochemical studies, which predicted similar reactivity between all complexes.

**Table 5.** Epoxidation of aromatic alkenes catalysed by **Ru(pydic)(terpyDP)** and **Ru(pydic)(terpyTP)**.

			
Complex	Substrate (R)	Yield (%) <sup>a</sup>	Time (h) <sup>a</sup>
<b>Ru(pydic)(terpyDP)</b>	H	60	2.5
	Ph	97	7
	Me	99	5
<b>Ru(pydic)(terpyTP)</b>	H	48	3.5
	Ph	90	8
	Me	98	5
<b>Ru(pydic)(terpy)<sup>82</sup></b>	H	39	3
	Ph	99	1
	Me	99	3

All reactions were carried out using 0.5 mmol of styrene in 10 mL of 9:1 dichloromethane/methanol as solvent. <sup>a</sup> Yields determined by GC analysis by interpolation of calibrations plots.

As expected, epoxide products were analysed by chiral HPLC and a racemic mixture was obtained in all cases. The chiral centers of **Ru(pydic)(terpyDP)** and **Ru(pydic)(terpyTP)** are quite far from the catalytic center, thus no enantioselectivity was induced. It would have been interesting to compare the

## Chapter 3

enantioselectivity in a hypothetical reaction in gel phase, but unfortunately, as it is explained previously, both complexes were not able to gelate any solvent.

### 3.4 Summary and conclusions

In this chapter, two new functionalized LMWGs were synthesized using two well known peptide-based gelators and a terpyridine derivative. They were able to gelate a wide range of solvents, being the best mgc values of 49 mg/mL in methanol, and 43 mg/mL in 2-propanol, for **terpyDP** and **terpyTP**, respectively. The incorporated terpyridine moiety reduced their gelating efficiency (higher mgc values), but it favored the gelation of solvents of different nature.

The aggregation of both compounds followed a helical-like structure confirmed by the CD spectra of xerogels from both compounds. Furthermore, theoretical calculations supported this helicity. The structures of the calculated aggregates showed that the relative function positions were well defined, remaining the terpyridine moieties inside the fibril and the peptide part spinning around them.

Both gelators were complexed with  $\text{Ru}^{2+}$  and  $\text{Pd}^{2+}$  in order to get metallogelators, but the obtained complexes were not able to gelate any solvent. Moreover, all complexes were insoluble in most organic solvents, specially the  $\text{Pd}^{2+}$  complex. These results confirmed that a rational design of metallogelators is still a big challenge.

$\text{Ru}^{2+}$  complexes were used as catalysts in the benchmark reaction of epoxidation of alkenes in solution. They presented moderate to good yields, being comparable with an analogous  $\text{Ru}^{2+}$  complex from the literature. The electrochemical studies of all complexes agreed with these findings. Nevertheless, no asymmetric induction was accomplished in these reactions.



**4. Synthesis of Proline / Cyclobutane Amino  
Acid-Containing Tripeptides:  
Organocatalysts for Asymmetric Aldol  
Additions**

---





## 4. Synthesis of Proline / Cyclobutane Amino Acid-Containing Tripeptides: Organocatalysts for Asymmetric Aldol Additions

### 4.1 Introduction

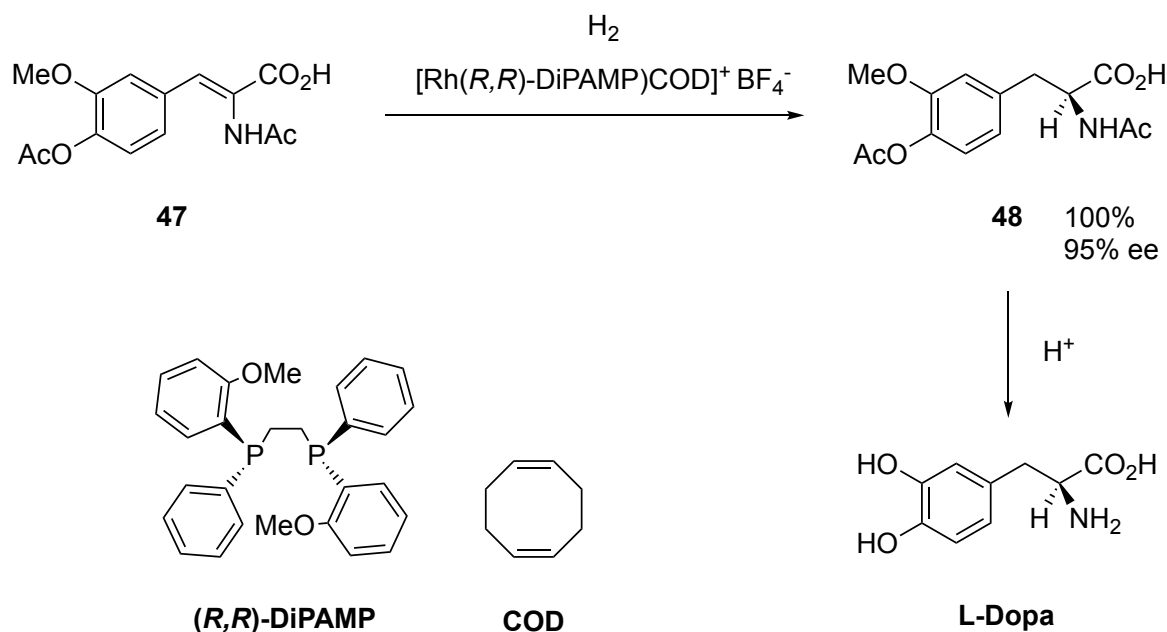
During the last decades, the interest in the synthesis of enantiopure compounds has increased notably, since the spatial arrangement of carbon atoms within molecules could dramatically change their properties. The compound thalidomide is a well-known example, which was used as a treatment of nausea in pregnant women. This drug was used as racemate, being the *R* isomer the responsible of the therapeutic behaviour. The problem was that its stereogenic centers can epimerize under physiologic conditions and the *S* isomer generates teratogenic effects on the fetus. For this reason, its commercialization caused a tragedy in the 60's when about 10000 infants were born with a malformation in the limbs.<sup>88,89</sup> Beyond that point, the stereochemistry of drugs was conscientiously considered, and therefore, asymmetric transformations with the aim of preparing enantiopure compounds for their use in many applications, specially in medicine, have been deeply investigated.

The classical approach for the separation of racemic mixtures, such as crystallization, or chromatographic resolution on chiral columns are usually expensive and slow methodologies. One of the most effective and costless manners to obtain these molecules is the asymmetric or enantioselective catalysis. It consists in the transformation of achiral substrates into stereoisomeric products in unequal proportions, by the use of small amounts of enantiomerically pure catalysts.

Some of the first enantioselective catalysis were performed using transition metal complexes in the second half of the 20<sup>th</sup> century, which allowed low catalyst loading and achieved high asymmetric inductions. These compounds use chiral organic ligands, which provide the chiral environment, to coordinate a transition metal, like palladium or ruthenium, resulting a catalyst with great impact in the enantioselective formation of C-C or C-heteroatom bonds.<sup>90-92</sup> Knowles, Noyori and Sharpless received the Nobel price for the study of enantioselective reactions of high interest using chiral metal complexes. For example, Knowles and co-workers

## Chapter 4

at Monsanto Company developed an asymmetric olefin hydrogenation reaction using a rhodium complex. This reaction allowed the industrial synthesis of the rare amino acid **L-Dopa** which is useful in the Parkinson disease treatment (Scheme 9).<sup>93</sup>



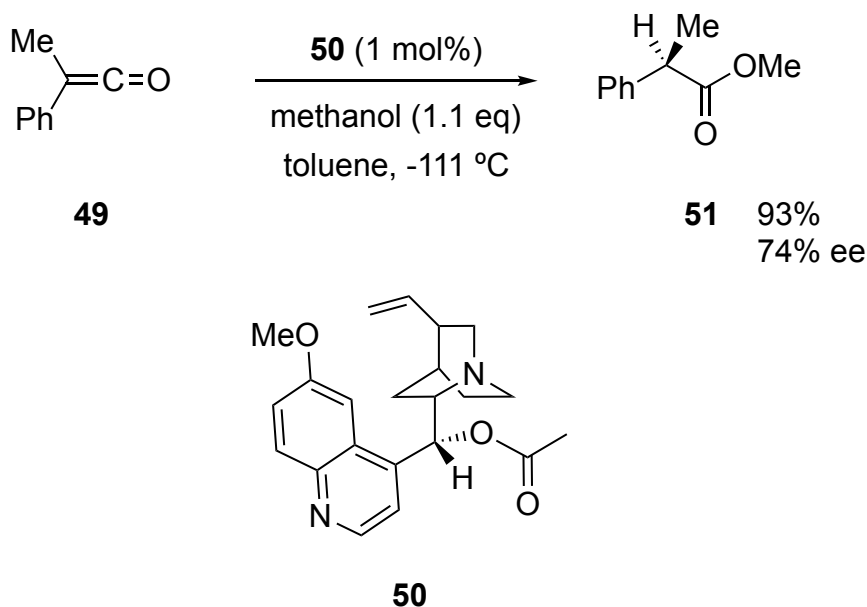
**Scheme 9.** Monsanto synthesis of **L-Dopa** through asymmetric hydrogenation using a chiral Rh complex as catalyst.

Although the study of metal complexes as catalysts is still of high interest for researchers nowadays, the practical procedures to use these catalysts require very rigorous conditions, such as air sensitive techniques or even the preparation in glove boxes due to their air and moisture sensitivity. Moreover, most of the transition metals are highly toxic, so the complete separation and purification of the final products adds even more issues in their employment. Overall, these problems require an especial long-term storage and care handling that originates high cost on a large scale, making their use in the industry very difficult.

Another type of enantioselective catalysis is achieved using biocatalysts. This sort of catalysis benefits from the employment of biological macromolecules, such as enzymes, to catalyse asymmetric transformations. Their chiral tridimensional structures properly bind and orient the substrates inducing

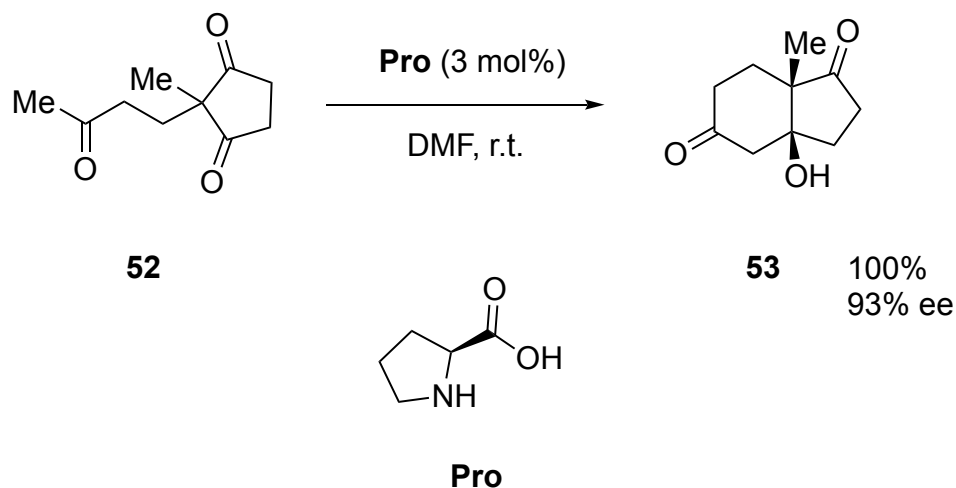
asymmetry. Even though they are usually expensive, their employment in the industrial scale is increasing, providing high enantioselectivities under mild conditions.<sup>94</sup> Unfortunately, the low stability of enzymes as well as their specificity makes them useful in a only few chemical transformations.

The third main type of enantioselective catalysis makes use of chiral organocatalysts, which are small organic molecules that efficiently induce chirality in organic transformations.<sup>95–98</sup> The very first enantioselective organocatalyzed reaction was the addition of HCN to benzaldehyde catalyzed by the chiral alkaloids quinine and quinidine, reported in 1912.<sup>99</sup> Unluckily, the resulting products only afforded optical yields of less than 10%. It was not until almost 40 years later that Pracejus and coworkers achieved a notable 74% ee in the addition of methanol to **49**, using the quinine derivative **50** as chiral organocatalyst (Scheme 10).<sup>100</sup>



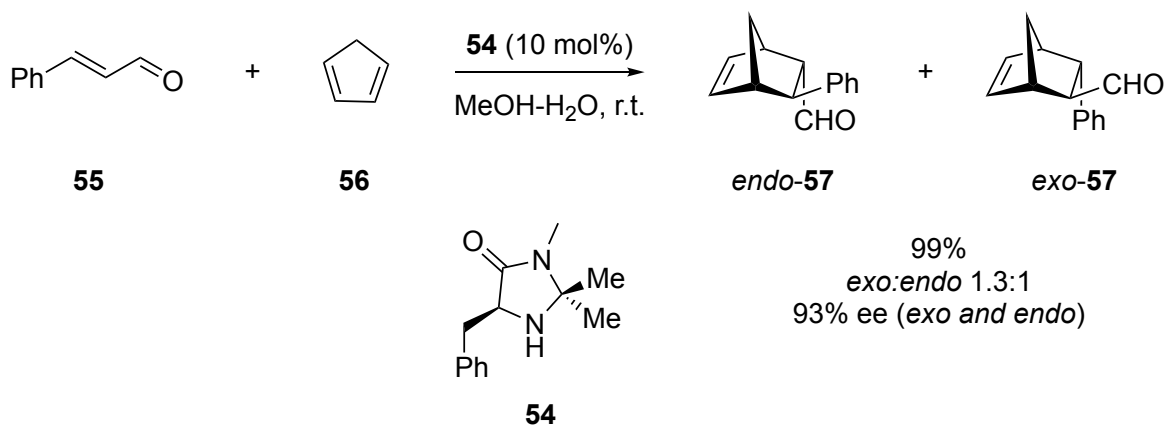
**Scheme 10.** Methanol addition to a ketene catalyzed by **50**.

Another notable example of enantioselective organocatalysis was found simultaneously by Eder, Sauer and Wiechert,<sup>101</sup> and Hajos and Parrish.<sup>102</sup> They reported an asymmetric intramolecular aldol reaction of triketone **52** catalyzed by (*L*)-proline (**Pro**), obtaining excellent enantioselectivities (Scheme 11).



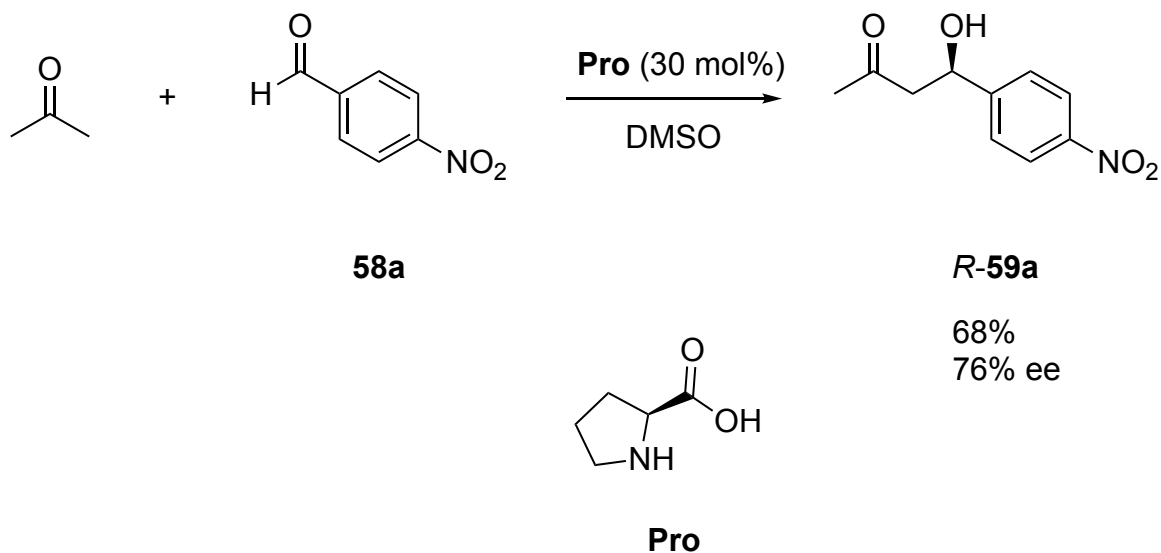
**Scheme 11.** The Hajos-Parrish reaction catalyzed by (*L*)-proline (**Pro**).

Despite these first examples of enantioselective organocatalysis, there were not considerable improvements in this field for decades, possibly due to the great success of metal-based catalyst for enantioselective transformations in those years. The turnover in the subject of enantioselective organocatalysis occurred in 2000 when MacMillan and List reported iminium and enamine based organocatalyst, respectively, turning organocatalysis into one of the big fields of organic chemistry. MacMillan and coworkers reported an asymmetric Diels-Alder reaction of  $\alpha,\beta$ -unsaturated aldehydes with cyclopentadiene catalyzed by the phenylalanine derivative **54**. An iminium intermediate formed by reaction of **54** with aldehyde **55** was rationalized as the active species, obtaining the products with excellent enantioselectivities (Scheme 12).<sup>103</sup>



**Scheme 12.** Diels-Alder reaction catalyzed by secondary amine **54**.

At the same time, List, Barbas and coworkers, making use of Barbas expertise in catalytic aldolases, revisited the Hajos-Parrish-Eder-Sauer-Wiechert reaction approach, reporting the first (*L*)-proline (**Pro**) catalyzed asymmetric intermolecular aldol reaction with also good enantioselectivities (Scheme 13).<sup>104</sup>



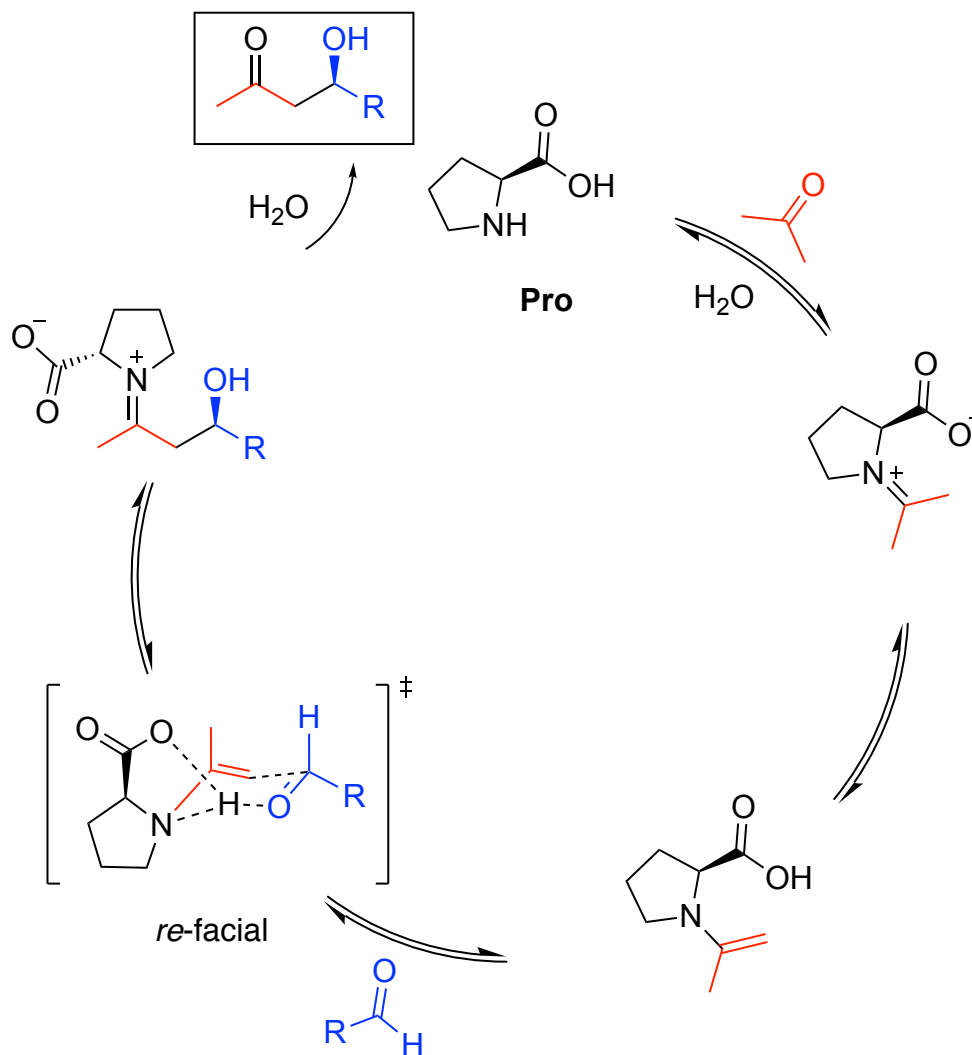
**Scheme 13.** Aldol reaction catalyzed by **Pro**.

As mentioned above, an enamine-based intermediate was proposed as active species in this reaction. Enamine catalysis can be considered as a special case of the iminium-based catalysis, where first an iminium intermediate is formed between a secondary amine and a carbonyl compound (with an acidic  $\alpha$  proton), and evolves to an enamine, which is the responsible of the nucleophilic attack on the aldehyde, ideally with enantiofacial selectivity.

Different publications suggested that both functionalities of **Pro** are involved in the step that determines the enantioselectivity of the aldol reaction. Several researchers postulated different transition states for this reaction, like Agami who hypothesized that two proline molecules were involved in the transition state.<sup>105</sup> However, the most accepted model for this reaction was suggested by List and Houk (Scheme 14).<sup>106–108</sup> They suggested that it could involve a chair-like Zimmerman-Traxler transition state. The amino function forms an enamine with the acetone, while the carboxylic acid fixes the aldehyde through a tricyclic hydrogen

## Chapter 4

bond, like a Brønsted acid co-catalyst. Their models predicted successfully the enantioselectivity observed in several aldol reactions catalyzed by **Pro** (Scheme 14).



**Scheme 14.** Schematic enamine-based mechanism of asymmetric aldol reaction catalyzed by **Pro**. The acetone and the aldehyde are remarked in red and blue, respectively.

Enamine-based organocatalysts are often compared with the natural activity of the Lys229 residue from aldolase I enzymes. In this analogous approach, nature uses this reaction in fundamental steps of the metabolism, for example in gluconeogenesis and glycolysis. Actually, List and Barbas were pursuing to mimic

the reactivity of aldolases I in their first publication of asymmetric intermolecular aldol reaction catalyzed by **Pro**. The remarkable enantioselectivity observed in the aldol reaction using **Pro** as catalyst inspired the use of this amino acid in Mannich, Michael and related reactions.<sup>109–113</sup>

Regardless the good performance shown in these reactions, the use of **Pro** as catalyst presented some disadvantages. Its better efficiency is achieved using DMSO and DMF as solvents, reducing the possibility of the full recovery of the catalyst. Another handicap is that in some examples a high catalyst loading is needed, even up to 30-35% increasing the costs of its use. Globally, these limitations make this catalyst not suitable for the industrial scale.

Several researchers have made great efforts trying to improve the performance of **Pro** by modifying or derivatizing different positions of the **Pro** scaffold. The most used strategy has been introducing different groups in the C-2 position (carboxylic acid), such as adding different bulky moieties or changing the H-bonding interactions by incorporating other functions. For example, some designs incorporate a tertiary amine (**60**),<sup>114</sup> a sulphonamide (**61**),<sup>115</sup> or a tetrazole (**62**) (Figure 34).<sup>116</sup>

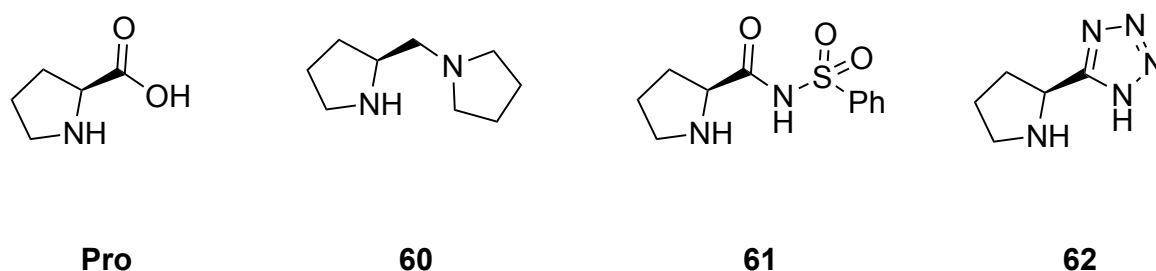


**Figure 34.** Proline derivatives used in asymmetric aldol reactions as catalysts.

Furthermore, taking advantage of the knowledge of the enamine-based mechanism, researchers have focused in designing other chiral organocatalysts achieving excellent stereoselectivity in several reactions.<sup>117,118</sup> As an example, Palomo and coworkers reported the first enamine mediated *anti*-selective Mannich reaction of aldehydes and unactivated imines (Figure 35). This reaction was



## Chapter 4

catalyzed by **63**, among other related catalysts, achieving good yields and high enantioselectivities.

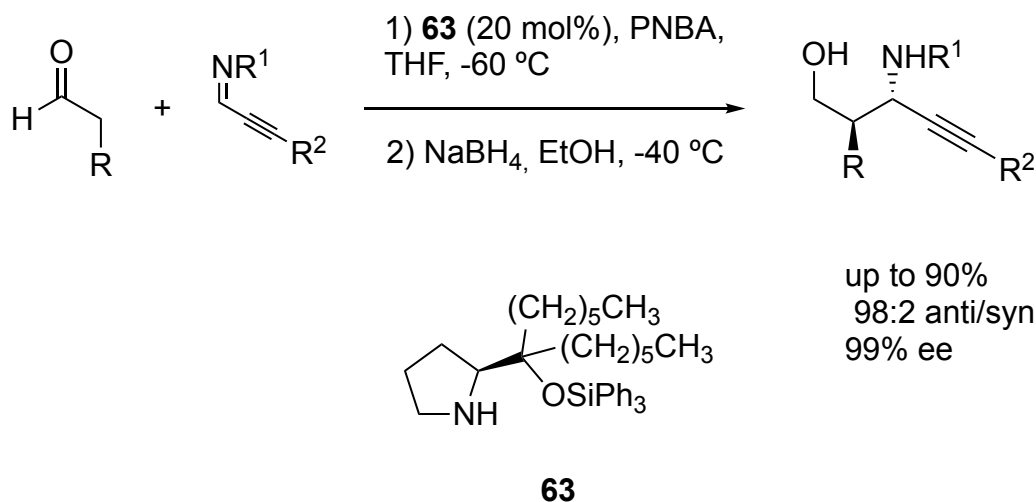


**Figure 35.** *Anti*-selective Mannich reaction catalyzed by **63**.

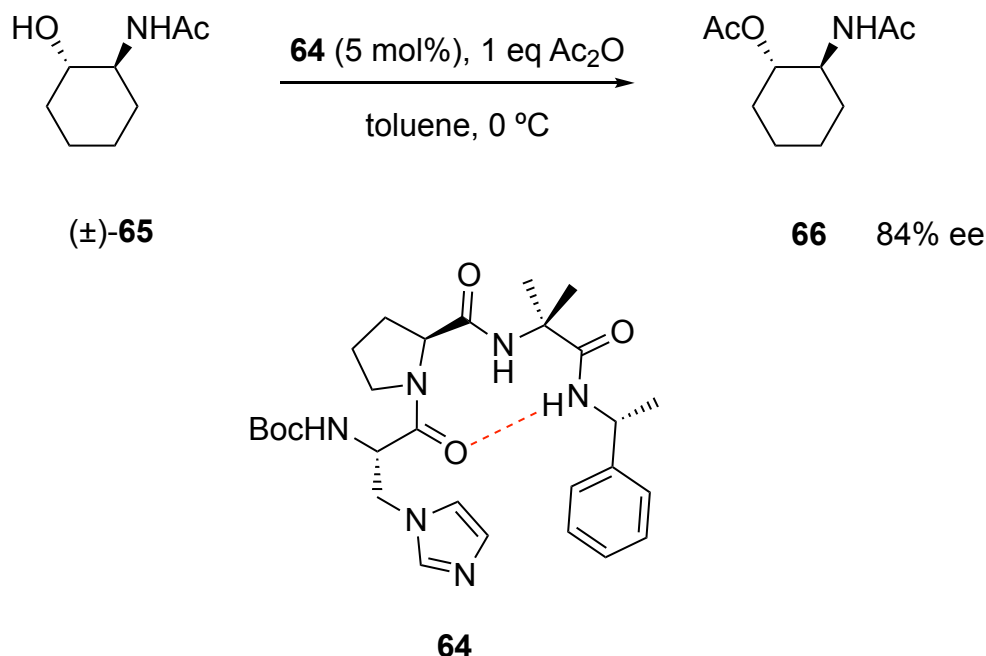
### 4.3.1 Short peptides as organocatalysts

The use of short peptides as organocatalysts in asymmetric reactions has grown during the last two decades.<sup>119,120</sup> The enormous variety of possible combinations of natural and non-natural amino acids allow the preparation of chiral catalysts for several different applications. In the attempt to mimitize enzymes, a privileged peptide conformation with an adequate orientation of its functional groups is crucial for high reactivity and selectivity in organocatalysis. For enzymes, this is achieved through long amino acid sequences that fold into highly ordered structures, creating a defined environment in which a reaction can be catalyzed.

The first examples for the use of short peptides in catalysis were reported in the decade of 1980, by Inoue and coworkers,<sup>121</sup> with the use of a cyclic dipeptide as catalyst for stereoselective hydrocyanations of aldehydes, by Julià<sup>122</sup> on the epoxidation of chalcones by polypeptides and by Ueoka and coworkers, on the enantioselective hydrolysis of esters using a tripeptide.<sup>123</sup>

Nevertheless, it was not until 20 years later that this area expanded to the mainstream research, for example with the publication of Miller and coworkers

where they reported a tripeptide containing a non-natural amino acid **64** that catalyzed the kinetic resolution of racemic alcohols, like **65**, by acetylation (Scheme 15).<sup>124</sup>



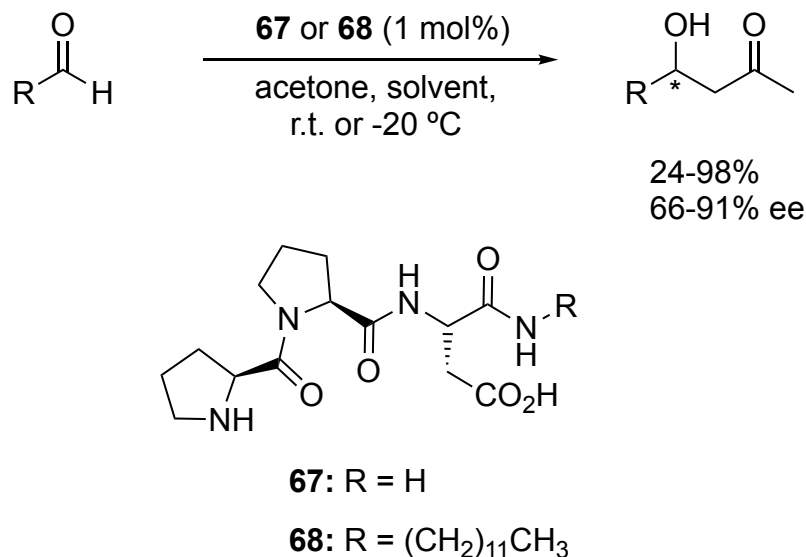
**Scheme 15.** Kinetic resolution by acetylation using tripeptide **64**. The H-bond responsible for the major conformation is remarked in red.

In this work, the conformation of the peptide was found to be crucial for the selectivity of the reaction. Tripeptide **64** presented a major conformation (up to 90%), while an epimer of **64** had a major conformation corresponding to 75%. When both were tested in the kinetic resolution of alcohol **65**, it was observed that the selectivity of the epimer decreased to 53% ee while tripeptide **64** achieved 84% ee.

Organocatalysts based on short peptides have been explored for a great number of reactions, specially in C-C bond formations such as Morita-Baylis-Hilman reactions, nitroalkane additions, Friedel-Crafts alkylations, and Michael and aldol additions. As mentioned above, (*L*)-proline is one of the most explored organocatalysts for the aldol reaction. The inclusion of this natural amino acid in short peptides has been used by different researchers with the aim of improving its performance. An excellent example was reported by Wennemers and coworkers,

## Chapter 4

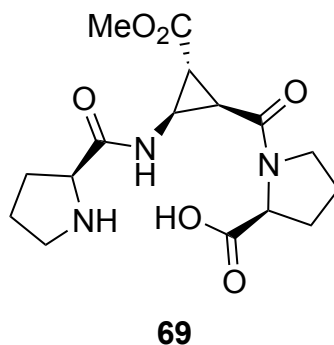
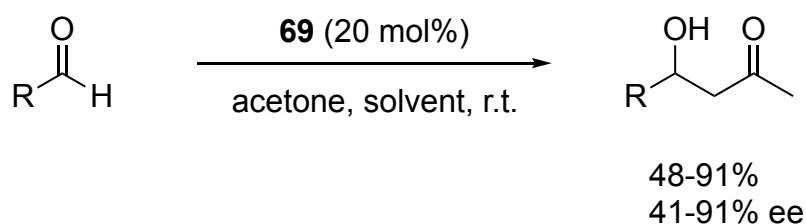
that explored the catalytic activity of H-Pro-Pro-Asp-NH<sub>2</sub> tripeptide **67** and alkylated derivative **68** in the aldol reaction (Scheme 16).<sup>125</sup>



**Scheme 16.** Aldol reaction catalyzed by peptides **67** and **68**, respectively.

Peptide **68** proved that the presence of the alkyl chain does not change the catalytic properties compared with **67**, but provided higher solubilities in a wide range of solvents. It was observed that the absolute configuration of the aldol product was the same in DMSO, MeOH and DMF, while in non-polar solvents such as *n*-hexane the opposite enantiomer was favoured. Surprisingly, the addition of amounts of water to DMSO or MeOH reversed the enantioselectivity of the aldol product. This switch of the enantioselectivity by only changing the solvent was not usual. NMR and CD studies of peptide **68** in the absence and presence of water revealed that remarkable conformational changes, which demonstrated that they are probably responsible for the variation of the enantioselectivity observed experimentally.

Another example was reported by Reiser and coworkers. They described the synthesis of short  $\alpha,\beta$ -tripeptides that contain a *cis*- $\beta$ -cyclopropane amino acid residue in combination with (*L*)-proline. These peptides were tested as organocatalysts in inter- and intramolecular aldol reaction achieving high yields and stereoselectivities (Scheme 17).<sup>126</sup>



**Scheme 17.** Aldol reaction catalyzed by peptide **69**.

In that work, the best performance was accomplished using tripeptide **69**, which was attributed to the remarkable stabilization of secondary structures of the incorporated and conformationally restricted *cis*- $\beta$ -cyclopropane amino acid unit.

In conclusion, although it has been proved by some researchers that short peptides can be excellent organocatalysts for asymmetric transformations, the development of these catalysts present some difficulties. They are usually unordered and can adopt several conformations, difficulting the disposition of the active groups in a cooperative manner required for the catalysis. Furthermore, the large number of natural and non-natural amino acids makes the possible combinatorial sequences immesurable, so an intelligent approach is needed. Consequently, the rational design of a short peptide-based organocatalyst is still a huge challenge.



## 4.2 Objectives

In this part of the thesis, the synthesis of several tripeptides consisting of two proline residues located in the terminal positions and a cyclobutane-containing amino acid (CBAA) in the center was proposed. In their design, (*L*)- or (*D*)-proline as well as both enantiomers of *cis*  $\beta$ - or  $\gamma$ -CBAA were considered (Figure 36).

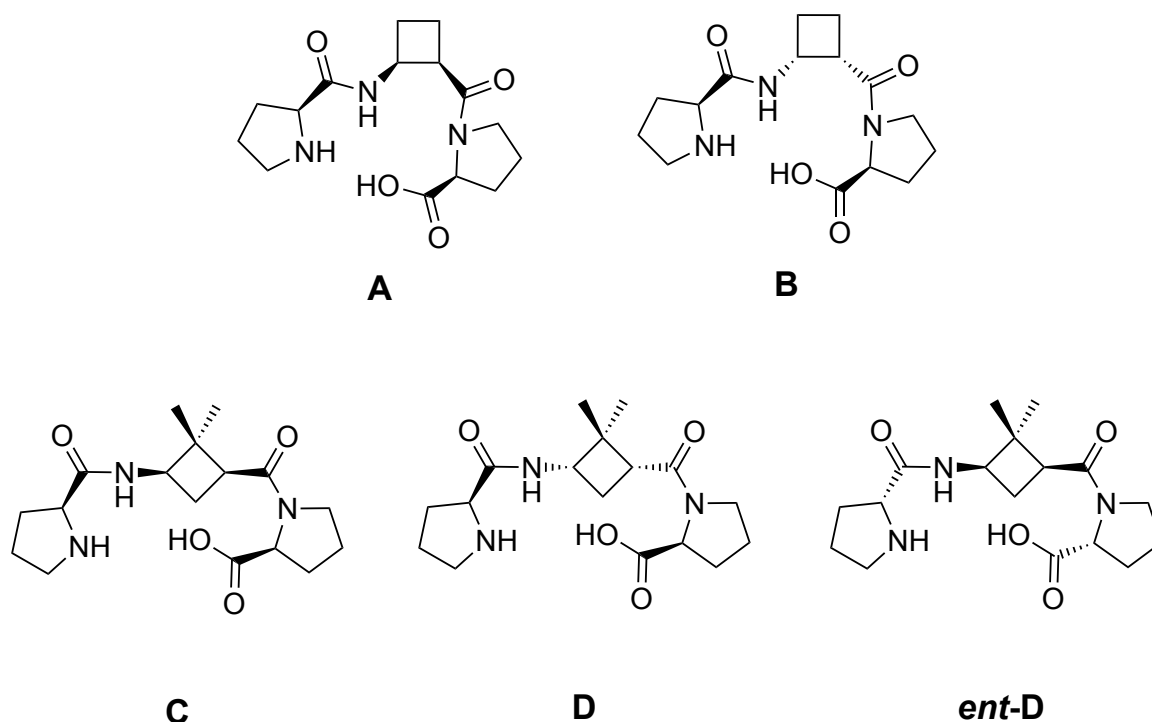


**Figure 36.** Proposed new tripeptides.

The objectives of this part are:

- The synthesis of these tripeptides.
- The study of their catalytic activity in the aldol reaction using different aldehydes, ketones and solvents under different conditions. Preliminary studies in the Michael reaction.
- The investigation of the influence of the chirality of the proline and cyclobutane-based residues as well as their nature as  $\beta$ - or  $\gamma$ -amino acids in the enantioselectivity.

## Chapter 4

- The rationalization of the origin of the stereoselectivity found in the organocatalyzed reactions.

## 4.3 Results and discussion

The results of this part of the thesis are presented in four parts. First, the synthesis of the new tripeptides is described (section 4.3.1). After, the results of the catalyzed reactions are explained (section 4.3.2) followed by the structural study of peptide **D** (section 4.3.3). Finally, theoretical calculations are used to rationalize the experimental results (4.3.4).

### 4.3.1 Synthesis of tripeptides

Considering the acquired experience in our research group preparing cyclobutane-based amino acids, the studied tripeptides were synthesized through the following general retrosynthetic pathways (Figure 37 and Figure 38).

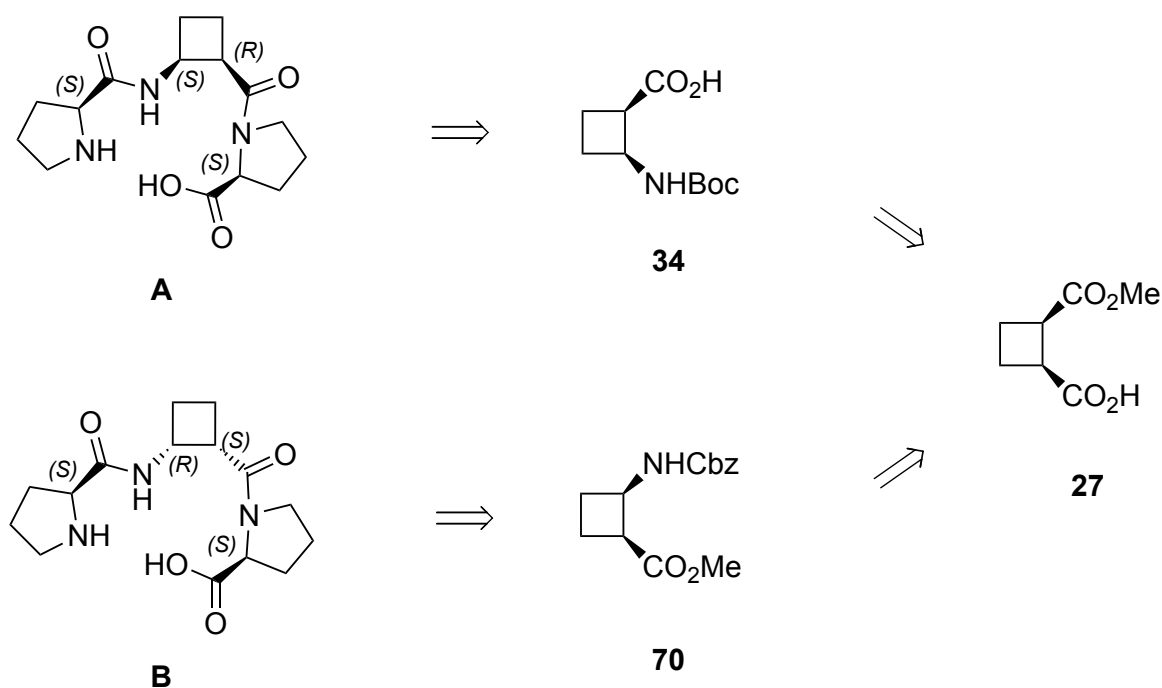


**Figure 37.** General retrosynthetic pathway for  $\alpha,\beta,\alpha$ -tripeptides **A** and **B**. Absolute configuration of the stereogenic centers are shown.

The preparation of the cyclobutane-based  $\beta$ - or  $\gamma$ -amino acids **34**, **70**, **71** and **72** were already reported in our research group.<sup>5,6,11,127</sup> Compounds **A** and **D** were



## Chapter 4

previously synthesized for the first time by Carme Robledillo in her master thesis. In this thesis, the synthesis of the tripeptides was repeated and optimized to perform the proposed catalytic studies. Compound **ent-D** was prepared by Carlos Elvira in his bachelor work supervised by Prof. R. M. Ortuño, and myself. The proline-based derivatives were purchased from commercial sources in an enantiopure form.

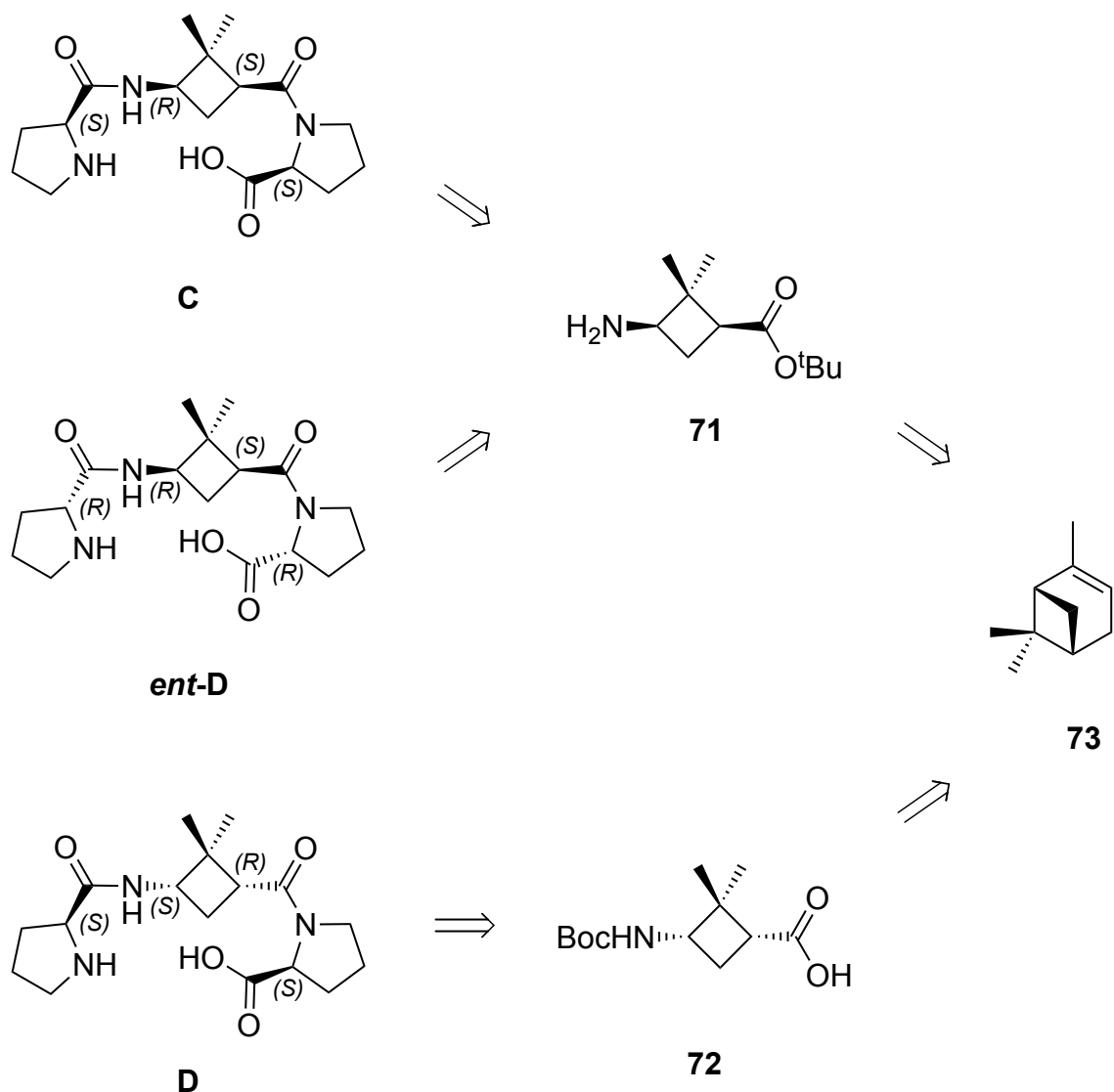


**Figure 38.** General retrosynthetic pathway for  $\alpha,\gamma,\alpha$ -tripeptides **C**, **D** and **ent-D**. Absolute configuration of the stereogenic centers are shown.

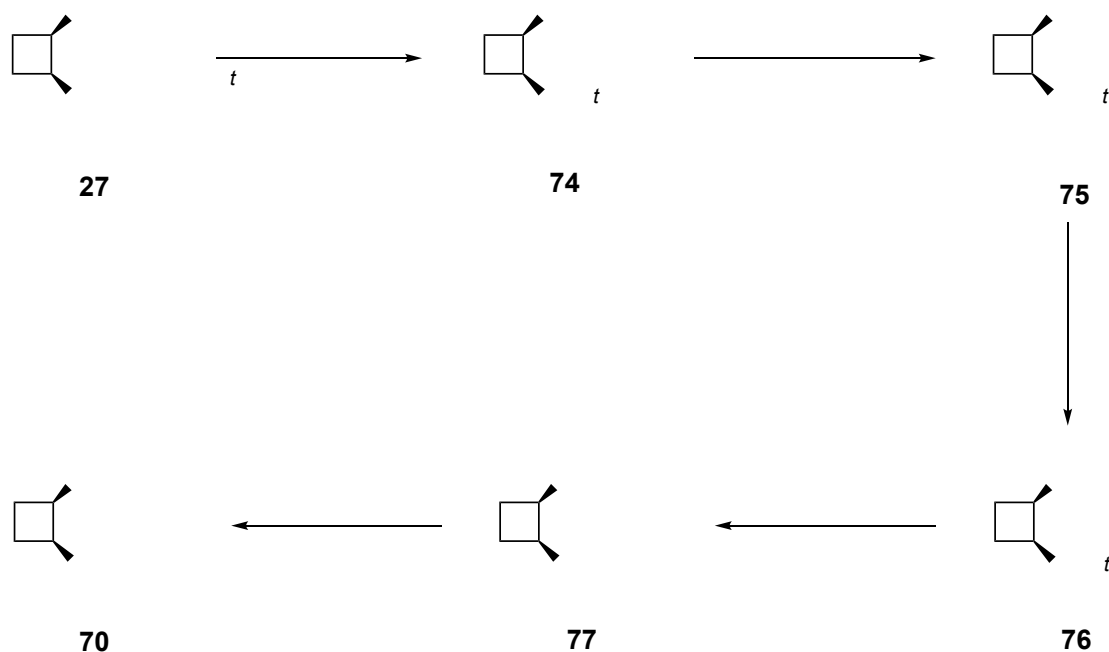
It should be noted that tripeptides **A** and **B** are diastereoisomers, since both have two (*L*)-proline units, but different enantiomers of the  $\beta$ -amino acid residue.

Also, tripeptides **C** and **D** are diastereoisomers since they contain two (*L*)-proline amino acids, but they have different enantiomers of the  $\gamma$ -amino acid residue. To understand the influence of the chirality of the proline residue, tripeptides **ent-D** was prepared with (*D*)-proline and  $\gamma$ -amino acid **71**. So, tripeptides **D** and **ent-D** are enantiomers.

The synthetic routes to prepare all tripeptides and their intermediates are explained below.

#### 4.3.1.1 Synthesis of protected $\beta$ -amino acids **34** and **70**.

The synthesis of  $\beta$ -amino acid **34** is explained in chapter 3. The synthetic route of the protected  $\beta$ -amino acid **70** can be achieved in a 36% overall yield from enantiopure half-ester **27**. The synthetic route is described in Scheme 18.



**Scheme 18.** Synthetic route of amino acid **70**.

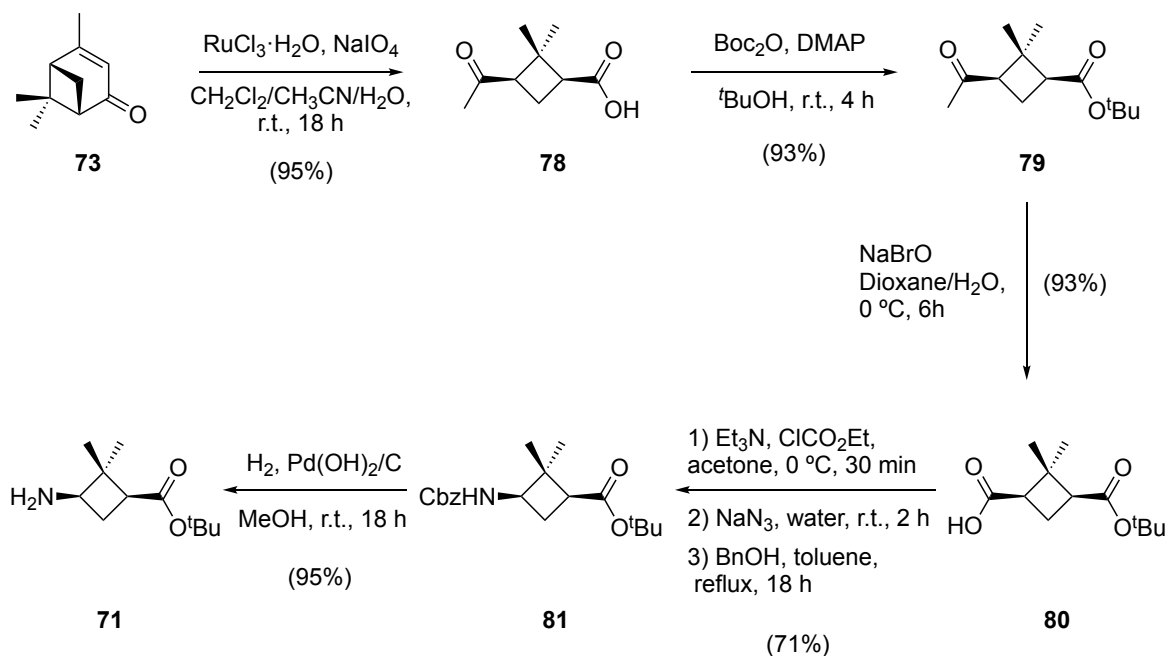
The synthesis of  $\beta$ -amino acid **70** started with the protection of half-ester **27** as *tert*-butyl ester **74**, by reacting the free carboxylic acid group with Boc anhydride and a catalytic amount of DMAP in *tert*-butanol, in 73% yield. Then, diester **74** was

## Chapter 4

saponified with sodium hydroxide under mild conditions. The obtained half-ester **75** was reacted with ethyl chloroformate followed by a treatment with sodium azide to produce the correspondent acyl azide. Next, the isocyanate formed by heating the acyl azide was reacted with benzyl alcohol under reflux conditions to obtain protected amino acid **76** in 54% yield. After, its *tert*-butyl ester function was acyolyzed by reaction with TFA in the presence of triethyl silane and the resulting carboxylic acid **77** was transformed to the corresponding methyl ester **70** with methyl iodide and cesium carbonate, in almost quantitative yields for both steps.

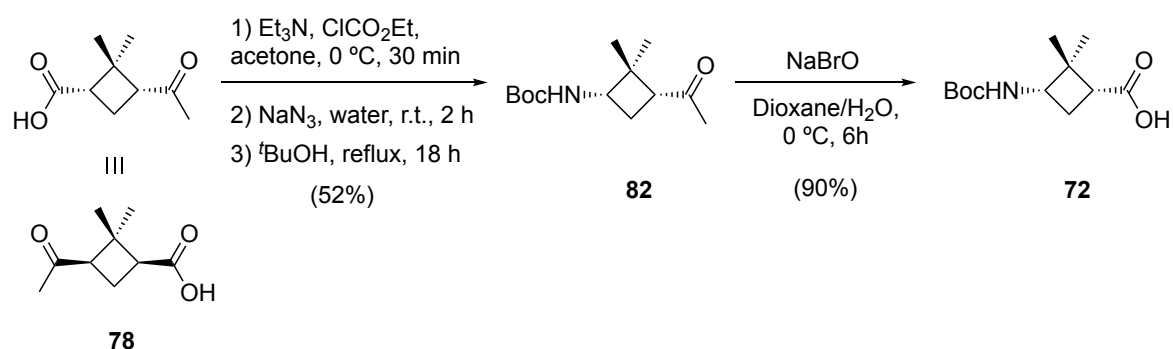
### 4.3.1.2 Synthesis of protected $\gamma$ -amino acids **71** and **72**

The synthesis of  $\gamma$ -amino acids **71** and **72** can be achieved in 55% and 44% overall yield, in 5 and 3 steps, respectively, from enantiopure and commercially available (-)-verbenone **73**. The synthetic routes are described in Scheme 19 and Scheme 20.



**Scheme 19.** Synthetic route for amino acid **71**

In the first step of the synthesis of **71**, a catalytic oxidation of (-)-verbenone led to (-)-*cis*-pinononic acid **78** without epimerization. Then, the carboxylic acid group was transformed into a *tert*-butyl ester in 93% yield using Boc anhydride and catalytic amount of DMAP in *tert*-butanol. In the following step, the methyl ketone **79** was submitted to a Lieben degradation to afford carboxylic acid **80**. Consecutively, **80** was transformed into benzyl carbamate **81** following a 3-step procedure including a Curtius rearrangement in 71% yield. Finally, the hydrogenation of **81** catalyzed by Pd(OH)<sub>2</sub>/C provided amine **71** in 95% yield.



**Scheme 20.** Synthetic route for amino acid **72**. The relative orientation has been flipped to easier compare with tripeptide **D**.

The synthetic route for amino acid **72** started with the same transformation, the oxidation of (-)-verbenone to obtain free carboxylic acid **78**. In Scheme 20, the relative orientation of **78** was flipped to compare more easily with tripeptide **D**. The carboxylic acid **78** was transformed into *tert*-butyl carbamate **82** in 52% yield and consecutively, it was submitted to a Lieben degradation with sodium hypobromite to afford carboxylic acid **72** in 90% yield.

#### 4.3.1.3 Synthesis of tripeptides **A**, **B**, **C** and **D**.

Tripeptides **A** and **B** can be synthesized in 48% and 58% overall yield from enantiopure  $\beta$ -amino acids **34** and **70**, respectively. The synthetic route of tripeptides **C**, **D** and *ent*-**D** can be achieved in a 41%, 32% and 46% overall yield from amino acids **71** and **72**, respectively. The synthetic routes are described in Figure 39.

Chapter 4

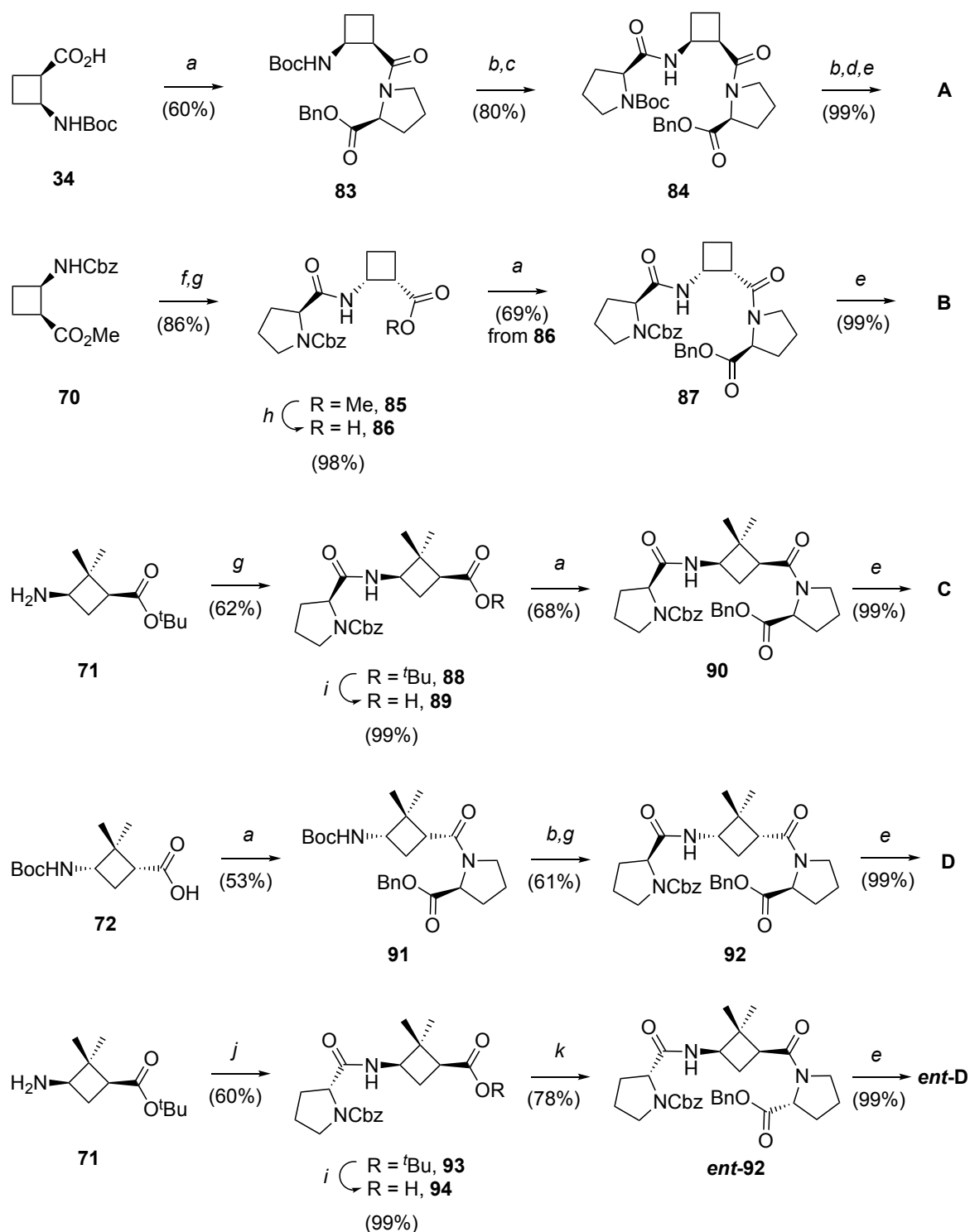


**Figure 39.** Synthesis of tripeptides **A**, **B**, **C**, **D** and **ent-D**. Reagents: (a): PyBOP, DiPEA,  $\text{NH}(\text{HCl})\text{-}(L)\text{-Pro-OBn}$ ,  $\text{CH}_2\text{Cl}_2$ ; (b): 2 M HCl in THF; (c): PyBOP, DiPEA,  $N\text{-Boc-}(L)\text{-Pro}$ ,  $\text{CH}_2\text{Cl}_2$ ; (d):  $\text{NaHCO}_3$ . (e):  $\text{H}_2$ ,  $\text{Pd}(\text{OH})_2/\text{C}$ ,  $\text{CH}_3\text{OH}$ ; (f):  $\text{H}_2$ ,  $\text{Pd}(\text{OH})_2/\text{C}$ , HCl  $\text{CH}_3\text{OH}$ ; (g): PyBOP, DiPEA,  $N\text{-Cbz-}(L)\text{-Pro}$ ,  $\text{CH}_2\text{Cl}_2$ ; (h): 1) 0.25 M NaOH, 2) HCl; (i):  $\text{H}_3\text{PO}_4$ , toluene; (j): PyBOP, DiPEA,  $N\text{-Cbz-}(D)\text{-Pro}$ ; (k): PyBOP, DiPEA,  $\text{NH}(\text{HCl})\text{-}(D)\text{-Pro-OBn}$ ,  $\text{CH}_2\text{Cl}_2$ .

The synthesis of **A** started with the coupling between amino acid **34** and *NH*(HCl)-(*L*)-Proline-OBn in the presence of DiPEA and using PyBOP as coupling agent to obtain **83** in 60% yield. The resulting dipeptide **83** was selectively deprotected in the *N*-terminus followed by its coupling with *N*-Boc-(*L*)-proline to achieve protected tripeptide **84** in 80% yield. Finally, Boc carbamate removal followed by secondary amine neutralization and then a hydrogenolysis of the benzyl ester rendered tripeptide **A** in 99% yield.

The preparation of **B** started with the selective deprotection of **70** by hydrogenation in the presence of hydrochloric acid in order to avoid ring opening of the cyclobutane ring through a push-pull mechanism involving the amino group and the ester. The ammonium salt was directly submitted to react with *N*-Cbz-(*L*)-proline in the presence of PyBOP and DiPEA, producing dipeptide **85** in 86% yield. Then, a mild saponification followed by protonation and coupling of the resulting carboxylic acid **86** with *NH*(HCl)-(*L*)-Pro-OBn led to protected tripeptide **87** in 69% yield. Finally, full deprotection by hydrogenolysis with Pd(OH)<sub>2</sub>/C as catalyst provided tripeptide **B** in 99% yield.

The synthesis of tripeptide **C** started with the coupling between **71** and *N*-Cbz-(*L*)-proline, acquiring dipeptide **88** in 62% yield. After, deprotection of *tert*-butyl ester with phosphoric acid followed by coupling with *NH*(HCl)-(*L*)-Pro-OBn led to protected tripeptide **90** in 68% yield. Finally, deprotection by hydrogenolysis with Pd(OH)<sub>2</sub>/C as catalyst provided tripeptide **C** in 99% yield.

Tripeptide **D** was obtained starting with the coupling between amino acid **72** and *NH*(HCl)-(*L*)-Proline-OBn using PyBOP as coupling agent in 53% yield. The resulting dipeptide **91** was selectively deprotected with hydrochloric acid, followed by coupling with *N*-Cbz-(*L*)-proline to achieve protected tripeptide **92** in 61% yield. Finally, the hydrogenation of both benzyl protections afforded tripeptide **D** in 99% yield. The synthesis of *ent*-**D** is analogous to the preparation of **C**, starting from amino acid **71**, but using the corresponding (*D*)-proline derivative instead of (*L*)-proline.

### 4.3.2 Catalyzed reaction studies

Tripeptides **A**, **B**, **C**, **D** and **ent-D** were studied as organocatalyst in aldol reactions in different conditions, and using different ketones and aldehydes.

As benchmark reaction, catalysts **A**, **B**, **C**, **D** and **ent-D** were tested in an aldol reaction between acetone and *p*-nitrobenzaldehyde. In general, 5 mol% of the catalyst was used in the reaction test with 0.2 mmol of the aldehyde in 2 mL of solvent at room temperature. Some variations in the catalyst amount, the concentration of the aldehyde, the temperature and the solvent were carried out in order to get more insight on the effect of these changes in the activity of the catalyst to find the optimal reaction conditions regarding chemical yield and enantioselectivity. The results are summarized in Table 6.

**Table 6.** Aldol reaction between acetone and **58a** catalyzed by **A**, **B**, **C**, **D** and **ent-D**.

Entry	Catalyst	Solvent <sup>a</sup>	mol % catalyst	Conc. aldehyde [M]	T (°C)	Time (h)	Yield <sup>b</sup> (%)	e.r. <sup>c</sup>	Abs. Con. <sup>d</sup>
1	<b>A</b>	1	5	0.1	r.t.	5	90	68:32	<i>S</i>
2		1	20	0.1	r.t.	4	95	69:31	<i>S</i>
3		2	5	0.1	r.t.	48	80	73:27	<i>R</i>
4		3	5	0.1	r.t.	48	90	69:31	<i>R</i>
5	<b>B</b>	1	5	0.1	r.t.	24	66	54:46	<i>R</i>
6		1	5	0.1	-20	48	17	50:50	-
7		1	5	0.3	r.t.	24	86	52:48	<i>S</i>
8		1	20	0.1	r.t.	24	96	50:50	-
9		1	20	0.1	-20	48	56	43:47	<i>R</i>

10		2	5	0.1	r.t.	24	64	62:38	<i>R</i>
11		2	20	0.1	r.t.	18	99	63:37	<i>R</i>
12	<b>C</b>	1	5	0.1	r.t.	24	77	83:17	<i>S</i>
13		1	5	0.1	-20	24	39	89:11	<i>S</i>
14		1	5	0.3	r.t.	24	54	81:19	<i>S</i>
15		1	20	0.1	r.t.	4	96	82:18	<i>S</i>
16		1	20	0.1	-20	24	69	90:10	<i>S</i>
17		2	5	0.1	r.t.	24	97	60:40	<i>R</i>
18		2	20	0.1	r.t.	18	99	60:40	<i>R</i>
19		<b>D</b>	1	5	0.1	r.t.	2	97	88:12
20	1		5	0.1	0	3	99	90:10	<i>S</i>
21	1		5	0.1	-20	15	99	93:7	<i>S</i>
22	1		5	0.3	r.t.	0.75	99	86:14	<i>S</i>
23	1		5	0.3	0	2.5	99	93:7	<i>S</i>
24	1		10	0.1	r.t.	1	95	87:13	<i>S</i>
25	1		15	0.1	r.t.	1	93	86:14	<i>S</i>
26	1		20	0.1	r.t.	1	92	87:13	<i>S</i>
27	2		5	0.1	r.t.	59	97	68:32	<i>R</i>
28	2		5	0.3	r.t.	24	85	71:29	<i>R</i>
29	2		10	0.1	r.t.	59	97	67:33	<i>R</i>
30	2		15	0.1	r.t.	59	99	68:32	<i>R</i>
31	2		20	0.1	r.t.	24	99	69:31	<i>R</i>
32	3		5	0.1	r.t.	48	48	68:32	<i>R</i>
33	3		5	0.3	r.t.	48	67	68:32	<i>R</i>
34	3		20	0.1	r.t.	24	80	69:31	<i>R</i>
35	4		5	0.1	r.t.	5	95	61:39	<i>S</i>
36	<b>ent-D</b>	1	5	0.1	0	2.5	95	93:7	<i>R</i>
37		2	5	0.1	r.t.	63	95	68:32	<i>S</i>
38		3	5	0.1	r.t.	63	40	70:30	<i>S</i>
39		4	5	0.1	r.t.	5	95	60:40	<i>R</i>
40		5	5	0.1	r.t.	24	<10	73:27	<i>S</i>
41		6	5	0.1	r.t.	63	<10	77:23	<i>S</i>
42		7	5	0.1	r.t.	63	<10	74:26	<i>S</i>

<sup>a</sup> All reactions were carried out using 0.2 mmol of *p*-nitrobenzaldehyde and the according volume of the corresponding solvent (2 mL for 0.1 M in aldehyde reactions and 0.7 mL for



## Chapter 4

the 0.3 M in aldehyde reactions). Solvent: 1: anhydrous acetone; 2: acetone/water 10:1 (v/v); 3: acetone/water 3:1 (v/v); 4: acetone/methanol 10:1 (v/v); 5: acetone/methanol 3:1 (v/v); 6: anhydrous methanol; 7: methanol/water 10:1 (v/v). <sup>b</sup> Isolated yield. <sup>c</sup> e.r. determined by chiral HPLC. <sup>d</sup> Absolute configuration of the major enantiomer. Assigned by comparing the HPLC data with the literature (section 7.20).

Results show that catalyst **A** in anhydrous acetone gives the aldol product in good yield after 5 hours with moderate levels of enantioselectivity (entry 1). The increase of the mol% of catalyst to 20 mol% does not lead to significant improvement of the results, and only the reaction time was one hour shorter (entry 1). The use of acetone/water mixtures slows the reaction down severely but yields after 48 hours are maintained when compared to those in anhydrous acetone. Interestingly, there is a switch of the enantioselectivity observed, being now the *R* enantiomer the major one (entries 3 and 4).

The reaction with 5 mol% of catalyst **B** in anhydrous acetone at room temperature is slower than with catalyst **A**, and the enantioselectivity observed is poor. Results do not improve in terms of enantioselectivity by reducing the temperature to -20 °C (entry 6), increasing the concentration of the aldehyde to 0.3 M (entry 7), incrementing the catalyst concentration to 20 mol% (entry 8) or by the combination of several of these factors. The use of a mixture of acetone/water 10:1 (v/v) leads to slightly better results in terms of enantioselectivity, although they are still low, showing a preference for the *R* enantiomer of the aldol product (entries 10 and 11). These results prove that the absolute configuration of the  $\beta$ -cyclobutane amino acid present in catalyst **B** induces a peptide conformation in the transition state that is less active than **A** for the aldol reaction to take place.

The results obtained for this aldol reaction in anhydrous acetone with 5 mol% of catalyst **C** at room temperature are moderate in terms of yield. The reaction takes 24 hours to reach completion and the resulting enantioselectivity is good (entry 12). When the reaction is carried out under the same conditions but at -20 °C, an increase of the enantioselectivity is observed, but the yield after 24 hours is lower (entry 13). When the amount of catalyst is increased and the temperature lowered, the best results in terms of enantioselectivity with an acceptable yield are obtained

(entry 16). The use of an acetone/water 10:1 mixture leads to very good yields but also to a loss of enantioselectivity together with a switch of the chirality of the major enantiomer obtained to the *R* absolute configuration (entries 17 and 18).

Catalyst **D** seems to be the best for this aldol reaction. The reaction is fast (2 hours), gives excellent yields (97%) and with good levels of enantioselectivity (88:12) when anhydrous acetone is used as solvent, 5 mol% catalyst, the concentration of aldehyde is 0.1 M and at room temperature (entry 19). The selectivity favours the aldol product with *S* absolute configuration. The effect of lowering the temperature to -20 °C maintaining all the other parameters fixed shows an improvement of the enantioselectivity, leading to the best results (93:7) together with an increase of the reaction time (15 hours) to reach completion (entry 21). The increase of the aldehyde concentration to 0.3 M together with setting the temperature to 0 °C leads to the best levels of enantioselectivity achieved (93:7) and excellent yield in only 2.5 hours (entry 23). These levels of enantioselectivity are of the same order as the best results obtained for small peptides used as catalysts in the literature.<sup>125,126</sup> Experiments carried out with increasing amounts of catalyst **D** show that there is no major improvement with respect to those obtained using 5 mol% of the catalyst (entries 24-26). When mixtures of acetone/water 10:1 (v/v) are used, the reaction slows down, when compared with similar conditions using anhydrous acetone, and the enantioselectivities are again switched (entries 27-31). When mixtures of acetone/water are enriched in the content of water up to 3:1 (v/v) ratio, in general the reaction is slower and the yields are lower than when less water is used (entries 32-34). In terms of enantioselectivity, the values are similar to those obtained with acetone/water 10:1 (v/v) mixtures.

It is important to highlight that the catalyst could be recovered in all cases through extraction from the aqueous layer resultant from the work up of the reaction test with diethyl ether and subsequent lyophilisation. The yields of recovery were around 90% and the catalyst could be reused without any loss in performance.

Overall, in acetone, the major enantiomer of the formed aldol product showed *S* configuration in all cases using peptides **A**, **C** and **D**, independently of the chirality of the corresponding CBAA. Peptide **B** is an exception, where the *R* isomer is major in some cases, but the enantioselectivity is too poor to consider the

## Chapter 4

asymmetric induction important. On the contrary, as expected, the *R* enantiomer was the major product obtained when the benchmark reaction was catalyzed by catalyst **ent-D** (with two units of (*D*)-Proline) in anhydrous acetone. These results suggest that the predominant absolute configuration of the adducts is controlled by the chirality of proline, since the same major enantiomer is obtained independently of the CBAA chirality in each case. Nevertheless, the chirality of the CBAA had a significant effect on the rate of the reaction. Reactions catalyzed by **D** are above 10 times faster than those catalyzed by **C**.

Remarkably, the observed enantioselectivity is lowered and reversed in the presence of water, being the *R* enantiomer the major one when catalyst **A**, **C** and **D** were used, and the *S* enantiomer when catalyst **ent-D** was used. Additionally, the rate of formation of the aldol product is decreased when water is added. This switch in enantioselectivity was not observed when some amounts of water were added to acetone for the analogous cyclopropane-proline tripeptide from Reiser's group,<sup>126</sup> but it has been reported in other cases with proline derived catalysts.<sup>125,128</sup> In order to see if the mixtures of acetone with another protic polar solvent would behave the same way, first, a 10:1 acetone/methanol mixture was tested using **D** and **ent-D** as catalyst. In this case, the reaction time was more similar to that of using anhydrous acetone, but the enantioselectivity was similar to those obtained when acetone/water mixtures were used (entries 35 and 39). Importantly, though, the selectivity favours the *S* enantiomer, just like in the cases where anhydrous acetone was used. On contrary, when the ratio of methanol was increased, the switch in the enantioselectivity was observed, being the *S* enantiomer the major one in the reaction catalyzed by **ent-D** (entry 5-6). These results suggest that the presence of a protic solvent provokes a switch in the enantioselectivity of the reactions, although different ratios are required depending on the solvent, being more efficient in the case of water than methanol.

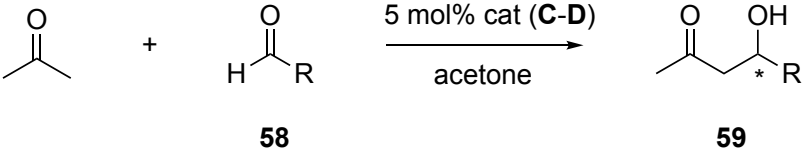
$\gamma$ -Cyclobutane-based catalysts **C** and **D** perform clearly better than those containing a  $\beta$ -cyclobutane amino acid, **A** and **B**. This factor shows that the substitution of the cyclobutane ring, and consecutively the spatial arrangement of its functions, is crucial for the satisfactory encounter of the enamine (resulting from

the activation of the ketone with the secondary amine of one terminal proline residue of the peptide catalyst) with the aldehyde.

#### 4.3.2.1 Aldol reactions using different aldehydes and ketones.

Once best conditions for the aldol reaction were found, catalysts **C** and **D** were tested with other aldehydes and using acetone. These results are shown in Table 7.

**Table 7.** Aldol reactions between acetone and various aldehydes catalysed by **C** and **D**, respectively.

						
Entry	Catalyst <sup>a</sup>	R	Time (h)	Yield (%) <sup>b</sup>	e.r. <sup>c</sup>	Abs. Config. <sup>d</sup>
1	<b>C</b>	a) <i>p</i> -NO <sub>2</sub> -Ph	24	77	83:17	<i>S</i>
2		b) Ph	30	55	82:18	<i>S</i>
3	<b>D</b>	a) <i>p</i> -NO <sub>2</sub> -Ph	2	97	88:12	<i>S</i>
4		c) <i>p</i> -Br-Ph	2	95	86:14	<i>S</i>
5		d) <i>p</i> -Cl-Ph	2	99	89:11	<i>S</i>
6		e) <i>p</i> -CF <sub>3</sub> -Ph	2	90	86:14	<i>S</i>
7		f) <i>p</i> -MeO-Ph	72	1	-	-
8		g) <i>o</i> -NO <sub>2</sub> -Ph	2	99	85:15	<i>S</i>
9		h) <i>o</i> -Br-Ph	2	95	85:15	<i>S</i>
10		b) Ph	3	90	87:13	<i>S</i>
11		i) <i>c</i> -C <sub>6</sub> H <sub>11</sub>	6	50	82:18	<i>S</i>

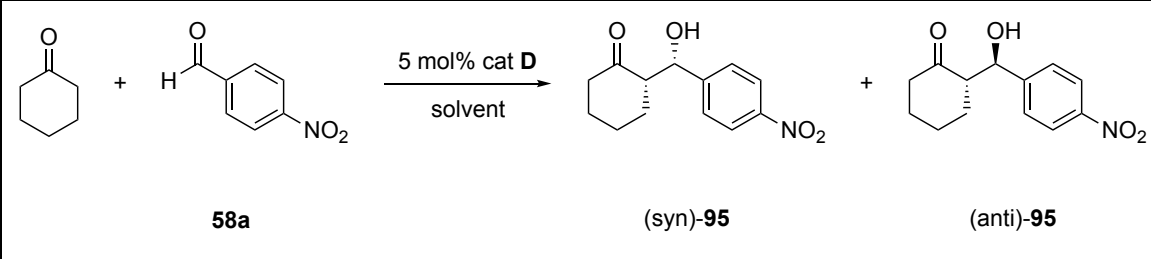
<sup>a</sup> All reactions were carried out using 0.2 mmol of aldehyde in 2 mL of anhydrous acetone at 20 °C. <sup>b</sup> Isolated yield. <sup>c</sup> e.r. determined by chiral HPLC. <sup>d</sup> Absolute configuration of the major enantiomer. Assigned by comparing the HPLC data with the literature (section 7.20).

## Chapter 4

As expected, results for catalyst **C** were slightly better for *p*-nitrobenzaldehyde than for benzaldehyde in terms of yields due to the activation exerted by the electron-withdrawing nitro group in the *para* position, but the enantioselectivity ratio was the same (entries 1-2). For catalyst **D**, *ortho*- or *para*-substituted aromatic aldehydes and benzaldehyde results were very similar to those obtained for *p*-nitrobenzaldehyde (entries 3, 4, 5, 6, 8, 9 and 10). Steric hindrance of the substituents in the *ortho* position did not show any influence on reactivity or stereoselectivity. In the case of using *p*-anisaldehyde, no reaction was observed (entry 7). As expected, the electron donating methoxy group in the *para* position deactivates the aldehyde. The use of the more challenging cyclohexanecarboxaldehyde led to the formation of the corresponding aldol product in 50% yield after 6 hours with an enantiomeric ratio of 82:18, which is similar to the enantioselectivity observed for the aromatic substrates (entry 11).

To further explore the scope of the reaction with catalyst **D**, aldol reactions between *p*-nitrobenzaldehyde and cyclohexanone were carried out. Two different sets of conditions were tested, and in this case, enantioselectivity and diastereoselectivity were considered. The results are shown in Table 8.

**Table 8.** Aldol reactions between cyclohexanone and *p*-nitrobenzaldehyde catalysed by **D**.

						
Entry	Solvent	Time (h)	Yield (%) <sup>c</sup>	d.r. <sup>d</sup> (syn:anti)	e.r. syn <sup>d,e</sup>	e.r. anti <sup>d,e</sup>
1	MeOH <sup>a</sup>	24	0	-	-	-
2	neat <sup>b</sup>	5	99	1:2	70:30	78:22

<sup>a</sup> The reaction was carried out at 20 °C, using 0.2 mmol of *p*-nitrobenzaldehyde and 0.2 mL of cyclohexanone in 2 mL of methanol. <sup>b</sup> 0.2 mmol of *p*-nitrobenzaldehyde in 2 mL of cyclohexanone. <sup>c</sup> Isolated yield. <sup>d</sup> d.r. and e.r. determined by chiral HPLC. <sup>e</sup> Absolute configuration of the major diastereoisomers: syn (2*S*,1'*S*); anti: (2*R*,1'*S*). Assigned by comparing the HPLC data with the literature (section 7.20).

Results showed that in the case of using methanol as solvent, the reaction did not proceed (entry 1), in contrast with the results reported for some other peptides.<sup>125</sup> Otherwise, the reaction worked in 99% yield after 5 hours when neat cyclohexanone was used (entry 2). The diastereomeric ratio was 1:2 in favour of anti-**94**. The enantiomeric ratio was 70:30 for the syn diastereoisomer and 78:22 for the anti. These results are comparable to those reported in the bibliography for  $\beta$ -containing tripeptides as catalysts.<sup>126</sup>

#### 4.3.2.2 Michael reaction using *trans*- $\beta$ -nitrostyrene.

To further investigate catalysts **C** and **D** in other chemical processes, Michael reactions between ketones and *trans*- $\beta$ -nitrostyrene were tested. Two different sets of conditions were tested, and in this case, enantioselectivity and diastereoselectivity were considered. The results are shown in Table 9.

Using acetone as solvent, results showed moderate yields and poor enantioselectivity using **C** or **D** as catalysts after 24 hours (Entries 1 and 2). In the case of **D**, carrying out the reaction using methanol as solvent, the yield was lower than when acetone was used, but the same enantioselectivity was obtained (entry 3). Otherwise, reaction with cyclohexanone gave excellent yields after 24 hours using neat conditions. Although both showed low enantioselectivities, reactions catalyzed by **C** showed higher enantioselectivities than those catalyzed by **D** (entries 4 and 5). On the contrary, as shown above, in the aldol reaction, **D** displayed slightly better enantioselectivities than **C**.

**Table 9.** Michael reactions between acetone/cyclohexanone and *trans*- $\beta$ -nitrostyrene catalysed by **C** and **D**.

Entry	Product	Catalyst	Solvent	Time (h)	Yield (%) <sup>c</sup>	d.r. <sup>d</sup> (syn:anti)	e.r. syn <sup>d,e</sup>	e.r. anti <sup>f</sup>
1	 96	<b>C</b>	Acetone	24	58	X	56:44	
2		<b>D</b>	Acetone	24	76	X	56:44	
3		<b>D</b>	MeOH <sup>a</sup>	24	54	X	56:44	
4	 97	<b>C</b>	neat <sup>b</sup>	24	95	17:1	66:34	-
5		<b>D</b>	neat <sup>b</sup>	24	96	13:1	58:42	-

<sup>a</sup> The reaction was carried out at 20 °C, using 0.2 mmol of *trans*- $\beta$ -nitrostyrene and 0.4 mL of acetone in 1.6 mL of methanol. Methanol/acetone, 4:1 (v/v). <sup>b</sup> 0.2 mmol of *trans*- $\beta$ -nitrostyrene in 2 mL of cyclohexanone. <sup>c</sup> Isolated yield. <sup>d</sup> d.r. and e.r. determined by chiral HPLC. <sup>e</sup> Absolute configuration of the major diastereoisomers. Assigned by comparing the HPLC data with the literature. <sup>f</sup> e.r. of anti diastereoisomer was not determined due to the low product obtained.

### 4.3.3 Structural studies of catalyst **D**.

Structural and conformational studies were carried out with catalyst **D** by means of NMR spectroscopy in order to understand how stereochemical features influence the reactivity and the enantioselective induction. Catalyst **D** was chosen because it gave the best results in most of all reactions tested. These studies were carried out with the collaboration of Dr. Pau Nolis, from the Servei de Resonància

Magnètica Nuclear (SeRMN) from the Universitat Autònoma de Barcelona, where high resolution NMR experiments were carried out.

First of all, catalyst **D** was studied using deuterated acetone,  $(\text{CD}_3)_2\text{CO}$ , as solvent, with the aim of using analogous conditions to those used in the catalyzed reaction studies. The analysis of the  $^1\text{H}$  NMR spectrum demonstrates the presence of at least two species in about 60:40 proportion. The significant shift of the signals of the protons in the alpha position of the secondary amine (compared with the same signals that in the protected precursor **92**), along with a new peak appearing at 189 ppm in the  $^{13}\text{C}$  NMR spectrum pointed towards the formation of an iminium species. As showed in Scheme 14 in the introduction of this part of the thesis, secondary amines react with ketones forming iminium species, being this process reversible. In order to corroborate these hypothesis, a new sample of **D** was dissolved in  $\text{CD}_3\text{CN}$  and, subsequently, anhydrous non-deuterated acetone was added. The  $^1\text{H}$  NMR spectra was recorded and two singlets around 2.5 ppm were observed. SELNOESY experiments revealed the proximity of these singlets with the protons on the proline residue. Moreover, an HMBC spectrum showed cross peaks between the two singlet signals with the iminium group carbon appearing at 189 ppm, confirming the hypothesis (Figure 40).

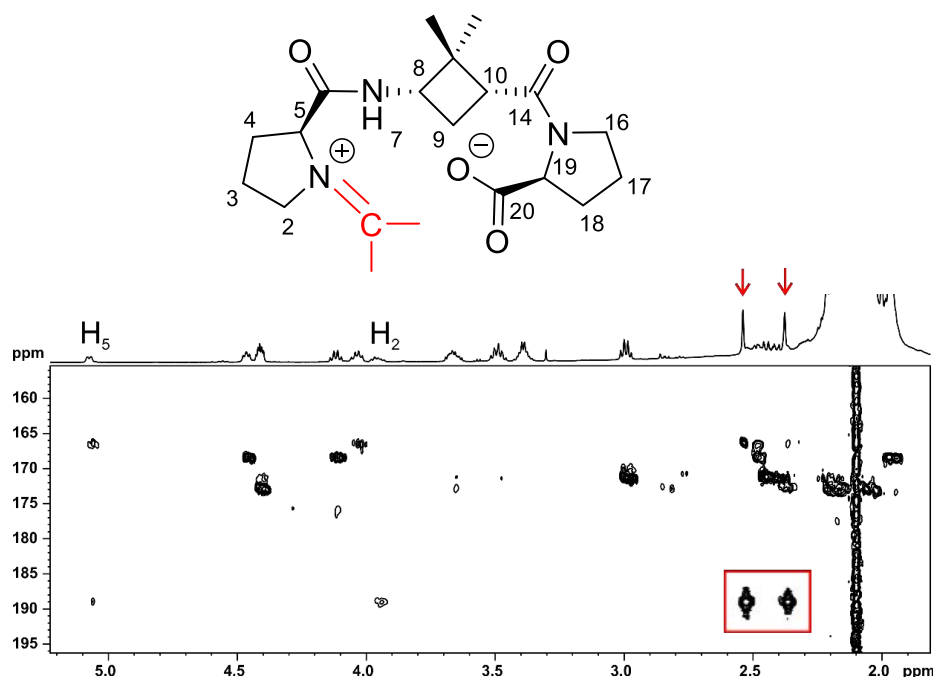


**Figure 40.** Proposed iminium intermediate and expansion of the HMBC spectra of **D** (600 MHz, 298 K) in  $\text{CD}_3\text{CN}$  containing 100 mL of non-deuterated acetone.



## Chapter 4

Having proved that the use of deuterated acetone did not allow the study of the catalyst itself, a conformational study of **D** was carried out in  $\text{CD}_3\text{CN}$ , as an equivalent polar non-protic solvent. These experiments revealed the presence of two major conformers. The major conformation was confirmed by selective ROESY experiments (Figure 41).

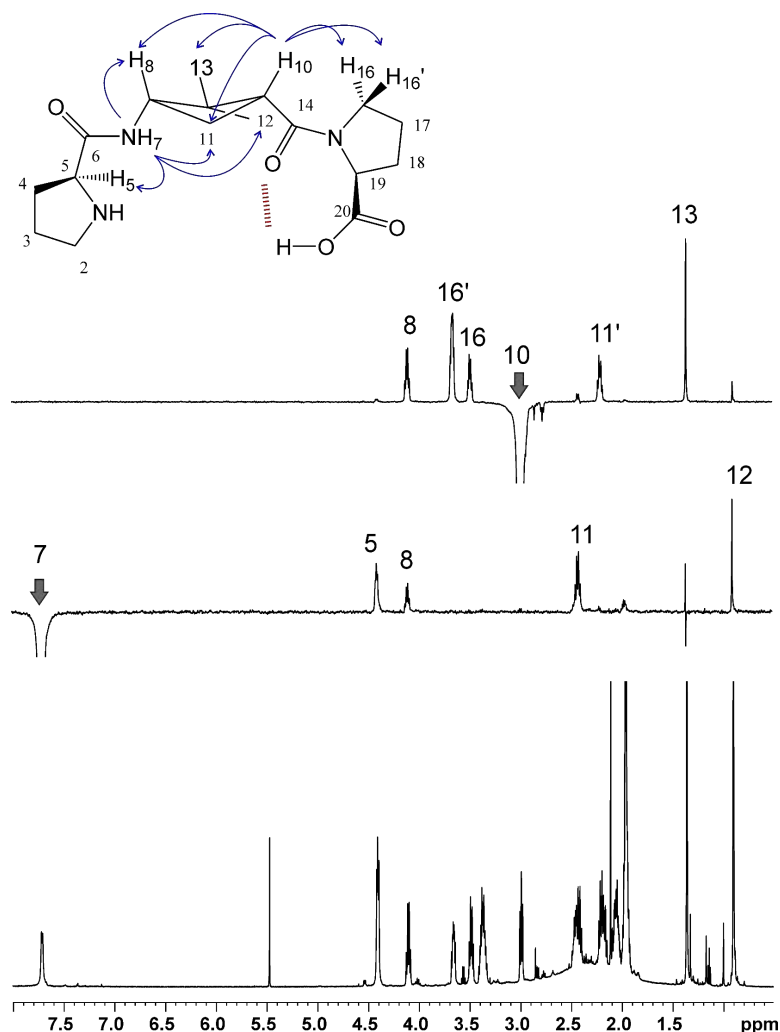


**Figure 41.** Selective ROESY spectra of **D** ( $\text{CD}_3\text{CN}$ , 600 MHz, 298 K)

The integration of distinctive signals for both conformers in the  $^1\text{H}$  NMR spectrum determined a 93:7 proportion between conformations. ROE and NOE contacts identified the two conformations as *cis/trans* rotamers, which result from rotation around one of the amide bonds, being the major conformation the *trans*-amide bond rotamer. Also, the conformational study was performed in  $\text{CD}_3\text{OD}$  to

try to rationalize some catalytic experiments carried out in this solvent. The results were very similar to those obtained for  $\text{CD}_3\text{CN}$ , but the ratio of conformers was 82:18 in this case. The structure of main conformations and the contacts between H atoms found in the NMR experiments are shown in Figure 42.

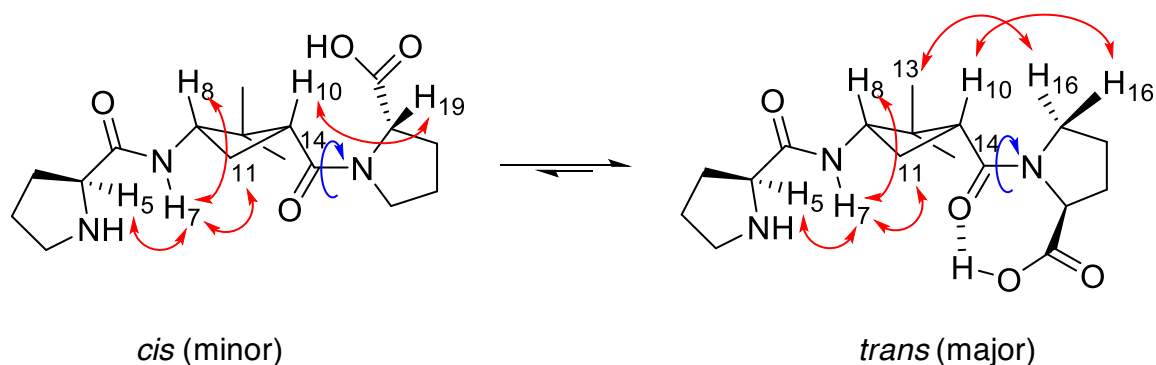


**Figure 42.** Equilibrium of the two main conformations of catalyst **D** in  $\text{CD}_3\text{CN}$  and in  $\text{CD}_3\text{OD}$  solution. In red contacts from NMR experiments are shown. In blue, bond rotation responsible for two conformations.

The major conformation presents a hydrogen bond between the oxygen atom in CO14 and the hydrogen atom of the carboxylic acid group. This is supported by the existence of ROE contacts between H16' and H10' and between methyl 13 and H16, respectively. The minor conformer does not present the hydrogen bond between CO14 and the acid proton, because it presents ROE contacts between H10 and H19. So, in this case, the peptide bond between C14 and NH15 is rotated and the carboxylic acid is located far from CO14. Both conformers have in common the proximity between NH7 and H11, H5 and H8, respectively, as it is shown in NOESY experiments. So, we can conclude the secondary amine is fixed because there is not a rotation in the other peptidic bond (between C6 and NH7).

The prevalence of the *trans* rotamer can be easily explained by the stabilization provided by inter-residue hydrogen-bonding. This rotamer could be maintained in the active conformation of the catalyst, having both the amine and

## Chapter 4

the carboxylic acid groups of the bifunctional catalyst in a close spatial proximity and inducing stereoselectivity.

As it is mentioned in section 4.3.2 of this chapter, the use of acetone/water and methanol/water mixtures instead of dry acetone as solvent reverses the enantioselectivity of the reactions. There are also various examples in the literature in organocatalyzed reactions where the enantioswitching is controlled by the solvent polarity.<sup>125,129–131</sup> Wennemers and coworkers<sup>125</sup> attributed this fact to a change in the conformation preference of the catalyst in the presence or absence of water, as deduced by circular dichroism spectroscopy. For that reason, we studied catalyst **D** using CD spectroscopy in pure methanol, in pure water solutions, as well as in various mixtures of both solvents. The obtained spectra are shown in Figure 43.

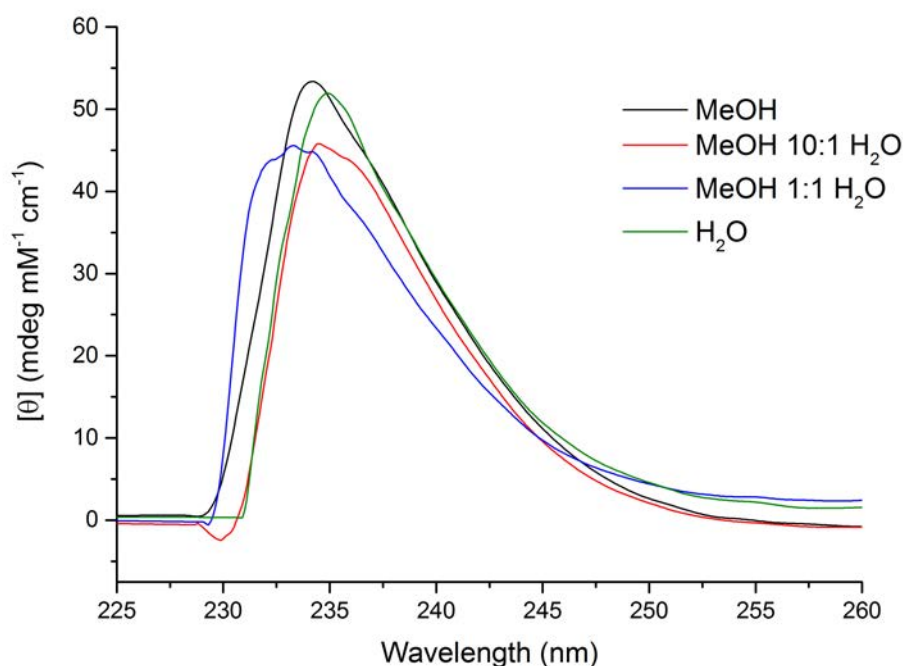


**Figure 43.** CD spectra of solutions 2.5 mM of catalyst **D** in MeOH (black), MeOH/H<sub>2</sub>O 10:1 (red), MeOH/H<sub>2</sub>O 1:1 (blue) and in H<sub>2</sub>O (green).

The experiments could not be carried out in acetone, acetonitrile or any equivalent polar non-protic solvent because they absorb in this region of the spectra. CD spectra of catalyst **D** using different methanol and water mixtures showed a single band, corresponding to the amides of the tripeptide. In pure

methanol, the maximum is at 234 nm, in pure water at 235, in methanol/water 10:1 at 235 and in methanol/water 1:1 at 233 nm. There are not big differences in the shape of all spectra and neither in their peak maximum. With these results, we can conclude that there are not significant changes between the conformations of catalyst **D** in methanol, water and their mixtures.

To confirm this hypothesis,  $^1\text{H}$  NMR experiments of catalyst **D** in pure deuterated methanol, and in deuterated methanol/water mixtures were studied. The obtained spectra are shown in Figure 44.

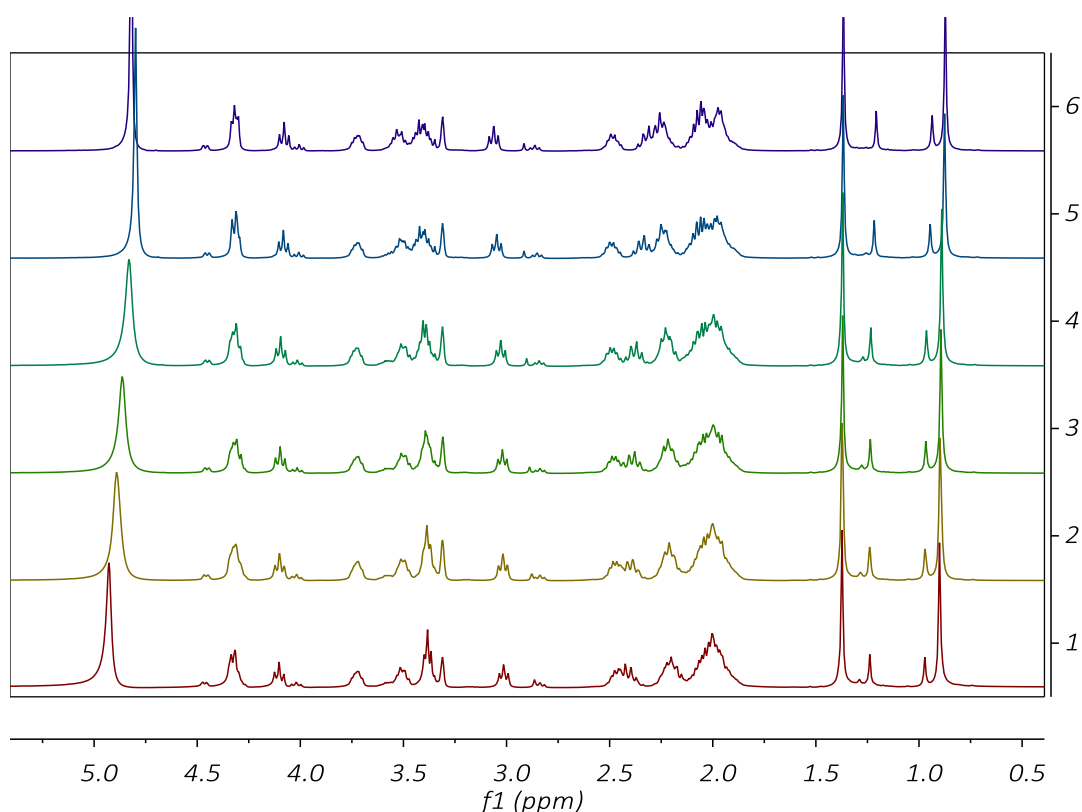


**Figure 44.**  $^1\text{H}$  NMR (400 MHz, 298 K) spectra of catalyst **D** using different deuterated solvents ( $\text{CD}_3\text{OD}$  and  $\text{D}_2\text{O}$ ). (1)  $\text{CD}_3\text{OD}$ ; (2)  $\text{CD}_3\text{OD}/\text{D}_2\text{O}$  20:1; (3)  $\text{CD}_3\text{OD}/\text{D}_2\text{O}$  10:1; (4)  $\text{CD}_3\text{OD}/\text{D}_2\text{O}$  5:1; (5)  $\text{CD}_3\text{OD}/\text{D}_2\text{O}$  2:1; (6)  $\text{CD}_3\text{OD}/\text{D}_2\text{O}$  1:1.

Comparing the  $^1\text{H}$  NMR spectra of catalyst **D** using different ratios of  $\text{CD}_3\text{OD}$  and  $\text{D}_2\text{O}$  did not show any important alteration. The signals did not shift and the relative integration of both conformations of catalyst **D** did not change. Nevertheless, it should be remembered that the conformational studies are carried out using the catalyst **D** itself, which is not the active species that is responsible for

the C-C bond formation. As mentioned before, the active species is the enamine formed by the reaction of the catalyst with the aldehyde, which could have different conformations.

### 5.3.4 Theoretical studies

Theoretical calculations were carried out to study the conformations of the catalysts, and to gain insight in how stereochemical features influences the reactivity and the enantioselectivity in the aldol reaction. The theoretical calculations were carried out by Prof. Vicenç Branchadell from our research group. First, the conformation of the catalyst **D** was studied to compare the obtained structure with the NMR information. A conformational search using molecular mechanics was accomplished, and after, the most stable structure was optimized in methanol using quantum mechanics using M06-2X/6-31G(d) level of theory. The resulting structure is shown in Figure 45.

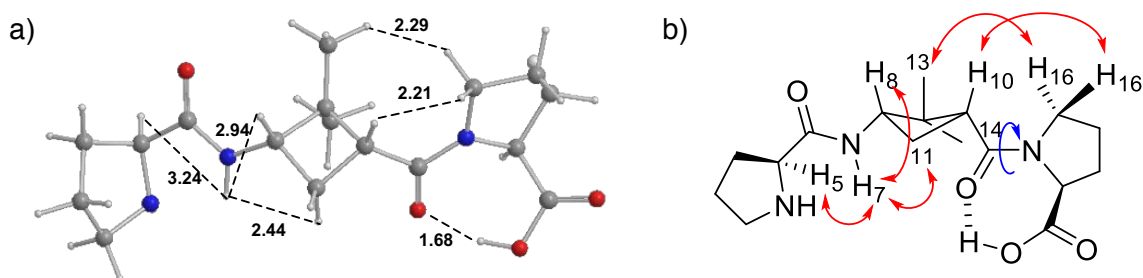


**Figure 45.** a) Major *trans* rotamer calculated for catalyst **D**. Selected interatomic distances are in Å. b) Major rotamer found in NMR studies in methanol.

Theoretical calculations were in close agreement with the NMR experiments. The higher stability of the *trans* rotamer was explained by the stabilization provided by an intramolecular hydrogen bond between the carboxylic acid function and the carbonyl of one amide. Theoretical calculations suggested that this rotamer is maintained in the active conformation of the catalyst, where the secondary amine and the carboxylic acid function are oriented towards the same position.

### 5.3.4.1 Mechanistic study and stereoselectivity

In order to rationalize the catalytic results obtained with catalyst **D**, a detailed computational study of the mechanism of the reaction was performed. The simplified proposed mechanism is shown in (Figure 46).

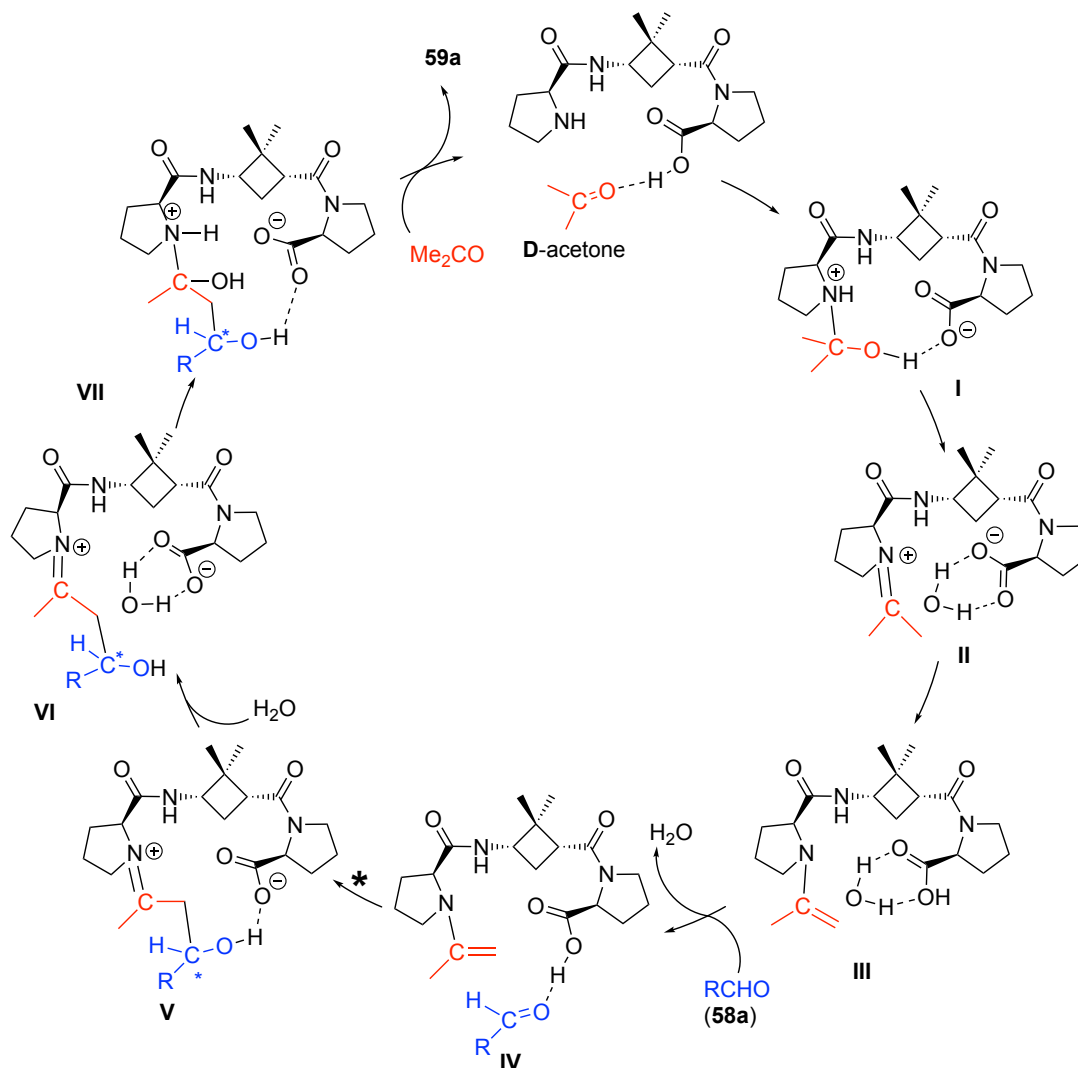


**Figure 46.** Mechanism for the aldol reaction between acetone and aldehyde **58a** catalyzed by tripeptide **D**. Rate determining step and new stereogenic center are remarked with asterisks.

The mechanism is analogous to that proposed by List and Houk.<sup>107,108,132</sup> In a first stage, catalyst **D** reacts with acetone through the formation of a N-C bond *via* a series of intermediates involving the ammonium species **I**, and iminium, **II**, and an enamine **III**. Then, aldehyde **58a** is activated by the carboxylic acid function of

## Chapter 4

III, and the new C-C bond is formed (IV to V). After that, the addition of a water molecule helps to liberate the aldol product **59a** and the recovery of the catalyst. The enantioselectivity of the reaction is determined by the transition state of the reaction between the enamine intermediate and the aldehyde in the step remarked with an asterisk in Figure 46.

For that reason, we have analyzed the diastereomeric transition states that lead to the formation of both enantiomers of the aldol product **59a**. A schematic representation and the calculated structures of these transition states are shown in Figure 47.

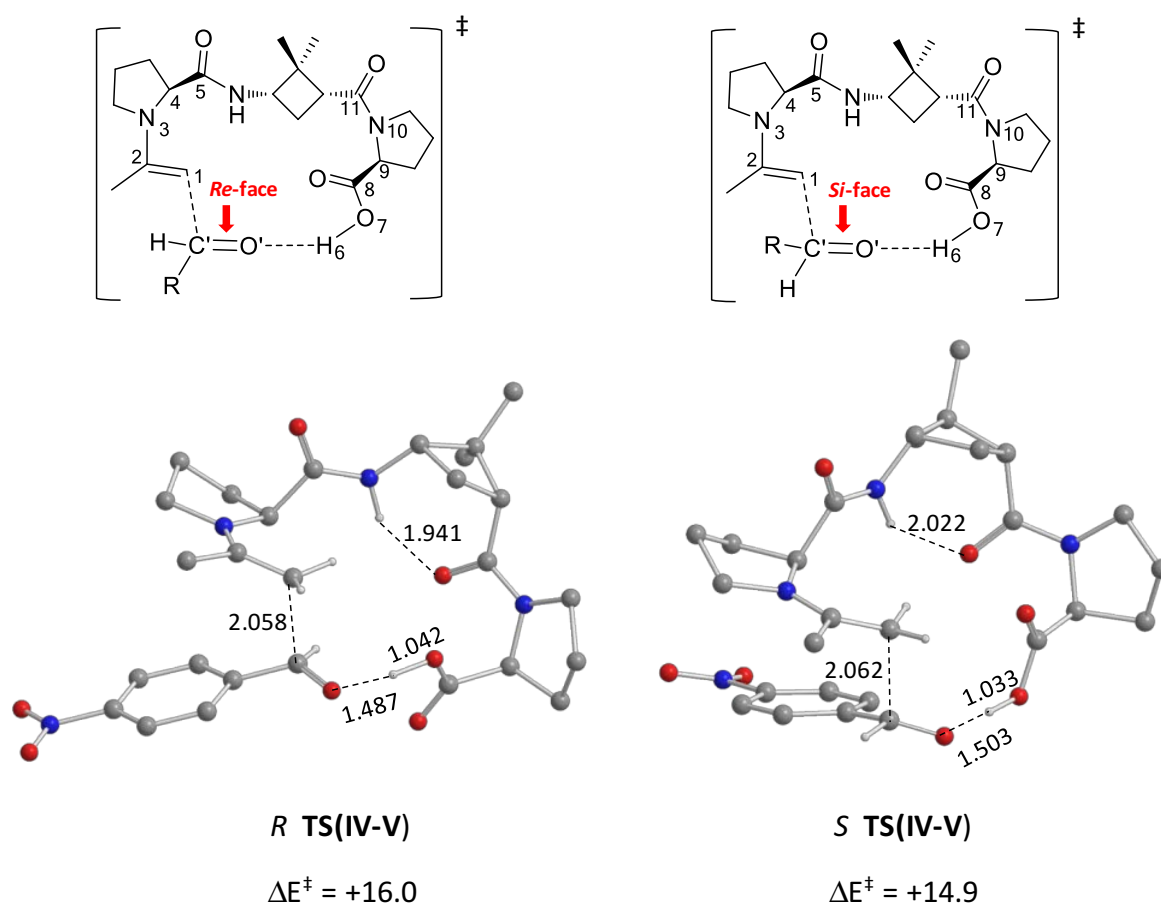


**Figure 47.** Schematic representation and calculated structures and energies of the diastereomeric TS of the reaction of the enamine derived from **D** with **58a**. The *Re/Si* enantiotopic faces of the aldehyde are indicated. Noncritical hydrogen atoms have been omitted for clarity. Selected interatomic distances are in Å and the energies are in kcal/mol. Numbering of the atoms is arbitrary.

The conformation of the transition states presents an intramolecular and intra-residue hydrogen bond in the enamine fragment and involve the NH and CO groups directly bounded to the cyclobutane. The transition states showed that the acidic proton is required for effective catalysis to occur. This acidic proton fixes the oxygen atom of carbonyl of the aldehyde while the enamine attacks the carbonyl. We can observe that the formation of *R* aldol enantiomer is due to the nucleophilic attack of the enamine to the *Re*-face of the aldehyde carbonyl group, while the *S* enantiomer comes from the *Si*-attack.

The differences of energy barriers are in agreement with experimental results in anhydrous acetone. In the calculated transition states, the *S* product is the favorable one and its difference with *R* is 1.1 kcal/mol, resulting a predicted e.r. at 25 °C of 90:10 with the 6-31(d) basis set.

As mentioned before, the use of acetone/water mixtures instead of dry acetone as solvent reversed the enantioselectivity of the reactions. The transition states in which the proton transfer between the carboxyl group of the enamine and the carbonyl group of the aldehyde takes place through an intercalated water molecule have been studied. It should be pointed out that a water molecule is already present in intermediate **III** (Figure 46), and its release to allow the coordination of the aldehyde molecule may become disfavored as the concentration of water increases. The schematic representations and the calculated structures of the transition states in the presence of a water molecule are shown in Figure 48.

The interaction with this water molecule stabilizes the *R* and *S* transition states by 13.7 and 7.2 kcal mol<sup>-1</sup>, respectively, becoming the *R* transition state lower in energy than the *S*. These results are in qualitative agreement with the observed reversion of the enantioselectivity of the reaction. The accommodation of this water molecule requires a modification of the relative orientation of the aldehyde molecule with respect to the enamine favouring the nucleophilic attack to the *Re*-face of the carbonyl, thus leading to the *R* enantiomer, as experimentally observed.



## Chapter 4

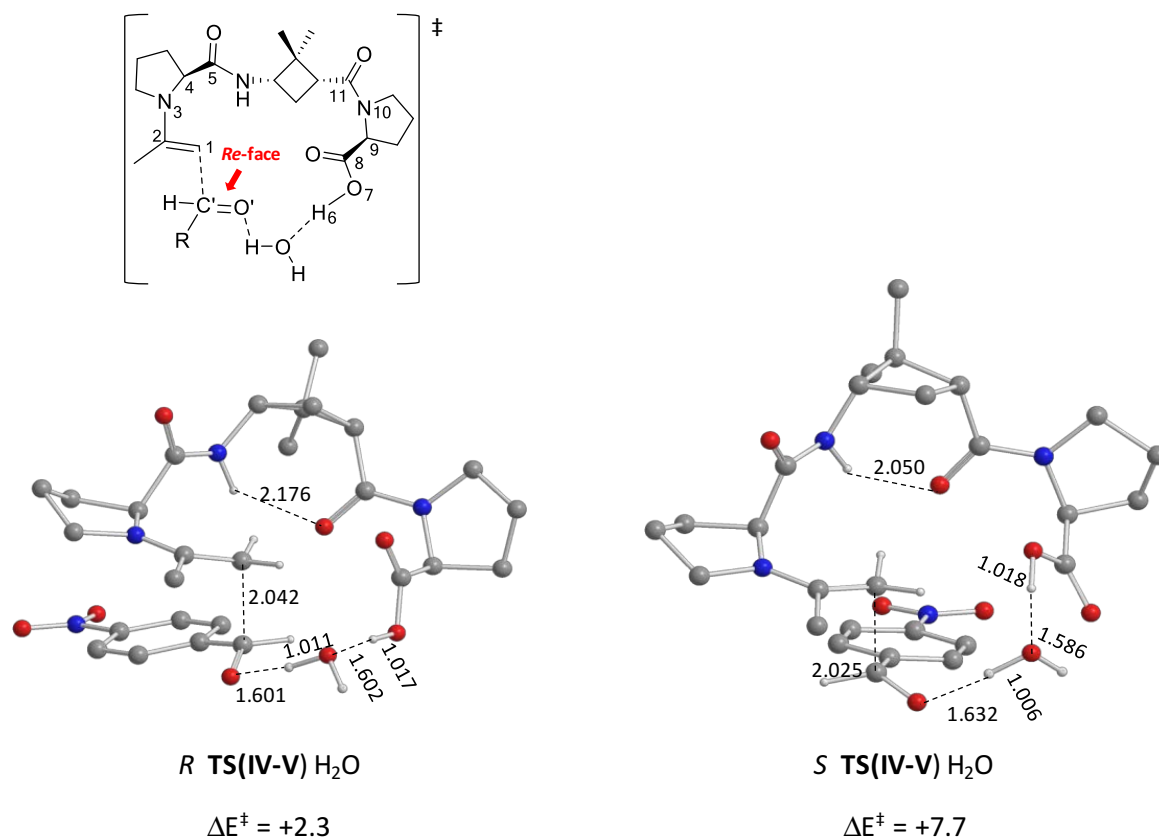


**Figure 48.** Schematic representation of the preferential nucleophilic attack and calculated structures and energies of the TS corresponding to the reactions of the enamine derived from catalyst **D** with **58a** in the presence of a water molecule. Noncritical hydrogen atoms have been omitted for clarity. Selected interatomic distances are in Å and the energies are in kcal/mol.

## 4.4 Summary and conclusions

In this part of the thesis, five new hybrid tripeptides were synthesized by an alternate combination of two (*L*)- or (*D*)-proline residues and one  $\beta$ - or  $\gamma$ -CBAA.

They were tested as organocatalysts in the aldol reaction between several aldehydes and acetone or cyclohexanone, under water-free conditions or in homogeneous acetone/water and acetone/methanol mixtures. Results showed that  $\beta$ -amino acid containing peptides **A** and **B** presented poor reactivity and enantioselectivity, probably due to the severe conformational restrictions imposed by the rigidity of the 1,2-disubstituted cyclobutane moiety. Gratefully,  $\gamma$ -amino acid containing peptides **C**, **D** and *ent-D* presented excellent reactivity (up to 99% yield in 2 hours) and good enantioselectivities (up to 88:12 e.r. at r.t. and 93:7 e.r. at 0 °C). These results were rationalized by means of theoretical calculations, which point out that the active conformation in the transition state reproduces the major conformation observed by <sup>1</sup>H NMR spectroscopy for the isolated catalyst. The predominant absolute configuration of the adducts is controlled by the chirality of proline, since the same major enantiomer is obtained independently of the CBAA chirality in each case. The first tests in the Michael addition resulted in moderate reactivity and poor enantioselectivity for  $\gamma$ -amino acid containing peptides **C** and **D**.

Noteworthy, the enantioselectivity in aldol reactions was reversed in the presence of water. Using <sup>1</sup>H NMR and CD spectroscopies it was shown that conformational changes are not responsible for this reversion. Calculations suggested that a water molecule simultaneously coordinates the catalyst and the aldehyde promoting a change in the geometry of the transition state, inducing a different preferential approach to the enantiotopic face of the aldehyde.

Remarkably, the switch of enantioselectivity by using (*L*)- or (*D*)-proline or alternatively, the use of anhydrous or aqueous solvents allows the unequivocal preparation of the desired aldol enantiomer (Figure 49).

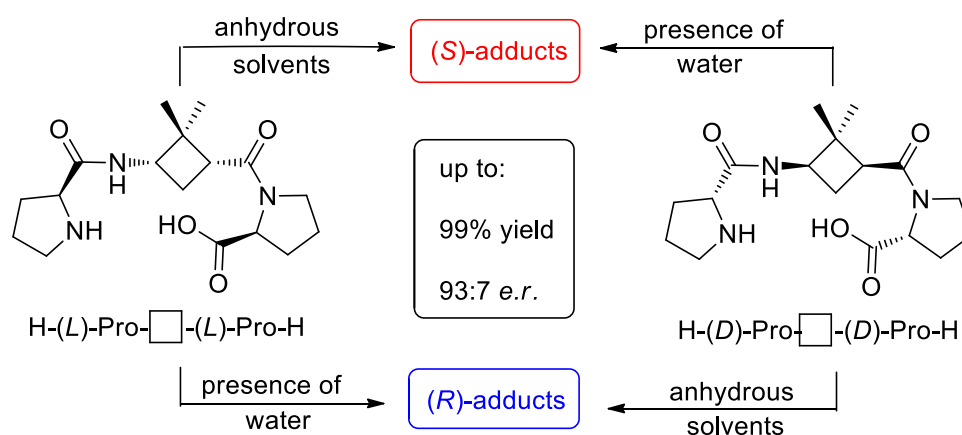


**Figure 49.** Representation of the factors controlling the enantioselectivity.

The almost quantitative yields and good enantioselectivities achieved under easy reaction conditions, especially with catalyst **D**, confers these peptide catalysts with interesting properties to be employed in aldol reaction and to be further explored in other chemical processes.

**5. Gd<sup>3+</sup> and Mn<sup>2+</sup> Complexes of Open-chain Ligands as Potential New MRI Contrast Agents: Synthesis, Stability, Inertness, Structure and Relaxation Studies**

---



## 5. Gd<sup>3+</sup> and Mn<sup>2+</sup> Complexes of Open-chain Ligands as Potential New MRI Contrast Agents: Synthesis, Stability, Inertness, Structure and Relaxation Studies

### 5.1 Introduction

Medical imaging technologies allow to acquire highly detailed information about the human body without the exigency of surgery. These techniques include radiography, ultrasonography, echocardiography and magnetic resonance imaging. (MRI). Over the last years, MRI has become one of the most important and efficient tools in medical diagnosis and biomedical research.<sup>133</sup> The boundaries of MRI are in a continuous expansion, even it has been combined with drug targeting systems becoming useful for monitoring biodistribution, target site accumulation and drug release.<sup>134</sup>

MRI was discovered in 1973 by Nobel Prize winners Lauterbur and Mansfield. It is based on the Nuclear Magnetic Resonance phenomenon.<sup>135–137</sup> The word “nuclear” was deleted in the switch to imaging to prevent the alarm of the patients, who could relate this word with radioactivity. MRI does not expose the patient to ionizing radiation, hence, it is a non-invasive technique, and it provides real-time monitoring of molecular events occurring even at the cellular level. MRI outcomes from the magnetic properties of protons, one of the most abundant nuclides in the human body since 60-70% of the body weight is made of water and fat. MRI is based on the measurement of water proton relaxation rates in human tissues, and provides three-dimensional high-resolution images (Figure 50).<sup>138</sup>

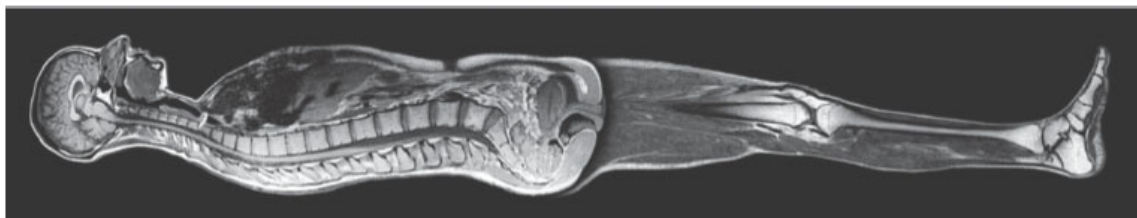


**Figure 50.** MRI image of a human body.<sup>139</sup>

## Chapter 5

$^1\text{H}$  atoms can be considered as charged rotating spheres and they have an inherent magnetic dipole moment resulting from their electrical charge and spin. In the presence of a strong and external magnetic field, these atoms begin to precess around the axis of this magnetic field,  $B_0$ . This precession takes place at a certain frequency ( $\nu_0$ ), called Larmor frequency, and it is described by the nature of the atom and the strength of the magnetic field. There are two possible precessions, the parallel and the antiparallel along the longitudinal axis of  $B_0$  (z axis by definition) and their orientation determines the energy level of the spin. The resulting net magnetization ( $M_0$ ) is originated by the difference in the energy of these two levels. Since there are more protons in the the parallel level because it is less energetic, the total magnetization vector remains parallel to  $B_0$  (Figure 51).

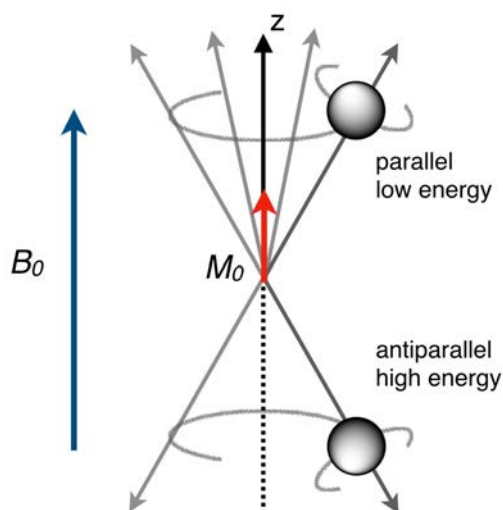


**Figure 51.** Proton spin in the presence of a constant magnetic field. Net  $M_0$  remains parallel to  $B_0$  due to the lower state is more populated.

The basic NMR experiment consists in applying a radiofrequency pulse (RF) to this system induced by a perpendicular magnetic field by the action of a RF coil. Then, this RF pulse flips the magnetization ( $M$ ) into the xy plane (Figure 52b). When the pulse is finished, the system returns to equilibrium. The return to equilibrium of magnetization is characterized by the relaxation time.

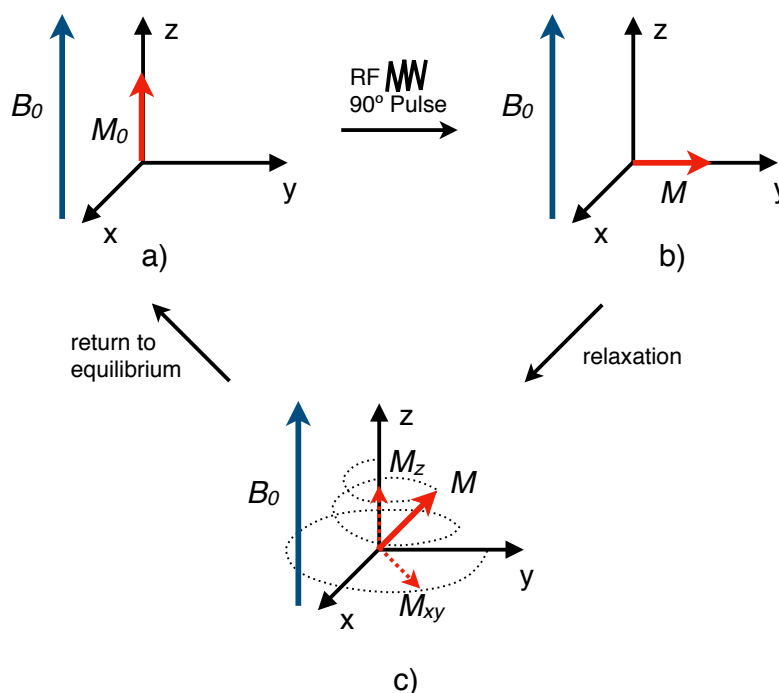


**Figure 52.** a) Net magnetization ( $M_0$ ) at equilibrium in a permanent magnetic field ( $B_0$ ). b) RF pulse is applied and the magnetization ( $M$ ) is flipped to the xy plane. c)  $M$  precesses around the z axis returning to the equilibrium.

After the RF pulse, the z component of the magnetization increases exponentially with a constant time ( $T_1$ ) and the xy component decreases exponentially with a constant time ( $T_2$ ). These time constants are called longitudinal relaxation time ( $T_1$ ) and transverse relaxation time ( $T_2$ ) (Figure 53).<sup>133</sup>

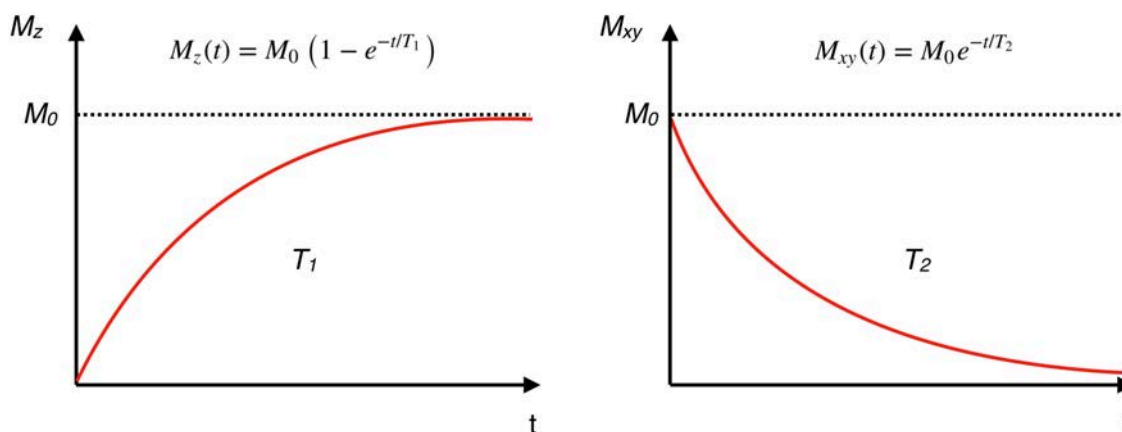


**Figure 53.** Description of the relaxation process on the z axis (left) and on the xy plane (right).



The intensity and resolution of the MR images depend on the density of water protons,  $\rho$ ,  $T_1$  and  $T_2$ . The contrast of the image is originated due to the variation of these parameters among the tissues. Tissues with high longitudinal relaxation rates,  $1/T_1$ , produce higher signal intensity, displaying brighter regions in the image, whereas the increase of the transversal relaxation rates,  $1/T_2$ , will result in a decreased signal, producing darker regions. Diagnostic information can be obtained since the proton density, and more importantly, the relaxation rates can be different in healthy and damaged tissues. However, to obtain high resolution images, in general, the use of external contrast agents is needed to enhance the contrast of the images, and moreover, to reduce the time of clinic examinations.

### 5.1.1 Contrast agents for MRI

Contrast agents (CA) are compounds that improve the sensitivity and the specificity of MRI experiments. These compounds are usually composed of paramagnetic species containing unpaired electrons, such as  $Gd^{3+}$ ,  $Mn^{2+}$  and  $Fe^{2+}$ , and are able to reduce the relaxation times,  $T_1$  and/or  $T_2$ , of the solvent protons that are coordinated to the metal ion. The exchange of the coordinated water molecule with the solvent protons spreads the relaxation to other water molecules from the tissue, enhancing its contrast.

Among all the paramagnetic metal ions,  $Gd^{3+}$  is the most used one, because it presents the best effect on  $T_1$ , due to its seven unpaired electrons.<sup>140</sup> To obtain high resolution images, a large dose intravenously injected is needed. Unfortunately,  $Gd^{3+}$  and  $Mn^{2+}$  ions are highly toxic for living organisms. They can interact with different endogenous metabolites and interfere in  $Ca^{2+}$  regulated transmission processes due to its similar ionic radius, being the lethal dose  $LD_{50}$  value of free  $Gd^{3+}$  of 0.1 mmol/kg.<sup>141,142</sup> For that reason, to prevent the presence of these free metal ions, they are complexed with different multidentate ligands. The ligands with O- and N-donor atoms are the most utilized ones to complexate  $Gd^{3+}$  and  $Mn^{2+}$ , because these metal ions form predominantly ionic bonds in their complexes. The polyamino carboxylate-based ligands used in  $Gd^{3+}$  complexes are usually octadentate, because at least one coordination site of  $Gd^{3+}$  ion should

remain free in order to bind a water molecule. For the same reason, ligands used in  $\text{Mn}^{2+}$  complexes are hexadentate.

The open-chain complex **Gd(DTPA)** was the first  $\text{Gd}^{3+}$  complex approved for clinic MRI applications in 1988 by the US Food and Drug Administration (FDA).<sup>143–146</sup> One year later, it was discovered that the macrocyclic complex **Gd(DOTA)** presents higher kinetic inertness (Figure 54).

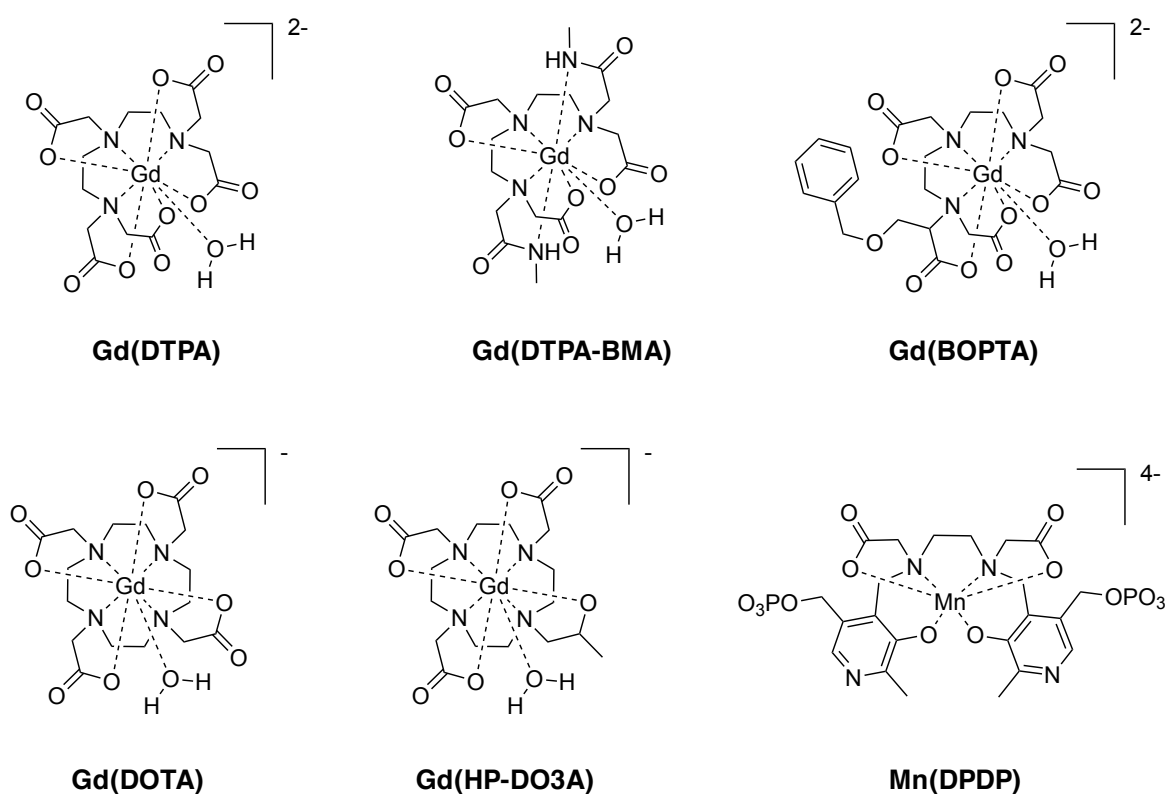


**Figure 54.**  $\text{Gd}^{3+}$  and  $\text{Mn}^{2+}$  complexes used as MRI contrast agents approved by the US FDA.

Most of the approved MRI contrast agents are derivatives of these two structures. As shown in Figure 54, both complexes have negative charges and this was related with pain in patients when they were injected. For that reason, some neutral contrast agents were developed, like **Gd(DTPA-BMA)**, although recent studies showed that negatively charged contrast agents prevent endogenous anion binding.<sup>147,148</sup> The previously mentioned contrast agents are not specific and their

## Chapter 5

distribution is extracellular.<sup>149</sup> Furthermore, they are hydrophilic and excreted from the body through the kidneys in around 2 hours.<sup>150</sup> The development of contrast agents with lipophilic groups, like **Gd(BOPTA)**, allowed the improvement of the images of the brain and the livers, due to a different biodistribution.<sup>151</sup> The investigation of contrast agents with high organ specificity is still a big challenge for the researchers.<sup>152–154</sup>

The only Mn-based contrast agents approved for the clinic use is the **Mn(DPDP)**.<sup>155,156</sup> Its distribution is specific (liver and brain) and intracellular.<sup>157</sup> Nowadays its use is very limited because other Gd<sup>3+</sup> complexes presented better results in the same systems.

More recently, the problem of Gd<sup>3+</sup> toxicity has been taken to a new dimension with the discovery of a new pathology, the nephrogenic systemic fibrosis (NFS). This new disease was observed in patients with renal insufficiency who received a Gd<sup>3+</sup> contrast agent.<sup>158,159</sup> A correlation between this disease with the type of contrast agent used, mostly complexes with less thermodynamical stability and kinetically labile was found.<sup>160,161</sup> High thermodynamic stabilities are needed to ensure the complete complexation at physiological pH, and a strong kinetic inertness to prevent the release of free metal.<sup>162–171</sup> Both factors are directly related to the *in vivo* safety application of contrast agents.

As mentioned above, linear ligands usually present faster dissociation kinetics than macrocyclic ligands. In the last years, highly inert linear ligands were studied and the relationship between ligand structure and efficiency-stability were rationalized. Some examples of rigid linear ligands used in Gd<sup>3+</sup> and Mn<sup>2+</sup> complexes are shown in Figure 55.

In these studies, the incorporation of rigid functions in the ligand structure improved the stability and inertness of the lanthanide complexes significantly. The highly rigid complex **Gd(Cddadpa)** afforded high thermodynamic stabilities and unprecedented kinetic inertness for a linear ligand, being its results comparable with those of some macrocyclic complexes.<sup>172</sup>

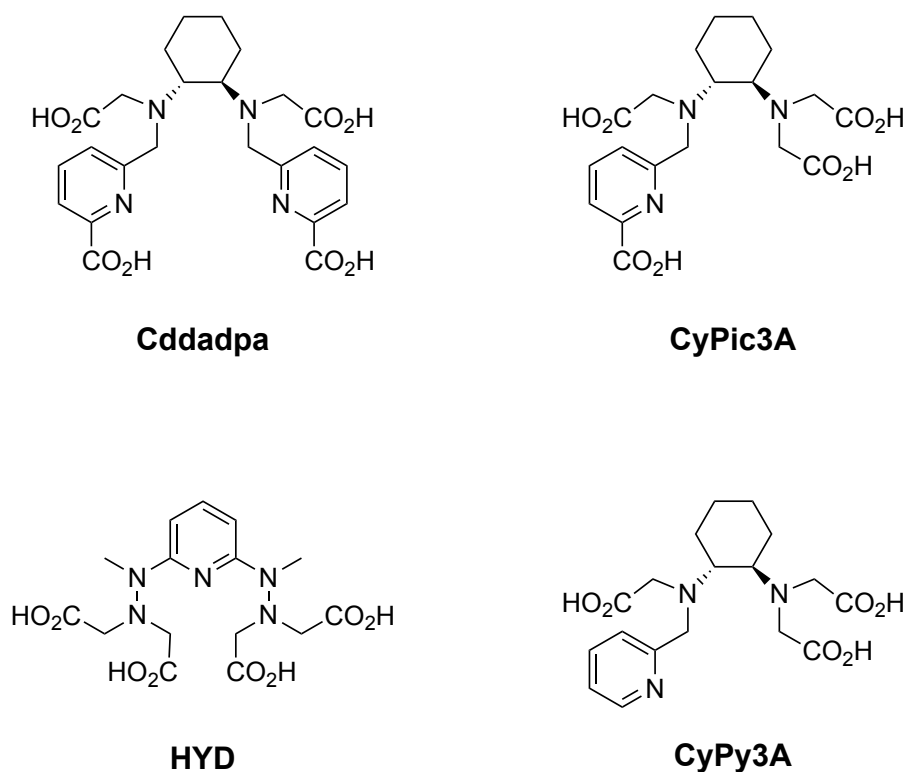


**Figure 55.** Structures of new and rigid ligands used in Gd<sup>3+</sup> and Mn<sup>2+</sup> complexes that afforded good stabilities and inertness.

Usually, complexes with hydration states higher than one present low kinetic inertness, but the incorporation of the picolinate and the cyclohexane function in **Gd(CyPic3A)** and **Gd(HYD)** showed similar results to **Gd(DTPA)**.<sup>173,174</sup> Furthermore, lowering the ligand basicity, for example in **Gd(HYD)** with hydrazine functions, was identified as an important factor to improve the kinetic inertness.<sup>175</sup> Finally, the Mn<sup>2+</sup>-based complex, **Mn(CyPy3A)**, gave good inertness and it could be a Gd alternative for patients who suffer from chronic kidney disease.<sup>155</sup>

### 5.1.2 Design of contrast agents

The design of more efficient contrast agents for MRI requires the understanding of the mechanism of water proton relaxation. The solvent nuclear relaxation in presence of dilute paramagnetic species is described by the Solomon, Bloembergen and Morgan theory.<sup>176–178</sup> The efficiency of a contrast agent is measured with its relaxivity ( $r_1$ ). It is defined as the enhancement of the longitudinal

## Chapter 5

relaxation rate of the water protons per millimol per litre of paramagnetic compound (Equation 1).

$$\frac{1}{T_{1,obs}} = \frac{1}{T_{1,d}} + r_1[CA] \quad \text{Equation 1}$$

Where  $1/T_{1,obs}$  is the observed solvent relaxation rate and  $1/T_{1,d}$  is the relaxation rate in the absence of paramagnetic compound and  $[CA]$  is the concentration of paramagnetic compound in mmol/L.

The  $Mn^{2+}$  or  $Gd^{3+}$  contrast agents increase the relaxation rates of the water protons through two contributions: the inner sphere relaxivity ( $r_1^{IS}$ ), due to the water molecules directly bonded to the metal ion, and the outer sphere relaxivity ( $r_1^{OS}$ ), as the result of the water molecules of the solvent that diffuse in the environment of the complex. These inner sphere water molecules exchange with the bulk solvent and the paramagnetic influence is propagated.

$$r_1 = r_1^{IS} + r_1^{OS} \quad \text{Equation 2}$$

The total contribution of the outer sphere is the less important. It is difficult to control because the outer sphere relaxivity depends mainly on the random translational diffusion which is hard to modulate. Some researchers also consider another contribution, which is called second sphere, due to water molecules that are not bonded to the metal ion but remain in the proximity of the complex for a long time.<sup>179,180</sup> Usually, the second sphere water molecules interact with the complex through hydrogen bonds through carboxylate or phosphonate functions of the ligand. However, this contribution is usually negligible or it is taken into account in the outer-sphere term.

The inner sphere relaxivity is calculated with Equation 3.

$$r_1^{IS} = \frac{1}{1000} \frac{q}{55.5} \frac{1}{T_{1m} + \tau_m}$$

Equation 3

Where  $q$  is the number of water molecules coordinated to the paramagnetic ion,  $\tau_m$  is the lifetime of a water molecule in the inner sphere (equal to the reciprocal water exchange rate,  $1/k_{ex}$ ) and  $T_{1m}$  is the longitudinal relaxation rate of inner sphere protons.  $T_{1m}$  is dependent on the rotational correlation time ( $\tau_R$ ), the electron spin relaxation times ( $T_{1e}$  and  $T_{2e}$ ) and the exchange rate of the inner sphere water molecules ( $k_{ex}$ ). These parameters can be modified in order to enhance the relaxivity:

- *The number of water molecules in the inner sphere,  $q$ .* The relaxivity is directly proportional to  $q$ . Although, contrast agents with three water molecules have been studied, only contrast agents with one water molecule are approved for clinical applications.<sup>181–183</sup> Complexes with high hydration levels are less thermodynamically stable, increasing the risk of the release of free metal. Moreover, these water molecules can be replaced by endogenous anions, decreasing the efficiency of the contrast agent.<sup>184</sup>
- *The exchange rate between the bound water molecules and the solvent,  $k_{ex}$ .* When the water exchange is slow, the paramagnetic effect will not be transmitted to the solution. On the contrary, when it is too fast, the bound water molecule will not have stayed enough time to feel the paramagnetic presence of the metal ion. So, an optimal value of this parameter is needed to maximize its effects.<sup>164,185</sup>
- *The rotational correlation time,  $\tau_R$ .* It describes the molecular tumbling of the Gd-water proton vector. This parameter is the most important and it is the limiting factor of the relaxivity of low molecular and not supramolecular-based contrast agents. For small chelates, the relaxivity increases with the molecular weight, but for big complexes this relation is not maintained. During the last years, different strategies have been focused in the optimisation of this parameter, such as the use of macromolecules or large aggregates.<sup>186,187</sup>

## Chapter 5

- *Electronic relaxation times,  $T_{1e}$  and  $T_{2e}$ , and the distance between water protons and the metal ion,  $r_{GdH}$ . These parameters influence the relaxivity, however, it is difficult to modulate with the structure of the ligand and small success has been achieved.*

In Figure 56, a schematic representation of important parameters in a  $Gd^{3+}$  complex is shown.

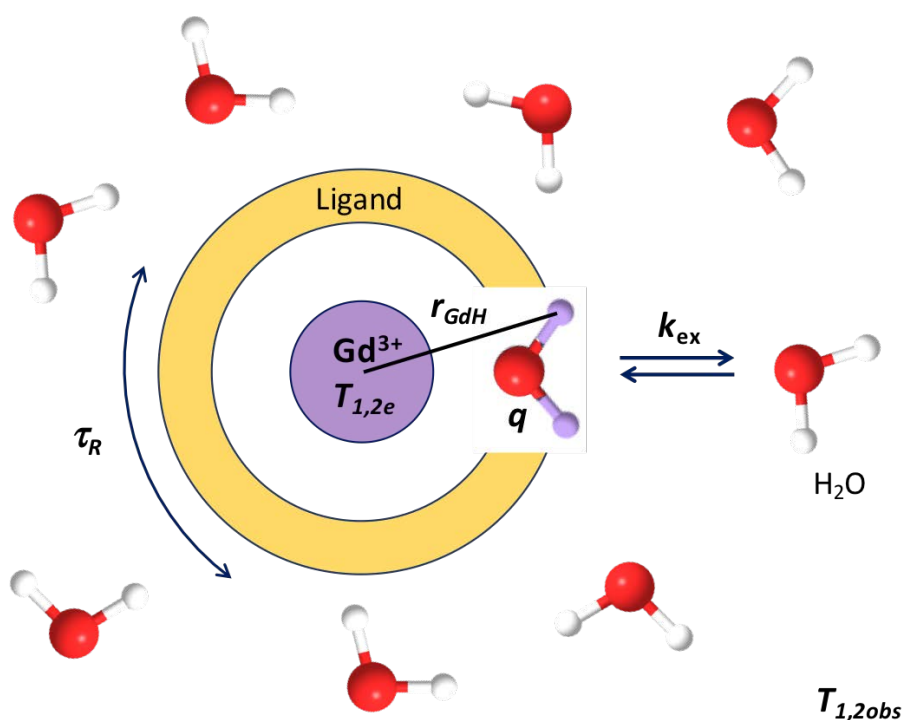
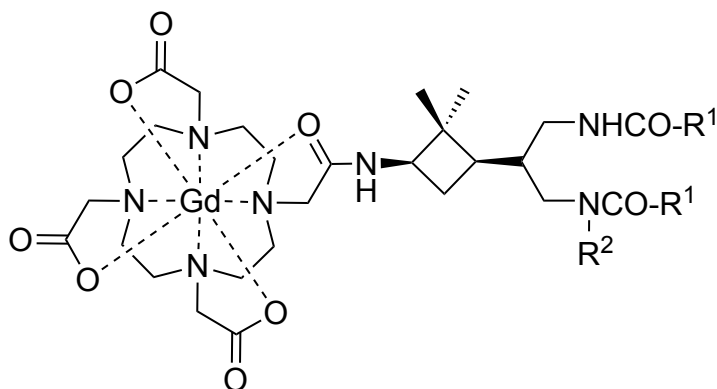


**Figure 56.** Schematic representation of the parameters that influence the relaxivity.

The design of new ligands for the exploration of highly efficient contrast agents should take into account the optimisation of these parameters. According to the Solomon, Bloembergen and Morgan equations, the full optimisation of all parameters could achieve relaxivity values up to  $100 \text{ mM}^{-1}\text{s}^{-1}$  at 20 MHz in complexes with one water molecule in the first sphere. Nowadays, the relaxivities of commercial contrast agents are in the range of 4 to  $6 \text{ mM}^{-1}\text{s}^{-1}$ , so there is still a long journey ahead for the researchers to keep investigating in this interdisciplinary field.

In our research group, cyclobutane-cored triamines conjugated to a **Gd(DOTA)** were studied few years ago. The different substitution of the amine of the complex was found to be an important factor for high relaxivities (Figure 57).<sup>188</sup>



- 98** a:  $R^1 = \text{OBn}$ ,  $R^2 = \text{H}$   
 b:  $R^1 = p\text{-NO}_2\text{-C}_6\text{H}_4$ ,  $R^2 = \text{H}$   
 c:  $R^1 = \text{Me}$ ,  $R^2 = \text{H}$   
 d:  $R^1 = \text{OBn}$ ,  $R^2 = \text{Me}$

**Figure 57.** Structures of  $\text{Gd}^{3+}$  complexes based on cyclobutane-cored triamines conjugated with **Gd(DOTA)**.

Carbamate **98a** and *p*-nitrobenzamide **98b** exhibited  $r_1$  values lower than **Gd(DOTA)** whereas the value for *N*-methylcarbamate **98d** was similar to that of the reference. The case of acetamide-based complex, **98c**, manifested better contrast enhancement than **Gd(DOTA)** showing stronger positive contrast enhancement on  $T_1$ -weighted images and higher  $r_1$  (Figure 58).

Computational studies suggested that the amine protecting groups in the cyclobutane side-chains played an important role in the water exchange rate. In this case, the strength of the  $\text{Gd-OH}_2$  bond is influenced by the presence of aromatic protecting groups which hinder water exchange.

These results instigated us to use the rigid cyclobutane scaffold for the preparation and further study of new contrast agents.



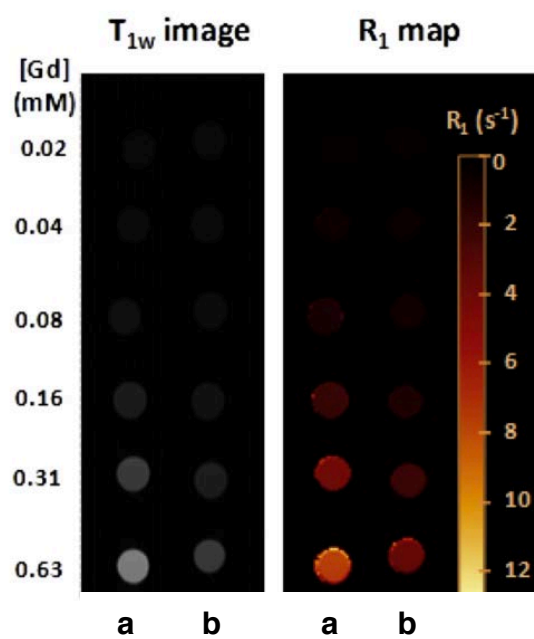


**Figure 58.**  $T_1$ -weighted images and  $r_1$  map of phantoms of solutions of (a) **98c** and (b) **Gd(DOTA)** at various concentrations.

## 5.2 Objectives

In this part of the thesis, the synthesis of two new chiral cyclobutane-based ligands, **L1** and **L2**, was proposed to be complexed with  $\text{Gd}^{3+}$  and  $\text{Mn}^{2+}$  and studied as potential MRI contrast agents (Figure 59).

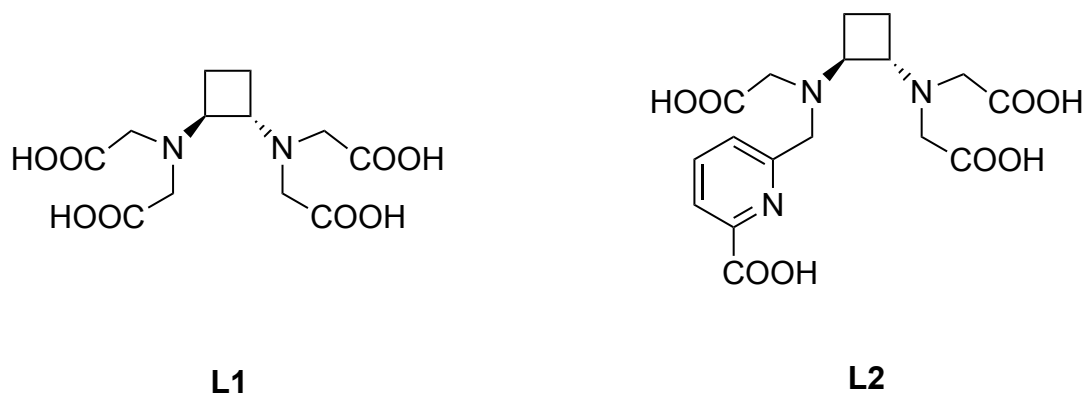


**Figure 59.** Structures of the two target ligands.

It should be noticed that **L1** has 6 coordinating centers, while **L2** has 7. Then, among all complexes, **Mn(L1)** and **Gd(L2)** might be the most interesting for clinical use, considering their theoretical hydration numbers (1 and 2, respectively). The comparison between complexes with each ligand would give us information about the influence of the incorporated picolinate function. Furthermore, the effect of different hydration numbers in the stability, the inertness and the efficiency of the other **Gd(L1)** and **Mn(L2)** complexes would be rationalized. The obtained results would be compared with the studies of related contrast agents from the literature.

The objectives of this part are:

- The synthesis of these two ligands (**L1** and **L2**) to prepare the corresponding metal complexes.
- The potentiometric study of both ligands and their metal complexes to understand their basicity and thermodynamic stability.
- The study of their kinetic inertness using  $\text{Cu}^{2+}$  as exchanging metal.
- The study of the exact number of water molecules in the inner sphere,  $q$ , under different conditions.

## Chapter 5

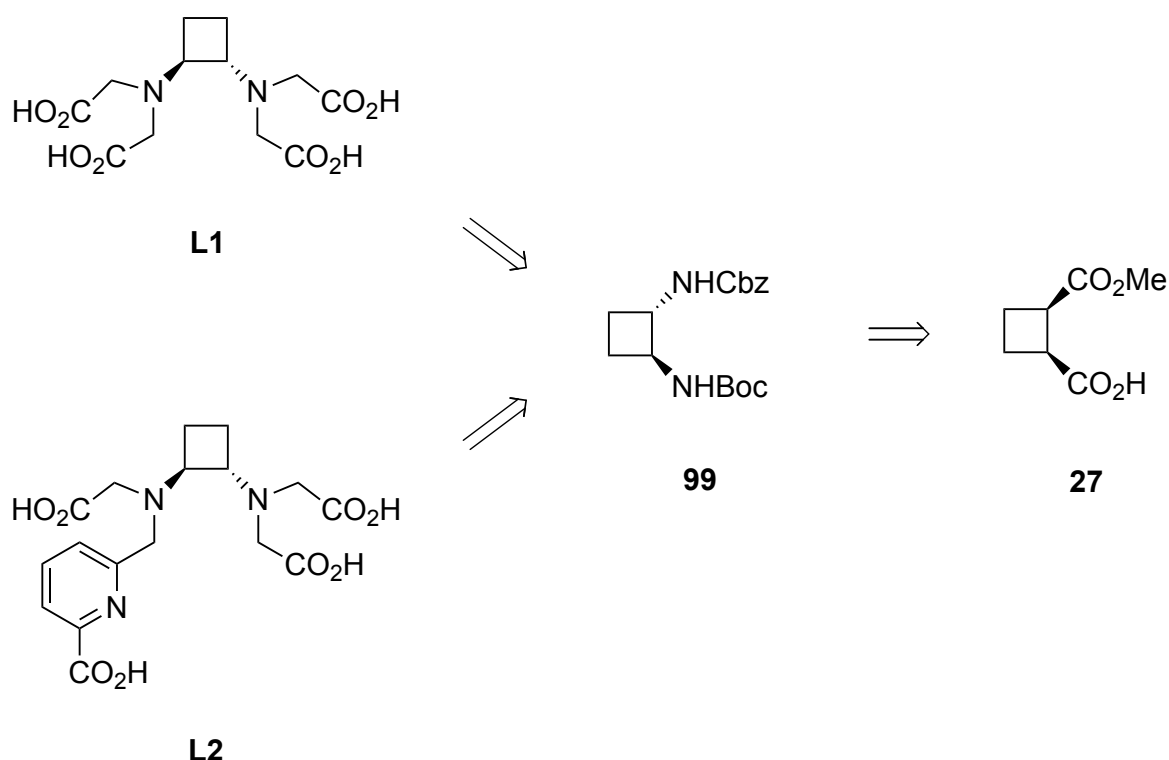
- The study of the relaxivity under different conditions and the physico-chemical parameters that influence it.

## 5.3 Results and discussion

The results of this chapter of the thesis are presented in five parts. First, the synthesis of both ligands is described in section 5.3.1. After, the potentiometric and kinetic studies are explained (section 5.3.2 and 5.3.3) followed by the luminescence studies (section 5.3.4). Finally, relaxometric measurements are discussed (section 5.3.5). This work was carried out in collaboration with Prof. Éva Jakab Tóth from Centre de Biophysique Moléculaire in Orléans (France).

### 5.3.1 Synthesis of Ligands

Taking into account the acquired background in our research group preparing cyclobutane-based diamines, the target ligands were synthesized through the following general retrosynthetic pathway (Scheme 21).



**Scheme 21.** General retrosynthetic pathway for ligands **L1** and **L2**.

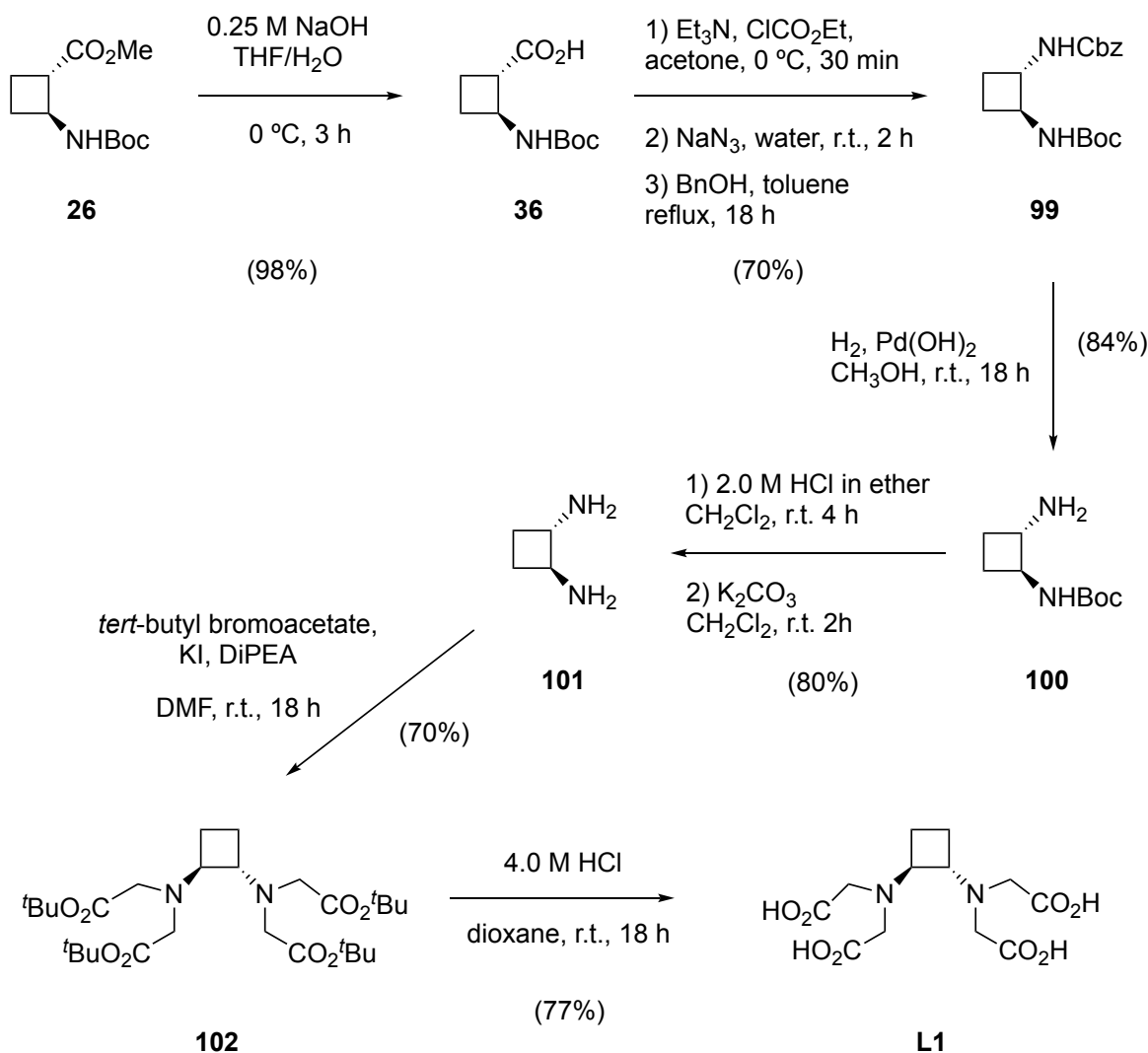
The retrosynthetic pathways for both ligands have a key and common intermediate **99**. *trans*-Diamine **99** was prepared according to the procedures

## Chapter 5

described by our research group.<sup>15,19</sup> The synthesis was stereoselective and led to both compounds in an enantiopure form. The synthetic routes for **L1** and **L2** and the intermediate **99** are presented below.

### 5.3.1.1 Synthesis of protected *trans*-diamine **99** and **L1**

The synthetic route for protected *trans*-diamine **99** can be achieved in two steps from orthogonally diprotected amino acid **26**, which synthesis is explained in chapter 3. **L1** can be synthesized in 4 steps in a 36% overall yield from diamine **99**. The synthetic route is described in Scheme 22.



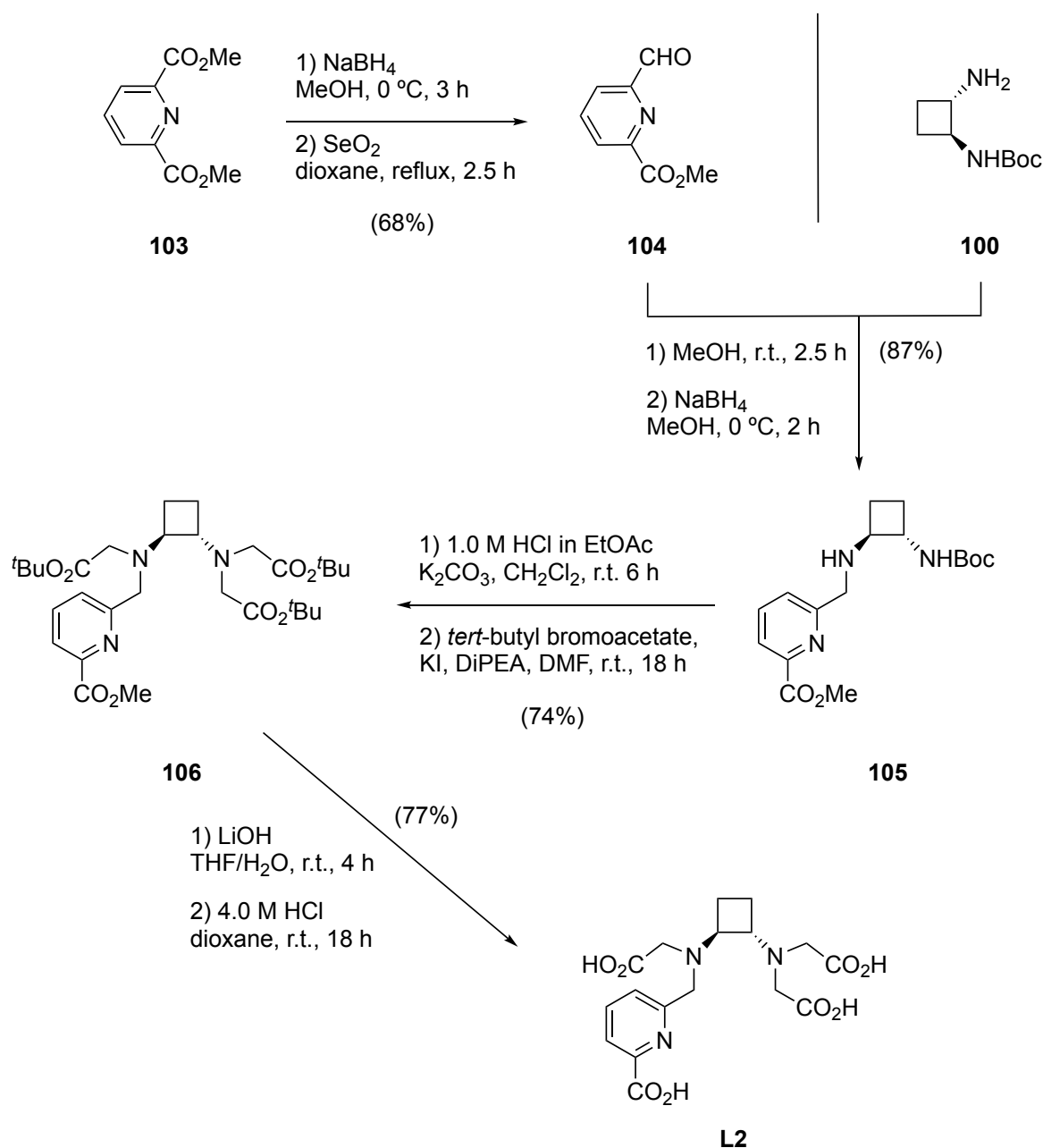
**Scheme 22.** Synthetic route for key intermediate **99** and Ligand **L1**.

The synthesis of **L1** started with the saponification of *trans*- $\beta$ -amino acid **26** with sodium hydroxide under mild conditions in 98% yield. Then, the acid was treated with ethyl chloroformate followed by a treatment with sodium azide to produce the corresponding acyl azide. Later, the acyl azide was heated to yield the corresponding isocyanate and reacted with benzyl alcohol under reflux conditions in toluene to achieve *trans*-diamine **99** in 70% yield. After that, the diamine was deprotected stepwise. Hydrogenolysis of Cbz carbamate to achieve half-protected **100** and subsequent the acidolysis of Boc carbamate **100** followed by a treatment with potassium carbonate afforded the neutral and free diamine **101** in 67% yield (for both deprotections). Consecutively, diamine **101** was alkylated using *tert*-butyl bromoacetate in the presence of DiPEA and KI to obtain the protected ligand **102** in 70% yield. Finally, *tert*-butyl ester removal by acidolysis afforded **L1** in 77% yield.

### 5.3.1.2 Synthesis of ligand L2

The synthetic route of ligand **L2** can be achieved in a convergent synthesis of 4 steps in 34% overall yield from dimethyl pyridine 2,6 dicarboxylate, **103**. The synthetic route is described in Scheme 23.

Ligand **L2** was obtained starting with a partial reduction of pyridine-2,6-dicarboxylate with sodium borohydride to afford aldehyde **104** in 68% yield. Diamine **101** was synthesized using the synthetic route described before in Scheme 22. After that, the reaction of aldehyde **104** and mono-protected diamine **100**, *via* reductive amination gave the secondary amine **105** in 87% yield. Then, the removal of the Boc-protected amino group in **105** using hydrochloric acid followed by a basic treatment and an alkylation with *tert*-butyl bromoacetate in the presence of DiPEA and KI produced the protected ligand **106** in 70% yield. In the last step, methyl ester removal by saponification using lithium hydroxide followed by an acidolysis of *tert*-butyl esters produced **L2** in 77% yield.



Scheme 23. Synthetic route for ligand L2.

### 5.3.2 Potentiometric studies

The protonation constants for L1 and L2 as well as the stability constants of their metal complexes formed with different metal ions (Gd<sup>3+</sup>, Mn<sup>2+</sup> and Zn<sup>2+</sup>) were determined by pH-potentiometric titrations. This method is the most important and widely used for describing the equilibrium process of metal complexes of polyamino polycarboxylate ligands in solution. This method can only be used if the equilibrium is rapidly reached, which is generally accepted for linear ligands, but not for

macrocyclic ones. In this part of the chapter, **L1** and **L2** are compared with different linear ligands from the literature (Figure 60).<sup>169,173,189–191</sup>

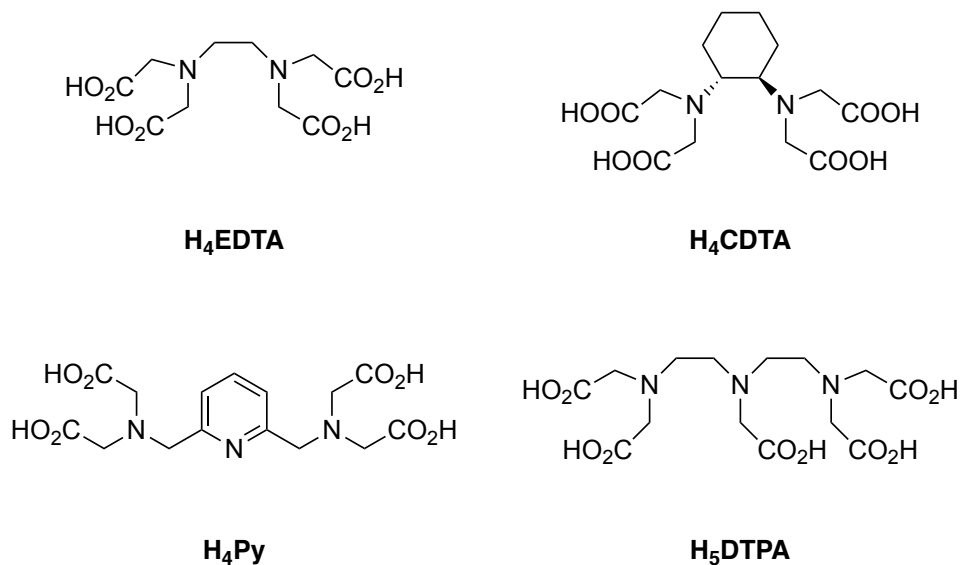


**Figure 60.** Structure of relevant ligands described in the literature as part of MRI contrast agents.

The proton concentration of an aqueous solution containing the metal complex is influenced by the protonation constants of the ligand and the interaction between the metal ion and the different species of the protonated ligand. So, the comprehension of the ligand protonation constants is fundamental for determining the stability constants of the metal complexes.

Protonation constants of ligands,  $K_i$ , stability constants of complexes,  $K_{ML}$ , and protonation constants of complexes,  $K_{MH_iL}$ , are described and defined in Equations 4-6.

$$K_i = \frac{[H_iL]}{[H_{i-1}L][H^+]} \quad \text{Equation 4}$$

$$K_{ML} = \frac{[ML]}{[M][L]} \quad \text{Equation 5}$$

$$K_{MH_iL} = \frac{[M(H_iL)]}{[M(H_{i-1}L)][H^+]} \quad \text{Equation 6}$$



## Chapter 5

Where  $[M]$ ,  $[L]$ , and  $[ML]$  are the equilibrium concentrations of free metal ion, deprotonated ligand, and deprotonated complex, respectively.

First, both ligands, **L1** and **L2** at 2mM concentration in water were studied in the absence of metal ion, by titrating them with standardized NaOH. Once the titrations were finished, a retitration using also previously standardized HCl was carried out. The titrations curves are shown in Figure 61.

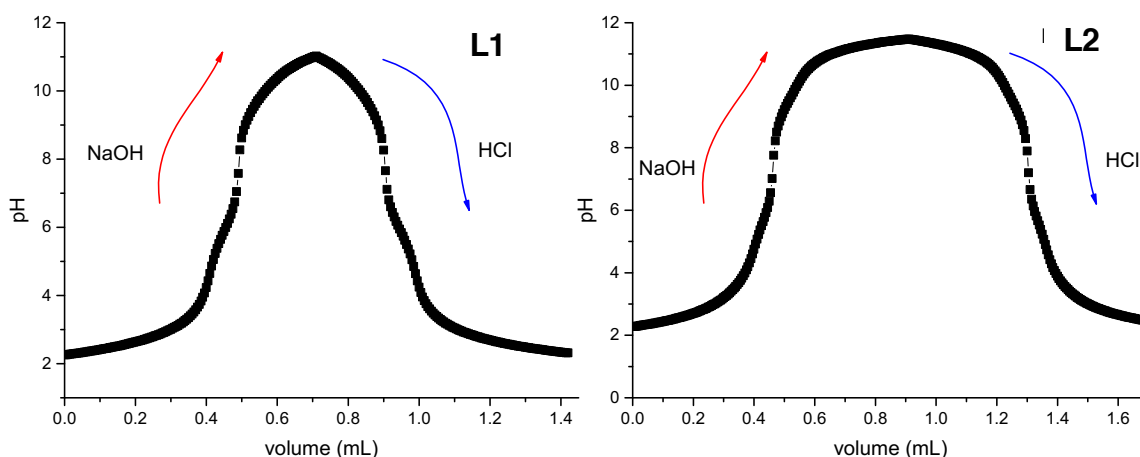


**Figure 61.** Potentiometric titration curves of aqueous solutions of **L1** and **L2** using 0.100 M NaOH and 0.101 M HCl.  $[L] = 2 \text{ mM} + 0.1 \text{ M KCl}$ , 25 °C in  $N_2$  (1atm).

The plots of these titrations showed a symmetric curve when the NaOH was changed by HCl. So, the ligands are stable at this range of pH and the equilibrium was reached rapidly, which is necessary to study protonation and stability constants by pH-potentiometry. To avoid dilution effects, only the first base-based titration was considered to calculate the protonation constants of both ligands, which were calculated using computer software Hyperquad 2008<sup>192</sup> considering Equations 4-6. At least 2 or 3 different independent experiments were carried out to determine these values. The results are shown in (Table 10)

Once both ligands were studied, the stability constants of the metal complexes of **L1** and **L2** were also determined from direct potentiometric titrations, as the complex formation was fast. The titrations of the metal complexes were

performed at the same conditions that before but containing 1 equivalent of metal cation ( $\text{Gd}^{3+}$ ,  $\text{Mn}^{2+}$ ,  $\text{Zn}^{2+}$ ). The titrations curves of **L1** and **L2** in the absence and presence of  $\text{Gd}^{3+}$ ,  $\text{Mn}^{2+}$  and  $\text{Zn}^{2+}$  are shown in Figure 62.

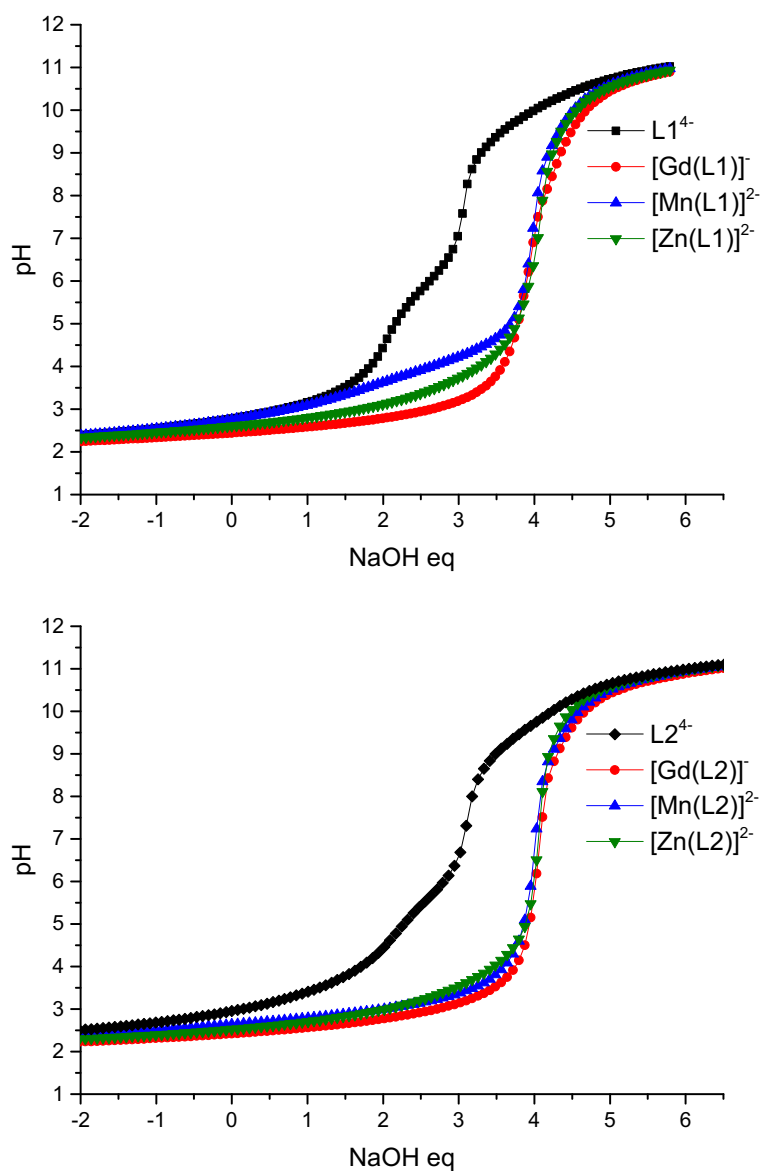


**Figure 62.** Potentiometric pH titrations curves for the ligands **L1** (top) and **L2** (bottom) in the absence (black) and in the presence of some metal ions (red,  $\text{Gd}^{3+}$ ; blue,  $\text{Mn}^{2+}$ ; green,  $\text{Zn}^{2+}$ ) at 1:1 metal/ligand ratio.  $[\text{M}] = [\text{L}] = 2 \text{ mM} + 0.1 \text{ M KCl}$ ,  $25 \text{ }^\circ\text{C}$  in  $\text{N}_2$  (1atm).

## Chapter 5

Figure 62 shows that in the presence of a metal, the equivalence point of the curves is shifted to higher equivalents of NaOH, indicating the formation of the metal ligand complexes. This shift was also used to calculate and to confirm the real concentration of the ligand stock solution and the resulting concentration was equal to that calculated before. Above pH 10, in some titrations a solid started to precipitate, possibly due to the formation of a hydroxo complex, which could be insoluble. For that reason, only experimental data below that point were used to fit the curves and to calculate the stability constants. To calculate the stability constants and the protonation of the complexes, titration curves were refined using the same computer software Hyperquad 2008 used before.<sup>192</sup> All stability and protonation constants are shown in Table 10

Five protonation constants were determined for **L1** and **L2**. For **L1**, the two first  $\log K_i$  values correspond to the protonation of the two amines. The next protonation constants could be attributed to the protonation of the carboxylate functions. Since the ligand **L2** has an additional pyridine moiety, the protonation sequence is not straightforward. For example, in the studies of the relative ligand **Py**, the protonation of the pyridine function was not observed in the typically studied pH-range (2-12).<sup>173</sup> So, we could hypothesize that the correlation of protonation constants of **L2** could be the same as **L1**. Though the first protonation constant of **L1** is 0.08 units of  $\log K$  bigger than **L2**, its global basicity is 1.4 units higher, due to the incorporated pyridine.

Comparing protonation constants of **L1** related ligands, we can observe that the first protonation constant of **L1** is slightly higher than for **EDTA** and **CDTA**. The differences between total basicity of these ligands could be attributed to the structural rigidity of the cyclohexyl or cyclobutyl unit compared with the ethylene bridging unit, which is more flexible. First protonation constant of **L2** is also slightly higher than that of **Py** but lower than for **DTPA** and the global basicity of **L2** is lower than that of **Py** and **DTPA**.

**Table 10.** Protonation constants and standard deviations of **L1**, **L2** and stability constants of their metal complexes (25 °C, I = 0.1 M KCl). Results for some relevant ligands from the literature are also shown.<sup>169,173,189–191</sup>

	<b>Ligand 1</b>	<b>Ligand 2</b>	<b>EDTA</b>	<b>CDTA</b>	<b>Py</b>	<b>DTPA</b>
<b>log K<sub>1</sub><sup>H</sup></b>	9.66 ±0.01	9.58±0.02	9.18	9.36	8.95	9.93
<b>log K<sub>2</sub><sup>H</sup></b>	5.85 ±0.01	6.00±0.04	6.00	5.95	7.85	8.37
<b>log K<sub>3</sub><sup>H</sup></b>	3.06±0.02	3.78±0.04	2.58	3.62	3.38	4.18
<b>log K<sub>4</sub><sup>H</sup></b>	2.08±0.03	2.33±0.05	2.29	2.57	2.48	2.71
<b>log K<sub>5</sub><sup>H</sup></b>	1.71±0.08	2.07±0.05	-	1.49	-	2.00
<b>Σ log K<sub>i</sub><sup>H</sup></b>	22.35	23.75	20.05	22.99	22.66	27.19
<b>log K<sub>GdL</sub></b>	14.73±0.01	17.41±0.01	16.28		18.60	22.03
<b>log K<sub>GdHL</sub></b>	2.38±0.03	2.36±0.02	-		-	1.96
<b>log K<sub>MnL</sub></b>	10.26±0.01	14.71±0.01	12.46	14.32	-	14.54
<b>log K<sub>MnHL</sub></b>	4.07±0.02	3.25±0.01	2.95	2.90	-	4.37
<b>log K<sub>ZnL</sub></b>	12.26±0.01	15.22±0.01	14.61	19.32	15.85	17.45
<b>log K<sub>ZnHL</sub></b>	4.10±0.01	3.78±0.01	-	-	3.81	5.08

All complexes formed by Gd<sup>3+</sup>, Mn<sup>2+</sup> and Zn<sup>2+</sup> ions and **L1** and **L2** presented a nonprotonated and a monoprotonated mononuclear complex species. The monoprotonated complexes were observed at low pH. It could be attributed to the protonation of a non-coordinating carboxylate function.

The stability constants (log K<sub>i</sub>) of **Gd(L2)**, **Mn(L2)** and **Zn(L2)** are higher than those with **L1**, which is reasonable, because the structure of **L2** has one extra coordinating site. Stability constants of **Gd(L1)** and **Mn(L1)** are slightly lower than **Gd(EDTA)**, **Mn(EDTA)**, and **Mn(CDTA)**, respectively, indicating that the incorporated cyclobutane residue does not favor the thermodynamic stability.

## Chapter 5

Analogous results are obtained if we compare the stability constant of **Gd(L2)** with some ligands. It is 1.2 units lower than **Gd(Py)** and 4.62 units lower than **Gd(DTPA)**. Although the **Mn(L2)** complex may not be interesting for MRI applications, because it should not have any water molecule directly coordinating the metal, it was studied to gain some insight about structure and stability. Surprisingly, the stability of **Mn(L2)** is the highest of Mn complexes of the Table, indicating that a correlation between different metals and ligands is not clear.

It has been demonstrated that *in vivo* toxicity of Gd and Mn complexes is due to the release of free  $\text{Gd}^{3+}$  and  $\text{Mn}^{2+}$  ions, which can be assisted by transmetallation with endogenous cations, such as  $\text{Zn}^{2+}$ ,  $\text{Cu}^{2+}$  or  $\text{Ca}^{2+}$ .<sup>133,193,194</sup> Gratefully, the stability constants of **Gd(L1)** and **Gd(L2)** are higher than **Zn(L1)** and **Zn(L2)**, preventing the transmetallation with Zn cations, which is crucial for clinical applications. Unfortunately, **Mn(L1)** is less thermodynamically stable than **Zn(L1)**, but it could still have potential if it afforded high relaxivities and had high kinetic inertness.

The species distribution in function of the pH has also been studied to understand in which range of pH the complexes are thermodynamically stable. Species distribution plots were calculated using the experimental protonation and stability constants using the computing software HySS (Figure 63).<sup>195</sup>

In Figure 63, the molar fraction of the species of different systems are represented in function of the pH. For example, **L1** in water at pH = 7.3 is in 96% in its monoprotinated species ( $\text{L1H}^{3-}$ ) and 3.6% in its diprotinated form ( $\text{L1H}_2^{2-}$ ). Only at pH = 12, we can observe in 99.6% the completely deprotonated form of **L1** ( $\text{L1}^{4-}$ ).

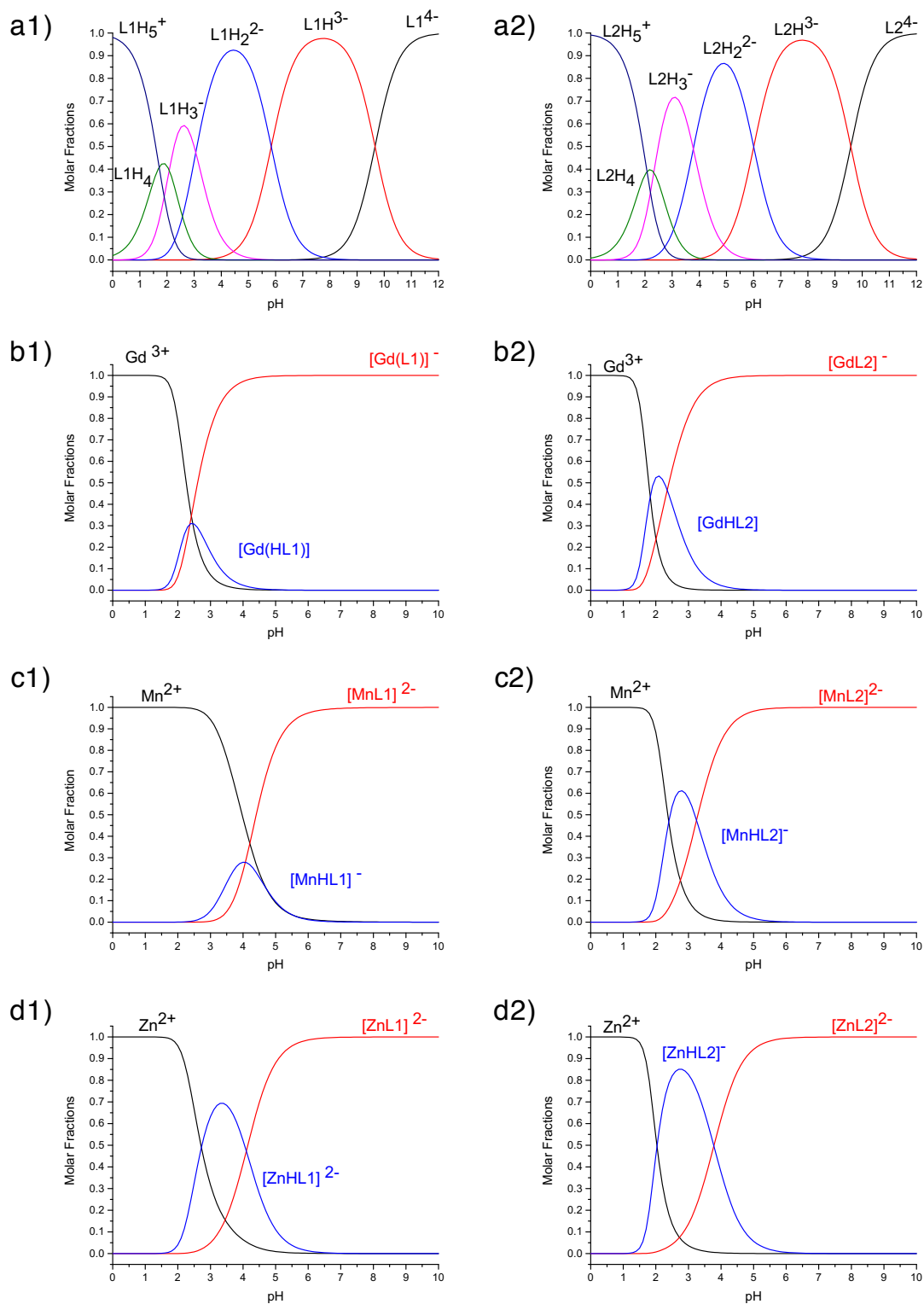


**Figure 63.** Species distribution curves of the ligands in absence of metal (a), and with  $Gd^{3+}$  (b),  $Mn^{2+}$  (c) and  $Zn^{2+}$  (d) of L1 (1) and L2 (2), respectively.

## Chapter 5

The species distribution curves for the metal complexes show in which range of pH these complexes are stable enough to be used. The knowledge of these stability ranges is crucial to perform the structural and relaxometric studies in order to avoid the possibility of releasing free metal which would then conduct to erroneous values. These curves have been calculated considering one equivalent of ligand and metal, but it may be mentioned that adding more equivalents of ligand can be a good solution if a complex is not stable enough for its study at the desired pH. Quantitative results are shown in Table 11.

**Table 11.** pH ranges where complexes are thermodynamically stable and molar fractions in percentage of the complexes at pH = 3, 5 and 7.

Complex	Stability ML pH range <sup>a</sup>	Complex ML (pH = 3) (%)	Complex ML (pH = 5) (%)	Complex ML (pH = 7) (%)
<b>Gd(L1)</b>	4.5-10	75.3	99.7	100
<b>Gd(L2)</b>	4.4-10	81.2	99.8	100
<b>Mn(L1)</b>	6.6-10	0.4	81.4	99.5
<b>MnL2</b>	5.3-10	32.4	98.2	100
<b>Zn(L1)</b>	6.2-10	5.0	88.0	100
<b>Zn(L2)</b>	5.8-10	13.7	99.3	100

<sup>a</sup> pH values at which molar fraction of complexes are higher than 99 %. Beyond pH = 10 it has not been determined.

As it is shown in Table 11, Gd complexes have a wider usable pH range, followed by Zn complexes and Mn complexes. Gd complexes are completely stable at pH = 5, but Mn and Zn complexes need higher pH to be stable. As it is mentioned above, these pH ranges will be taken into account to perform the structural, relaxometric and kinetic studies.

### 5.3.3 Kinetic inertness studies

Kinetic inertness is a key parameter for the safe application of  $\text{Gd}^{3+}$  complexes as contrast agents, because the dissociation products of the complexes, especially the free metal, are highly toxic. Even some authors have indicated that a high kinetic inertness is more important than the thermodynamic stability for *in vivo* applications, since the complex must remain intact inside the human body.<sup>196–198</sup> Usually, the kinetic stability is characterized by rate constants of exchange reactions that might take place *in vivo*. In these conditions, the reaction mechanism of dissociation of  $\text{Gd}^{3+}$  chelates consists in different pathways. The overall map of dissociation reactions considered is shown in Figure 64.

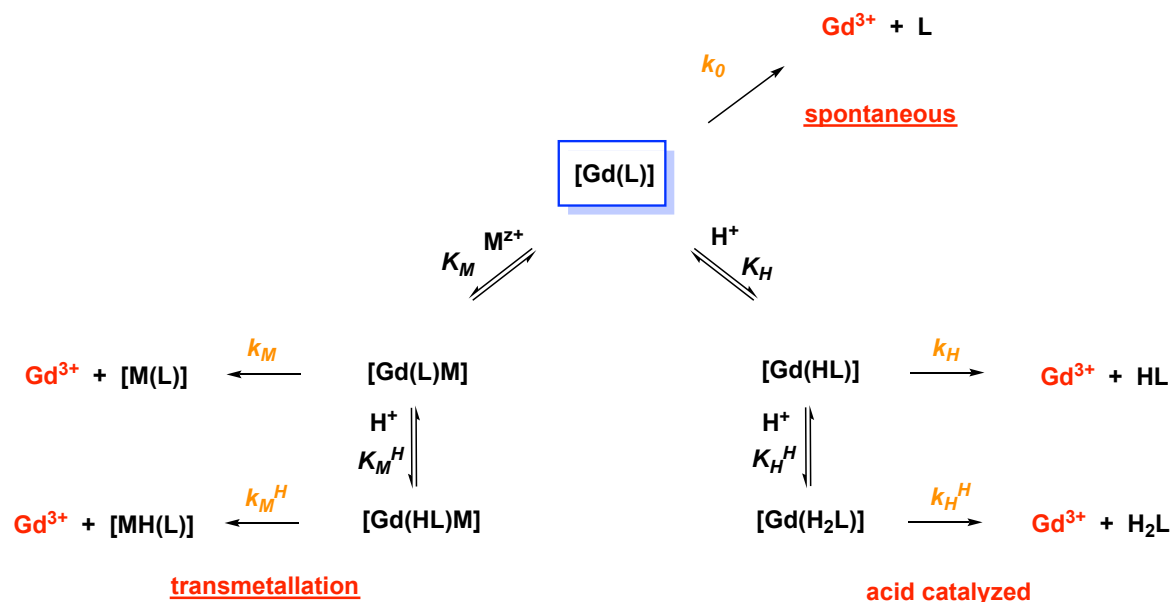


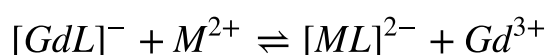
**Figure 64.** Different pathways considered for the dissociation of  $\text{Gd}^{3+}$  chelates. Free  $\text{Gd}^{3+}$  ions are remarked in red and kinetic constants are highlighted in orange for an easier visualization.

The *in vivo* dissociation of  $\text{Gd}^{3+}$  complexes can occur through different mechanistic pathways: spontaneous dissociation, acid catalyzed dissociation and transmetallation which involves the direct attack of the exchanging metal ion on the complex.<sup>133,196</sup> The spontaneous dissociation is characterized by the rate constant  $k_0$ . Two different acid catalyzed paths are considered, the monoprotated and the



## Chapter 5

diprotonated, characterized by the protonation constants  $K_H$  and  $K_H^H$  and the rate constants  $k_H$  and  $k_H^H$ , respectively. In transmetallation reactions a key dinuclear complex  $[Gd(L)M]$  is formed in the first step, characterized by the stability constant  $K_M$ . This species can dissociate directly releasing free  $Gd^{3+}$  or it can be protonated and the dissociation occurs through the proton-metal-assisted pathway. The hydroxide-assisted dissociation is not taken into account because it is not relevant in most cases.<sup>166</sup> The dissociation reactions are studied in the presence of high excess of exchanging metal ion ( $M^{2+}$ ), to ensure the pseudo first order conditions.



The rate of dissociation can be expressed by Equation 7 in the presence of high excess of the exchange metal ion.  $k_{obs}$  is the observed pseudo-first order rate constant and  $[GdL]_t$  is the total concentration of the GdL complex.

$$-\frac{d[Gd(L)]_t}{dt} = k_{obs}[Gd(L)]_t \quad \text{Equation 7}$$

Taking into account each dissociation pathway, the concentration of the GdL complex can be expressed as the sum of the concentrations of the different reactive species. Considering the complex protonation constants  $K_H$  and  $K_H^H$ , as well as the stability constants of the dinuclear intermediate  $K_M$  and  $K_M^H$ , the pseudo first order rate constant,  $k_{obs}$  can be expressed as Equation 8.

$$k_{obs} = \frac{k_0 + k_1[H^+] + k_2[H^+]^2 + k_3[M] + k_4[M][H^+]}{1 + K_H[H^+] + K_H K_H^H [H^+]^2 + K_M[M] + K_M^H [M][H^+]} \quad \text{Equation 8}$$

Where  $k_1 = k_H K_H$ ,  $k_2 = k_H^H K_H K_H^H$ ,  $k_3 = k_M K_M$  and  $k_4 = k_M^H K_M K_M^H$ .

Generally, the macrocyclic complexes, like **Gd(DOTA)** are more inert than linear complexes, like **Gd(DTPA)** due to the compact and rigid structure of the macrocycles.<sup>162,199</sup> In most cases, the dissociation of  $Gd^{3+}$  complexes made of linear ligands is *via* acid-assisted transmetallation while the dissociation kinetics of macrocyclic complexes are independent of the exchanging metal and go through proton-assisted pathways.<sup>162,200,201</sup> As explained in the introduction of this chapter, the use of rigid open-chain ligands (Figure 55), such as **Gd(Cddadpa)**, **Gd(HYD)** or **Gd(Py)** produced higher kinetic inertness than some  $Gd^{3+}$  complexes with macrocyclic ligands, like, **DO3A**.<sup>162,172,173,175</sup>

The kinetic inertness of **Gd(L2)** has been characterized by studying the exchange reaction with the use of  $Cu^{2+}$  as exchanging ion.  $Cu^{2+}$  is typically the most efficient among physiologically relevant metal ions to promote transmetallation reactions with  $Gd^{3+}$  complexes. The dissociation was monitored using UV-Vis spectrophotometry.

To begin with, the UV-Vis spectra of **Gd(L2)** and **Cu(L2)** were recorded to know the wavelength where the absorbance changes significantly. The UV-Vis spectra of **L2**, **Gd(L2)** and **Cu(L2)** are shown in Figure 65, in which we can observe that the maximum difference in absorbance is at 245 nm.

The exchange reactions were followed at that wavelength in the pH range of 3.35-4.90. The pH was lowered to speed up the exchange reaction, since at physiologic pH it usually takes days to complete. The exchange reactions at pH 3.35 took place in 2 hours, while at pH 4.90 the reaction times were about 8 hours, which are slow enough to monitor. The evolution of the absorbance vs time at 245 nm was monitored at different conditions and the least squares fit of this data using an exponential function allowed to obtain  $k_{obs}$  at different pH and  $Cu^{2+}$  concentrations. For example, in Figure 66, the variation of absorbance due to an exchange reaction using 40 equivalents of  $Cu^{2+}$  at pH = 3.5 is shown.

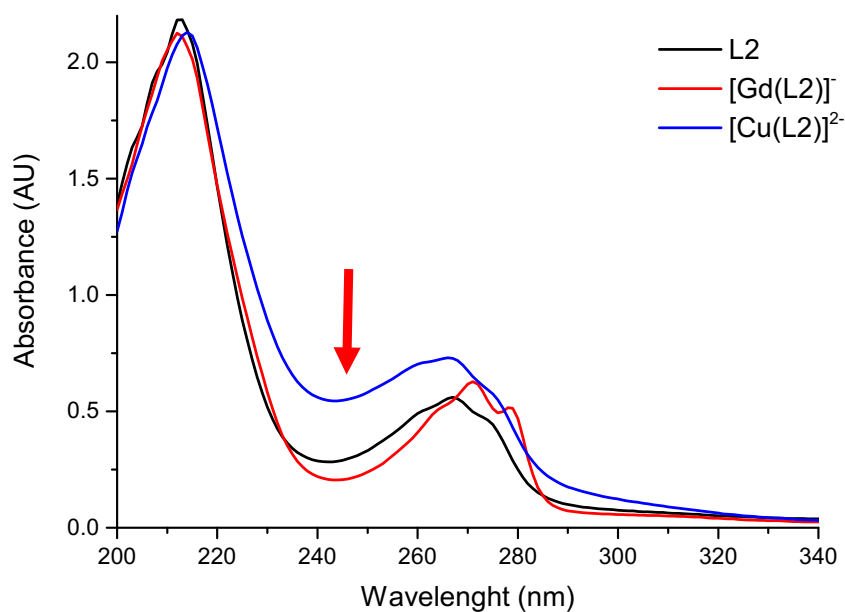


**Figure 65.** UV-Vis spectra of aqueous 0.1 M solutions of **L2**, **Gd(L2)** and **Cu(L2)** + 0.15 M NaCl, 50 mM methylpiperazine buffer (pH = 7) at 25 °C.

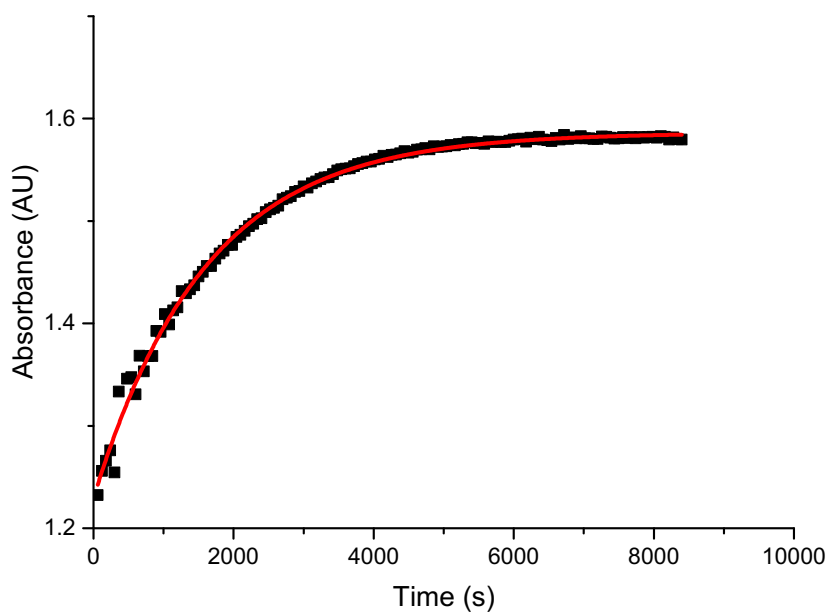


**Figure 66.** Variation of the absorbance at 245 nm due to the dissociation reaction of 0.11mM **Gd(L2)** at pH = 3.5 after adding 40 equivalents of  $\text{Cu}^{2+}$  (0.15 M NaCl, 50 mM methylpiperazine buffer at 25 °C). Monoexponential fit is shown in red.

The plot of  $k_{\text{obs}}$  values at different pH in function of the  $\text{Cu}^{2+}$  concentration is shown in Figure 67.

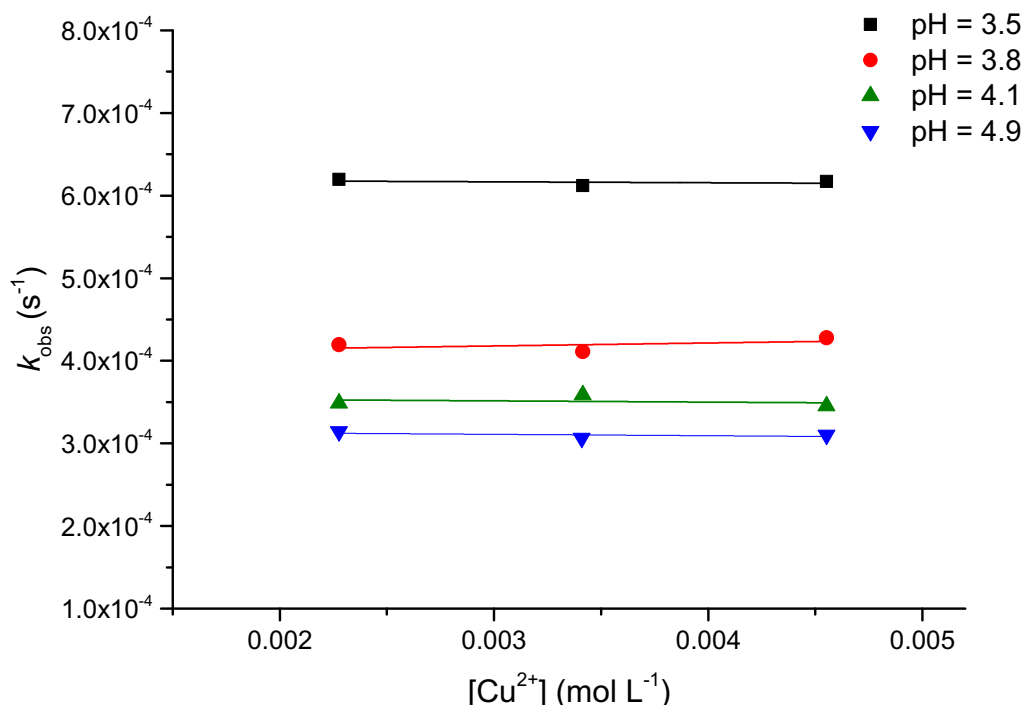


**Figure 67.**  $k_{\text{obs}}$  values for the exchange reaction of **Gd(L2)** in function of  $\text{Cu}^{2+}$  concentration at different pH (3.5, 3.8, 4.1, 4.9). Lines represent the linear fit of each pH.

The results indicate that the dissociation of the complex accelerates when the pH is decreased but it is independent of the  $\text{Cu}^{2+}$  concentration. The linear fit of the  $k_{\text{obs}}$  values of each pH range confirmed that dissociation of **Gd(L2)** is not dependent of  $\text{Cu}^{2+}$  concentration showing in all cases a slope of 0. So, the release of  $\text{Gd}^{3+}$  in this complex is produced mostly through a spontaneous and acid catalyzed dissociation, in contrary of some complexes formed by linear ligands like **DTPA**.<sup>162</sup>

As it is mentioned above, the concentration of  $\text{Cu}^{2+}$  ions did not play any role in the complex dissociation, so we plotted the dependency of the rate constants  $k_{\text{obs}}$  in function of the proton concentration (Figure 68).

The fitting of the experimental data as well as the quadratic dependency of  $k_{\text{obs}}$  with the proton concentration indicate that  $K_{\text{H}}[\text{H}^+] + K_{\text{H}}K_{\text{H}}^{\text{H}}[\text{H}^+]^2 \ll 1$ . Then, in

## Chapter 5

our case, Equation 8 that describes all possible dissociation pathways can be simplified to Equation 9.

$$k_{obs} = k_0 + k_1[H^+] + k_2[H^+]^2 \quad \text{Equation 9}$$

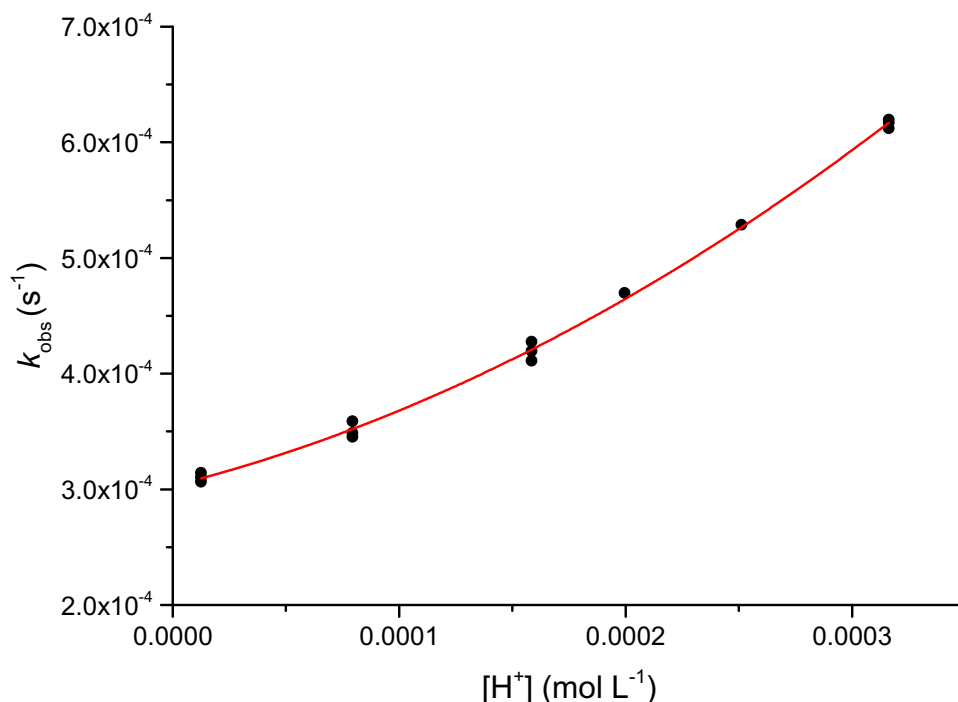


**Figure 68.**  $k_{obs}$  values for the exchange reaction of **Gd(L2)** in function of proton concentration. The red line represents the linear fit using Equation 9.

In Figure 68 we can observe that the fitting of  $k_{obs}$  values using Equation 9 are coherent with the experimental values. Quantitative results are shown in Table 12. In this Table, the dissociation constants from some relevant and related ligands studied before in the literature are shown too.

Three different rate constants were determined for the exchange reaction of **Gd(L2)** with  $\text{Cu}^{2+}$ . The spontaneous dissociation characterized by  $k_0$  was found to be  $3 \cdot 10^{-4} \text{ s}^{-1}$ . It cannot be compared with the values of analogous complexes because usually this constant value is zero, or its standard deviation is higher than itself. In our case, the standard deviation found was acceptable. The monoprotonated and diprotonated dissociations are characterized by  $k_1$  and  $k_2$  that

contain the kinetic rates constants  $k_H$  and  $k_H^H$ , respectively. The value of  $k_1$  is  $0.49 \text{ M}^{-1} \text{ s}^{-1}$  and  $k_2$  is  $1583 \text{ M}^{-1} \text{ s}^{-2}$  and their standard deviations are acceptable ( $\leq 10\%$ ).

**Table 12.** Dissociation rate constants of **Gd(L2)** and their s.d., as well as the constants of some relevant ligands used in  $\text{Gd}^{3+}$  complexes as MRI contrast agents.

162,172,173,175

	<b>L2</b>	<b>Py<sup>a</sup></b>	<b>DTPA</b>	<b>Cddadpa</b>	<b>DO3A</b>
$k_0 (\text{s}^{-1})$	$3.0 \cdot 10^{-4} \pm 3.5 \cdot 10^{-6}$	-	-	-	-
$k_1 (\text{M}^{-1} \text{s}^{-1})$	$0.49 \pm 0.05$	0.17	0.58	0.016	0.023
$k_2 (\text{M}^{-1} \text{s}^{-2})$	$1583 \pm 151$	520	$9.7 \cdot 10^4$	-	-
$k_3^{\text{Cu}} (\text{M}^{-1} \text{s}^{-1})$	-	-	0.93	$6.8 \cdot 10^{-4}$	-

Dissociation rate constants of Gd complexes using  $\text{Cu}^{2+}$ . <sup>a</sup>  $\text{Eu}^{3+}$  was used as exchanging metal ion.

The rate constant  $k_1$  of **Gd(L2)** complex is almost three times higher than the values measured for the analogous **Gd(Py)** complex, and much higher than **Gd(Cddadpa)** and **Gd(DO3A)**, complexes with high kinetic inertness. Gratefully, it is a little lower than the constant for **Gd(DTPA)**. The constant  $k_2$  that characterizes the diprotonated dissociation of the complex is also higher than the one for **Gd(Py)** and much lower than **Gd(DTPA)**. For **Gd(Cddadpa)** and **Gd(DO3A)** this constant was not observed, or it was found to be almost zero.

As explained above, the use of up to 40 equivalents the endogenous  $\text{Cu}^{2+}$  ion does not affect the dissociation process of **Gd(L2)** in contrast to **Gd(DTPA)** under same conditions. Under physiological conditions, the dissociation of **Gd(DTPA)** occurs mostly by  $\text{Zn}^{2+}$  or  $\text{Cu}^{2+}$  transmetallation, which is not important for **Gd(L2)**, and also the proton assisted dissociation of **Gd(L2)** is smaller.<sup>162</sup> The lower basicity of **Gd(L2)** could explain the difference between both complexes.

. **Gd(DTPA)** was approved as MRI contrast agent for United States Food and Drugs Administration for medical applications. Therefore, **Gd(L2)**'s *in vivo*

toxicity should be at least lower than **Gd(DTPA)** since toxicity should be directly proportional to the thermodynamic stability combined with kinetic inertness.<sup>202,203</sup> Then, we can conclude that **Gd(L2)** could be used safely and without risk for healthy patients (Most contrast agents are contraindicated for patients with kidney diseases).<sup>204</sup>

### 5.3.4 Luminescence studies for determining $q$

Luminescence spectroscopy was carried out to analyze the number of water molecules coordinated to the metal ion,  $q$ . The determination of this parameter in aqueous solution is essential to comprehend the features that rule the relaxivity since the inner sphere proton relaxivity is linearly proportional to  $q$ .<sup>133</sup> There are different methodologies to obtain  $q$  for lanthanide complexes, but none of them can be applied directly to  $Gd^{3+}$  complexes with accuracy.

The most widely method used for determining the hydration number of lanthanide complexes is luminescence spectroscopy by measuring the luminescence lifetimes of solutions of  $Eu^{3+}$  and  $Tb^{3+}$  chelates.<sup>205</sup> Most of lanthanide ions present luminescence, but some of them have higher emission due to the energetic differences between the excited and the ground state of each one.  $Eu^{3+}$  and  $Tb^{3+}$  are the most used, because their emission is in the visible range and their luminescence lifetimes are long, in contrast to  $Gd^{3+}$ .<sup>140,206</sup>  $Eu^{3+}$  and  $Tb^{3+}$  are neighbors of  $Gd^{3+}$  in the periodic table, so they have very similar ionic radius, thus, this methodology applied to their chelates should provide a good estimation for the hydration number of the corresponding  $Gd^{3+}$  complex.

Horrocks and Sudnick<sup>207,208</sup> proposed a method that consists in the measurement of luminescence lifetimes of excited states of  $Eu^{3+}$  and  $Tb^{3+}$  in separated solutions of  $H_2O$  and  $D_2O$ . OH oscillators of coordinated water molecules provide an efficient non-radiative pathway for deexcitation of the excited state of the lanthanide ion. These oscillators act independently, and OD oscillators of coordinated  $D_2O$  molecules are more inefficient to achieve this deexcitation. This difference between the efficiency of both oscillators is directly related with the number of water molecules coordinated to the lanthanide ion. The following empiric

equation (Equation 10) is used to calculate  $q$  from the differences of luminescence decay lifetimes in  $\text{H}_2\text{O}$  and  $\text{D}_2\text{O}$ ,  $\tau_{\text{H}_2\text{O}}$  and  $\tau_{\text{D}_2\text{O}}$ , respectively.

$$q = A \left( \frac{1}{\tau_{\text{H}_2\text{O}}} - \frac{1}{\tau_{\text{D}_2\text{O}}} - B \right)$$

Equation 10

Where  $A$  is a specific constant for each lanthanide ion related to the efficiency of this ion to deexcitation, and  $B$  is a correction factor when polyaminopolycarboxylate-based ligands are used. These empirical constant take values of  $A = 1.2$  and  $B = 0.25$ <sup>209</sup> or  $A = 1.11$  and  $B = 0.31$ <sup>210</sup> both for  $\text{Eu}^{3+}$ .

In this thesis, the luminescence decay lifetimes of **Eu(L1)** and **Eu(L2)** have been recorded to study the number of water molecules directly coordinated to the metal,  $q$ . Then, the results will give us a robust estimation of this values in **Gd(L1)** and **Gd(L2)**. First, the absorption, emission and excitation spectra of **Eu(L2)** were recorded to know the maximum wavelength where the decay lifetime would be registered. The absorption spectrum of **L2** and **Eu(L2)**, as well as the emission and excitation spectra of **Eu(L2)** are shown in Figure 69.

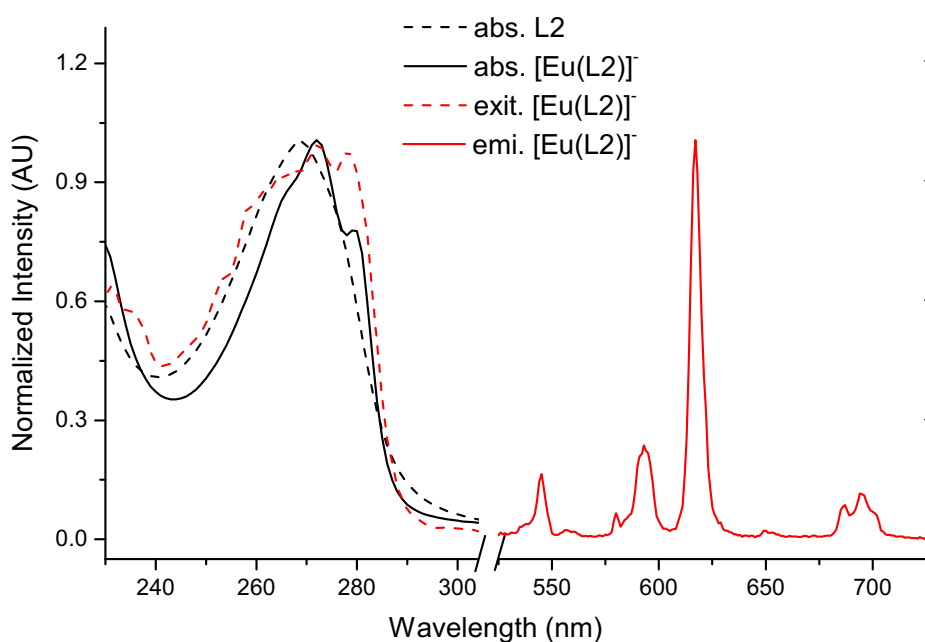


**Figure 69.** Absorption spectra of **L2**, and absorption, excitation and emission spectra of **Eu(L2)**. (0.21 mM EuL, 0.1 M Hepes buffer, pH = 7, 25 °C).



## Chapter 5

Absorption spectra showed a single band due to the combination of  $\pi$ - $\pi^*$  and  $n$ - $\pi^*$  transitions of the picolinate function. The maximum in the excitation spectrum is at 272 nm. The picolinate function is used to produce a more efficient excitation, so then a higher emission of  $\text{Eu}^{3+}$  is obtained. **Eu(L1)** does not have a picolinate function or any other UV-Vis chromophore, so the excitation was performed directly through the  $\text{Eu}^{3+}$  ion at 396 nm. The emission spectra of  $\text{Eu}^{3+}$  complexes showed  $^5\text{D}_0 \rightarrow ^7\text{F}_J$  ( $J = 0 - 4$ ) transitions with maxima at 616 nm expected for this metal ion. Then, the decay of the emission intensity was recorded at 616 nm, following an excitation at 272 nm for the **Eu(L2)** and at 396 nm for the **Eu(L1)**. The direct excitation of the metal at 396 nm in the **Eu(L2)** gave similar results. In Figure 70 the time-dependence of the emission intensity of **Eu(L1)** and **Eu(L2)** is shown.

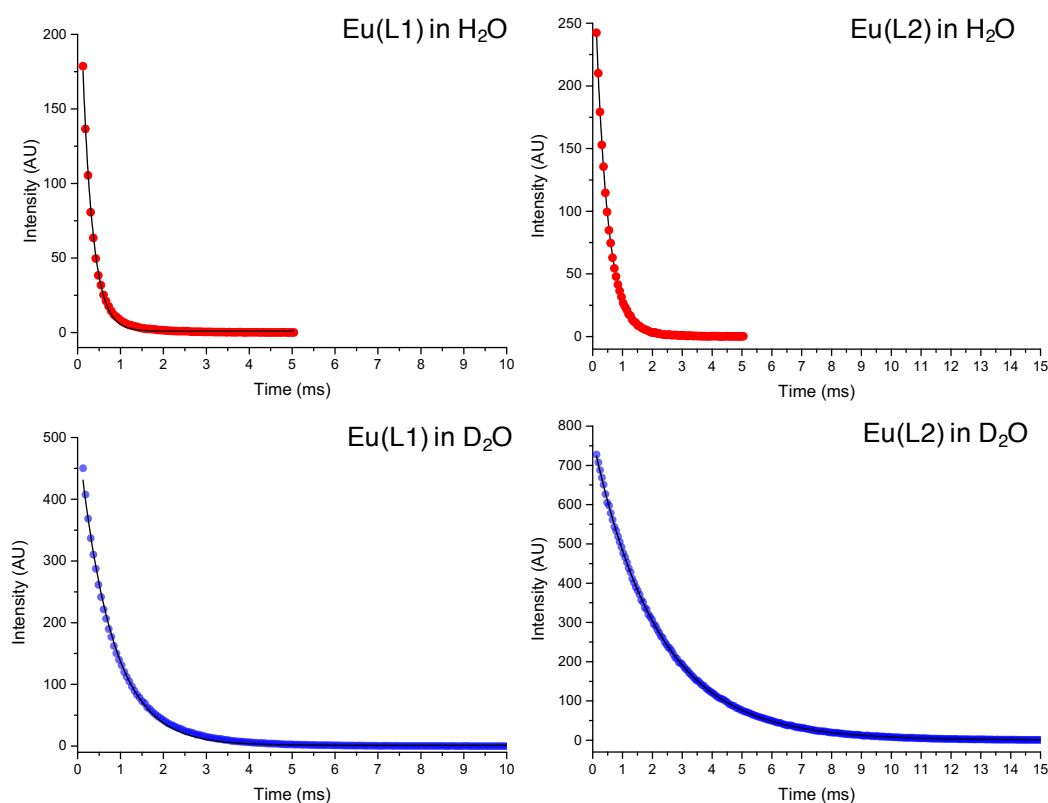


**Figure 70.** Time-dependence on luminescence intensity of **Eu(L1)** (left) and **Eu(L2)** (right) in  $\text{H}_2\text{O}$  (red) and  $\text{D}_2\text{O}$  (blue). Concentrations of complexes were 0.21 mM, 0.1 M HEPES buffer, pH, pD = 7, 25 °C. Monoexponential fits are in black.

In Figure 70, it is shown that the decay of the intensity of the emission in H<sub>2</sub>O is much faster than in D<sub>2</sub>O, because the O-H oscillator is more efficient than the O-D oscillator. These curves were fitted using the exponential fit to obtain the number of molecules directly coordinated to Eu<sup>3+</sup>. Luminescence lifetimes and  $q$  values are shown in Table 13.

**Table 13.** Luminescence lifetimes ( $\tau$ ) of **Eu(L1)** and **Eu(L2)** complexes and number of water molecules coordinated ( $q$ ) to Eu<sup>3+</sup> ion.

Complex	$\tau_{\text{H}_2\text{O}}$ (ms)	$\tau_{\text{D}_2\text{O}}$ (ms)	$q^a$	$q^b$
<b>[Eu(L1)]<sup>+</sup></b>	0.241	0.760	3.1	2.8
<b>[Eu(L2)]<sup>+</sup></b>	0.405	2.16	2.1	1.9

$q$  obtained from <sup>a</sup>Equation 10 with A = 1.2 and B = 0.25.  $q^b$  Equation 10 with A = 1.11 and B = 0.31.

As explained above, the luminescence lifetime values in D<sub>2</sub>O are much higher than those in H<sub>2</sub>O. The hydration values ( $q$ ) obtained with Beeby's constants<sup>209</sup> are a slightly higher than 3 and 2 for **Eu(L1)** and **Eu(L2)**, respectively, but lower than 3 and 2 using Horrocks A and B empirical constants.<sup>210</sup> Then, we can consider that the calculated number of water molecules ( $q$ ) for **Eu(L1)** is 3 and for the **Eu(L2)** is 2, as expected.

In conclusion,  $q = 3$  for **Gd(L1)** and  $q = 2$  for **Gd(L2)** (Figure 71). Thus, we can assume that Gd<sup>3+</sup> ion in the **Gd(L1)** has 9 coordinating sites, 6 of them occupied by **L1** (it coordinates 4 oxygen atoms from carboxylate functions and 2 nitrogen atoms from the tertiary amines) and the other 3 sites are occupied by water molecules. On the other hand, Gd<sup>3+</sup> ion in the **Gd(L2)** complex has 9 coordinating sites, 7 of them occupied by **L2** (it coordinates 4 oxygen atoms from carboxylate functions and 3 nitrogen atoms from the tertiary amines and the pyridine) and 2 water molecules.

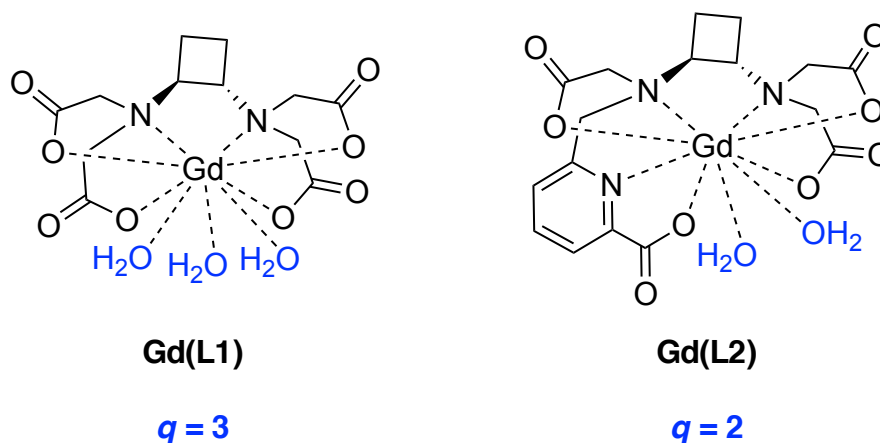


**Figure 71.** Structures and  $q$  values of **Gd(L1)** and **Gd(L2)** in water. Charges have been omitted for clarity.

#### 5.3.4.1 Anion binding studies

The replacement of water molecules by endogenous anions has been tested to investigate the potential of **Gd(L2)** in *in vivo* applications. Also, **Gd(L1)** has been studied to investigate the effect of adding a third water molecule in the first coordination sphere. Unsaturated lanthanide complexes that contain more than one inner-sphere water molecules are able to bind biological relevant anions, such as carbonate, phosphate or citrate to form ternary complexes.<sup>211,212</sup> The formation of these adducts requires a replacement of one or more Gd-bonded water molecules by the anions. The resistance to anion binding is a crucial property for retaining high relaxivity in a biological environment.<sup>213</sup> Indeed, the relaxivity will drastically decrease if one or more water molecules are displaced by an anion. For example, the relaxivity of the macrocyclic **Gd(DO3A)** complex, which contains 2 water molecules, decreases to the half in the presence of different anions.<sup>214</sup> However, several Gd linear complexes with two water molecules like **Gd(HYD)** do not bind anions or the binding is very weak.<sup>190,215</sup> In some cases, the ability to resist the binding is due to water molecules of the inner sphere occupying non-adjacent locations around the metal.<sup>216</sup> In other cases, like **Gd(CyPic3A)** the absence of ternary complex formation with biological relevant anions is explained by the electrostatic repulsion between the negatively charged complex and the anions.<sup>174</sup>

The structure of **Gd(L2)** is analogous to **Gd(CyPic3A)**, so beforehand we could expect the same behavior.

There are different methodologies to study the anion binding, like measuring the relaxivity or the luminescence decay lifetimes in the presence of different equivalents of anions. In this thesis, the formation of ternary complexes between **Gd(L1)** or **Gd(L2)** and carbonate and phosphate has been studied by measuring the luminescence lifetime of their related  $\text{Eu}^{3+}$  complexes in  $\text{H}_2\text{O}$  and  $\text{D}_2\text{O}$ . We have chosen carbonate and phosphate because they are generally responsible for the relaxivity decrement in biological media. Furthermore, they interact with the metal ion in a different manner; phosphate has been demonstrated to interact in a monodentate way, while carbonate interacts in a bidentate manner. The decay of the emission intensity of **Eu(L1)** and **Eu(L2)** in the presence of 10 and 50 equivalents of carbonate and phosphate were independently recorded in  $\text{H}_2\text{O}$  and  $\text{D}_2\text{O}$ . 50 equivalents of carbonate or phosphate are above the physiological concentrations of this anions in human plasma. The conditions were the same that those in section 5.3.4 for determining the  $q$  in the absence of anions, but in this case, the pH was shifted to 7.4. In Table 14,  $q^a$  values in the absence and presence of phosphate and carbonate are shown, and in Figure 72,  $q$  is plotted in function of the anion equivalents for an easier visualization.

**Table 14.**  $q^a$  Values of **Eu(L1)** and **Eu(L2)** in the absence and the presence of 10 and 50 equivalents of phosphate and carbonate, respectively.

Complex	$q^a$ values				
	EuL	phosphate		carbonate	
		10 eq	50 eq	10 eq	50 eq
<b>[Eu(L1)]<sup>-</sup></b>	3.1	2.4	2.4	2.0	2.1
<b>[Eu(L2)]<sup>-</sup></b>	2.1	2.2	2.1	2.1	2.0

$q^a$  obtained from Equation 10 with  $A = 1.2$  and  $B = 0.25$ . 0.21 mM EuL, 0.1 M Hepes buffer, pH, pD = 7.4, 25 °C

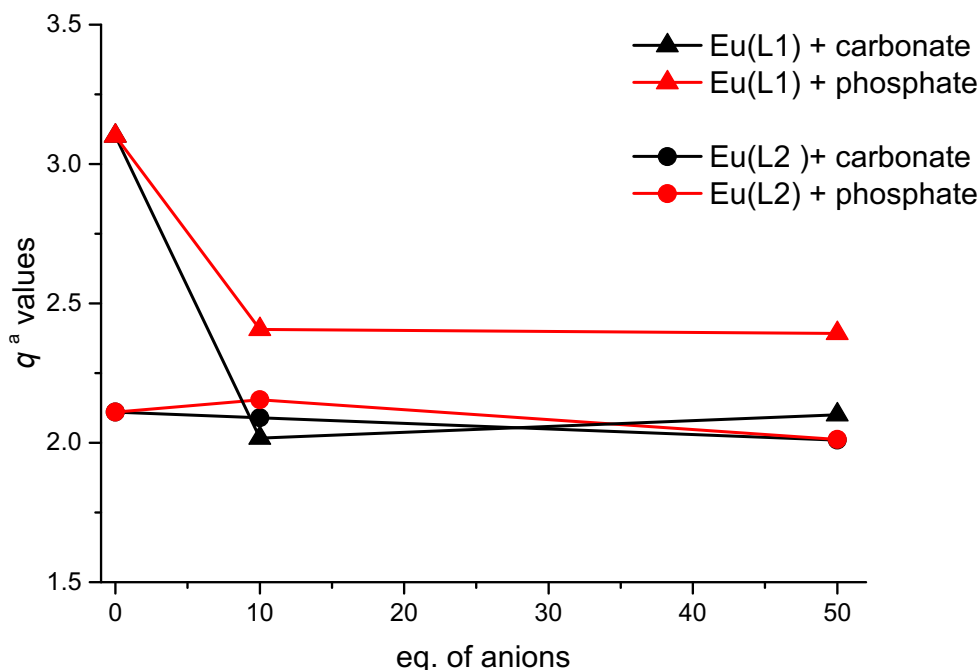


**Figure 72.**  $q^a$  values of **Eu(L1)** (triangles) and **Eu(L2)** (circles) in the absence and presence of different equivalents of carbonate (black) and phosphate (red).

The resulting  $q$  values of **Eu(L2)** did not show any decrease with the addition of 10 and 50 equivalents of phosphate or carbonate. This result excludes the formation of ternary  $\text{Eu}^{3+}$  complexes with these anions. So, we could expect the same behavior in the analogous **Gd(L2)** complex, making this complex suitable for biological experiments without suffering any relaxivity decrease. On the contrary, the number of water molecules of the **Eu(L1)** complex decreased 22% when phosphate was added and up to 35% in the presence of carbonate. In this case, we observed the same behavior using 10 or 50 equivalents, so the concentration of the anion molecule doesn't play a key role. Then, the presence of anions at any concentration would decrease the relaxivity in the analogous **Gd(L1)** complex.

The reduction of  $q$  value of **Eu(L1)** complex in the presence of carbonate or phosphate compared to the maintenance of the  $q$  value for **Eu(L2)** is very

interesting. Both complexes have the same negative charge (one negative), preventing the interaction with anions. **Eu(L2)** has one picolinate moiety which could change the distribution of the charge density but not the global charge. So, we could hypothesize that the reason of the different behavior of both complexes could be the structural location of the water molecules in the complexes (Figure 73).

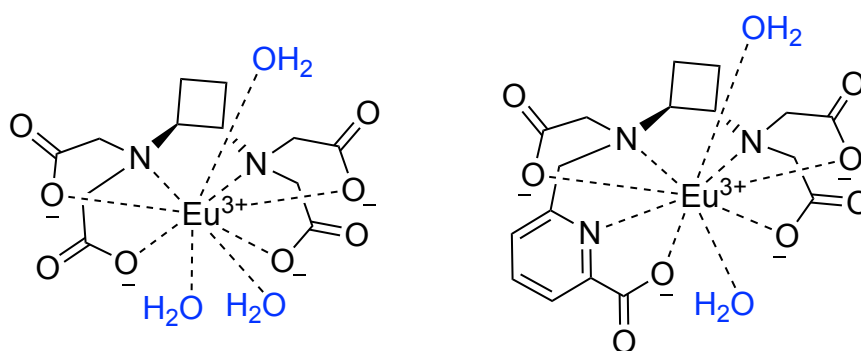


**Figure 73.** Proposed relative location of water molecules in the structure of **Eu(L1)** and **Eu(L2)** in water.

As remarked in Figure 73, one possible explanation could be that the two water molecules in the **Eu(L2)** complex are separated, occupying non-adjacent positions in the structure of the complex, preventing the binding of bidentate anions like carbonate. When the third water molecule is added in the **Eu(L1)** complex, this water could be located close to another water molecule. This could explain why the  $q$  value of **Eu(L1)** is smaller in the presence of carbonates (that binds in a bidentate manner) than in the presence of phosphate anions.

We wanted to study the structure of **Eu(L1)** and **Eu(L2)** complexes, as well as the **Gd(L1)** and **Gd(L2)** by X-ray diffraction analyses, in order to get more insight of the relative position of the water molecules in the complex. Unfortunately, unsuitable crystals were obtained.

### 5.3.5 Relaxivity studies

As mentioned in the Introduction of this chapter, the efficiency of a contrast agent (CA) for magnetic resonance imaging is described with its relaxivity ( $r_1$ ), which is defined as the enhancement of the longitudinal relaxation rate of the water protons per millimol per liter of paramagnetic compound (see Equation 1).

The relaxivity is governed by different physico-chemical parameters, including electron relaxation parameters, rotational correlation times and water exchange rate. To ensure robust results, it is convenient to estimate these parameters independently. In this part of the thesis, the relaxivity and the parameters that influence it for **Gd(L1)**, **Gd(L2)**, and **Mn(L1)** have been studied by proton nuclear magnetic relaxation dispersion ( $^1\text{H}$  NMRD) profiles and temperature-dependent  $^{17}\text{O}$  NMR. The mentioned physico-chemical parameters were calculated using simultaneously the data of both techniques. In the following pages, the results of both techniques are explained and after the resulting determined physico-chemical parameters are discussed.

#### 5.3.5.1 NMRD Profiles

$^1\text{H}$  NMRD profiles represent the dependence of the relaxation rates or relaxivity in function of the applied magnetic field ( $B_0$ ) or the Larmor frequency in a logarithmic scale. The relaxivity of a proton spin is function of several parameters, like temperature, sample composition, pressure and magnetic field. NMRD profiles are useful tools to separate the interaction mechanisms and dynamics that influence the relaxation. All the equations and parameters that describes the relaxivity are explained in detail in section 7.14.

NMRD profiles of **Gd(L1)**, **Gd(L2)** and **Mn(L1)** were recorded in aqueous solution at 25 °C, 37 °C and 50 °C in the frequency range of 0.04 to 80 MHz, that corresponds to magnetic fields of  $9.4 \cdot 10^{-4}$  T to 1.9 T. An extra amount of ligand (more than 1:1 metal-ligand ratio) was added to the solutions of metal complexes to ensure the complete complexation and avoid the presence of free  $\text{Gd}^{3+}$  or free  $\text{Mn}^{2+}$  ions. The  $^1\text{H}$  NMRD profiles of **Gd(L1)** and **Gd(L3)** are shown in Figure 74 and Figure 75.

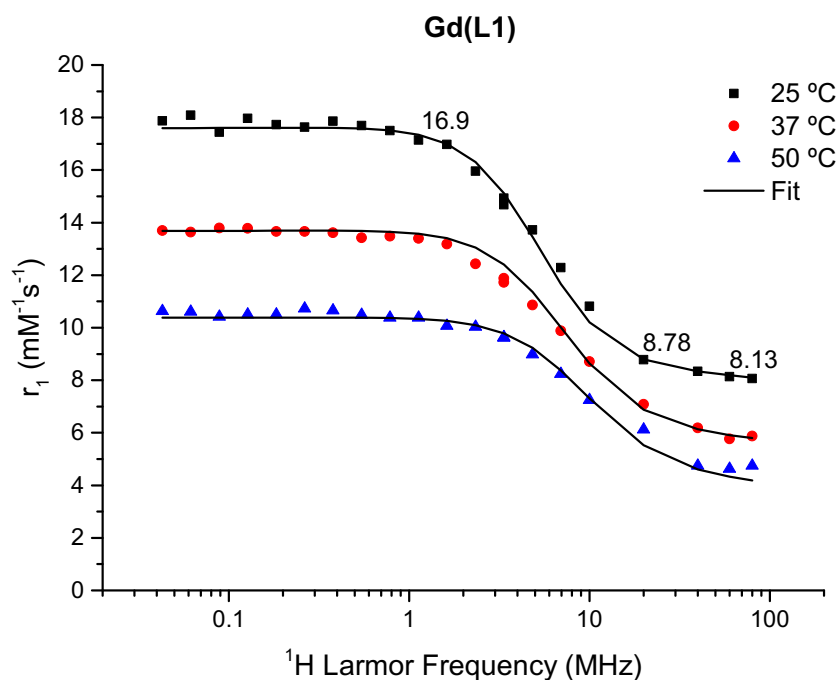


**Figure 74.** NMRD profiles of 1.88 mM **Gd(L1)** + 6% **L1** at 25 °C (black), 37 °C (red) and 50 °C (blue) at pH = 7. Black curves represent the simultaneous fit.

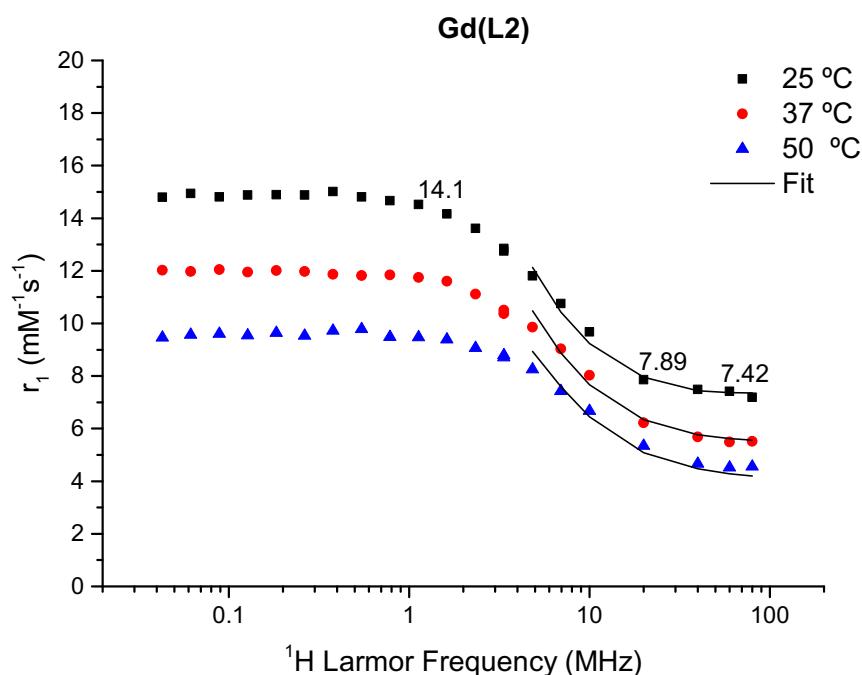


**Figure 75.** NMRD profiles of 1.91 mM **Gd(L2)** + 5% **L1** at 25 °C (black), 37 °C (red) and 50 °C (blue) at pH = 7. Black curves represent the simultaneous fit.

The NMRD profiles and the values of relaxivities of **Gd(L1)** and **Gd(L2)** are coherent with three and two water molecules in the inner sphere, respectively



## Chapter 5

(Table 15). The relaxivity values decrease with the temperature, which is consistent with a faster rotation of the complex at higher temperatures, being the limitant factor of the relaxivity. The shapes of the NMRD curves for **Gd(L1)** and **Gd(L2)** are typical for small and non-macromolecular  $Gd^{3+}$  chelates as we expected. Relaxivity values are constant at low Lamor frequency, and at higher values than 1 MHz,  $r_1$  starts to diminish until approximately 60 MHz, where the values are almost constant again. The fitting with the Solomon-Bloembergen and Morgan (SBM) theory are represented in black curves, and explained in section 5.3.5.1. The relaxivity values of **Gd(L1)** and **Gd(L2)** were compared with those values of some relevant and related ligands from the literature (Table 15).

**Table 15.** Relaxivity values of **Gd(L1)** and **Gd(L2)**, and Gd complexes from the literature.<sup>163,173,174</sup>

Field and $q$	Gd(L1)	Gd(L2)	Gd(CyPic3A)	Gd(HYD)	Gd(DTPA)
20 MHz <sup>a</sup>	8.78	7.86	8.3	7.71	4.3
60 MHz <sup>b</sup>	8.13	7.42	7.9	-	-
$q$	3	2	2	2	1

$r_1$  values in  $mM^{-1}s^{-1}$  at 25 °C. <sup>a</sup> 0.47 T. <sup>b</sup> 1.4 T.

Coherently, the relaxivity of **Gd(L1)** is 0.92 units higher at 20 MHz than **Gd(L2)** because it has one more water molecule coordinating in the inner sphere. This difference is even smaller at 60 MHz. The relaxivity of a  $Gd^{3+}$  complex with one water molecule, which it is usually around  $4 mM^{-1}s^{-1}$  at 25 °C, can be doubled by adding a second water molecule by modifying the structure of the ligand. If a third water molecule is added, the relaxivity will increase a little bit more, but not the double, and more importantly, the stability and the inertness of the complex will decrease significantly. So, globally, it is not worth designing complexes with three water molecules in the inner sphere, and we could suggest that the optimal hydration number for a small complex is two.

Comparing the relaxivity of **Gd(L2)** with the values of analogous complexes we can observe that the relaxivity is similar. The relaxivity of **Gd(L2)** at 20 MHz and 25 °C is 0.15 units higher than **Gd(HYD)**, but lower than **Gd(CyPic3A)**. **Gd(CyPic3A)** has a cyclohexane unit in its structure instead of a cyclobutane, and it presents 0.44 units higher relaxivity than **Gd(L2)**. So, in this case, the cyclobutane unit does not favor the relaxivity compared with a cyclohexane bridge. Unfortunately, there is no information about the rotational correlation times or electron-spin relaxation rates of **Gd(CyPic3A)** in the literature, so we cannot rationalize the differences between the relaxivity of both complexes.

The  $^1\text{H}$  NMRD profiles of **Mn(L1)** are shown in Figure 76.

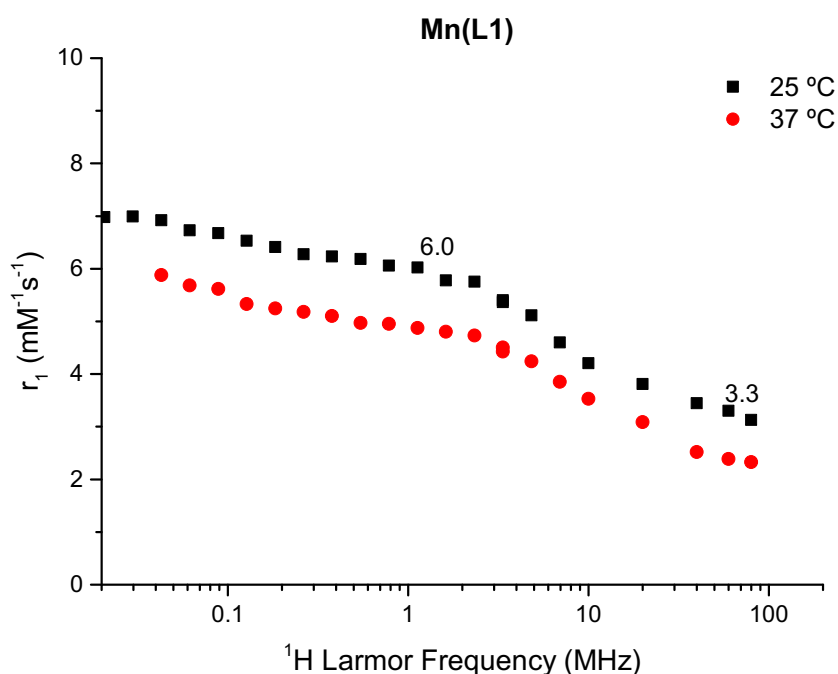


**Figure 76.** NMRD profiles of 3.29 mM **Mn(L1)** + 15% **L1** at 25 °C (black) and 37 °C (red) at pH = 7.4.

Even the  $^1\text{H}$  NMRD profiles of **Mn(L1)** are coherent with one water molecule in the inner sphere, the profiles were not as we expected. At low magnetic fields the relaxivity values are not constant and they still increase at lower magnetic fields. This effect could be explained by the presence of free  $\text{Mn}^{2+}$ . For that reason, we repeated the experiments adding an extra 5%, 10% and 15% (Figure 76) amount

## Chapter 5

of **L1** and we also increased the pH to 7.4 to avoid the presence of free  $\text{Mn}^{2+}$ . Even adding up 15% of extra amount of **L1** the same results were obtained. That fact as well as the low thermodynamic stability of **Mn(L1)** found in the potentiometric studies of this complex (section 5.3.2) could explain the presence of free  $\text{Mn}^{2+}$ . For this reason, we compared the relaxivity of **Mn(L1)** with the values for some analogous  $\text{Mn}^{2+}$  complexes from the literature to investigate if **Mn(L1)** relaxivity is higher to find other evidence of free  $\text{Mn}^{2+}$  (Table 16).

**Table 16.** Relaxivity values of **Mn(L1)**, and **Mn(EDTA)**, **Mn(CDTA)** and **Mn(CyPy3A)** from the literature.<sup>155,217</sup>

Temperature	Mn(L1)	Mn(EDTA)	Mn(CDTA)	Mn(CyPy3A)
25 °C	3.3	-	-	2.8
37 °C	2.4	2.2	2.1	2.1
<i>q</i>	1	1	1	1

$r_1$  values in  $\text{mM}^{-1}\text{s}^{-1}$  at 60 MHz or 1.4 T

The relaxivity of **Mn(L1)** at 25 °C is  $3.3 \text{ mM}^{-1}\text{s}^{-1}$  and it is 0.5 units higher than **Mn(CyPy3A)** at the same temperature. Increasing the temperature, the relaxivity of **Mn(L1)** decreases to  $2.4 \text{ mM}^{-1}\text{s}^{-1}$  and it is more similar but still higher than the values of **Mn(EDTA)**, **Mn(CDTA)** and **Mn(CyPy3A)**. This comparison and the evidence that the thermodynamic stability of **Mn(L1)** is the lowest of all the table could be another confirmation of the presence of free  $\text{Mn}^{2+}$ . It should be remarked that looking at the NMRD profile and comparing the  $r_1$  values, the proportion of free  $\text{Mn}^{2+}$  could be very small, even less than 1%. Notwithstanding, free  $\text{Mn}^{2+}$  is toxic at very low concentrations and safe contrast agents should avoid any presence of this cation. These results suggested that **Mn(L1)** is not interesting for clinical applications.

### 5.3.5.2 $^{17}\text{O}$ NMR studies

$^{17}\text{O}$  NMR variable temperature measurements are used to evaluate the parameters that describe the water exchange rate and rotational dynamics on paramagnetic complexes. Equations and parameters that describes  $^{17}\text{O}$  NMR are explained in detail in 7.15.

In  $^{17}\text{O}$  NMR experiments, the transverse and longitudinal  $^{17}\text{O}$  relaxation rates,  $1/T_1$ ,  $1/T_2$ , and the  $^{17}\text{O}$  chemical shifts,  $\omega$ , are independently measured from samples containing the paramagnetic compound and from a reference, such as acidic water or a diamagnetic compound. The differences of these parameters between the sample and the reference are named reduced transverse or longitudinal  $^{17}\text{O}$  relaxation rate,  $1/T_{1r}$ ,  $1/T_{2r}$  and  $^{17}\text{O}$  reduced chemical shift,  $\Delta\omega_r$ .

The  $^{17}\text{O}$  NMR measurements are done at different temperatures because there are different water exchange kinetics at different temperature ranges. In the slow exchange region, the reduced transverse relaxation rates increase with temperature. In this region, the water exchange rate,  $k_{ex}$ , is determined by  $1/T_{2r}$ . In the fast exchange rate region at high temperatures,  $T_{2r}$  decreases with temperature and it is determined by  $1/T_{2m}$ , which is the transverse relaxation rate of the coordinated water. Sometimes, the inflection point of these two different kinetic regions can be observed in the working temperature range of this method (273-373 K).

The longitudinal and transverse  $^{17}\text{O}$  relaxation rates ( $1/T_1$ ,  $1/T_2$ ) and the chemical shifts were measured at 9.36 T in aqueous solutions of **Gd(L1)**, **Gd(L2)** and **Mn(L1)** in a temperature range of 275-348 K. Longitudinal  $^{17}\text{O}$  relaxation rates ( $1/T_1$ ) data were not used because the differences between the paramagnetic solutions and the references were not high enough to get reproducible results. It is common for diluted systems at high magnetic fields. Nevertheless, the transverse  $^{17}\text{O}$  relaxation rates ( $1/T_2$ ) and chemical shifts data were robust and they are plotted in function of temperature in Figure 77 for **Gd(L1)** and **Gd(L2)** and in Figure 78 for **Mn(L1)**.

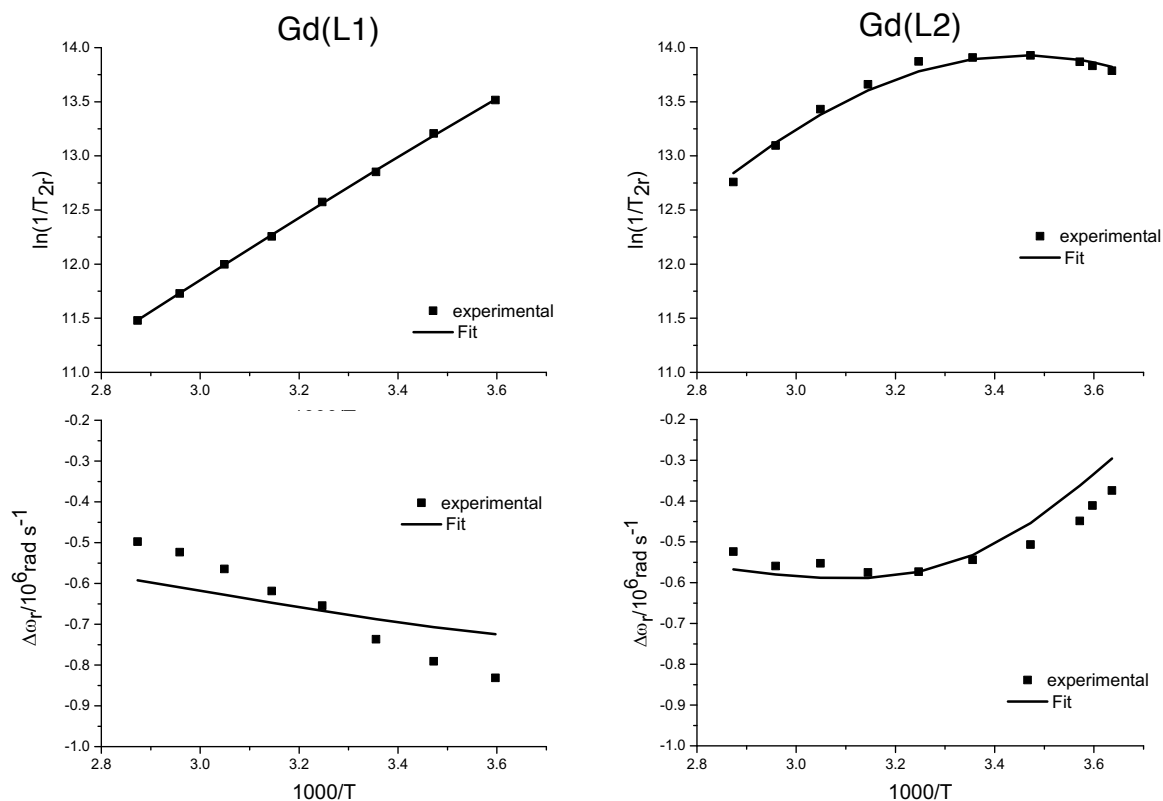


**Figure 77.** Reduced transverse  $^{17}\text{O}$  NMR relaxation rates (top) and  $^{17}\text{O}$  NMR chemical shifts (bottom) of a solution of 15.3 mM **Gd(L1)** and 14.5 mM **Gd(L2)** at pH = 6.5. The black lines represent the simultaneous fit.

In Figure 77 and Figure 78, we can observe the logarithmic dependency of the reduced transverse relaxation rates  $1/T_{2r}$  and chemical shifts with the temperature. For the **Gd(L1)** and **Mn(L1)** only the fast-kinetic region is observed, where  $T_{2r}$  decrease with temperature. The solvent limitation didn't permit to perform the experiments at lower temperature to observe the slow exchange region. On the contrary, in the  $1/T_{2r}$  and  $\Delta\omega_r$  plots of **Gd(L2)** a change over of the function associated with the two different exchange regions is observed. The fitting of these curves at the slow kinetic region allowed to determine the water exchange rate more accurately than in the cases where this region is not observed.

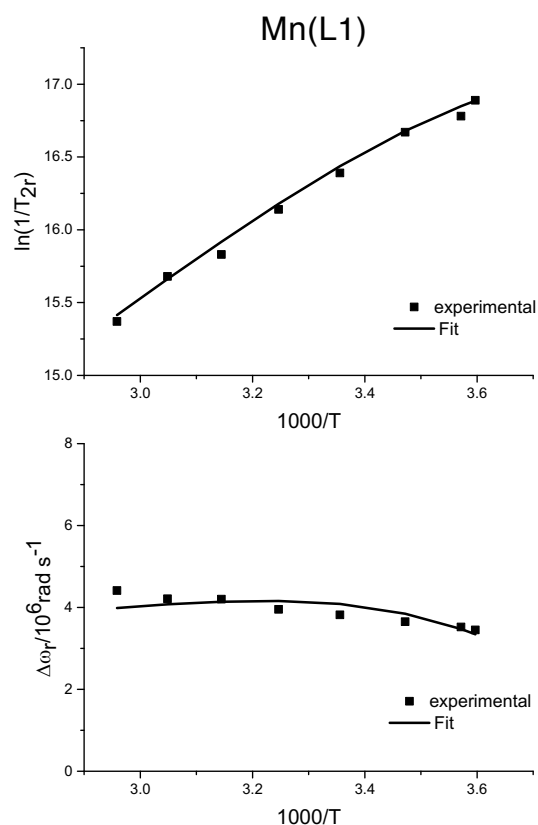


**Figure 78.** Reduced transverse  $^{17}\text{O}$  NMR relaxation rates (top) and  $^{17}\text{O}$  NMR chemical shifts (bottom) of a solution of 4.9 mM **Mn(L1)** at pH = 7.0. The black lines represent the simultaneous fit.

The black lines shown in Figure 77 and Figure 78 correspond to the simultaneous fitting of these experiments and the NMRD curves with the SBM theory. In the  $\Delta\omega_r$  curves, we noticed that the fit is slightly worse than the  $1/T_{2r}$ -fit. Moreover, at higher temperatures the fitted curves are always lower than the experimental points while at low temperatures it is the other way. For this fitting, we fixed the hydration number ( $q$ ) found in the luminescence experiments, but this value can be temperature-dependent. Usually, at high temperature, the complex tends to dehydrate and at low temperature to hydrate. Thus, in the calculations at high temperature the  $q$  values used are higher than the real ones and at low temperatures the  $q$  values used are lower. This effect could explain the differences between the fitting and the data points at high and low temperatures. Nevertheless, globally, it did not change the resulting parameters that are explained below.

### 5.3.5.3 Physicochemical parameters that rule the relaxivity

The parameters that describe the relaxivity of **Gd(L1)**, **Gd(L2)** and **Mn(L1)** complexes have been determined by analyzing simultaneously the experimental  $^1\text{H}$  NMRD and  $^{17}\text{O}$  NMR data using the Solomon-Bloembergen-Morgan (SBM) theory. Details and equations used for the least-square fitting are widely explained in section 7.14 and 7.15.

The simultaneous fitting of **Gd(L1)** was achievable at all frequencies range, but the fitting of **Gd(L2)** was not good at low Larmor frequencies, so only data up to 5 MHz were used. The simultaneous fitting of  $^1\text{H}$  NMRD and  $^{17}\text{O}$  NMR can be complicated at low magnetic fields. At that region, the electronic contribution of relaxation times is more important, but in our case, we were not interested in detailed information about electron spin relaxation. So, we used the SBM theory at medium and high Larmor frequencies, where it gives us information about dynamic processes, like rotational correlation times and water exchange rates.

In the analysis of **Gd(L1)** and **Gd(L2)**, the following parameters have been calculated: the water exchange rate ( $k_{ex}^{298}$ ), the activation enthalpy of the water exchange ( $\Delta H^\ddagger$ ), the rotational correlation time ( $\tau_{RH}^{298}$  and  $\tau_{RO}^{298}$ ) and its activation energy ( $E_R$ ), the electron spin relaxation parameters ( $\tau_V^{298}$  and  $\Delta^2$ ) and the scalar coupling constant ( $A/\hbar$ ). The diffusion constant ( $D_{GdH}^{298}$ ) and its activation energy ( $E_{GdH}^{298}$ ) were fixed to  $26 \cdot 10^{-10} \text{ m}^2\text{s}^{-1}$  and  $20 \text{ KJ mol}^{-1}$ , respectively. Also, the Gd-water oxygen ( $r_{GdO}$ ) distance was fixed to  $2.5 \text{ \AA}$ , the Gd-water proton ( $r_{GdH}$ ) distance to  $3.1 \text{ \AA}$ .<sup>218</sup> The closest approach between the outer sphere protons and the  $\text{Gd}^{3+}$  ion ( $a_{GdH}$ ) was fixed to  $3.5 \text{ \AA}$  and the quadrupolar coupling constant ( $\chi(1+\eta^2/3)^{1/2}$ ) has been set to the value of pure water, 7.58 MHz. As it was demonstrated in the luminescence experiments, hydration numbers ( $q$ ) were fixed to 3 and 2 for **Gd(L1)** and **Gd(L2)**, respectively. Furthermore, the scalar coupling constant was fixed at  $-3.1 \cdot 10^6 \text{ rad s}^{-1}$  for **Gd(L1)**.<sup>147,178,219</sup>

The best fit parameters obtained from  $^{17}\text{O}$  NMR and NMRD profiles experiments are shown in Table 17. Furthermore, the parameters of the analogous complexes **Gd(HYD)** and **Gd(DTPA)** are also shown in the Table.<sup>175,220</sup>

**Table 17.** Parameters and standard deviations obtained from the simultaneous fitting  $^{17}\text{O}$  NMRD and NMRD profiles of **Gd(L1)**, **Gd(L2)**, **Gd(HYD)**, and **Gd(DTPA)**.<sup>175,220</sup>

	<b>Gd(L1)</b>	<b>Gd(L2)</b>	<b>Gd(HYD)</b>	<b>Gd(DTPA)</b>
$k_{ex}^{298}$ ( $10^6 \text{ s}^{-1}$ )	127.4±15	10.0±2.3	7.8	3.3
$\Delta H^\ddagger$ ( $\text{kJ mol}^{-1}$ )	21.7±3.6	36.1±7.3	43.5	51.6
$\tau_{RH}^{298}$ (ps)	66.0±1.7	91.9±3.4	92.6	58
$E_R$ ( $\text{kJ mol}^{-1}$ )	23.8±0.6	20.1±1.3	21.0	17.3
$\tau_V^{298}$ (ps)	14.9±2.0	2.6±0.5	2.1	
$A/\hbar$ ( $10^6 \text{ rad s}^{-1}$ )	-3.1 <sup>a</sup>	-3.0±0.4	-4.0	-3.8
$\Delta^2$ ( $10^{20} \text{ s}^{-2}$ )	0.44±0.07	0.46±0.13	0.55	
$q^a$	3	2	2	1
$\tau_{RH}/\tau_{RO}$	1 <sup>a</sup>	1 <sup>a</sup>	0.79	-

<sup>a</sup> Fixed values were used in the optimization.

The resulting fit values of water exchange rate,  $k_{ex}$ , were  $127.4 \cdot 10^6 \text{ s}^{-1}$  and  $10.0 \cdot 10^6 \text{ s}^{-1}$  for **Gd(L1)** and **Gd(L2)**, respectively, which is one order of magnitude higher for **Gd(L1)**. The complex **Gd(L1)** has three water molecules in the inner sphere and it explains the higher  $k_{ex}$  value, being within the same order of magnitude as the  $\text{Gd}(\text{H}_2\text{O})_8^{3+}$  ion ( $800 \cdot 10^6 \text{ s}^{-1}$ ). On the contrary, the calculated values of rotational correlation time,  $\tau_{RH}^{298}$ , were 66 and 91.9 ps, for **Gd(L1)** and **Gd(L2)**, respectively. In this case, this value is higher for **Gd(L2)** because its ligand is bigger due to the presence of the picolinate function. The electron-spin parameter  $\tau_V^{298}$  is one order of magnitude higher for **Gd(L1)**, but same values of  $\Delta^2$  were found. The small differences in the relaxivity of **Gd(L1)** and **Gd(L2)** are explained because the higher values  $k_{ex}$  and  $\tau_V^{298}$  of **Gd(L1)** are counteracted by the lower value of  $\tau_{RH}^{298}$  compared with **Gd(L2)**. So, as commented before, the incorporation of a third water molecule in the inner sphere of the complex is not worth it, because it favors



## Chapter 5

a faster water exchange rate but lowers the rotational correlation time and resulting similar values of relaxivities.

The analysis of the data of **Gd(L2)** shows some similar results to the parameters of the **Gd(HYD)** complex.<sup>223</sup> The rotational correlation time ( $\tau_{RH}^{298}$ ) and its activation energy ( $E_R$ ) have almost the same values, due to the similar size and molecular weight of both complexes. Also, the electron-spin parameters ( $\tau_V^{298}$  and  $\Delta^2$ ) are within the same magnitude order. The major differences between these two complexes are in the values of water exchange rate, that is  $2.2 \cdot 10^6 \text{ s}^{-1}$  units higher for **Gd(L2)**. The similitude of these parameters and the slightly higher water exchange rate found for **Gd(L2)** explain the slightly higher relaxivity of our complex compared with **Gd(HYD)**.

Comparing the parameters found for the **Gd(L2)** complex with the values of some approved and commercial contrast agents such as **Gd(DTPA)** and **Gd(DOTA)** we can observe that our complex values are optimized.<sup>176</sup> The water exchange rate of **Gd(L2)** is three times higher than the value of **Gd(DTPA)** and two times higher than **Gd(DOTA)** ( $k_{ex} = 4.1 \cdot 10^6 \text{ s}^{-1}$ ).<sup>133</sup> Furthermore, the rotational correlation time of **Gd(L2)** is around 1.5 times higher than **Gd(DTPA)** and similar than **Gd(DOTA)** (77 or 90 depending on the optimization).<sup>220</sup> These results could conclude that changes in the ligand structures can notably modify the physico-chemical parameters of their corresponding complexes.

The analysis of **Mn(L1)** was carried out a little bit differently. The NMRD profiles of this complex were not good enough for the fitting of the SBM theory, and only the  $^{17}\text{O}$  NMR data was used. For that reason, only the water exchange rate ( $k_{ex}^{298}$ ) and its the activation enthalpy ( $\Delta H^\ddagger$ ), and the scalar coupling constant ( $A/\hbar$ ) were calculated. The  $1/\tau_{s1}^{298}$  parameter, which is the sum of the of  $k_{ex}$  and  $1/T_{1e}$ , and the hydration number ( $q$ ) were fixed.

The best fit parameters obtained  $^{17}\text{O}$  experiments with **Mn(L1)** are shown in Table 18. Furthermore, the parameters of some analogous complexes from the literature are also shown.<sup>155</sup>

**Table 18.** Parameters and standard deviations obtained in the fitting of  $^{17}\text{O}$  NMR of **Mn(L1)**, **Mn(EDTA)**, **Mn(CDTA)** and **Mn(PyC3A)**.<sup>155</sup>

	<b>Mn(L1)</b>	<b>Mn(EDTA)</b>	<b>Mn(CDTA)</b>	<b>MnPyC3A</b>
$k_{ex}^{298}$ ( $(10^6 \text{ s}^{-1})$ )	247.8±11.5	590 <sup>b</sup>	270 <sup>b</sup>	100 <sup>b</sup>
$\Delta H^\ddagger$ (kJ mol <sup>-1</sup> )	21.5±1.8	36.7	35.8	37.2
$A/\hbar$ ( $10^6 \text{ rad s}^{-1}$ )	37.1±0.6	37.9	31.4	28.7
$1/\tau_{s1}^{298}$ ( $10^6 \text{ kJ mol}^{-1}$ ) <sup>a</sup>	30	-	-	-
$q^a$	1	1	1	1

<sup>a</sup> Fixed values were used in the optimization. <sup>b</sup> water exchange rate at 310 K.

The scalar coupling constant of **Mn(L1)** is equal to the constant of **Mn(EDTA)** and similar to the values of the others  $\text{Mn}^{2+}$  complexes, indicating that our calculations were robust. The calculated water exchange rate of **Mn(L1)** was  $247.8 \cdot 10^6 \text{ s}^{-1}$ . Even if a direct comparison with the values of **Mn(EDTA)**, **Mn(CDTA)** and **Mn(PyC3A)** is not possible because they are at different temperatures, the calculated  $k_{ex}$  for **Mn(L1)** could be acceptable. We can compare the activation enthalpy of the water exchange ( $\Delta H^\ddagger$ ), and the **Mn(L1)** value is the highest of all the Table. Although it is hard to rationalize the absolute value of this constant, our results could confirm once again, the presence of a small amount of free  $\text{Mn}^{2+}$ .

The  $1/\tau_{s1}^{298}$  parameter, which is the sum of the of the water exchange rate ( $k_{ex}$ ) and the electron-spin relaxation rate ( $1/T_{1e}$ ) was fixed to  $3 \cdot 10^{-7} \text{ s}^{-1}$ . Changing the value in the range of  $3\text{-}7 \cdot 10^{-7} \text{ s}^{-1}$  didn't change significantly the  $k_{ex}$ . The contribution of  $k_{ex}$  is the 89% of  $1/\tau_{s1}^{298}$ . It confirms that the weight of the water exchange rate in the correlation time that rules the relaxation processes is very important in the  $\text{Mn}^{2+}$  complexes, and it explains why we only observe the fast kinetics region in the  $^{17}\text{O}$  NMR experiments.



## 5.4 Summary and conclusions

In this part of the thesis, two ligands containing 1,2-cyclobutane diamines were synthesized and complexed with  $\text{Gd}^{3+}$  and  $\text{Mn}^{2+}$ . Potentiometric measurements showed that **Gd(L2)** has a high stability constant,  $K_i$  (17.4), comparable with other bishydrated  $\text{Gd}^{3+}$  complexes, while that for **Gd(L1)** is lower (14.7). Unfortunately, the thermodynamic stability of **Mn(L1)** was lower than other  $\text{Mn}^{2+}$  complexes (10.3). Thus, the incorporated picolinate function played an important role in the properties of these complexes.

The kinetic inertness of **Gd(L2)** was studied using the exchange reaction with  $\text{Cu}^{2+}$ . The spontaneous and acid catalyzed dissociation pathways were investigated, obtaining lower dissociation constants for **Gd(L2)** than those for **Gd(DTPA)**, which is a contrast agent approved for medical applications. Since toxicity is proportional to the kinetic inertness, we can assume that **Gd(L2)** could be used without risk in patients.

Luminescence experiments of analogous  $\text{Eu}^{3+}$  complexes confirmed that  $q = 3$  for **Gd(L1)** and  $q = 2$  for **Gd(L2)**. In the presence of phosphate or carbonate anions, the hydration number of **Eu(L1)** decreased while it kept constant for **Eu(L2)**. This result predicts that **Gd(L2)** relaxivity should remain constant in *in vivo* applications.

Relaxivity values ( $r_1$ ) of **Gd(L1)**, **Gd(L2)** and **Mn(L1)** were 8.78, 7.86 and 3.3  $\text{mM}^{-1}\text{s}^{-1}$  at 20 MHz and 25 °C, respectively. Overall, the incorporation of a third water molecule in **Gd(L1)** is not worthy because the stability decreases considerably. **Gd(L2)** relaxivity is similar to the values of bishydrated  $\text{Gd}^{3+}$  complexes. Unfortunately, the NMRD profiles of **Mn(L1)** suggested the presence of free  $\text{Mn}^{2+}$ , making this complex not suitable for clinical applications. The fitting of the SBM theory in  $^1\text{H}$  NMRD profiles and  $^{17}\text{O}$  NMR revealed a high water exchange rate constant,  $k_{\text{ex}}^{298}$ , ( $10 \cdot 10^6 \text{ s}^{-1}$ ) and long rotational correlation time,  $\tau_{\text{RH}}^{298}$ , (91.9 ps) for **Gd(L2)**, explaining the good relaxivity values of this complex.

Overall, results suggest that **Gd(L2)** is a good and safe candidate to be used as contrast agent for clinical MRI.



## **6. General Conclusions**

---



## 6. General Conclusions

The study of three different systems containing chiral cyclobutane-based molecules has been carried out during this thesis. The previous experience of our research group on stereoselective synthetic strategies has been used to prepare the new compounds. Many different techniques have been used to study these systems.

**Functionalized low molecular weight gelators (LMWG):** Two peptide-based LMWGs have been functionalized with a terpyridine-based moiety. These new compounds were able to gelate different solvents. The properties and morphology of these gels have been studied by SEM, CD and theoretical calculations, suggesting that the aggregation of these compounds followed a helical-like structure. These two new gelators were complexed with  $\text{Ru}^{2+}$  and  $\text{Pd}^{2+}$  to get metallogelators, but the resulting complexes were not able to gelate any solvents.  $\text{Ru}^{2+}$  complexes were tested as catalysts in epoxidation of alkenes, presenting results comparable with analogous  $\text{Ru}^{2+}$  complexes from the literature.

**Tripeptides as catalysts.** Different hybrid tripeptides containing proline and  $\beta$ - or  $\gamma$ -CBAAs residues were studied.  $\beta$ -Amino acid containing peptides presented poor reactivity and enantioselectivity, while  $\gamma$ -amino acid containing peptides gave excellent reactivity and good enantioselectivity in the aldol reaction. The absolute D or L configuration of proline was the factor controlling the enantioselectivity. Noteworthy, this enantioselectivity was reversed in the presence of water. Computational calculations indicated that a change in the geometry of the transition state could explain this reversion.

**MRI contrast agents.** Two new cyclobutane diamine-based ligands were studied and complexed with  $\text{Gd}^{3+}$  and  $\text{Mn}^{2+}$ .  $\text{Gd}^{3+}$  complexes showed suitable features as contrast agents for MRI, due to their high stability, inertness and relaxivity, mainly found for the bishydrated complex. Results were rationalized and compared with clinically approved agents, indicating that one of these new complexes is a potential candidate for medical applications. The low stability of the  $\text{Mn}^{2+}$  complex together with the results from relaxometric studies indicated that this complex is not applicable for clinical purposes.





## **7. Experimental Methodologies**

---



## 7. Experimental Methodologies

### 7.1 $^1\text{H}$ NMR and $^{13}\text{C}$ NMR spectroscopy

$^1\text{H}$  NMR and  $^{13}\text{C}$  NMR spectra were recorded at *Servei de Resonància Magnètica Nuclear* from the Universitat Autònoma de Barcelona (UAB) in Bellaterra and at *Centre de Biophysique Moléculaire (CBM)* from CNRS in Orléans, France.

The spectrometers used in the UAB were:

- AC 250 Bruker for  $^1\text{H}$  at 250 MHz and  $^{13}\text{C}$  at 62.5 MHz.
- AVANCE 360 Bruker for  $^1\text{H}$  at 360 MHz and  $^{13}\text{C}$  at 90 MHz.
- ARX 400 Bruker for  $^1\text{H}$  at 400 MHz and  $^{13}\text{C}$  at 100 MHz.
- AV 600 Bruker for  $^1\text{H}$  at 600 MHz and  $^{13}\text{C}$  at 150 MHz.

The spectrometers used in the CBM was:

- Avance III HD 600 equipped with a BBFO probe for  $^1\text{H}$  at 600 MHz and  $^{13}\text{C}$  at 150 MHz.

Chemical shifts of signals are given in ppm, using as reference the following values:

- $\text{CDCl}_3$ :  $\delta$  7.28 and 77.16 for  $^1\text{H}$  and  $^{13}\text{C}$ , respectively.
- $\text{CD}_3\text{OD}$ :  $\delta$  3.31 and 49.00 for  $^1\text{H}$  and  $^{13}\text{C}$ , respectively.
- $\text{DMSO}-d_6$ :  $\delta$  3.33 and 39.52 for  $^1\text{H}$  and  $^{13}\text{C}$ , respectively.
- $\text{D}_2\text{O}$ :  $\delta$  4.79 for  $^1\text{H}$ .
- $\text{Acetone}-d_6$ :  $\delta$  2.05 and 29.84, 206.26  $^1\text{H}$  and  $^{13}\text{C}$ , respectively.

The abbreviations used to describe multiplicity of signals are: s (singlet), d (doublet), dd (doublet of doublets), t (triplet), dt (doublet of triplets), q (quartet), p (pentet), broad s (broad singlet), broad d (broad doublet), m (multiplet, denotes complex pattern).

NMR signals were assigned with the help of DEPT, NOESY, ROESY, COSY, TOCSY, HMBC and HSQC experiments.

## 7. Experimental Methodologies

### 7.2 Infrared spectroscopy (IR)

IR spectra in solid state were recorded on a Sapphire-ATR spectrophotometer, being the signal an average of 16 scans. Peaks are reported in  $\text{cm}^{-1}$ .

### 7.3 High resolution mass spectrometry (HRMS)

HRMS were recorded at *Servei d'Ànalisi Química* from the Universitat Autònoma de Barcelona in a Bruker Squire 3000 microTOFTQ spectrometer using ESI-MS (QTOF).

### 7.4 UV spectroscopy

The UV-Vis absorption spectra were measured in the *Laboratori d'Espectroscopia Molecular* from the Universitat Autònoma de Barcelona in a Hewlett Packard 8453 spectrophotometer and in a PerkinElmer Lambda 19 spectrometer equipped with Huber ministat cc1 thermostated cell holder in Centre de Biophysique Moléculaire (CBM) from CNRS in Orleans, France. Methanol and water were used as solvents, in the region  $\lambda = 190\text{-}800$  nm with data steps of 0.5 nm, with a 1 cm path length.

### 7.5 Circular dichroism spectroscopy (CD)

#### 7.5.1 CD in solution

The sample was dissolved in MeOH or H<sub>2</sub>O and it was measured in a 1 cm width quartz cuvette. CD spectra were recorded with JASCO-715 spectropolarimeter and were processed using Spectra Manager Software. In **Table 19** the experimental conditions used for recording the spectra are shown. A systematic treatment of the obtained data was done using the mentioned software.

**Table 19.** Experimental conditions to record the CD spectra.

Parameter	Value
Range	190-500 nm
Data pitch	0.5 nm
Scanning mode	continuous
Scanning speed	50-200 nm/min
Response	1-2 sec.
Band width	2-5 nm
Accumulation	1-4

### 7.5.2 CD in xerogel phase

Xerogels were prepared following the procedure described in section 7.9. Samples discs were prepared by mixing the xerogels at around 0.020-0.025 mmol/g of KBr (1.2-1.6 wt. %) in an agate mortar and pressing the mixture for 10 minutes.<sup>72,221</sup> Homogeneous translucent disks were obtained and the CD spectra were recorded using a JASCO-715 spectropolarimeter and were processed using the associated software. Smoothing and noise elimination were applied to obtain proper spectra following a systematic treatment.

Data recording was repeated at least 3 times rotating the pellet 120° in each one to obtain representative data and to avoid macroscopic influences. Solid state CD spectra were represented by dividing the obtained signal by the number of mmols of gelator per gram of KBr. As the optical length is not known, the units of the spectrum are mdeg mmol<sup>-1</sup>. However, to compare the shape of the spectra qualitatively, normalisations of the signal respect to the highest value were done.

## 7. Experimental Methodologies

### 7.6 Scanning electron microscopy (SEM)

SEM micrographs were recorded in Quanta 200 ESEM FEG apparatus equipped with a field-emission gun (FEG) in the *Institut de Ciència de Materials de Barcelona (ICMAB)*. Wet gels were disposed on a carbon film coated copper grid and dried by standing for 30 minutes on the grid. The resulting xerogels were introduced into the microscope chamber working at 30 Pa and 5 kV. For the EDX analyses the same apparatus equipped with an Energy Dispersive X ray (EDX) system for chemical analysis was used.

### 7.7 Chromatography

#### 7.7.1 Flash chromatography

Column chromatography was performed with Scharlau™ silica gel for flash chromatography (mean pore: 60 Å; particle size: 0.04-0.06 mm, 230-400 mesh (ASTM), using nitrogen as driving gas.

Some reactions were monitored by thin-layer chromatography (TLC) using ALUGRAM™ SIL/UV<sub>254</sub> pre-coated aluminium sheets. Layer of 0.20 mm of thickness covered with silica gel 60 with fluorescent indicator UV<sub>254</sub>.

Different methods were used to visualise the spots:

- Irradiation under a LED UV-light (UV<sub>254</sub>) using a VILBER LOURMAT™ lamp, VL-4LC model.
- Staining thin-layers under acidic solutions of vainillin in ethanol and heating them with a heat gun.
- Staining thin-layers under solutions of KMnO<sub>4</sub> in water and heating them with a heat gun.
- Saining thin-layers under acidic Hanessian solution (Cerium Molybdate) in water and heating with a heat gun.

### 7.7.2 Gas chromatography (GC)

Gas chromatographies were performed with an Agilent Technologies 6850 model equipped with FID detector. Samples were dissolved in an inert solvent and filtered through a microfilter. A capillary column Agilent HP-5MS (30 m x 250  $\mu\text{m}$  x 0.25  $\mu\text{m}$ ) was used. The GC conditions for the separation of different products are shown in section 7.19.

### 7.7.3 High-performance liquid chromatography (HPLC)

Enantiomeric excess was determined using a Waters 2690 chromatography system equipped with a Waters 996 ultraviolet detector. The HPLC conditions for the separation of enantiomers of each compound are shown in section 7.20. Samples were dissolved in an inert solvent (preferably in the used eluent) to afford 1-5 mg/mL solutions and filtered through a microfilter. Chirals columns used:

- CHIRALPACK™ AS column (25 cm x 0.46 cm). particle size: 10  $\mu\text{m}$ .
- CHIRALPACK AD column (25 cm x 0.46 cm). particle size: 10  $\mu\text{m}$ .
- CHIRALPACK AD-H column (25 cm x 0.46 cm). particle size: 5  $\mu\text{m}$ .

## 7.8 Electrochemical studies

Cyclic voltammetry (CV) and differential pulse voltammetry (DPV) experiments were performed on a BioLab potentiostat using three-electrode cell. A glassy carbon electrode (approx 2 mm diameter) was used as working electrode, a platinum wire as auxiliary electrode, and a saturated calomel electrode (SCE) as a reference electrode. Working electrodes were polished with 0.05  $\mu\text{m}$  alumina paste and washed with distilled water and acetone before measurements. The complexes were dissolved in methanol containing 0.1M of TBABF<sub>4</sub> as supporting electrolyte. CV were recorded at 0.1 V/s scan rate. DPV were recorded using pulse height of 0.01 V, pulse widths of 0.05 s, sampling widths of 0.02 s, pulse periods of 0.1 s, and quiet times of 2 s. In CV experiments we obtained reversible redox wave, so  $E_{1/2}$  values reported were estimated using Equation 11.<sup>222</sup>



## 7. Experimental Methodologies

$$E_{1/2} = \frac{1}{2}(E_{pa} + E_{pc}) \quad \text{Equation 11}$$

$E_{pa}$  is the anodic peak potential and  $E_{pc}$  is the cathodic peak potential.

In DPV experiments  $E_{1/2}$  reported values were estimated using Equation 12.<sup>222</sup>

$$E_p = E_{1/2} - \frac{\Delta E}{2} \quad \text{Equation 12}$$

$E_p$  is the peak potential and  $\Delta E$  is the pulse height.

### 7.9 Gelation studies

A small amount ( $5.0 \pm 0.1$  mg) of LMWG was weighed in a 2 mL transparent-glass vial with a septum screw-on cap. Then, a certain volume of the desired solvent was added and the vial closed. The minimum volume added was 0.05 mL. Then the mixture was heated under the boiling point of the solvent using a balloon system in order to avoid solvent pressure. Once a solution was obtained, the mixture was sonicated for 1 to 5 minutes. For high concentrations and for some solvents, a previous sonication was needed for a good solubilisation during heating and sonication time was usually shorter than for diluted gels. Then, the mixture was led to stabilize and to reach room temperature. To state that the mixture was a gel the tube inversion test was done just by turning the vial upside down. If the sample was a gel, it did not drop. The mixtures could also be classified as solutions or insoluble systems. To determine the minimum gelation concentration (*mgc*), a new volume of solvent was added to the gel and the process was repeated until no gel was formed: the last volume added determines the *mgc*.

Xerogels were prepared by removing the solvent of the gel under reduced pressure. When the amount of the required xerogel was high, this simple procedure was not followed because the gel splashed outside the vial. For that reason, xerogels were obtained after lyophilisation of the gels by immersion into liquid

nitrogen and connected to a Telstar Lyoquest freeze-drying system operating at -85 °C and 0.01 mbar.

## 7.10 Sample preparation for metal complexes

The ligand concentrations were determined by calculating the difference between two observed equilibrium points in the pH-potentiometric titration of the ligands alone. Also, calculating the difference between equilibrium points of the ligands alone and the ligands with the metals (1 eq) gave the same results. Gd, Zn and Eu (for luminescence lifetimes) concentrations were determined by titrating the metal solutions with standardised Na<sub>2</sub>H<sub>2</sub>EDTA in urotropine buffer (pH 5.6 – 5.8) in the presence of xylenol orange as an indicator.

Mn concentrations were studied by bulk magnetic susceptibility (BMS) measurements. Also, in the end of <sup>17</sup>O NMR experiments Gd complex concentration was rechecked by bulk magnetic susceptibility (BMS) shift. The BMS shifts of <sup>1</sup>H NMR signals for an inert reference caused by the addition of paramagnetic compounds were studied in order to determine the concentration of paramagnetic metal in solution Equation 13.<sup>223</sup>

$$\Delta_x = \frac{4\pi c s}{T} \left( \frac{\mu_{eff}}{2.84} \right) 10^3 \quad \text{Equation 13}$$

Where the concentration of paramagnetic solute is given by  $c$  in mol l<sup>-1</sup>,  $s$  is dependent on the shape of the sample and its position in the magnetic field.  $s = 1/3, -1/6$  and  $0$  for a cylinder parallel to the main field, a cylinder perpendicular to the main field, and a sphere, respectively.  $T$  is the absolute temperature and  $\mu_{eff}$  is the effective magnetic moment for a particular lanthanide ion.  $\Delta_x$  is measured for a reference compound, in our case, *tert*-butanol.

## 7.11 Potentiometric studies

Carbonate-free 0.1 M KOH and 0.1 M HCl were prepared from Fisher

## 7. Experimental Methodologies

chemical concentrates. Potentiometric titrations were performed in 0.1 M aqueous KCl under nitrogen atmosphere, and the temperature was controlled to  $25 \pm 0.1$  °C. The pH was measured in each titration with a combined micro pH glass electrode (Metrohm 6.0224.100) filled with 3 M KCl, and the titrant addition was automated by use of a 785 DMP titrino system (Metrohm). The electrode was calibrated in hydrogen ion concentration by titration of HCl with KOH in 0.1 M electrolyte solution.<sup>224</sup> The the electrode standard potential ( $E^0$ ) and the slope factor ( $f$ ) were determined before titrations using the Glee software.<sup>225</sup> Continuous potentiometric titrations with HCl and KOH 0.1 M were conducted in aqueous solution containing 5 mL of **L1** and **L2** 2 mM in KCl 0.1 M, with 2 min waiting between successive points. The titrations of the metal complexes were performed with the same ligand solutions containing 1 equivalent of metal cation, also with 2 min waiting time between two points.

Protonation constants of ligands, stability constants of complexes and protonation constants of complexes are described and defined in Equation 4-6.

$$K_i = \frac{[H_i L]}{[H_{i-1} L][H^+]} \quad \text{Equation 4}$$

$$K_{ML} = \frac{[ML]}{[M][L]} \quad \text{Equation 5}$$

$$K_{MH_i L} = \frac{[M(H_i L)]}{[M(H_{i-1} L)][H^+]} \quad \text{Equation 6}$$

Where [M], [L], and [ML] are the equilibrium concentrations of free metal ion, deprotonated ligand, and deprotonated complex, respectively. Experimental data were refined using the computer software Hyperquad 2008.<sup>192</sup> Species distribution plots were calculated taking the experimental constants using the computed software HySS.<sup>195</sup> The ionic product of water used at 25 °C was  $pK_w = 13.77$ , while the ionic strength was kept at 0.1 M.<sup>226</sup> Fixed values were used for  $pK_w$ , ligand acidity constants, and total concentrations of metal, ligand, and acid.

## 7.12 Kinetic measurements

The rates of the metal exchange reactions of **GdL2** were studied by following the formation of the **CuL2** complex using conventional UV-vis spectrophotometry. The exchange reactions were followed at 245 nm in the pH range of 3.35-4.90. The concentration of the complex was 0.11 mM, while Cu<sup>2+</sup> ion was added at high excess (10-40 equivalents) to ensure pseudo-first order conditions. The temperature in the samples was kept at 25 °C and the ionic strength of the solutions was kept constant by using 0.15 M NaCl. For keeping the pH constant, 50 mM methylpiperazine buffer was used. The pseudo-first-order rate constants ( $k_{obs}$ ) were calculated by fitting the absorbance vs the time data to the monoexponential function (Equation 14).

$$A_t = (A_0 - A_e)e^{-k_{obs}t} + A_e \quad \text{Equation 14}$$

Where  $A_0$ ,  $A_t$ , and  $A_e$  are the absorbance at time = 0 s, at time  $t$ , and at equilibrium, respectively. The fittings were performed with Origin 9.1 software by using standard least-squares procedure.

## 7.13 Lifetime measurements

Europium luminescence lifetimes were recorded on an Agilent Cary Eclipse fluorescence spectrophotometer by recording the decay of the emission intensity at 616 nm, following an excitation at 272 nm for the **L2** and at 396 nm for the **L1**. Excitation of the metal in the **L2** gave similar results. Concentrations of EuL of 0.21 mM in HEPES buffer 0.1 M in H<sub>2</sub>O and D<sub>2</sub>O solutions at pH, pD = 7. Same experiments but adding 10 and 50 equivalents of phosphate and carbonate were performed. The settings are showed in Table 20. Different decay curves were collected for each sample and the lifetimes were analysed as monoexponential decays and fitted using the spectrophotometer software.

## 7. Experimental Methodologies

**Table 20.** Experimental conditions to record luminiscence decay lifetimes.

Parameter	Value
Gate time	0.05 ms
Delay time	0.1 ms
Flash count	1
Total decay time (H <sub>2</sub> O)	5 ms
Total decay time (D <sub>2</sub> O)	15 ms
Cycles	100
PMT detector	800 mV

Equation 10 was used to calculate the number of water molecules coordinated to the europium chelate.

$$q = A \left( \frac{1}{\tau_{H_2O}} - \frac{1}{\tau_{D_2O}} - B \right) \quad \text{Equation 10}$$

where  $\tau_{H_2O}$  and  $\tau_{D_2O}$  are the luminiscence decay lifetimes recorded in water and deuterium oxide, respectively.  $A$  and  $B$  are constants that take values of values of  $A=1.2$  and  $B=0.25$ <sup>209</sup> or  $A=1.11$  and  $B=0.31$ <sup>210</sup> for Eu<sup>3+</sup>.

### 7.14 Relaxometric measurements

<sup>1</sup>H NMRD profiles were recorded on a Stelar SMARTracer Fast Field Cycling relaxometer (0.01-10 MHz) and a Bruker WP80 NMR electromagnet adapted to variable field measurements (20-80 MHz) and controlled by a VTC91 temperature control unit and maintained by a gas flow at CBM in Orléans. The concentrations of the dissolutions used were 1.88 mM **Gd(L1)** + 6% **L1**, 1.91 mM **Gd(L2)** + 5% **L2** and 3.29 mM **Mn(L1)**+ 15% **L1** at pH = 7. The temperature was determined by previous calibration with a Pt resistance temperature probe.

The least-squares fit of the <sup>1</sup>H NMRD data and simultaneous fit with the <sup>17</sup>O NMR data were performed using Visualiseur/Optimiseur in MATLAB 8.3

software<sup>227,228</sup>

### 7.14.1 Equations used for the analysis of the NMRD profiles

The observed longitudinal proton relaxation rate,  $1/T_{1,obs}$  is the sum of the diamagnetic and paramagnetic contributions as showed in Equation 1. The equations are expressed for  $Gd^{3+}$  complexes, and analogous equations were used for  $Mn^{2+}$ .

$$\frac{1}{T_{1,obs}} = \frac{1}{T_{1,d}} + \frac{1}{T_{1,p}} = \frac{1}{T_{1,d}} + r_1[Gd] \quad \text{Equation 1}$$

Where  $r_1$  is the proton relaxivity, and the concentration of the paramagnetic species (in this case Gd) is usually given in millimoles per litre ( $mmol L^{-1}$ ) for dilute systems.<sup>133</sup> The relaxivity can be separated into two terms; the inner and outer sphere, as showed in Equation 2.

$$r_1 = r_1^{IS} + r_1^{OS} \quad \text{Equation 2}$$

The inner sphere term is obtained in Equation 3, where  $q$  is the number of water molecules in the inner sphere,  $\tau_m$  is the lifetime of a water molecule in the inner sphere (equal to  $1/k_{ex}$ ,  $k_{ex}$  is the water exchange rate) and  $T_{1m}$  is the longitudinal relaxation rate of inner sphere protons.<sup>176,229–232</sup>

$$r_1^{IS} = \frac{1}{1000} \frac{q}{55.5} \frac{1}{T_{1m} + \tau_m} \quad \text{Equation 3}$$

The longitudinal relaxation rate of inner sphere protons,  $T_{1m}$  is expressed by Equation 15, where  $r_{GdH}$  is the electron spin-proton distance,  $\gamma$  is the nuclear

## 7. Experimental Methodologies

gyromagnetic ratio,  $\omega_I$  is the proton resonance frequency and  $\omega_S$  is the Larmor frequency of the  $Gd^{3+}$  electron spin.

$$\frac{1}{T_{1m}} = \frac{2}{15} \left( \frac{\mu_0}{4\pi} \right)^2 \frac{\hbar^2 \gamma_I^2 \gamma_S^2}{r_{GdH}^6} S(S+1) [3J(\omega_I; \tau_{d1}) + 7J(\omega_S; \tau_{d2})]$$

**Equation 15**

$$\frac{1}{\tau_{di}} = \frac{1}{\tau_m} + \frac{1}{\tau_{RH}} + \frac{1}{T_{ie}} \quad i = 1, 2$$

**Equation 16**

The  $\tau_{RH}$  is the overall rotational correlation time, and its assumed to have a simple exponential temperature dependence as showed in Equation 17.  $E_R$  is the corresponding activation energy.

$$\tau_{RH} = \tau_{RH}^{298} \exp \left\{ \frac{E_R}{R} \left( \frac{1}{T} - \frac{1}{298.15} \right) \right\}$$

**Equation 17**

The longitudinal and transverse electronic relaxation rates,  $1/T_{1e}$  and  $1/T_{2e}$  are expressed by Equations 18 and 19, where  $\tau_v$  is the electronic correlation time for the modulation of the zero-field-splitting interaction,  $E_v$  is the corresponding activation energy and  $\Delta^2$  is the mean square zero-field-splitting energy. We assumed a single exponential dependence of  $\tau_v$  versus temperature (Equation 18).<sup>233,234</sup>

$$\left( \frac{1}{T_{1e}} \right)^{ZFS} = \frac{1}{25} \Delta^2 \tau_v \{4S(S+1) - 3\} \left( \frac{1}{1 + \omega_S^2 \tau_v^2} + \frac{4}{1 + 4\omega_S^2 \tau_v^2} \right)$$

**Equation 18**

$$\left( \frac{1}{T_{2e}} \right)^{ZFS} = \Delta^2 \tau_v \left( \frac{5.26}{1 + 0.372\omega_S^2 \tau_v^2} + \frac{7.18}{1 + 1.24\omega_S^2 \tau_v^2} \right)$$

Equation 19

$$\tau_v = \tau_v^{298} \exp \left\{ \frac{E_v}{R} \left( \frac{1}{T} - \frac{1}{298.15} \right) \right\}$$

Equation 20

The outer sphere contribution can be described by Equation 21, where  $J^{OS}$  is associated spectral density function (Equation 22) and  $j = 1, 2$ .<sup>235,236</sup>

$$r_1^{OS} = \frac{32N_A\pi}{405} \left( \frac{\mu_0}{4\pi} \right)^2 \frac{\hbar^2 \gamma_S^2 \gamma_I^2}{a_{GdH} D_{GdH}} S(S+1) [3J^{OS}(\omega_I, T_{1e}) + 7J^{OS}(\omega_S, T_{2e})]$$

Equation 21

$$J^{OS}(\omega, T_{je}) = \left[ \frac{1 + \frac{1}{4} \left( i\omega\tau_{GdH} + \frac{\tau_{GdH}}{T_{je}} \right)^{1/2}}{1 + \left( i\omega\tau_{GdH} + \frac{\tau_{GdH}}{T_{je}} \right)^{1/2} + \frac{4}{9} \left( i\omega\tau_{GdH} + \frac{\tau_{GdH}}{T_{je}} \right) + \frac{1}{9} \left( i\omega\tau_{GdH} + \frac{\tau_{GdH}}{T_{je}} \right)^{3/2}} \right]$$

Equation 22

The diffusion coefficient for the diffusion of a water proton from the bulk of the solvent to the  $Gd^{3+}$ ,  $D_{GdH}$  is assumed to follow an exponential function versus the inverse of the temperature (Equation 23), where  $E_{GdH}$  is the activation energy and  $D_{GdH}^{298}$  is the diffusion coefficient at 298.15 K.

$$D_{GdH} = D_{GdH}^{298} \exp \left\{ \frac{E_{GdH}}{R} \left( \frac{1}{298.15} - \frac{1}{T} \right) \right\}$$

Equation 23

## 7.15 Temperature-dependent $^{17}O$ NMR spectroscopy

$^{17}O$  NMR spectroscopy was recorded at Centre de Biophysique Moléculaire (CBM) from CNRS in Orléans, France. The spectrometer used was Bruker Avance 400 (9.36 T, 54.2 MHz). The longitudinal and transverse  $^{17}O$  relaxation rates ( $1/T_1$ ,



## 7. Experimental Methodologies

$1/T_2$ ) and the chemical shifts were measured in aqueous solutions of **GdL1** (15.3 mM, pH = 6.5), **GdL2** (14.5 mM, pH = 6.5) and **MnL1** (4.9 mM, pH = 7) in a temperature range of 275-348 K. The temperature was calculated according to previous calibration with ethylene glycol and methanol.<sup>237</sup> An acidified water solution (HClO<sub>4</sub>, pH = 3.3) was used as external reference for the Gd complexes and ZnL1 (5.0 mM, pH = 7) for the Mn complex. Longitudinal relaxation times ( $T_1$ ) were obtained by the inversion-recovery method. The transverse relaxation times ( $T_2$ ) were obtained by the Carr-Purcell-Meiboom-Gill spin-echo technique.<sup>238</sup> The samples were sealed in glass spheres fitted into 10 mm NMR tubes to avoid susceptibility corrections of chemical shifts.<sup>239</sup> To improve sensitivity, <sup>17</sup>O-enriched water (10% H<sub>2</sub><sup>17</sup>O) was added to the solutions to reach around 1% enrichment. The <sup>17</sup>O NMR data have been treated according to the Solomon-Bloembergen-Morgan theory of paramagnetic relaxation (equations below). The least-squares fit of the <sup>17</sup>O NMR data was performed using Visualiseur/Optimiseur in MATLAB 8.3 software.<sup>227,228</sup>

### 7.15.1 Equations used for the analysis of the <sup>17</sup>O NMR

From the measured <sup>17</sup>O NMR relaxations rates and angular frequencies of the paramagnetic solutions,  $1/T_2$ ,  $1/T_1$ ,  $\omega$ , and from the reference,  $1/T_{2A}$ ,  $1/T_{1A}$  and  $\omega_A$ , it is possible to calculate the reduced relaxation rates and chemical shifts,  $1/T_{2r}$ ,  $1/T_{1r}$  and  $\Delta\omega_r$  (Equations 24-26), where  $1/T_{2m}$ ,  $1/T_{1m}$  are the relaxation rate of the bound water and  $\Delta\omega_m$  is the chemical shift difference between bound and bulk water,  $\tau_m$  is the mean residence time or the inverse of the water exchange rate  $k_{ex}$  and  $P_m$  is the mole fraction of the bound water.<sup>177,239</sup>

$$\frac{1}{T_{1r}} = \frac{1}{P_m} \left[ \frac{1}{T_1} - \frac{1}{T_{1A}} \right] = \frac{1}{T_{1m} + \tau_m} + \frac{1}{T_{1os}} \quad \text{Equation 24}$$

$$\frac{1}{T_{2r}} = \frac{1}{P_m} \left[ \frac{1}{T_2} - \frac{1}{T_{2A}} \right] = \frac{1}{\tau_m} \frac{T_{2m}^{-2} + \tau_m^{-1} T_{2m}^{-1} + \Delta\omega_m^2}{(\tau_m^{-1} + T_{2m}^{-1})^2 + \Delta\omega_m^2} + \frac{1}{T_{2OS}}$$

Equation 25

$$\Delta\omega_r = \frac{1}{P_m} (\omega - \omega_A) = \frac{\Delta\omega_m}{(1 + \tau_m T_{2m}^{-1})^2 + \tau_m^2 \Delta\omega_m^2} + \Delta\omega_{os}$$

Equation 26

The outer sphere contributions to the  $^{17}\text{O}$  relaxation rates  $1/T_{1OS}$  and  $1/T_{2OS}$  can be neglected according to previous studies.<sup>177</sup> Then Equations 24-26, can be further simplified into Equations 27 and 28.

$$\frac{1}{T_{1r}} = \frac{1}{T_{1m} + \tau_m}$$

Equation 27

$$\frac{1}{T_{2r}} = \frac{1}{T_{2m} + \tau_m}$$

Equation 28

The exchange rate is assumed to be described by the Eyring equation (Equation 29), where  $\Delta S^\ddagger$  and  $\Delta H^\ddagger$  are the entropy and enthalpy of activation for the water exchange process, and  $k_{ex}^{298}$  is the exchange rate at 298.15 °K.  $R$  is the usual gas constant whereas  $h$  and  $k_B$  are the Planck and Boltzmann constants, respectively.

$$\frac{1}{\tau_m} = k_{ex} = \frac{k_B T}{h} \exp \left\{ \frac{\Delta S^\ddagger}{R} - \frac{\Delta H^\ddagger}{RT} \right\} = \frac{k_{ex}^{298} T}{298.15} \exp \left\{ \frac{\Delta H^\ddagger}{R} \left( \frac{1}{298.15} - \frac{1}{T} \right) \right\}$$

Equation 29

## 7. Experimental Methodologies

In the transverse relaxation, the scalar contribution,  $1/T_{2sc}$ , is the most important. In Equation 30,  $1/\tau_{s1}$  is the sum of exchange rate and the electron spin relaxation rate constants.

$$\frac{1}{T_{2m}} \cong \frac{1}{T_{2sc}} = \frac{S(S+1)}{3} \left( \frac{A}{\hbar} \right)^2 \left( \tau_{s1} + \frac{\tau_{s2}}{1 + \omega_s^2 \tau_{s2}^2} \right) \quad \text{Equation 30}$$

$$\frac{1}{T_{s1}} = \frac{1}{\tau_m} + \frac{1}{T_{1e}} \quad \text{Equation 31}$$

The  $^{17}\text{O}$  longitudinal relaxation rates in  $\text{Gd}^{3+}$  solutions are the sum of the contribution of the dipole-dipole ( $dd$ ) and quadrupolar ( $q$ ) mechanism as expressed by Equations 32-34 for non-extreme narrowing conditions, where  $\gamma_s$  is the electron and  $\gamma_I$  is the nuclear gyromagnetic ratio ( $\gamma_s = 1.76 \cdot 10^{11} \text{ rad s}^{-1} \text{ T}^{-1}$ ,  $\gamma_I = -3.626 \cdot 10^7 \text{ rad s}^{-1} \text{ T}^{-1}$ ),  $r_{\text{GdO}}$  is the effective distance between the electron charge and the  $^{17}\text{O}$  nucleus,  $I$  is the nuclear spin (5/2 for  $^{17}\text{O}$ ),  $\chi$  is the quadrupolar coupling constant and  $\eta$  is an asymmetry parameter.

$$\frac{1}{T_{1m}} = \frac{1}{T_{1dd}} + \frac{1}{T_{1q}} \quad \text{Equation 32}$$

$$\frac{1}{T_{1dd}} = \frac{2}{15} \left( \frac{\mu_0}{4\pi} \right) \frac{\hbar \gamma_I^2 \gamma_s^2}{r_{\text{GdO}}^6} S(S+1) [3J(\omega_I; \tau_{d1}) + 7J(\omega_S; \tau_{d2})]$$

**Equation 33**

$$\frac{1}{T_{1q}} = \frac{3\pi^2}{10} \frac{2I+3}{I^2(2I-1)} \chi^2 (1 + \eta^2/3) [0.2J_1(\omega_I) + 0.8J_2(\omega_I)]$$

**Equation 34**

In Equation 26, the chemical shift of the bound water molecule,  $\Delta\omega_m$ , depends on the hyperfine interaction between  $\text{Gd}^{3+}$  electron spin and the  $^{17}\text{O}$  nucleus and is directly proportional to the scalar constant  $A/\hbar$ , as expressed in Equation 35.<sup>240</sup>

$$\Delta\omega_m = \frac{g_L\mu_B S(S+1)B}{3k_B T} \frac{A}{\hbar} \quad \text{Equation 35}$$

The isotropic Landé  $g$  factor is equal to 2.0 for  $\text{Gd}^{3+}$ ,  $B$  represents the magnetic field, and  $k_B$  is the Boltzmann constant.

## 7.16 Other details

- **Optical rotations**,  $[\alpha]_D$ , were measured using an a JASCO-715 spectropolarimeter and calculated from associated software. Moreover, some measurements were done using a PERKIN ELMER Polarimeter 341 using a 1 dm path in IQAC institute, from CSIC in Barcelona.
- **Melting points** were determined on a hot stage using a Kofler apparatus, REICHERT AUSTRIA model.
- **Micro-distillations** were carried out in a BÜCHI distiller, GKR-51 model.
- **Lyophilisation** of samples were done using a TELSTAR lyophilisator, model LyoQuest-85 and a Bioblock Scientific Advantec, alpha 2-4 LD model.
- **Photochemical reactions** were performed in a pyrex T-shaped photochemical reactor from TRALLERO&SCHLEE. Irradiation was emitted from a mercury lamp of 400 W medium pressure ELECTRO DH. Refrigeration at  $-40\text{ }^\circ\text{C}$  was performed using a C40P TERMO Scientific refrigerator, Phoenix II model.
- **Reagents** were used from different commercial sources and **Solvents** were directly used due to their high quality (synthesis and HPLC grade). **Deuterated solvents** were used directly from commercial source. If

## 7. Experimental Methodologies

necessary, reagents and solvents were further purified and dried using standard organic chemistry procedures.<sup>241</sup>

### 7.17 Computational details

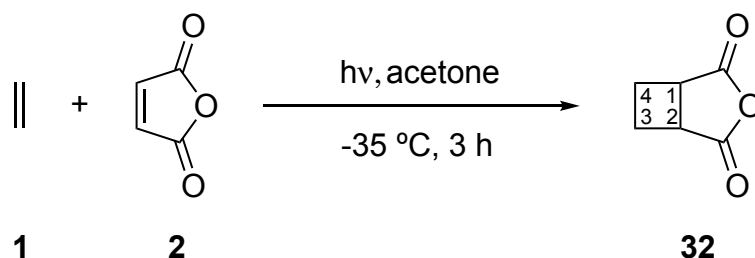
Computational studies were carried out with the help of Dr. Bernat Pi. A conformational search of each system was carried out using a mixed low mode/torsional sampling with the OPLS-2005 force field implemented in the MacroModel program to find and select an approximation of the most stable conformers.<sup>242–244</sup> The geometries of the lowest energy conformers of each system were optimized using Density Functional Theory (DFT) with the Gaussian09 program. We have used the M06-2X functional with the 6-31G(d) basis set. This functional was shown to describe correctly non-covalent interactions.<sup>245–247</sup>

For all the studied organogelators, once the geometry was obtained, the dimer was built up and the procedure was repeated. Then, the procedure was repeated with the tetramer. From the structure of the tetramer optimized with DFT, the internal dimer of the aggregate was selected to be the model of aggregation to build up the octamer and the dodecamer with the OPLS\_2005 force field. A minimization of the energy using molecular mechanics of the octamer and the dodecamer was carried out. Finally, a single point energy calculation in gas phase at the M06-2X/6-31G(d) level of theory is carried out to get the energy of each system.

Circular dichroism spectra were calculated by taking the optimized structure of the monomer in methanol solution and calculating 10-30 excited states with Gaussian09 using the TDDFT method with the M06-2X/6-311+G(d,p) level of theory. The prediction of the CD spectra of the dimer aggregates was carried out from the geometry of the internal tetramer of the octameric aggregate studying 20 excited states with the CAM-B3LYP/6-31G(d,p) level of theory. Representation of the predicted circular dichroism spectra were done using GaussSum software.<sup>76–80</sup>

## 7.18 Synthetic procedures

### 3-Oxabicyclo [3.2.0] heptane-2,4-dione, **32**



A solution of maleic anhydride, **2**, (1.52 g, 15.3 mmol) in acetone (500 mL) was cooled down to  $-35\text{ }^\circ\text{C}$ . The solution was saturated with ethylene for 10 minutes. The system was irradiated through a Pyrex filter for 30 minutes using a mercury-vapour lamp. After that, the system was cooled down again and the procedure was repeated three times. The solvent was removed under vacuum to afford pure compound **32** as a pale solid (1.93 g, 15.3 mmol, quantitative yield).

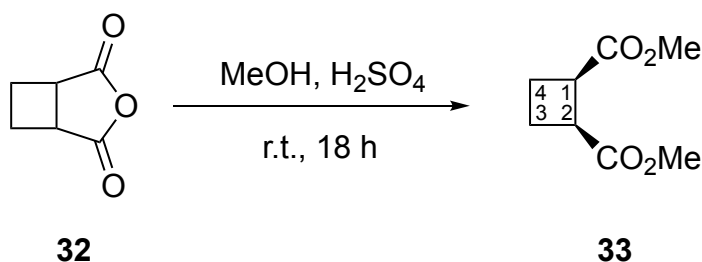
#### Spectroscopic data for compound **32**:

$^1\text{H NMR}$  (250 MHz,  $\text{CDCl}_3$ ):  $\delta$  2.35 (m, 2H), 2.74 (m, 2H), 3.52 (m, 2H,  $\text{H}_1$ ,  $\text{H}_2$ ).

Spectroscopic data are consistent with those reported in reference:

Tufariello, J. J.; Milowsky, A. S.; Al-Nuri, M.; Goldstein, S. *Tetrahedron Lett.*, **1987**, *28*, 267.

### Dimethyl (1*R*,2*S*)-cyclobutane-1,2-dicarboxylate, **33**



A solution of **32** (1.92 g, 15.1 mmol) and concentrated  $\text{H}_2\text{SO}_4$  (1.0 mL) in methanol (50 mL) was stirred at room temperature for 18 h. Dichloromethane (100

## 7. Experimental Methodologies

mL) was added to the organic phase and it was successively washed with water (2 x 50 mL) and brine (1 x 50 mL). The organic layer was then dried over MgSO<sub>4</sub>, filtered and concentrated to provide the crude as yellowish oil. The distillation of this crude under reduced pressure affords **33** as a colourless oil (2.15 g, 12.5 mmol, 83% yield).

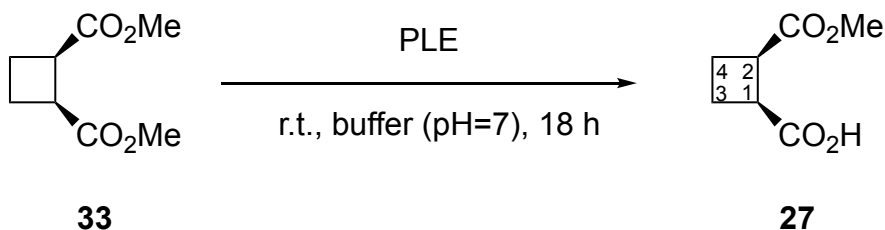
### Spectroscopic data for compound **33**:

<sup>1</sup>H NMR (250 MHz, CDCl<sub>3</sub>): δ 2.10 (m, 2H), 2.29 (m, 2H), 3.31 (m, 2H, H<sub>1</sub>, H<sub>2</sub>), 3.58 (s, 6H, Me).

Spectroscopic data are consistent with those reported in reference:

Sabbioni, G.; Jones, J. B. *J. Org. Chem.* **1987**, *52*, 4565.

### (1*R*,2*S*)-2-Methoxycarbonylcyclobutane-1-carboxylic acid, **27**



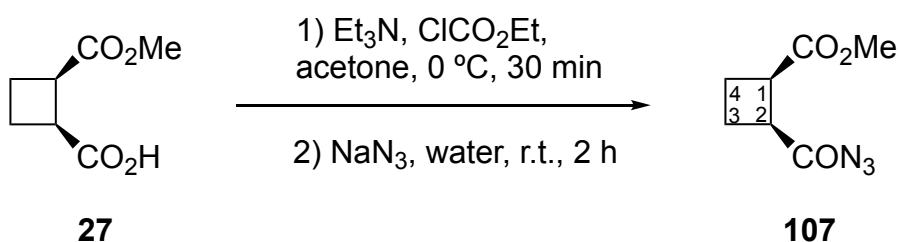
Diester **33** (3.61 g, 21.0 mmol) was dissolved in 250 mL of a buffer previously prepared from 0.1 M KH<sub>2</sub>PO<sub>4</sub> at pH 7.00. Pig liver esterase (PLE) (98 mg) was added to the solution and the mixture was stirred at room temperature for 18 h. The reaction was kept at pH 7 by adding a 1 M solution of NaOH. Then, the reaction mixture was washed with diethyl ether (2 x 100 mL), and 5% HCl was added to reach pH 2-3. The acid solution was extracted with ethyl acetate (4 x 150 mL) and the organic extracts were dried over magnesium sulfate. The solvent was evaporated under vacuum to dryness obtaining half-ester **27** as a yellow oil (3.15 g, 19.9 mmol, 95% yield, 97% ee).

**Spectroscopic data for compound 27:**

$^1\text{H NMR}$  (250 MHz,  $\text{CDCl}_3$ ):  $\delta$  2.23 (m, 2H), 2.41 (m, 2H), 3.43 (m, 2H, H<sub>1</sub>, H<sub>2</sub>), 3.69 (s, 3H, Me).

Spectroscopic data are consistent with those reported in reference:

Sabbioni, G.; Jones, J. B. *J. Org. Chem.* **1987**, *52*, 4565.

**Methyl (1*R*,2*S*)-2-azidocarbonylcyclobutane-1-carboxylate, 107**

To an ice-cooled solution of half-ester **27** (5.73 g, 36.2 mmol) in anhydrous acetone (80 mL), triethylamine (6.5 mL, 47.1 mmol, 1.3 eq) and ethyl chloroformate (4.5 mL, 47.1 mmol, 1.3 eq) were subsequently added. The mixture was stirred at 0 °C for 30 minutes. Then, sodium azide (5.9 g, 90.6 mmol, 2.5 eq) in 100 mL of water was added and the resultant solution was stirred at room temperature for 2 h. The reaction mixture was extracted with dichloromethane (4 x 100 mL), and the organic extracts were dried over magnesium sulphate. Solvents were removed under reduced pressure to give acyl azide **108** as a colourless oil (5.18 g, 28.3 mmol, 78 % yield), which was used in the next step without further purification. **WARNING:** This product should be carefully manipulated because of its explosive nature.



## 7. Experimental Methodologies

### Spectroscopic data for compound **108**:

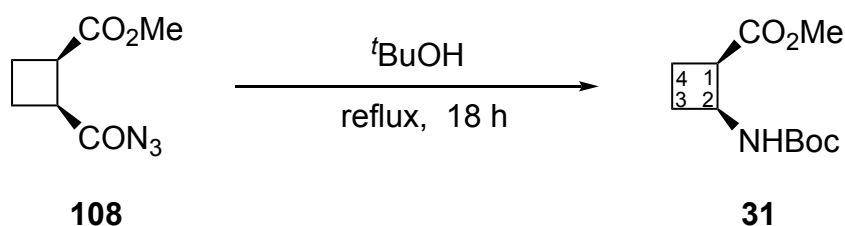
$^1\text{H}$  RMN (250 MHz, acetone- $d_6$ ):  $\delta$  2.27 (m, 4H, H<sub>3</sub>, H<sub>4</sub>), 3,54 (m, 2H, H<sub>1</sub>, H<sub>2</sub>), 3.68 (s, 3H, Me).

Spectroscopic data are consistent with those reported in reference:

Martín-Vilà, M.; Muray, E; P. Aguado, G.; Álvarez-Larena, A.; Branchadell, V.; Minguillón, C.; Giralt, E.; Ortuño, R. M. *Tetrahedron: Asymmetry*, **2000**, *11*, 3569.

### METHOD A:

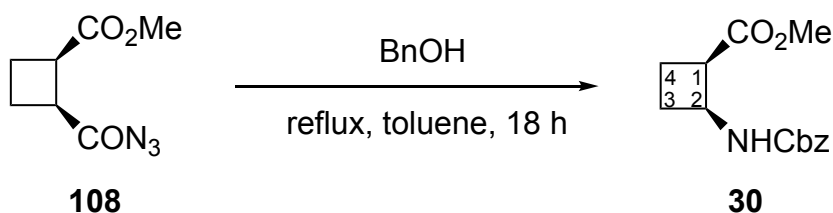
#### Methyl (1*R*,2*S*)-2-(*tert*-butoxycarbonylamino)cyclobutane-1-carboxylate, **31**



Acyl azide **108** (5.18 g, 28.3 mmol) was dissolved in 30 mL of *tert*-butanol. The mixture was heated to reflux and stirred for 18 h. Then, the solvent was evaporated under vacuum, and the residue was purified by column chromatography (4:1 hexane-EtOAc as eluent) affording the carbamate **31** as a white solid (4.21 g, 18.4 mmol, 65% yield).

### METHOD B, Step 1:

#### Methyl (1*R*,2*S*)-2-(benzyloxycarbonylamino)cyclobutane-1-carboxylate, **30**



## 7. Experimental Methodologies

A solution of **108** (2.54 g, 13.8 mmol) and benzyl alcohol (1.43 mL, 16.6 mmol, 1.2 eq) in toluene (50 mL) was heated to reflux for 18 hours. Toluene was removed under reduced pressure and then the excess of benzyl alcohol was eliminated by lyophilisation or by distillation under vacuum at 150 °C. The residue was chromatographed on silica gel (3:1 hexane-EtOAc as eluent) to afford carbamate **30** as an oil (3.39 g, 12.8 mmol, 92% yield).

### Spectroscopic data for compound **30**:

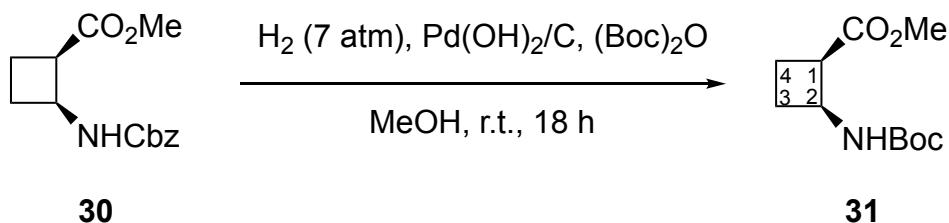
**<sup>1</sup>H NMR** (250 MHz, CDCl<sub>3</sub>): δ 1.97 (m, 2H), 2.18-2.43 (m, 2H), 3.39 (m, 1H, H<sub>1</sub>), 3.66 (s, 3H, Me), 4.46 (m, 1H, H<sub>2</sub>), 5.08 (s, 2H, CH<sub>2</sub>-Ph), 5.64 (broad s., 1H, NH), 7.34 (m, 5H, H<sub>ar</sub>).

Spectroscopic data are consistent with those reported in reference:

Martín-Vilà, M.; Muray, E; P. Aguado, G.; Álvarez-Larena, A.; Branchadell, V.; Minguillón, C.; Giralt, E.; Ortuño, R. M. *Tetrahedron: Asymmetry*, **2000**, *11*, 3569.

METHOD B, Step 2:

### Methyl (1*R*,2*S*)-2-(*tert*-butoxycarbonylamino)cyclobutane-1-carboxylate, **31**



Carbamate **30** (3.04 g, 11.5 mmol) in methanol (15 mL) was hydrogenated under 7 atmospheres of pressure in the presence of Pd(OH)<sub>2</sub>/C (0.35 g, 20% weight) and Boc<sub>2</sub>O (3.2 mL, 13.9 mmol, 1.2 eq) at r.t. overnight. The reaction mixture was filtered through Celite and solvent was removed under vacuum and the residue was purified by column chromatography (4:1 hexane-EtOAc as eluent) affording carbamate **31** as a white solid (2.17 g, 9.5 mmol, 82% yield).

## 7. Experimental Methodologies

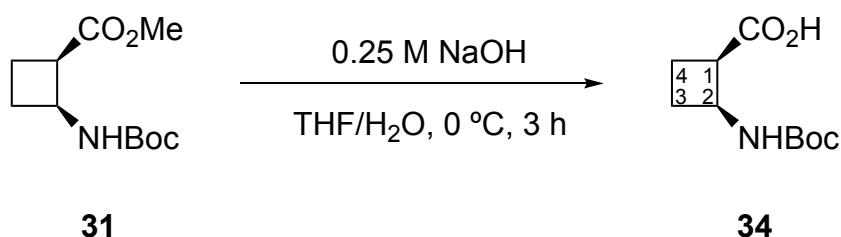
### Spectroscopic data for compound **31**:

$^1\text{H NMR}$  (250 MHz,  $\text{CDCl}_3$ ):  $\delta$  1.38 (s, 9H, *t*Bu), 1.87-1.97 (m, 2H), 2.25 (m, 2H), 3.35 (m, 1H,  $\text{H}_1$ ), 3.67 (s, 3H, Me), 4.41 (m, 1H,  $\text{H}_2$ ), 5.33 (br. s., 1H, *NH*).

Spectroscopic data are consistent with those reported in reference:

Izquierdo, S.; Rúa, F.; Sbai, A.; Parella, T.; Álvarez-Larena, A.; Branchadell, V.; Ortuño, R. M. *J. Org. Chem.*, **2005**, *70*, 7963.

### (1*R*,2*S*)-2-(*tert*-Butoxycarbonylamino)cyclobutane-1-carboxylic acid, **34**



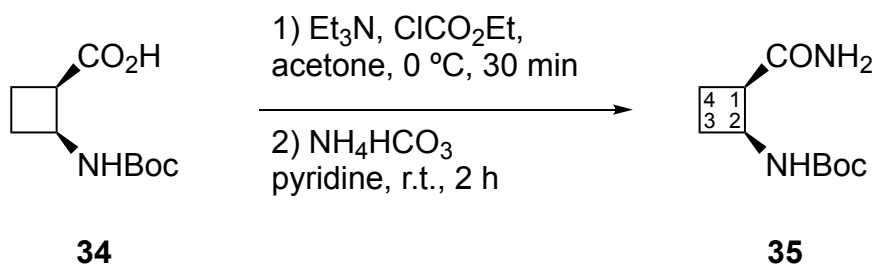
To an ice-cooled solution of ester **31** (790 mg, 3.4 mmol) in a 1:10 THF-water mixture (55 mL), a 0.25 M NaOH solution (34 mL, 8.6 mmol, 2.5 eq) was added and the resultant mixture was stirred for 3 h (Reaction progress was monitored by TLC). The reaction mixture was washed with dichloromethane (20 mL), and 5% HCl aqueous solution was added to the aqueous phase to reach pH 2. The acid solution was extracted with ethyl acetate (4 x 50 mL) and dried over magnesium sulphate. The solvent was removed at reduced pressure to afford **34** as a white solid (720 mg, 3.3 mmol, 98% yield) without purification.

### Spectroscopic data for compound **34**:

$^1\text{H NMR}$  (250 MHz,  $\text{CDCl}_3$ ):  $\delta$  1.45 (s, 9H, *t*Bu), 1.70-2.35 (m, 4H,  $\text{H}_3$ ,  $\text{H}_4$ ), 3.36 (m, 1H,  $\text{H}_1$ ), 4.35 (m, 1H,  $\text{H}_2$ ), 5.57 (broad s, 1H, *NH*).

Spectroscopic data are consistent with those reported in reference:

Izquierdo, S.; Rúa, F.; Sbai, A.; Parella, T.; Álvarez-Larena, A.; Branchadell, V.; Ortuño, R. M. *J. Org. Chem.*, **2005**, *70*, 7963.

**tert-Butyl ((1*S*,2*R*)-2-carbamoylcyclobutyl)carbamate, 35**

A mixture containing the free acid **34** (2.01 g, 9.34 mmol) in anhydrous acetone (50 mL), ethyl chloroformate (1.8 mL, 10.5 mmol) and triethylamine (1.9 mL, 14 mmol) was stirred at 0 °C and under a nitrogen atmosphere for 30 minutes. Then, ammonium bicarbonate (2.21 g, 28.01 mmol, 3 eq) and pyridine (1.9 mL, 23.34 mmol, 2.5 eq) were added and the mixture was stirred at room temperature for 2 h. EtOAc was added and the solution was washed with water (4 × 15 mL) and then dried under vacuum to give the desired product. Flash chromatography (EtOAc/hexane, 3:2) provided the free amide **35** as a white powder (1.70 g, 7.94 mmol, 85% yield).

**Spectroscopic data for compound 35:**

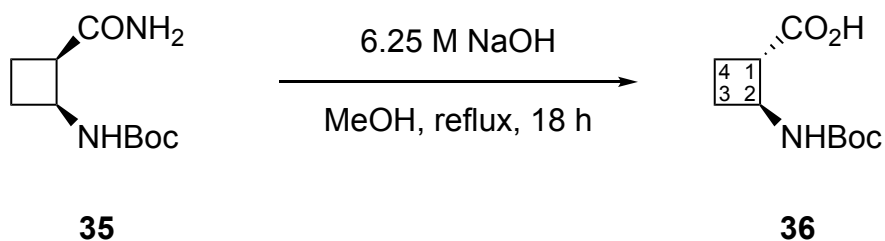
<sup>1</sup>H NMR (250 MHz, CDCl<sub>3</sub>): δ 1.42 (s, 9H, *t*Bu), 1.83-2.41 (c.a., 4H), 3.49 (m, 1H, H<sub>1</sub>), 4.41 (m, 1H, H<sub>2</sub>), 5.33 (br. s., 2H, NH<sub>2</sub>), 5.53 (br. s., 1H, NH).

Spectroscopic data are consistent with those reported in reference:

Fernandes, C.; Pereira, E.; Faure, S.; Aitken, D. J., *J. Org. Chem.* **2009**, *74*, 3217.

## 7. Experimental Methodologies

### (1*S*,2*S*)-2-(*tert*-Butoxycarbonylamino)cyclobutane-1-carboxylic acid, **36**



A solution of **36** (140 mg, 0.65 mmol) in MeOH (15 mL) was treated with 6.25 M NaOH aqueous solution (5.2 mL) and the mixture was heated to reflux overnight. Methanol was then removed by careful evaporation under reduced pressure and the residual aqueous phase was washed with EtOAc (3 × 20 mL). The aqueous phase was then cooled at 0 °C, while concentrated HCl was added slowly until pH 2. The aqueous phase was then extracted with EtOAc (3 × 60 mL) and the combined organic extracts were dried with MgSO<sub>4</sub> and concentrated under vacuum. After flash chromatography (EtOAc as eluent) the free acid **36** was obtained as a white powder (110 mg, 0.51 mmol, 78% yield).

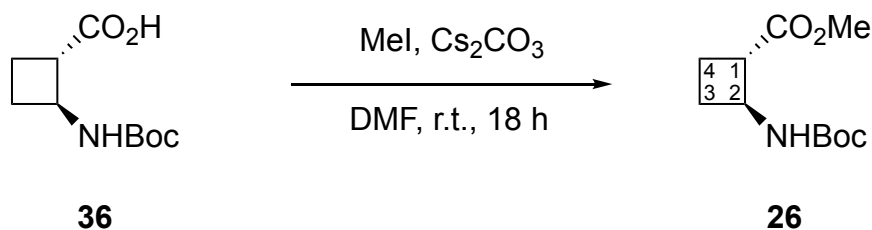
#### Spectroscopic data for compound **36**:

<sup>1</sup>H NMR (250 MHz, CDCl<sub>3</sub>): δ 1.44 (s, 9H, *t*Bu), 1.88-2.22 (c.a., 4H, H<sub>3</sub>, H<sub>4</sub>), 3.10 (m, 1H, H<sub>1</sub>), 4.14 (m, 1H, H<sub>2</sub>), 6.28 (broad s, 1H, *NH*).

Spectroscopic data are consistent with those reported in reference:

Fernandes, C.; Pereira, E.; Faure, S.; Aitken, D. J., *J. Org. Chem.* **2009**, *74*, 3217.

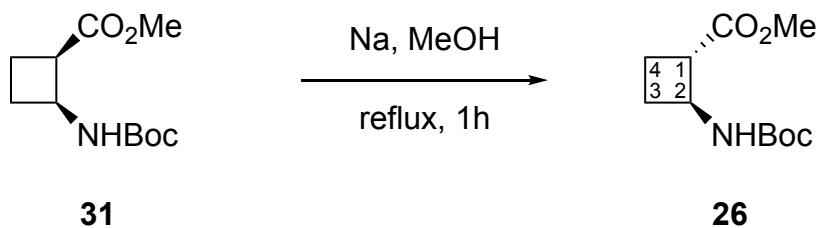
**Methyl (1*S*,2*S*)-2-(*tert*-butoxycarbonylamino)cyclobutane-1-carboxylate, **26****



Acid **36** (0.12 g, 0.51 mmol) and  $\text{Cs}_2\text{CO}_3$  (0.16 g, 0.56 mmol, 1.1 eq) were dissolved in DMF (5 mL). Then, MeI (0.03 mL, 0.56 mmol, 1.1 eq) was added and the mixture was stirred at room temperature overnight. The excess of MeI was removed by bubbling  $\text{N}_2$  and EtOAc (5 mL) was added. The solution was washed with saturated  $\text{NaHCO}_3$  (3 x 5 mL) and brine (5 mL). The organic phase was dried over  $\text{MgSO}_4$ , filtered and evaporated under reduced pressure to give ester **26** as an oil (0.11 g, 0.44 mmol, 86% yield).

METHOD B

**Methyl (1*S*,2*S*)-2-(*tert*-butoxycarbonylamino)cyclobutane-1-carboxylate, **26****



Na (190 mg, 8.26 mmol) was dissolved in anhydrous MeOH (85 mL) at room temperature under nitrogen. Compound **31** (420 mg, 1.83 mmol) was added to the resulting solution and the mixture was stirred at reflux for 1 h. After cooling in an ice bath, the reaction was quenched by addition of 1 M HCl (17 mL). Excess of MeOH was evaporated under reduced pressure and the aqueous layer was extracted with EtOAc (3 x 40 mL). The combined organic layers were dried ( $\text{MgSO}_4$ ), filtered and evaporated to give a white solid that was purified by chromatography (hexane/EtOAc, 1:3) to afford **26** as a white powder (250 mg, 1.10 mmol, 60%).

## 7. Experimental Methodologies

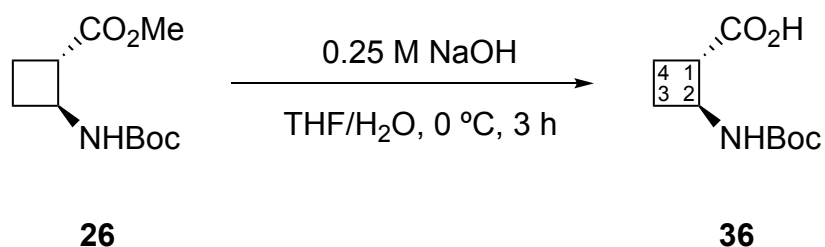
### Spectroscopic data for compound **26**:

$^1\text{H NMR}$  (250 MHz,  $\text{CDCl}_3$ ):  $\delta$  1.43 (s, 9 H, *t*Bu), 1.93 (m, 3H,  $\text{H}_{3-4}$ ), 2.25 (m, 1H,  $\text{H}_3$ ), 2.98 (m, 1 H,  $\text{H}_1$ ), 3.67 (s, 3H,  $\text{CH}_3$ ), 4.21 (m, 1 H,  $\text{H}_2$ ), 4.77 (br s, 1H, NH).

Spectroscopic data are consistent with those reported in reference:

Fernandes, C.; Gauzy, C.; Yang, Y.; Roy, O.; Pereira, E. ; Faure, S. ; Aitken, D. J. *Synthesis* **2007**, 14, 2222.

### (1*S*,2*S*)-2-(*tert*-Butoxycarbonylamino)cyclobutane-1-carboxylic acid, **36**



To an ice-cooled solution of ester **26** (790 mg, 3.4 mmol) in a 1:10 THF-water mixture (55 mL), 0.25 M sodium hydroxide aqueous solution (34 mL, 8.6 mmol, 2.5 eq) was added and the resultant mixture was stirred for 3 h. (Reaction progress was monitored by TLC). The reaction mixture was washed with dichloromethane (20 mL), and 5% HCl aqueous solution was added to the aqueous phase to reach pH 2. The acid solution was extracted with ethyl acetate (4 x 50 mL) and dried over  $\text{MgSO}_4$ . Solvent was removed at reduced pressure to afford **36** as a white crystalline solid (720 mg, 3.34 mmol, 98% yield) without need of further purification.

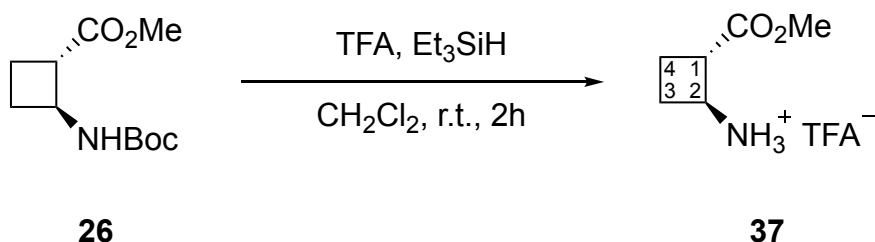
**Spectroscopic data for compound 36:**

$^1\text{H NMR}$  (250 MHz,  $\text{CDCl}_3$ ):  $\delta$  1.44 (s, 9H, *t*Bu), 1.88-2.22 (m, 4H,  $\text{H}_3$ ,  $\text{H}_4$ ), 3.10 (m, 1H,  $\text{H}_1$ ), 4.14 (m, 1H,  $\text{H}_2$ ), 6.28 (broad s, 1H, NH).

Spectroscopic data are consistent with those reported in reference:

Fernandes, C.; Pereira, E.; Faure, S.; Aitken, D. J. *J. Org. Chem.* **2009**, *74*, 3217.

**(1*S*,2*S*)-2-(Methoxycarbonyl)cyclobutan-1-amonium trifluoroacetate, 37**



To a solution of compound **26** (0.34 g, 1.48 mmol) in anhydrous  $\text{CH}_2\text{Cl}_2$  was added  $\text{Et}_3\text{SiH}$  (0.71 mL, 4.45 mmol, 3.0 eq) and TFA (1.49 mL, 19.24 mmol, 13 eq) at 0 °C with continuous stirring. The temperature was gradually increased to room temperature, and the mixture was stirred for 2 h. The organic solvent was evaporated under reduced pressure and the excess of TFA was eliminated by lyophilisation. The crude obtained **37** (0.34 g, quantitative yield) was used in the next step without further purification.

**Spectroscopic data for compound 37:**

$^1\text{H NMR}$  (250 MHz,  $\text{CD}_3\text{OD}$ ):  $\delta$  2.13-2.40 (m, 4H,  $\text{H}_3$ ,  $\text{H}_4$ ), 3.41 (m, 1H,  $\text{H}_1$ ), 3.69 (s, 3H, Me), 4.05 (m, 1H,  $\text{H}_2$ ), 7.88 (broad s, 1H,  $\text{NH}_3^+$ ).

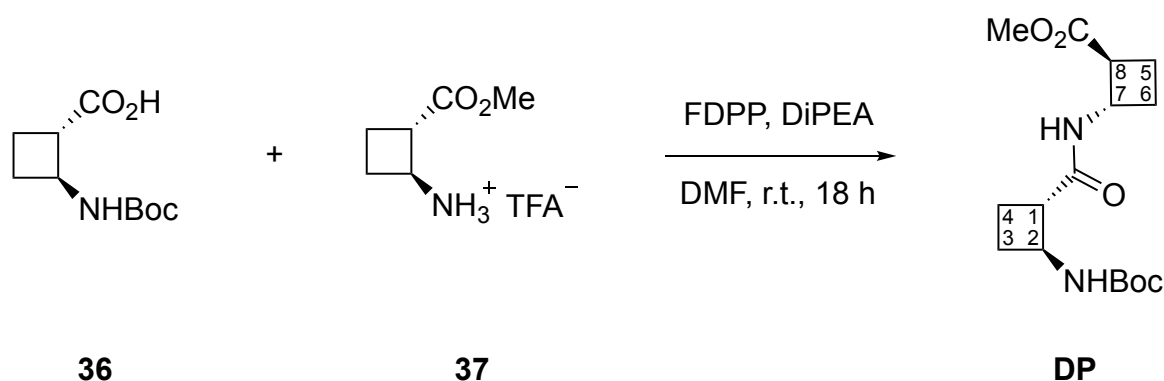
Spectroscopic data are consistent with those reported in reference:

Torres, E.; Gorrea, E.; Da Silva, E.; Nolis, P.; Branchadell, V.; Ortuño, R. M. *Org. Lett.*, **2009**, *11*, 2301-2304



## 7. Experimental Methodologies

### Dipeptide, DP



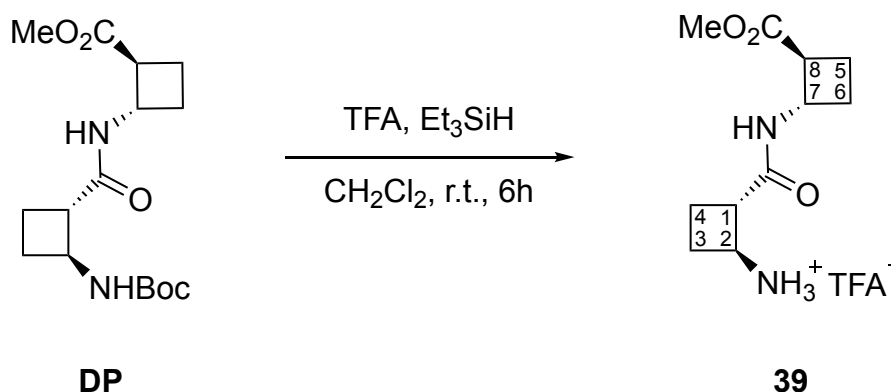
A solution containing the free carboxylic acid **36** (0.31 g, 1.44 mmol), the amine **37** (0.34 g, 1.44 mmol, 1.0 eq), DIPEA (0.74 mL, 4.32 mmol, 3.0 eq), and FDPP (0.66 g, 1.73 mmol, 1.2 eq) in anhydrous DMF (15 mL) was stirred at room temperature overnight. Then, ethyl acetate (20 mL) was added and the combined organic layers were washed with saturated aqueous NaHCO<sub>3</sub> (3 x 15 mL). The organic layer was dried over MgSO<sub>4</sub> and solvents were removed under reduced pressure. The residue was purified by column chromatography using ethyl acetate-hexane (3:2) as eluent to afford **DP** (0.36 g, 77%) as a white solid.

#### Spectroscopic data for compound DP:

<sup>1</sup>H NMR (250 MHz, CDCl<sub>3</sub>): δ 1.48 (s, 9H, *t*Bu), 1.68-2.29 (m, 8H, H<sub>3</sub>, H<sub>4</sub>, H<sub>5</sub>, H<sub>6</sub>), 2.87 (m, 1H, H<sub>1</sub>), 3.13 (m, 1H, H<sub>8</sub>), 3.74 (s, 3H, Me), 4.14 (m, 1H, H<sub>2</sub>), 4.55 (m, 1H, H<sub>7</sub>), 4.92 (m, 1H, NH), 8.50 (m, 1H, NH).

Spectroscopic data are consistent with those reported in reference:

Torres, E.; Gorrea, E.; Da Silva, E.; Nolis, P.; Branchadell, V.; Ortuño, R. M. *Org. Lett.*, **2009**, *11*, 2301-2304

**Trifluoroacetate salt of DP, 39**

To a solution of compound **DP** (0.13 g, 0.40 mmol) in anhydrous  $\text{CH}_2\text{Cl}_2$  was added  $\text{Et}_3\text{SiH}$  (0.08 mL, 0.52 mmol, 1.3 eq) and TFA (0.40 mL, 5.18 mmol, 13.0 eq) at room temperature, and the mixture was stirred for 6 h. The organic solvent was evaporated under reduced pressure and the excess of TFA was eliminated by lyophilisation. The crude of **39** (0.13 g, 98%) was used in the next step without further purification.

**Spectroscopic data for compound 39:**

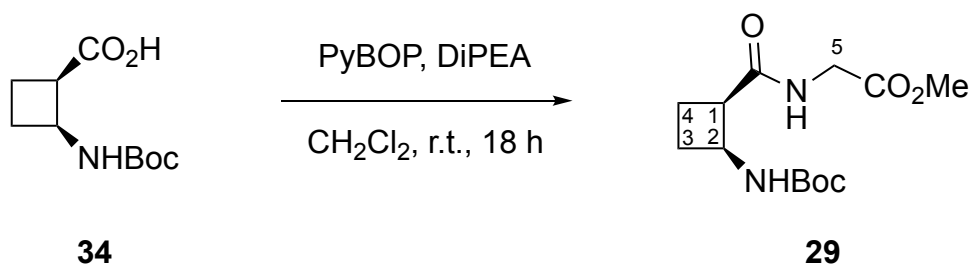
$^1\text{H NMR}$  (250 MHz,  $\text{CD}_3\text{OD}$ ):  $\delta$  1.66-2.40 (m, 8H,  $\text{H}_3$ ,  $\text{H}_4$ ,  $\text{H}_5$ ,  $\text{H}_6$ ), 2.90 (m, 1H,  $\text{H}_1$ ), 3.36 (m, 1H,  $\text{H}_8$ ), 3.71 (s, 3H, Me), 4.16 (m, 1H,  $\text{H}_2$ ), 4.50 (m, 1H,  $\text{H}_7$ ), 7.72 (m, 1H,  $\text{NH}_3^+$ ), 8.72 (m, 1H, NH).

Spectroscopic data are consistent with those reported in reference:

Torres, E.; Gorrea, E.; Da Silva, E.; Nolis, P.; Branchadell, V.; Ortuño, R. M. *Org. Lett.*, **2009**, *11*, 2301-2304

## 7. Experimental Methodologies

### Methyl ((1*R*,2*S*)-2-(*tert*-butoxycarbonylamino)cyclobutane-1-carbonyl)glycinate, **29**



Acid **34** (1.10 g, 5.11 mmol) and PyBOP (3.45 g, 6.64 mmol, 1.3 eq) were dissolved in CH<sub>2</sub>Cl<sub>2</sub> (15 mL) and DiPEA (4.6 mL, 25.6 mmol, 5 eq) was added under nitrogen atmosphere. After stirring for 10 min GlyMe·HCl (0.83 g, 6.64 mmol, 1 eq) in DMF (5 mL) were added and the reaction was stirred at room temperature overnight. Then, the solution was washed with saturated NaHCO<sub>3</sub> (3 x 20 mL) and brine (20 mL). The organic phase was dried over MgSO<sub>4</sub>, filtered and evaporated under reduced pressure to give crude compound. The crude was purified by column chromatography (EtOAc/hexane, 5:1) to give **29** (0.85 g, 2.96 mmol, 58%) as a white solid.

#### Spectroscopic data and physical constants for compound **29**:

**Mp**: 84-86 °C (CH<sub>2</sub>Cl<sub>2</sub>).

**[α]<sub>D</sub><sup>20</sup>**: -104 (c = 1.0, CH<sub>3</sub>OH).

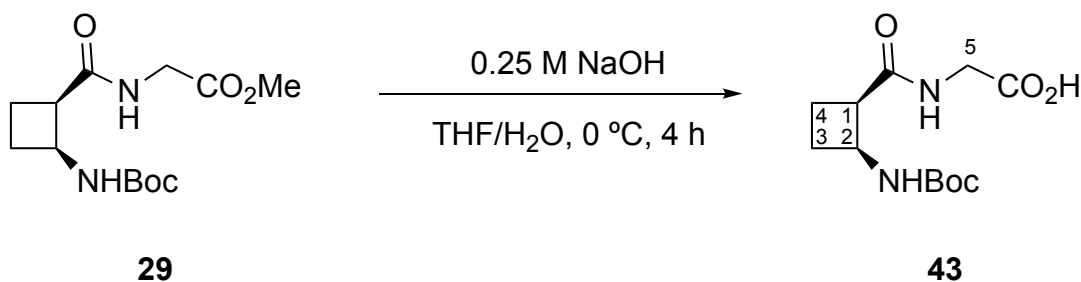
**IR** (ATR): 3336, 1759, 1682, 1681, 1650, 1513, 1170.

**<sup>1</sup>H NMR** (CDCl<sub>3</sub>, 250 MHz): δ 1.40 (s, 9H, *t*Bu), 1.90-2.30 (m, 4H, H<sub>3</sub>, H<sub>4</sub>), 3.28 (m, 1H, H<sub>1</sub>), 3.75 (s, 3H, Me), 4.06 (m, 2H, H<sub>5</sub>), 4.42 (m, 1H, H<sub>2</sub>), 5.45 (m, 1H, *NH*), 6.08 (m, 1H, *NH*).

**<sup>13</sup>C NMR** (CDCl<sub>3</sub>, 62.5 MHz): δ 18.7, 28.7, 29.9, 41.7, 46.7, 52.8, 79.8, 155.6, 170.6, 173.6.

**HRMS** (ESI) calculated for C<sub>13</sub>H<sub>22</sub>N<sub>2</sub>O<sub>5</sub>Na (M+Na<sup>+</sup>): 309.1421. Found: 309.1419

**((1*R*,2*S*)-2-(*tert*-Butoxycarbonylamino)cyclobutane-1-carbonyl)glycine, **43****



To an ice-cooled solution of dipeptide **29** (370 mg, 1.29 mmol) in a 1:4 mixture of THF/water (60 mL), 0.25 M aqueous NaOH solution (13 mL, 3.23 mmol) was added. The mixture was stirred at 0 °C for 4 h. The mixture was washed with CH<sub>2</sub>Cl<sub>2</sub> (1 x 20 mL) before being acidified to pH 2 with 2 M HCl. The aqueous layer was extracted with EtOAc (3 x 20 mL) and the organic layer was dried over anhydrous MgSO<sub>4</sub>, filtered and evaporated under reduced pressure to afford the corresponding carboxylic acid **43** (360 mg, quantitative) as a white solid. This compound was used without further purification.

**Spectroscopic data and physical constants for compound 43:**

**Mp:** 112-114 °C (CH<sub>2</sub>Cl<sub>2</sub>).

**[α]<sub>D</sub><sup>20</sup>:** -80 (c = 1.0, CH<sub>3</sub>OH).

**IR (ATR):** 3336, 2966, 1679, 1648, 1513.

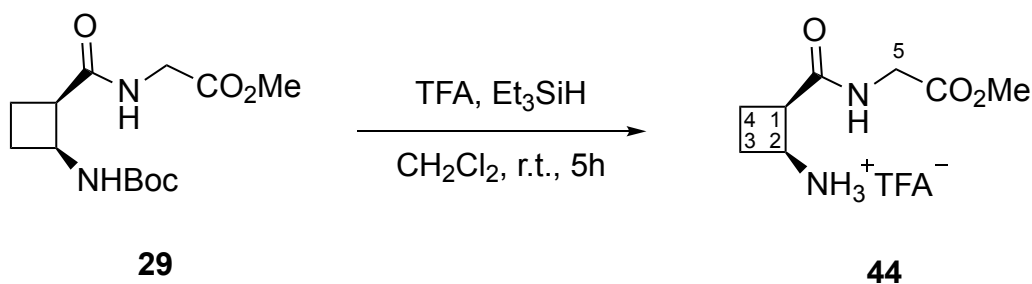
**<sup>1</sup>H NMR** (CDCl<sub>3</sub>, 250 MHz): δ 1.39 (s, 9H, *t*Bu), 1.90-2.31 (m, 4H, H<sub>3</sub>, H<sub>4</sub>), 3.34 (m, 1H, H<sub>1</sub>), 3.96 (m, 1H, H<sub>5</sub>), 4.11 (m, 1H, H<sub>5</sub>), 4.41 (m, 1H, H<sub>2</sub>), 5.57 (m, 1H, *NH*), 6.66 (m, 1H, *NH*).

**<sup>13</sup>C NMR** (CDCl<sub>3</sub>, 62.5 MHz): δ 18.0, 28.2, 30.2, 41.6, 46.1, 79.8, 155.7, 173.7.

**HRMS** (ESI) calculated for C<sub>12</sub>H<sub>20</sub>N<sub>2</sub>O<sub>5</sub>Na (M+Na<sup>+</sup>): 295.1264. Found: 295.1261

## 7. Experimental Methodologies

### Trifluoroacetate salt of **29**, **44**



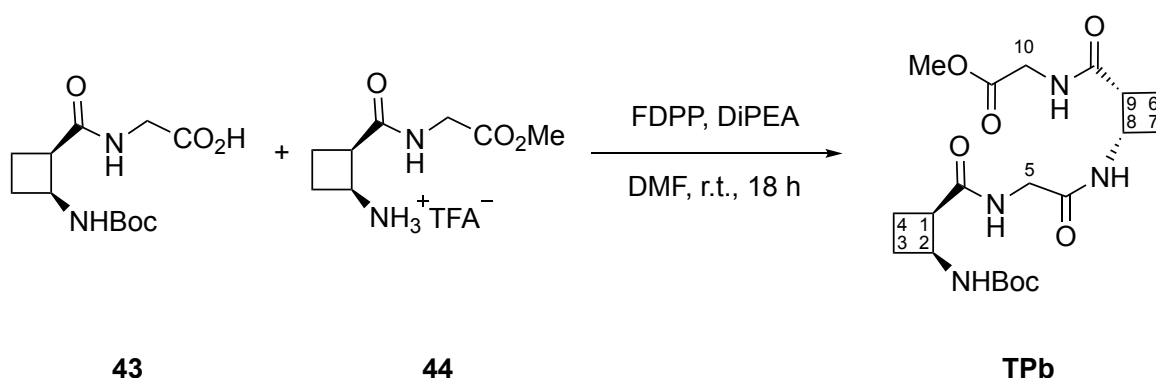
To a solution of compound **44** (0.35 g, 1.22 mmol) in anhydrous  $\text{CH}_2\text{Cl}_2$  (20 mL) was added  $\text{Et}_3\text{SiH}$  (0.58 mL, 3.66 mmol, 3 eq) and TFA (1.22 mL, 15.9 mmol, 13.0 eq) at room temperature, and the mixture was stirred for 5 h. The organic solvent was evaporated under reduced pressure and the excess of TFA was eliminated by lyophilisation. The crude of **44** (0.37 g, quantitative yield) was used in the next step without further purification.

#### Spectroscopic data for compound **44**:

$^1\text{H NMR}$  (250 MHz,  $\text{CD}_3\text{OD}$ ):  $\delta$  2.15-2.48 (m, 4H,  $\text{H}_3$ ,  $\text{H}_4$ ), 3.43 (m, 1H,  $\text{H}_1$ ), 3.71 (s, 3H, Me), 3.96 (m, 2H,  $\text{H}_5$ ), 4.01 (m, 1H,  $\text{H}_2$ ).

Spectroscopic data are consistent with those reported in reference:

Celis, S.; Gorrea, E.; Nolis, P.; Illa, O.; Ortuño, R, M. *Org. Biomol. Chem.*, **2012**, *10*, 861-868.

Tetrapeptide, **TPb**

A solution containing the free carboxylic acid **43** (0.35 g, 1.29 mmol), the amine **44** (0.36 g, 1.22 mmol, 1.0 eq), DIPEA (1.6 mL, 7.32 mmol, 6.0 eq), and FDPP (0.61 g, 1.59 mmol, 1.3 eq) in anhydrous DMF (21 mL) was stirred at room temperature overnight. Then, ethyl acetate (20 mL) was added and the combined organic layers were washed with saturated aqueous NaHCO<sub>3</sub> (3 x 15 mL). The organic layer was dried over MgSO<sub>4</sub> and solvents were removed under reduced pressure. The residue was purified by column chromatography using ethyl acetate as eluent to afford **TPb** (0.30 g, 57%) as a white solid.

**Spectroscopic data and physical constants for TPb:**

**Mp:** 168-170 °C (CH<sub>2</sub>Cl<sub>2</sub>).

**[α]<sub>D</sub><sup>20</sup>:** -157 (c = 1.0, CH<sub>3</sub>OH).

**IR (ATR):** 3327, 2952, 1733, 1681, 1639, 1516.

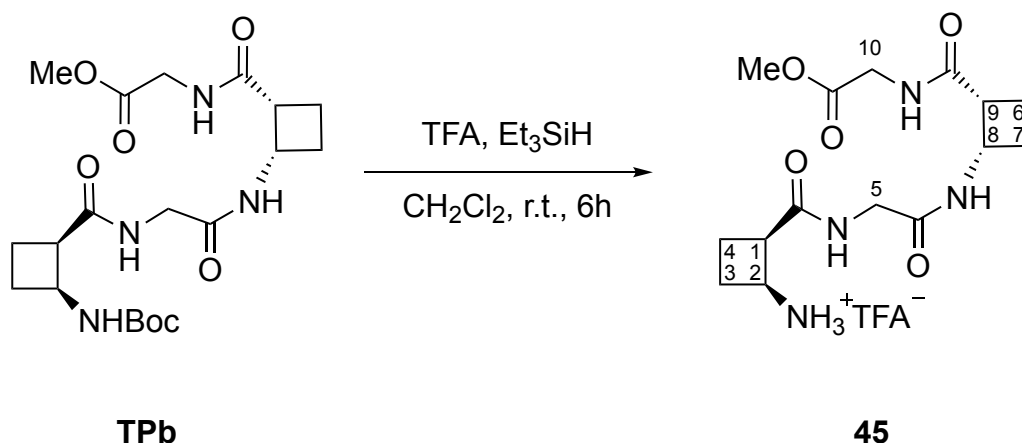
**<sup>1</sup>H NMR** (CDCl<sub>3</sub>, 400 MHz): δ 1.38 (s, 9H, *t*Bu), 1.88 (m, 2H), 2.05-2.29 (m, 6H), 3.27 (m, 2H, H<sub>1</sub>, H<sub>9</sub>), 3.74 (s, 3H, Me), 3.83 (m, 3H), 4.14 (m, 1H), 4.38 (m, 1H, H<sub>2</sub>), 4.69 (m, 1H, H<sub>8</sub>), 5.79 (m, 1H, NH), 6.61 (m, 1H, NH), 7.39 (m, 1H, NH), 7.89 (m, 1H, NH).

**<sup>13</sup>C NMR** (CDCl<sub>3</sub>, 100 MHz): δ 18.1, 18.5, 28.2, 28.8, 29.4, 41.3, 41.5, 43.0, 44.9, 45.5, 45.9, 46.4, 48.1, 52.3, 79.3, 155.3, 169.1, 171.0, 173.0.

**HRMS** (ESI) calculated for C<sub>20</sub>H<sub>32</sub>N<sub>4</sub>O<sub>7</sub>Na (M+Na<sup>+</sup>): 463.2163. Found: 463.2163

## 7. Experimental Methodologies

### Trifluoroacetate salt of TPb, **45**



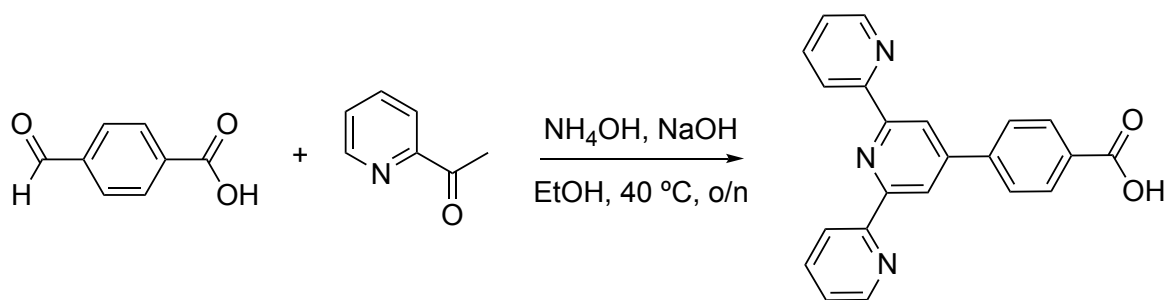
To a solution of compound **TPb** (0.36 g, 0.85 mmol) in anhydrous  $\text{CH}_2\text{Cl}_2$  (20 mL) was added  $\text{Et}_3\text{SiH}$  (0.4 mL, 2.55 mmol, 3 eq) and TFA (0.85 mL, 11.05 mmol, 13.0 eq) at room temperature, and the mixture was stirred for 6 h. The organic solvent was evaporated under reduced pressure and the excess of TFA was eliminated by lyophilisation. The crude of **45** (0.37 g, quantitative yield) was used in the next step without further purification.

#### Spectroscopic data for compound **45**:

$^1\text{H NMR}$  (250 MHz,  $\text{CD}_3\text{OD}$ ):  $\delta$  1.91-2.44 (m, 8H,  $\text{H}_3$ ,  $\text{H}_4$ ,  $\text{H}_6$ ,  $\text{H}_7$ ), 3.34-3.53 (m, 2H,  $\text{H}_1$ ,  $\text{H}_9$ ), 3.75 (s, 3H, Me), 3.79-4.06 (m, 5H,  $\text{H}_2$ ,  $\text{H}_5$ ,  $\text{H}_{10}$ ), 4.67 (m, 1H,  $\text{H}_8$ )

Spectroscopic data are consistent with those reported in reference:

Celis, S.; Gorrea, E.; Nolis, P.; Illa, O.; Ortuño, R, M. *Org. Biomol. Chem.*, **2012**, *10*, 861-868.

**4-([2,2':6',2''-Terpyridin]-4'-yl)benzoic acid, 40****40**

4-Formylbenzoic acid (5.57 g, 37.1 mmol) was dissolved in ethanol (120 mL). To this mixture was added 1-(pyridine-2-yl)ethanone (8.55 g, 70.6 mmol, 1.9 eq) and 6 mL of concentrated  $\text{NH}_4\text{OH}$  followed by the addition of  $\text{NaOH}$  (2.5 g) dissolved in 6 mL of  $\text{H}_2\text{O}$ . The reaction was stirred open to the air at  $40\text{ }^\circ\text{C}$  overnight during which time a white precipitate began to form. The reaction was cooled, and the precipitate was collected to give **40** (5.5 g). Allowing the filtrate to sit for an additional day yielded more precipitate, which yielded additional product (2.5 g). **40** was used without further purification (8.0 g, 61%) as a white solid.

**Spectroscopic data for compound 40:**

$^1\text{H NMR}$  (250 MHz,  $\text{DMSO-d}_6$ ):  $\delta$  7.52 (dd, 2H), 7.83 (d, 2H), 8.04 (dt, 2H), 8.07 (d, 2H), 8.64 (d, 2H), 8.72 (s, 2H), 8.76 (d, 2H).

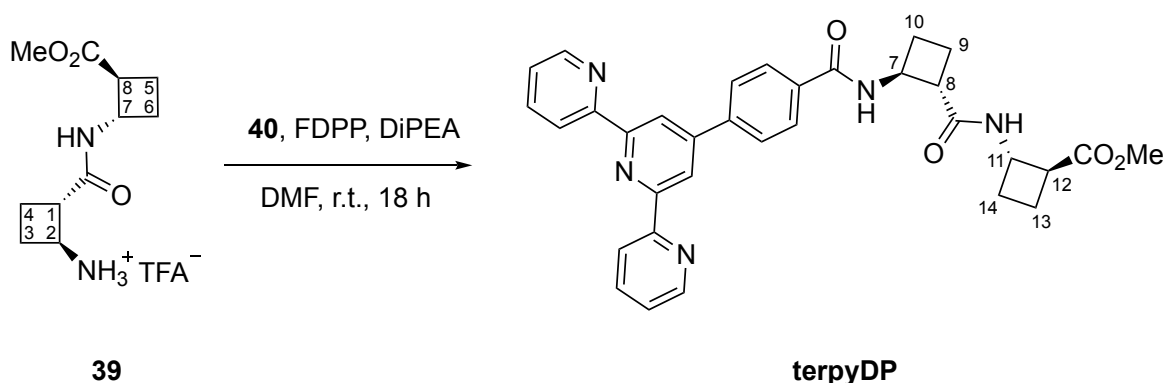
Spectroscopic data are consistent with those reported in reference:

Ashford, D. L.; Song, W.; Concepcion, J. J.; Glasson, C. R. K.; Brennaman, M. K.; Norris, M. R.; Fang, Z. F.; Templeton, J. L.; Meyer, T. J. *J. Am. Chem. Soc.* **2012**, *134*, 19189



## 7. Experimental Methodologies

### terpyDP



Acid **40** (0.141 g, 0.4 mmol) and FDPP (0.2 g, 0.52 mmol, 1.3 eq) were dissolved in DMF (8 mL) and DiPEA (0.25 mL, 1.6 mmol, 4 eq) was added under nitrogen atmosphere. After stirring for 10 min the amine **39** (0.136 g, 0.4 mmol, 1 eq) in DMF (6 mL) were added and the reaction was stirred at room temperature overnight. Then, the solution was washed with saturated NaHCO<sub>3</sub> (3 x 10 mL) and brine (10 mL). The organic phase was dried over MgSO<sub>4</sub>, filtered and evaporated under reduced pressure to give crude compound. The crude was purified by column chromatography (EtOAc, 1:1 to EtOAc/MeOH, 1:1) to afford **terpyDP** (0.140 g, 0.33 mmol, 63%) as a white solid.

#### Spectroscopic data and physical constants for terpyDP:

**Mp:** decomposition at 239 °C (CH<sub>3</sub>OH).

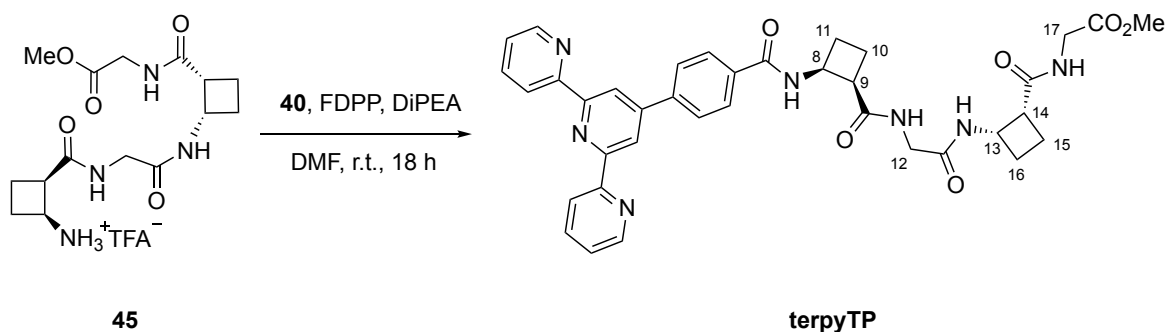
**[α]<sub>D</sub><sup>20</sup>:** +23 (c = 1.0, CH<sub>3</sub>OH).

**IR (ATR):** 3280, 2921, 2851, 2358, 1729, 1632, 1584 1541.

**<sup>1</sup>H NMR** (CDCl<sub>3</sub>, 400 MHz): δ 2.03 (m, 5H), 2.25-2.37 (m, 3H), 3.05 (m, 1H, H<sub>12</sub>), 3.24 (m, 1H, H<sub>8</sub>), 3.74 (s, 3H, Me), 4.59 (m, 2H, H<sub>7</sub>, H<sub>11</sub>), 6.69 (m, 1H, NH), 7.39 (m, 2H), 7.92 (m, 4H), 7.98 (m, 2H), 8.69 (m, 2H), 8.75 (m, 4H), 9.00 (m, 1H, NH).

**<sup>13</sup>C NMR** (CDCl<sub>3</sub>, 100 MHz): δ 18.7, 18.8, 24.5, 26.9, 46.6, 47.2, 49.6, 51.7, 118.8, 121.4, 124.0, 127.6, 133.5, 136.9, 142.2, 148.8, 149.1, 155.9, 156.1, 168.0, 172.1, 173.6.

**HRMS** (ESI) calculated for C<sub>33</sub>H<sub>31</sub>N<sub>5</sub>O<sub>4</sub>Na (M+Na<sup>+</sup>): 584.2268. Found: 584.2259

**terpyTP**

Acid **40** (0.170 g, 0.46 mmol) and FDPP (0.230 g, 0.6 mmol, 1.3 eq) were dissolved in DMF (15 mL) and DiPEA (0.5 mL, 3.2 mmol, 8 eq) was added under nitrogen atmosphere. After stirring for 10 min the amine **45** (0.160 g, 0.46 mmol, 1 eq) in DMF (6 mL) were added and the reaction was stirred at room temperature overnight. Then, the solution was washed with saturated NaHCO<sub>3</sub> (3 x 10 mL) and brine (10 mL). The organic phase was dried over MgSO<sub>4</sub>, filtered and evaporated under reduced pressure to give crude compound. The crude was purified by column chromatography (EtOAc, 1:1 to EtOAc/MeOH, 1:1) to afford **terpyTP** (0.280 g, 0.22 mmol, 49%) as a white solid.

**Spectroscopic data and physical constants for terpyTP:**

**Mp:** decomposition at 245 °C (CH<sub>3</sub>OH).

**[α]<sub>D</sub><sup>20</sup>:** -40 (c = 0.29, CH<sub>3</sub>OH).

**IR (ATR):** 3285, 2948, 1737, 1630, 1585 1537.

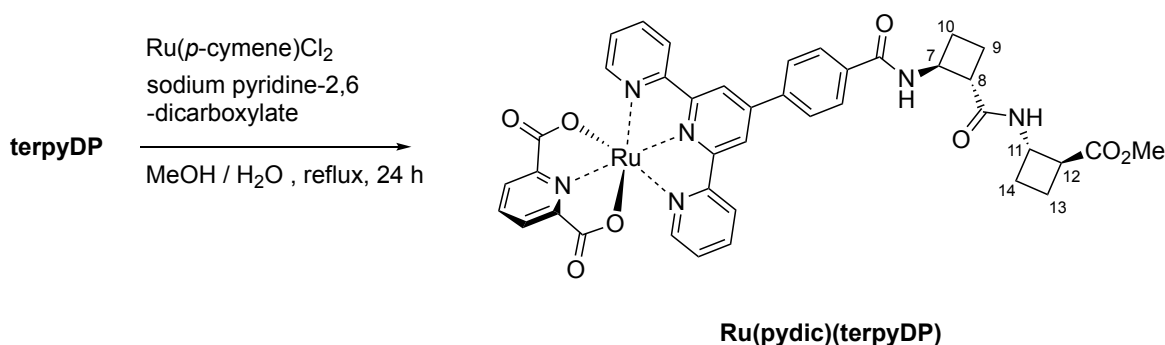
**<sup>1</sup>H NMR** (CDCl<sub>3</sub>, 400 MHz): δ 1.92-2.06 (m, 2H), 2.23 (m, 4H), 2.47 (m, 2H), 3.30 (m, 1H, H<sub>14</sub>), 3.43 (m, 1H, H<sub>9</sub>), 3.73 (s, 3H, Me), 3.82 (m, 2H), 4.05 (m, 1H), 4.21 (m, 1H), 4.68 (m, 1H), 4.99 (m, 1H), 6.44 (m, 1H, NH), 6.48 (m, 1H, NH), 7.06 (d, 1H, NH), 7.36 (m, 2H), 7.80 (d, 1H, NH), 7.88-7.93 (m, 6H), 8.65 (m, 2H), 8.72 (m, 4H).

**<sup>13</sup>C NMR** (CDCl<sub>3</sub>, 100 MHz): δ 18.1, 18.9, 28.8, 29.4, 30.5, 41.3, 45.0, 45.4, 52.4, 118.8, 121.3, 123.9, 127.9, 134.5, 136.9, 149.0, 149.3, 155.9, 171.1, 172.9.

**HRMS (ESI)** calculated for C<sub>37</sub>H<sub>37</sub>N<sub>7</sub>O<sub>8</sub>Na (M+Na<sup>+</sup>): 698.2698. Found: 698.2702

## 7. Experimental Methodologies

### Ru(pydic)(terpyDP)



[Ru(*p*-cymene)Cl<sub>2</sub>]<sub>2</sub> (43 mg, 0.07 mmol, 0.5 eq) and **terpyDP** (80 mg, 0.14 mmol, 1 eq) were dissolved in MeOH (2 mL) under N<sub>2</sub> atmosphere. Sodium 2-pyridine-2,6-dicarboxylate (30 mg, 0.14 mmol, 1 eq) was added in 0.6 mL of H<sub>2</sub>O and 1.2 mL of MeOH and the whole reaction mixture was heated at 60 °C for 1 h. After the reaction mixture was cooled to r.t. and CH<sub>2</sub>Cl<sub>2</sub> (20 mL) and H<sub>2</sub>O (20 mL) were added. The organic layer was separated and the aqueous layer was extracted with CH<sub>2</sub>Cl<sub>2</sub> (3 x 5 mL). The combined organic layer was dried over MgSO<sub>4</sub>, filtered and evaporated under reduced pressure to give crude compound. The crude was purified by column chromatography (CH<sub>2</sub>Cl<sub>2</sub> to CH<sub>2</sub>Cl<sub>2</sub>/MeOH, 100:5) to afford **Ru(pydic)(terpyDP)** (70 mg, 0.084 mmol, 60%) as a purple solid.

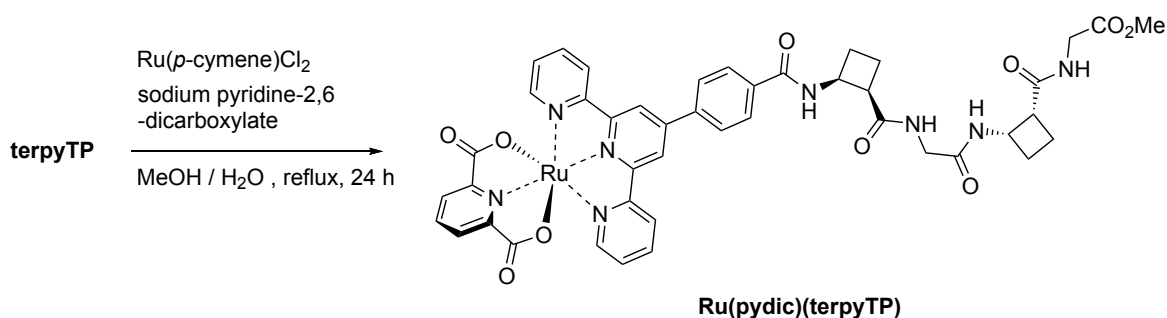
#### Spectroscopic data and physical constants for Ru(pydic)(terpyDP):

**IR** (ATR): 3261, 1725, 1615, 1540.

**<sup>1</sup>H NMR** (DMSO-*d*<sub>6</sub>, 400 MHz): δ 1.78-1.99 (m, 5H), 2.12 (m, 3H), 3.12 (m, 2H, H<sub>8</sub>, H<sub>12</sub>), 3.58 (s, 3H, Me), 4.34 (m, 1H), 4.53 (m, 1H), 6.84 (m, 1H), 7.46 (m, 1H), 7.57 (m, 2H), 7.78 (m, 1H), 7.91 (m, 1H), 8.00 (m, 2H), 8.10 (m, 2H), 8.20 (m, 2H), 8.34 (m, 3H), 8.87 (m, 2H), 8.95 (s, 2H).

**<sup>13</sup>C NMR** (DMSO-*d*<sub>6</sub>, 100 MHz): δ 18.8, 18.9, 22.6, 26.0, 26.9, 29.2, 29.5, 45.8, 47.1, 47.4, 51.9, 119.4, 123.9, 124.1, 124.2, 127.4, 127.7, 128.5, 135.2, 138.3, 138.8, 139.2, 144.2, 150.6, 150.9, 160.4, 160.9, 165.6, 166.5, 171.5, 171.8, 173.6.

**HRMS** (ESI) calculated for C<sub>40</sub>H<sub>34</sub>N<sub>6</sub>O<sub>8</sub>RuNa (M+Na<sup>+</sup>): 851.1385. Found: 851.1384

**Ru(pydic)(terpyTP)**

[Ru(*p*-cymene)Cl<sub>2</sub>]<sub>2</sub> (17 mg, 0.028 mmol, 0.5 eq) and **terpyTP** (38 mg, 0.055 mmol, 1 eq) were dissolved in MeOH (1 mL) under N<sub>2</sub> atmosphere. Sodium 2-pyridine-2,6-dicarboxylate (12 mg, 0.055 mmol, 1 eq) was added in 0.3 mL of H<sub>2</sub>O and 0.6 mL of MeOH and the whole reaction mixture was heated at 60 °C for 1 h. After the reaction mixture was cooled to r.t. and CH<sub>2</sub>Cl<sub>2</sub> (20 mL) and H<sub>2</sub>O (20 mL) were added. The organic layer was separated and the aqueous layer was extracted with CH<sub>2</sub>Cl<sub>2</sub> (3 x 5 mL). The combined organic layer was dried over MgSO<sub>4</sub>, filtered and evaporated under reduced pressure to give crude compound. The crude was purified by column chromatography (CH<sub>2</sub>Cl<sub>2</sub> to CH<sub>2</sub>Cl<sub>2</sub>/MeOH, 100:5) to afford **Ru(pydic)(terpyTP)** (28 mg, 0.030 mmol, 54%) as a purple solid.

**Spectroscopic data and physical constants for Ru(pydic)(terpyTP):**

**IR** (ATR): 3385, 1733, 1599, 1541.

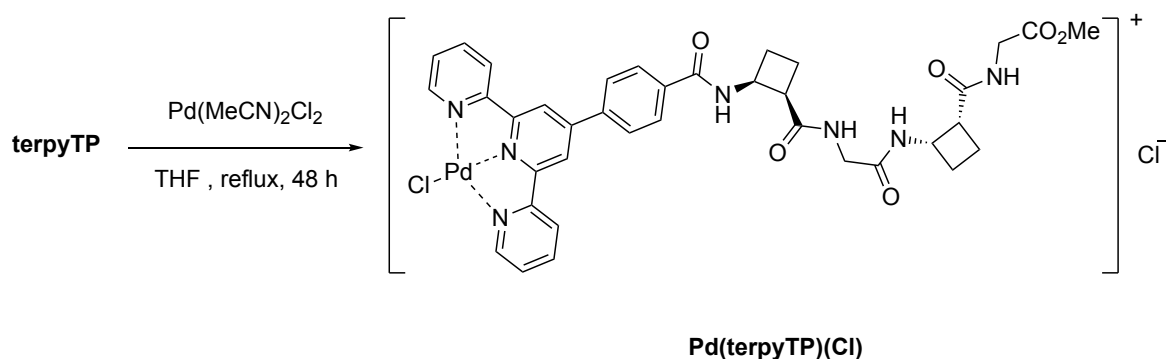
**<sup>1</sup>H NMR** (DMSO-*d*<sub>6</sub>, 400 MHz): δ 1.84-2.29 (m, 8H), 3.01 (m, 1H), 3.23 (m, 1H), 3.53 (m, 2H), 3.60 (s, 3H, Me), 3.83 (m, 2H), 4.50 (m, 1H), 4.80 (m, 1H), 6.88 (m, 1H), 7.52 (m, 2H), 7.61 (m, 1H), 7.81 (m, 2H), 7.96 (m, 2H), 8.05 (m, 2H), 8.19 (m, 2H), 8.34 (m, 3H), 8.51 (m, 1H), 8.65 (m, 1H), 8.89-8.97 (m, 4H).

**<sup>13</sup>C NMR** (DMSO-*d*<sub>6</sub>, 100 MHz): δ 18.8, 22.6, 27.0, 28.8, 29.0, 29.2, 29.3, 29.5, 31.8, 45.2, 52.2, 55.4, 119.4, 123.9, 124.1, 124.3, 127.3, 127.6, 127.8, 128.3, 135.5, 138.3, 138.8, 150.4, 150.6, 150.8, 160.4, 161.0, 168.5, 170.8, 171.0, 171.4, 171.5, 172.7, 173.1.

**HRMS** (ESI) calculated for C<sub>44</sub>H<sub>40</sub>N<sub>8</sub>O<sub>10</sub>RuNa (M+Na<sup>+</sup>): 965.1815. Found: 965.1824

## 7. Experimental Methodologies

### **Pd(terpyTP)(Cl)**



$\text{Pd}(\text{MeCN})_2\text{Cl}_2$  (40 mg, 0.148 mmol, 1 eq) and **terpyTP** (100 mg, 0.148 mmol, 1 eq) were dissolved in THF (5 mL) under  $\text{N}_2$  atmosphere and the reaction mixture was heated to reflux for 48 h. After the reaction mixture was cooled to r.t., filtered and washed with  $\text{CH}_2\text{Cl}_2$  (3 x 5 mL) and  $\text{H}_2\text{O}$  (2 x 5 mL). The precipitate was collected to afford **Pd(terpyTP)(Cl)** (101 mg, 0.117 mmol, 78%) as a dark solid.

#### **Spectroscopic data and physical constants for Pd(terpyTP)(Cl):**

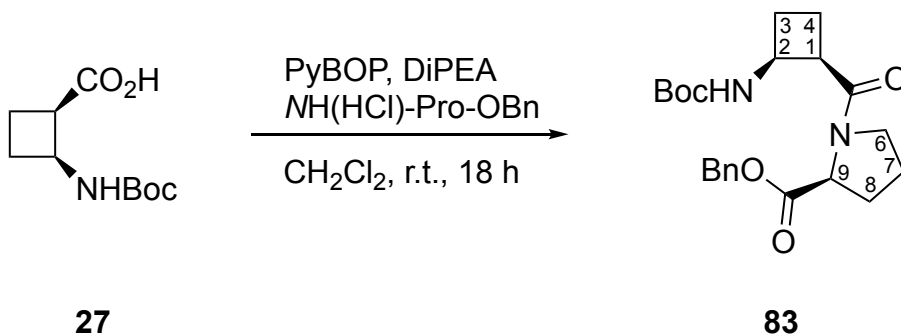
**IR (ATR):** 3315, 1720, 1645, 1543.

**$^1\text{H NMR}$  (DMSO- $d_6$ , 400 MHz):**  $\delta$  1.85-2.31 (m, 8H), 3.24 (m, 2H), 3.52 (m, 1H), 3.60 (s, 3H, OMe), 3.80 (m, 3H), 4.51 (m, 1H), 4.77 (m, 1H), 7.80 (m, 1H), 7.89 (m, 2H), 7.98 (m, 1H), 8.06 (m, 2H), 8.27 (m, 2H), 8.51 (m, 2H), 8.74 (m, 3H), 8.88 (m, 2H), 9.03 (s, 2H).

**$^{13}\text{C NMR}$  (DMSO- $d_6$ , 100 MHz):**  $\delta$  18.5, 18.9, 28.1, 28.7, 29.1, 29.4, 31.1, 41.0, 42.6, 44.6, 45.0, 46.0, 52.1, 121.9, 126.2, 128.3, 128.6, 129.3, 136.8, 137.2, 142.8, 152.1, 152.6, 154.9, 157.9, 165.3, 168.6, 171.0, 172.8, 173.0.

**HRMS (ESI) calculated for  $\text{C}_{37}\text{H}_{37}\text{N}_7\text{O}_6\text{ClPd}$  ( $\text{M}^+$ ):** 816.1534. Found: 816.1568

**Benzyl ((1*R*,2*S*)-2-(*tert*-butoxycarbonylamino)cyclobutane-1-carbonyl)-L-prolinate, **83****



Acid **27** (0.88 g, 4.1 mmol) and PyBOP (3.21 g, 6.2 mmol, 1.5 eq) were dissolved in CH<sub>2</sub>Cl<sub>2</sub> (50 mL) and DiPEA (2.83 mL, 16.4 mmol, 4 eq) was added under nitrogen atmosphere. After stirring for 10 min NH(HCl)-Pro-OBn (1.0 g, 4.1 mmol, 1 eq) in CH<sub>2</sub>Cl<sub>2</sub> (20 mL) was added and the reaction was stirred at room temperature overnight. Then, the solution was washed with saturated NaHCO<sub>3</sub> (3 x 20 mL) and brine (20 mL). The organic phase was dried over MgSO<sub>4</sub>, filtered and evaporated under reduced pressure to give crude compound. The crude was purified by column chromatography (EtOAc/hexane, 1:1) to give **83** (0.99 g, 2.5 mmol, 60%) as an oil.

**Spectroscopic data and physical constants for compound 83:**

**[α]<sub>D</sub><sup>20</sup>**: -123 (c = 1.2, CH<sub>2</sub>Cl<sub>2</sub>)

**IR** (ATR): 3327, 2976, 1744, 1706, 1633, 1500, 1434.

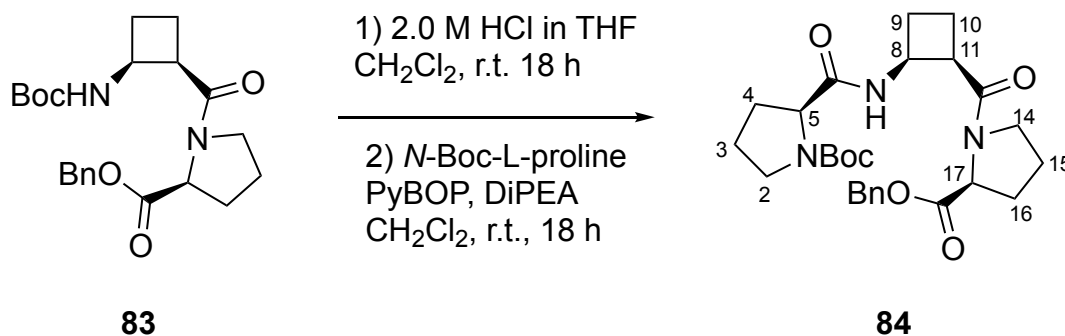
**<sup>1</sup>H NMR** (CDCl<sub>3</sub>, 250 MHz): δ 1.33 (s, 9H, *t*Bu), 1.88-2.66 (m, 8H, H<sub>3</sub>, H<sub>4</sub>, H<sub>7</sub>, H<sub>8</sub>), 3.43 (m, 3H, H<sub>1</sub>, H<sub>6</sub>), 4.45 (m, 2H, H<sub>2</sub>, H<sub>9</sub>), 5.16 (m, 2H, CH<sub>2</sub>-Ph), 5.75 (br d, 1H, *J* = 8.4 Hz), 7.27 (m, 5H, H<sub>ar</sub>).

**<sup>13</sup>C NMR** (CDCl<sub>3</sub>, 62.5 MHz): δ 18.5, 25.1, 28.7, 29.5, 29.6, 44.4, 46.4, 47.1, 59.1, 67.1, 79.4, 128.4, 128.6, 128.8, 136.1, 155.3, 172.4.

**HRMS** (ESI) calculated for C<sub>22</sub>H<sub>30</sub>N<sub>2</sub>O<sub>5</sub>Na (M+Na<sup>+</sup>): 425.2134. Found: 425.2047.

## 7. Experimental Methodologies

### ***tert*-Butyl(*S*)-2-(((1*S*,2*R*)-2-((*S*)-2-((benzyloxy)carbonyl)pyrrolidine-1-carbonyl)cyclobutyl)carbamoyl)pyrrolidine-1-carboxylate, **84****



Protected dipeptide **83** (0.22 g, 0.55 mmol) was dissolved in CH<sub>2</sub>Cl<sub>2</sub> (20 mL). A solution 2 M of HCl in THF (3.6 mL, 7.2 mmol, 13 eq) was added and the mixture was stirred overnight at room temperature. The evaporation of the solvent under reduced pressure affords the half-protected dipeptide. This product in CH<sub>2</sub>Cl<sub>2</sub> (6 mL) was added to a solution of *N*-Boc-L-proline (0.12 g, 0.55 mmol, 1 eq), PyBOP (0.43 g, 0.83 mmol, 1.5 eq) and DiPEA (0.38 mL, 2.2 mmol, 4 eq) in CH<sub>2</sub>Cl<sub>2</sub> (12 mL), which was stirred beforehand for 10 min under nitrogen atmosphere. The reaction mixture was stirred overnight at room temperature. The solution was washed with saturated NaHCO<sub>3</sub> (3 x 10 mL) and brine (10 mL). The organic phase was dried over MgSO<sub>4</sub>, filtered and evaporated under reduced pressure. Purification by column chromatography (EtOAc/hexane, from 1:1 to 1:0) gives **84** (0.22 g, 0.44 mmol, 80%) as an oil.

#### **Spectroscopic data and physical constants for compound **84**:**

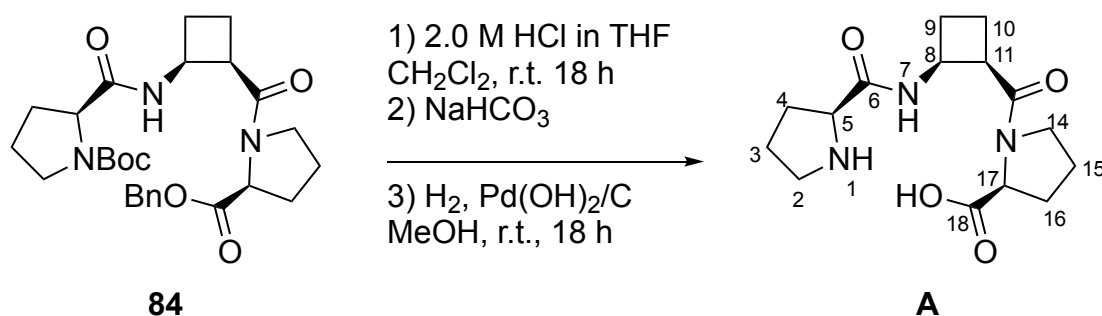
$[\alpha]_D^{20}$ : -40 (c = 1.6, CH<sub>2</sub>Cl<sub>2</sub>)

IR (ATR): 3327, 2976, 1744, 1705, 1633, 1500.

<sup>1</sup>H NMR (CDCl<sub>3</sub>, 250 MHz): δ 1.39 (s, 9H, *t*Bu), 1.77-2.24 (m, 12H, H<sub>3</sub>, H<sub>4</sub>, H<sub>9</sub>, H<sub>10</sub>, H<sub>15</sub>, H<sub>16</sub>), 3.39 (m, 5H, H<sub>2</sub>, H<sub>11</sub>, H<sub>14</sub>), 4.17 (m, 1H, H<sub>5</sub>), 4.51 (m, 1H, H<sub>17</sub>), 4.72 (m, 1H, H<sub>8</sub>), 5.07 (m, 2H, CH<sub>2</sub>-Ph), 7.28 (m, 5H, H<sub>ar</sub>).

<sup>13</sup>C NMR (CDCl<sub>3</sub>, 62.5 MHz): δ 18.3, 24.2, 24.7, 28.2, 28.4, 28.9, 29.2, 30.0, 42.9, 43.9, 46.8, 47.2, 58.4, 60.5, 66.7, 80.2, 128.0, 128.4, 135.6, 155.2, 171.7, 172.4.

HRMS (ESI) calculated for C<sub>27</sub>H<sub>37</sub>N<sub>3</sub>O<sub>6</sub> (M<sup>+</sup>): 499.2714. Found: 499.2712.

**Tripeptide A**

Protected tripeptide **84** (0.15 g, 0.3 mmol) was dissolved in CH<sub>2</sub>Cl<sub>2</sub> (10 mL). A solution of 2 M of HCl in THF (2 mL, 3.9 mmol, 13 eq) was added and the mixture was stirred overnight at room temperature. The solvent was evaporated under reduced pressure. The resulting crude was dissolved in water (4 mL) followed by the addition of a NaHCO<sub>3</sub> solution until pH = 9 was reached. This aqueous solution was extracted with CH<sub>2</sub>Cl<sub>2</sub> (3 x 20mL), dried over MgSO<sub>4</sub>, filtered and evaporated to give the half-protected tripeptide. This product was dissolved in CH<sub>3</sub>OH (8 mL) and Pd(OH)<sub>2</sub>/C (12 mg, 10% weight) was added. The mixture was stirred under 7 atm of H<sub>2</sub> at room temperature overnight. After this period, the crude was filtered through Celite and washed with CH<sub>3</sub>OH. The collected solvent was evaporated to provide **A** (92 mg, 0.3 mmol, 99%) as a white solid.

**Spectroscopic data and physical constants for A:**

**Mp:** 142-144 °C (CH<sub>3</sub>OH)

**[α]<sub>D</sub><sup>20</sup>:** -107 (c = 1.0, CH<sub>3</sub>OH)

**IR (ATR):** 3321, 2967, 2872, 1747, 1628, 1543.

**<sup>1</sup>H NMR** (CD<sub>3</sub>OD, 600 MHz): δ 1.83-2.17 (m, 9H, H<sub>3</sub>, H<sub>3'</sub>, H<sub>4</sub>, H<sub>9</sub>, H<sub>10</sub>, H<sub>15</sub>, H<sub>15'</sub>, H<sub>16</sub>, H<sub>16'</sub>), 2.38 (m, 3H, H<sub>4'</sub>, H<sub>9'</sub>, H<sub>10'</sub>), 3.27-3.36 (m, 2H, H<sub>2</sub>, H<sub>2'</sub>), 3.55 (m, 2H, H<sub>14</sub>, H<sub>14'</sub>), 3.67 (m, 1H, H<sub>11</sub>), 4.26 (m, 2H, H<sub>5</sub>, H<sub>17</sub>), 4.65 (m, 1H, H<sub>8</sub>).

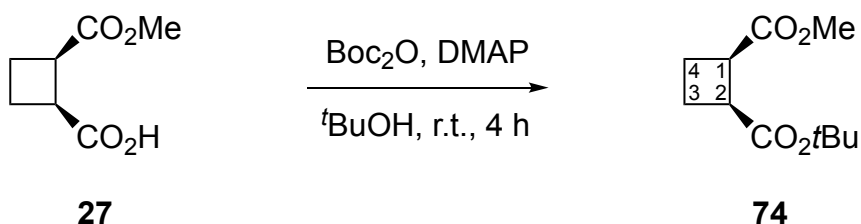
**<sup>13</sup>C NMR** (CD<sub>3</sub>OD, 150 MHz): δ 18.4 (C<sub>10</sub>), 23.7 (C<sub>3</sub>), 24.3 (C<sub>15</sub>), 25.8 (C<sub>9</sub>), 29.1 (C<sub>16</sub>), 30.2 (C<sub>4</sub>), 43.6 (C<sub>11</sub>), 46.1 (C<sub>2</sub>), 46.4 (C<sub>8</sub>), 46.9 (C<sub>14</sub>), 59.0 (C<sub>17</sub>), 59.5 (C<sub>5</sub>), 167.8 (C<sub>6</sub>), 171.0 (C<sub>12</sub>), 174.5 (C<sub>18</sub>).

**HRMS (ESI)** calculated for C<sub>15</sub>H<sub>23</sub>N<sub>3</sub>O<sub>4</sub> (M<sup>+</sup>): 309.1791. Found: 309.1782.



## 7. Experimental Methodologies

### 1-(*tert*-Butyl) 2-methyl (1*S*,2*R*)-cyclobutane-1,2-dicarboxylate, **74**



A solution of half-ester **27** (2.61 g, 16.5 mmol) in 54 mL of *tert*-butanol,  $\text{Boc}_2\text{O}$  (10.8 g, 49.5 mmol, 3 eq) and DMAP (0.60 g, 4.95 mmol, 0.3 eq) were subsequently added. The mixture was stirred at room temperature for 4 h. Then, the solvent was evaporated and the residue was purified by column chromatography (3:1 hexane-EtOAc as eluent) affording the product **74** as a white solid (2.58 g, 12.1 mmol, 73% yield).

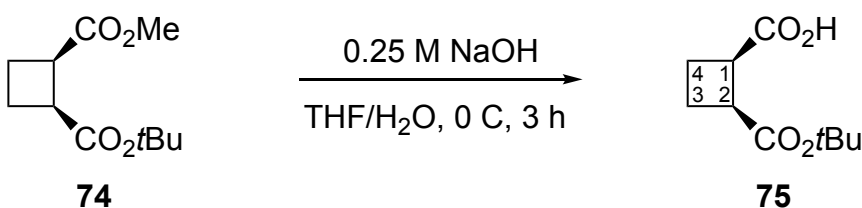
#### Spectroscopic data for compound **74**:

$^1\text{H NMR}$  (250 MHz,  $\text{CDCl}_3$ ):  $\delta$  1.43 (s, 9H, *t*Bu), 2.16 (m, 2H), 2.35 (m, 2H), 3.32 (m, 2H,  $\text{H}_1$ ,  $\text{H}_2$ ), 3.68 (s, 3H, Me).

Spectroscopic data are consistent with those reported in reference:

Izquierdo, S.; Martin-Vila, M.; Moglioni, A. G.; Branchadell, V.; Ortuno, R. M., *Tetrahedron: Asymmetry*, **2002**, *13*, 2403.

### (1*R*,2*S*)-2-(*tert*-Butoxycarbonyl)cyclobutane-1-carboxylic acid, **75**



To an ice-cooled solution of ester **74** (1.57 g, 7.33 mmol) in a 1:10 THF-water mixture (40 mL), 0.25 M sodium hydroxide aqueous solution (70 mL, 18.32 mmol, 2.5 eq) was added and the resultant mixture was stirred for 3 h. The reaction mixture was washed with dichloromethane (50 mL), and 5% HCl aqueous solution was added to the aqueous phase to reach pH 2. The acid solution was extracted with ethyl acetate (4 x 80 mL) and dried over magnesium sulphate. Solvent was

removed at reduced pressure to afford crude **75** as a yellowish oil (1.46 g, 7.29 mmol, 99% yield) without need of further purification.

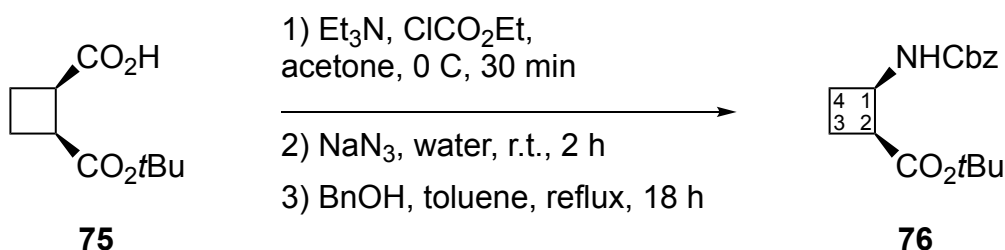
**Spectroscopic data for compound 75:**

<sup>1</sup>H NMR (250 MHz, CDCl<sub>3</sub>): δ 1.46 (s, 9H, *t*Bu), 2.22 (m, 2H), 2.38 (m, 2H), 3.38 (m, 2H, H<sub>1</sub>, H<sub>2</sub>).

Spectroscopic data are consistent with those reported in reference:

Izquierdo, S.; Martin-Vila, M.; Moglioni, A. G.; Branchadell, V.; Ortuno, R. M., *Tetrahedron: Asymmetry*, **2002**, *13*, 2403.

***tert*-Butyl (1*S*,2*R*)-2-((benzyloxycarbonyl)amino)cyclobutane-1-carboxylate, **76****



To an ice-cooled solution of half-ester **75** (1.46 g, 7.3 mmol) in anhydrous acetone (40 mL), triethylamine (1.3 mL, 9.5 mmol, 1.3 eq) and ethyl chloroformate (1.3 mL, 9.5 mmol, 1.3 eq) were subsequently added. The mixture was stirred at 0 °C for 30 minutes. Then, sodium azide (1.19 g, 18.2 mmol, 2.5 eq) in 25 mL of water was added and the resultant solution was stirred at room temperature for 2 h. The reaction mixture was extracted with dichloromethane (4 x 20 mL), and the organic extracts were dried over magnesium sulphate and the solvents were removed under reduced pressure. The crude was dissolved in toluene (50 mL) and benzyl alcohol (1.43 mL, 16.6 mmol, 1.2 eq) was added. Then, the mixture was heated to reflux for 18 hours. Toluene was removed under reduced pressure and then the excess of benzyl alcohol was eliminated by lyophilisation. The residue was chromatographed on silica gel (1:4 ethyl acetate-hexane as eluent) to afford carbamate **76** (1.19 g, 3.90 mmol, 54% yield).

## 7. Experimental Methodologies

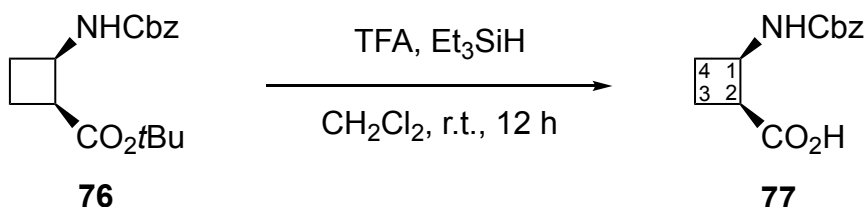
### Spectroscopic data for compound **76**:

$^1\text{H NMR}$  (250 MHz,  $\text{CDCl}_3$ ):  $\delta$  1.43 (s, 9H, *t*Bu), 1.95 (m, 2H), 2.20 (m, 1H), 2.34 (m, 1H), 3.25 (m, 1H,  $\text{H}_2$ ), 4.49 (m, 1H,  $\text{H}_1$ ), 5.08 (m, 2H,  $\text{CH}_2$ -Ph), 5.65 (d, 1H,  $J = 9.4$  Hz, NH), 7.34 (m, 5H,  $\text{H}_{\text{ar}}$ ).

Spectroscopic data are consistent with those reported in reference:

Izquierdo, S.; Martin-Vila, M.; Moglioni, A. G.; Branchadell, V.; Ortuno, R. M., *Tetrahedron: Asymmetry*, **2002**, *13*, 2403.

### (1*S*,2*R*)-2-((Benzyloxy)carbonylamino)cyclobutane-1-carboxylic acid, **77**



A mixture containing compound **76** (3.37 g, 11.0 mmol), TFA (11.7 mL, 152.1 mmol, 13 eq) and triethylsilane (2.5 mL, 30.0 mmol, 2.5 eq) in anhydrous dichloromethane (25 mL) was stirred at room temperature for 12 h. The solvent was evaporated and excess of TFA acid was removed by lyophilisation affording acid **77** as a yellowish oil (2.70 g, 10.8 mmol, 98% yield).

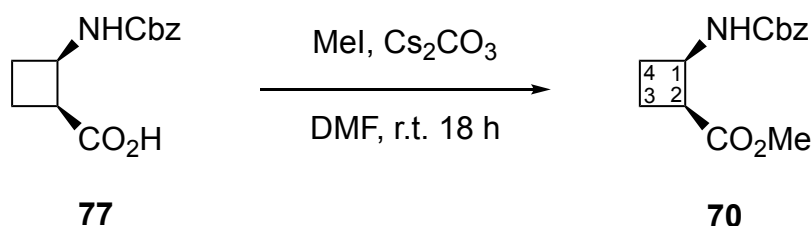
### Spectroscopic data for compound **77**:

$^1\text{H NMR}$  (250 MHz,  $\text{CDCl}_3$ ):  $\delta$  2.04 (m, 2H), 2.36 (m, 2H), 3.40 (m, 1H,  $\text{H}_2$ ), 4.54 (m, 1H,  $\text{H}_1$ ), 5.09 (m, 2H,  $\text{CH}_2$ -Ph), 5.83 (m, 1H, NH), 7.35 (m, 5H,  $\text{H}_{\text{ar}}$ ).

Spectroscopic data are consistent with those reported in reference:

Izquierdo, S.; Martin-Vila, M.; Moglioni, A. G.; Branchadell, V.; Ortuno, R. M., *Tetrahedron: Asymmetry*, **2002**, *13*, 2403.

**Methyl (1*S*,2*R*)-2-((benzyloxy)carbonylamino)cyclobutane-1-carboxylate, **70****



Acid **77** (0.9 g, 3.61 mmol) and  $\text{Cs}_2\text{CO}_3$  (1.29 g, 3.96 mmol, 1.1 eq) were dissolved in DMF (35 mL). Then, MeI (0.3 mL, 4.82 mmol, 1.3 eq) was added and the mixture was stirred at room temperature overnight. The excess of MeI was removed by bubbling  $\text{N}_2$  and EtOAc (25 mL) was added. The solution was washed with saturated  $\text{NaHCO}_3$  (3 x 20 mL) and brine (20 mL). The organic phase was dried over  $\text{MgSO}_4$ , filtered and evaporated under reduced pressure to give ester **70** as an oil (0.99 g, 3.76 mmol, 95% yield).

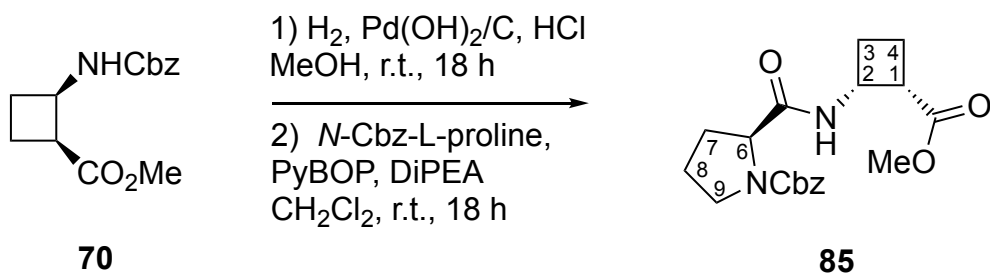
**Spectroscopic data for compound 70:**

$^1\text{H NMR}$  (250 MHz,  $\text{CDCl}_3$ ):  $\delta$  1.97 (m, 2H), 2.18-2.43 (m, 2H), 3.39 (m, 1H,  $\text{H}_2$ ), 3.66 (s, 3H, Me), 4.46 (m, 1H,  $\text{H}_1$ ), 5.08 (m, 2H,  $\text{CH}_2\text{-Ph}$ ), 5.64 (m, 1H, NH), 7.32 (m, 5H,  $\text{H}_{\text{ar}}$ ).

Spectroscopic data are consistent with those reported in reference:

Izquierdo, S.; Martin-Vila, M.; Moglioni, A. G.; Branchadell, V.; Ortuno, R. M., *Tetrahedron: Asymmetry*, **2002**, *13*, 2403.

**Benzyl(*S*)-2-(((1*R*,2*S*)-2 (methoxycarbonyl)cyclobutyl)carbamoyl)pyrrolidine-1-carboxylate, **85****



## 7. Experimental Methodologies

Amino acid **70** (0.8 g, 3.0 mmol) was dissolved in CH<sub>3</sub>OH (40 mL). Then, Pd(OH)<sub>2</sub>/C (80 mg, 10% weight) and 2 M HCl in THF (1.5 mL, 1eq) were added and the mixture was stirred under 7 atm of H<sub>2</sub> at r.t. overnight. After this period, the crude was filtered through Celite and washed with CH<sub>3</sub>OH. The collected solvent was evaporated to provide the half-protected amino acid. This product in CH<sub>2</sub>Cl<sub>2</sub> (20 mL) was added to a solution of *N*-Cbz-L-proline (0.75 g, 3.0 mmol, 1 eq), PyBOP (2.34 g, 4.5 mmol, 1.5 eq) and DiPEA (2.1 mL, 12 mmol, 4 eq) in CH<sub>2</sub>Cl<sub>2</sub> (25 mL), which was stirred beforehand for 10 min under nitrogen atmosphere. The reaction mixture was stirred overnight. The solution was washed with saturated NaHCO<sub>3</sub> (3 x 10 mL) and brine (10 mL). The organic phase was dried over MgSO<sub>4</sub>, filtered and evaporated under reduced pressure. Purification by column chromatography (EtOAc/hexane,1:) gives **85** (0.94, 2.6 mmol, 86%) as a white solid.

### Spectroscopic data and physical constants for compound **85**:

**Mp**: 46-47 °C (CH<sub>3</sub>OH)

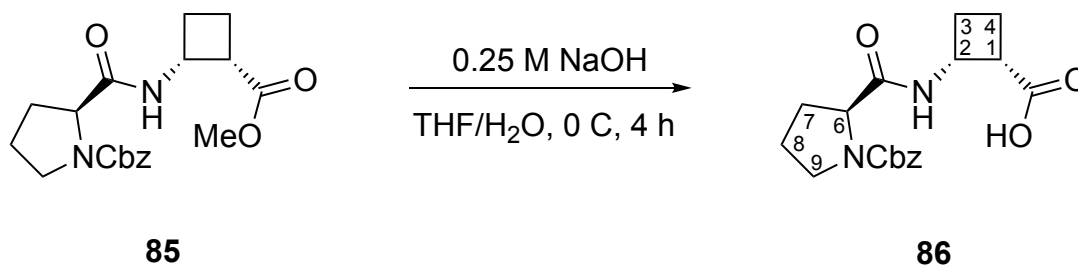
**[α]<sub>D</sub><sup>20</sup>**: +3 (c = 1.0, CH<sub>3</sub>OH)

**IR** (ATR): 3401, 2956, 1671, 1526, 1421.

**<sup>1</sup>H NMR** (CDCl<sub>3</sub>, 250 MHz): δ 1.88-2.22 (m, 8H, H<sub>3</sub>, H<sub>4</sub>, H<sub>7</sub>, H<sub>8</sub>), 3.35 (m, 1H, H<sub>1</sub>), 3.52 (m, 2H, H<sub>9</sub>), 3.65 (s, 3H, Me), 4.31 (m, 1H, H<sub>2</sub>), 4.67 (m, 1H, H<sub>6</sub>), 5.20 (m, 2H, CH<sub>2</sub>-Ph), 7.33 (m, 5H, H<sub>ar</sub>).

**<sup>13</sup>C NMR** (CDCl<sub>3</sub>, 90 MHz): δ 18.7, 19.1, 23.5, 24.4, 29.1, 31.0, 44.1, 44.5, 51.7, 60.6, 67.3, 127.9, 128.5, 136.4, 171.2, 174.4.

**HRMS** (ESI) calculated for C<sub>19</sub>H<sub>24</sub>N<sub>2</sub>O<sub>5</sub>Na (M+Na<sup>+</sup>): 383.1577. Found: 383.1580.

**(1*S*,2*R*)-2-((*S*)-1-((Benzyloxy)carbonyl)pyrrolidine-2-carboxamido)cyclobutane-1-carboxylic acid, **86****

To an ice-cooled solution of protected dipeptide **85** (0.5 g, 1.4 mmol) in 1:10 THF/water (60 mL), 0.25 M of NaOH aqueous solution (14 mL, 3.5 mmol, 2.5 eq) was added and the resultant mixture was stirred for 4 h. Then, the mixture was washed with CH<sub>2</sub>Cl<sub>2</sub> (20 mL) and 5% HCl aqueous solution was added to the aqueous phase to reach pH 2. The acid solution was extracted with EtOAc (3 x 20 mL) and the organic phases were dried over MgSO<sub>4</sub>, filtered and evaporated under reduced pressure to give compound **86** (0.47 g, 1.4 mmol, 98%) as white solid without need for further purification.

**Spectroscopic data and physical constants for compound 86:**

**Mp:** 70-71 °C (CH<sub>3</sub>OH).

**[α]<sub>D</sub><sup>20</sup>:** -18 (c = 0.8, CH<sub>3</sub>OH).

**IR (ATR):** 3306, 2952, 2881, 1701, 1655, 1524, 1409.

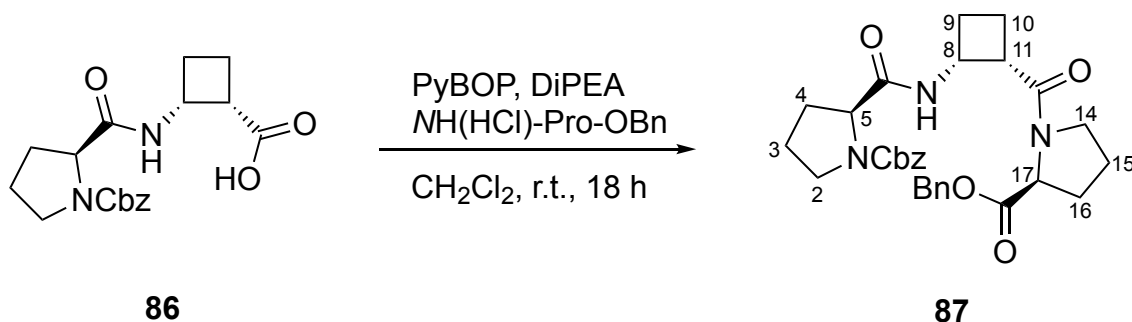
**<sup>1</sup>H NMR** (CDCl<sub>3</sub>, 250 MHz): δ 1.81-2.11 (m, 8H, H<sub>3</sub>, H<sub>4</sub>, H<sub>7</sub>, H<sub>8</sub>), 3.36 (m, 1H, H<sub>1</sub>), 3.50 (m, 2H, H<sub>9</sub>), 4.34 (m, 1H, H<sub>2</sub>), 4.71 (m, 1H, H<sub>6</sub>), 5.02 (m, 2H, CH<sub>2</sub>-Ph), 7.29 (m, 5H, H<sub>ar</sub>).

**<sup>13</sup>C NMR** (CDCl<sub>3</sub>, 90 MHz): δ 18.8, 28.4, 28.8, 29.5, 31.2, 43.9, 44.6, 47.0, 47.4, 60.9, 67.4, 127.8, 128.1, 128.5, 136.0, 155.8, 171.7, 176.5

**HRMS (ESI)** calculated for C<sub>18</sub>H<sub>22</sub>N<sub>2</sub>O<sub>5</sub>Na (M+Na<sup>+</sup>): 369.1421. Found: 369.1425

## 7. Experimental Methodologies

### **Benzyl (S)-2-(((1R,2S)-2-((S)-2-((benzyloxy)carbonyl)pyrrolidine-1-carbonyl)cyclobutyl)carbamoyl)pyrrolidine-1-carboxylate, **87****



Acid **86** (0.33 g, 0.95 mmol) and PyBOP (0.73, 1.4 mmol, 1.5 eq) were dissolved in CH<sub>2</sub>Cl<sub>2</sub> (12 mL) and DiPEA (0.25 mL, 3.8 mmol, 4 eq) was added under nitrogen atmosphere. After stirring for 10 min NH(HCl)-Pro-OBn (0.23 g, 0.95 mmol, 1 eq) in CH<sub>2</sub>Cl<sub>2</sub> (5 mL) were added and the reaction was stirred at room temperature overnight. Then, the solution was washed with saturated NaHCO<sub>3</sub> (3 x 10 mL) and brine (10 mL). The organic phase was dried over MgSO<sub>4</sub>, filtered and evaporated under reduced pressure to give crude compound **87**. The crude was purified by column chromatography (EtOAc/hexane, from 1:1 to 1:0) to afford **87** (0.35 g, 0.66 mmol, 69%) as a white solid.

#### **Spectroscopic data and physical constants for compound 87:**

**Mp:** 52-54 °C (CH<sub>3</sub>OH).

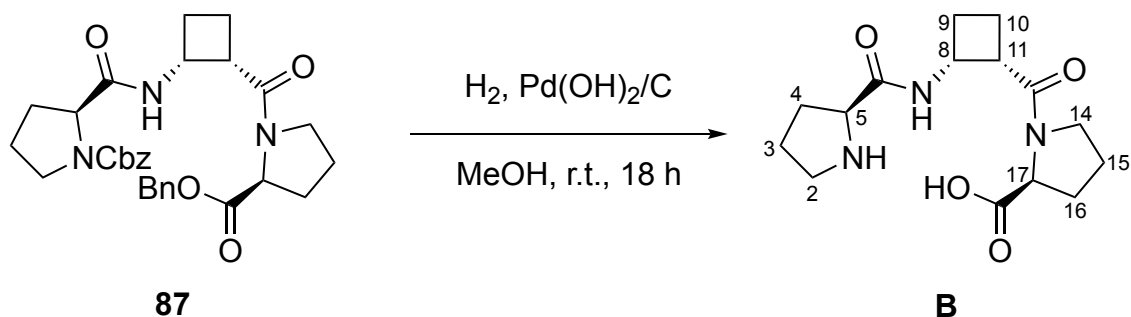
**[α]<sub>D</sub><sup>20</sup>:** -30 (c = 1.0, CH<sub>3</sub>OH).

**IR (ATR):** 3315, 2951, 2880, 1685, 1629, 1524.

**<sup>1</sup>H NMR** (CD<sub>3</sub>OD, 400 MHz): δ 1.88-2.30 (m, 12H, H<sub>3</sub>, H<sub>4</sub>, H<sub>9</sub>, H<sub>10</sub>, H<sub>15</sub>, H<sub>16</sub>), 3.51-3.60 (m, 5H, H<sub>2</sub>, H<sub>11</sub>, H<sub>14</sub>), 4.27 (m, 1H, H<sub>5</sub>), 4.58 (m, 1H, H<sub>17</sub>), 4.96 (m, 1H, H<sub>8</sub>), 5.24 (m, 4H, CH<sub>2</sub>-Ph), 7.39 (m, 10H, H<sub>ar</sub>).

**<sup>13</sup>C NMR** (CD<sub>3</sub>OD, 150 MHz): δ 17.4, 22.3, 23.6, 24.4, 24.7, 26.6, 28.9, 29.0, 29.8, 30.7, 31.7, 43.3, 43.9, 45.2, 45.5, 46.5, 59.4, 60.5, 67.1, 127.7, 128.1, 128.5, 136.2, 137.23, 155.6, 173.3.

**HRMS** (ESI) calculated for C<sub>30</sub>H<sub>35</sub>N<sub>3</sub>O<sub>6</sub>Na (M+Na<sup>+</sup>): 556.2418. Found: 556.2432.

**Tripeptide B**

Protected tripeptide **87** (0.24 g, 0.45 mmol) was dissolved in  $\text{CH}_3\text{OH}$  (12 mL) and  $\text{Pd}(\text{OH})_2/\text{C}$  (24 mg, 10% weight) was added. The mixture was stirred under 7 atm of  $\text{H}_2$  at room temperature overnight. After this period, the crude was filtered through Celite and washed with  $\text{CH}_3\text{OH}$ . The collected solvent was evaporated to provide **B** (0.14 g, 0.45 mmol, 99%) as a white solid without need for further purification.

**Spectroscopic data and physical constants for B:**

**Mp:** 173-176 °C ( $\text{CH}_3\text{OH}$ ).

**$[\alpha]_D^{20}$ :** -33 ( $c = 1.0, \text{CH}_3\text{OH}$ ).

**IR (ATR):** 3204, 2950, 1673, 1573, 1447.

**$^1\text{H NMR}$**  ( $\text{CD}_3\text{OD}$ , 400 MHz):  $\delta$  1.92-2.17 (m, 9H,  $\text{H}_3, \text{H}_3', \text{H}_4, \text{H}_9, \text{H}_{10}, \text{H}_{15}, \text{H}_{15}', \text{H}_{16}, \text{H}_{16}'$ ), 2.30-2.44 (m, 3H,  $\text{H}_4', \text{H}_9', \text{H}_{10}'$ ), 3.38 (m, 2H,  $\text{H}_2, \text{H}_2'$ ), 3.48 (m, 2H,  $\text{H}_{14}, \text{H}_{14}'$ ), 3.69 (m, 1H,  $\text{H}_{11}$ ), 4.31 (m, 1H,  $\text{H}_5$ ), 4.43 (m, 1H,  $\text{H}_{17}$ ), 4.81 (m, 1H,  $\text{H}_8$ ).

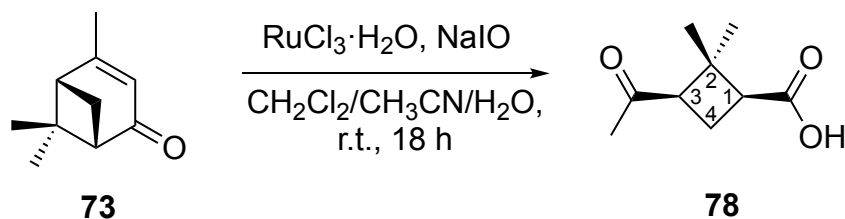
**$^{13}\text{C NMR}$**  ( $\text{CD}_3\text{OD}$ , 150 MHz):  $\delta$  16.7, 23.7, 24.1, 27.9, 29.4, 29.7, 43.3, 45.8, 59.7, 61.2, 168.2, 170.3, 177.9.

**HRMS (ESI)** calculated for  $\text{C}_{15}\text{H}_{24}\text{N}_3\text{O}_4$  ( $\text{M}+\text{H}^+$ ): 310.1761. Found: 310.1760.



## 7. Experimental Methodologies

### (1*S*,3*R*)-3-Acetyl-2,2-dimethylcyclobutane-1-carboxylic acid, **78**



To a stirred solution of (–)-verbenone **73** (4.5 mL, 29.3 mmol) in 2:2:3 dichloromethane/acetonitrile/water (240 mL) were added catalytic RuCl<sub>3</sub> hydrate (0.12 g, 0.02 eq) and NaIO<sub>4</sub> (26.3 g, 123.0 mmol, 4.2 eq). The mixture was stirred at room temperature for 18 h. The crude obtained was filtered through Celite® and the organic layer was extracted with dichloromethane (3 x 40 mL). Then, the combined organic extracts were dried over MgSO<sub>4</sub> and concentrated under vacuum to afford the (–)-*cis*-pinonic acid **78** (4.74 g, 95% yield), which is used without further purification.

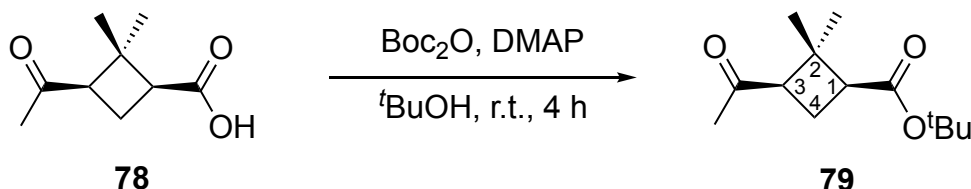
#### Spectroscopic data for compound **78**:

<sup>1</sup>H NMR (250 MHz, CDCl<sub>3</sub>): δ 0.97 (s, 3H, CH<sub>3</sub>), 1.45 (s, 3H, CH<sub>3</sub>), 1.91 (m, 1H, H<sub>4</sub>), 2.07 (s, 3H, COCH<sub>3</sub>), 2.62 (m, 1H, H<sub>4</sub>'), 2.86 (m, 2H, H<sub>1</sub>, H<sub>3</sub>).

Spectroscopic data are consistent with those reported in reference:

Burgess, K.; Li, S.; Rebenspies, J.; *Tetrahedron Lett.* **1997**, *38*, 1681-1684.

### *tert*-Butyl (1*S*,3*R*)-3-acetyl-2,2-dimethylcyclobutane-1-carboxylate, **79**



A solution of half-ester **78** (1.70 g, 9.99 mmol) in 35 mL of *tert*-butanol, Boc<sub>2</sub>O (6.54 g, 29.96 mmol, 3 eq) and DMAP (0.37 g, 3.00 mmol, 0.3 eq) were subsequently added. The mixture was stirred at room temperature for 4 h. Then,

the solvent was evaporated and the residue was purified by column chromatography (3:1 hexane-EtOAc as eluent) affording the product **79** as a white solid (2.10 g, 9.29 mmol, 93% yield).

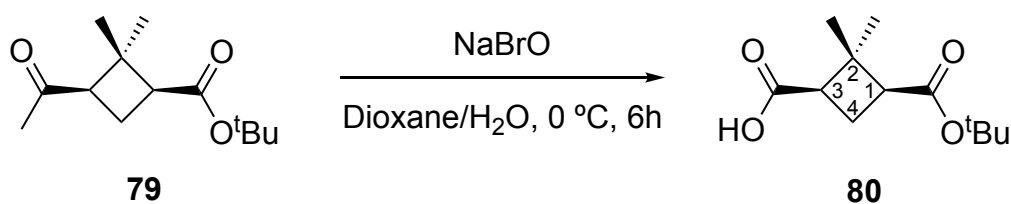
**Spectroscopic data for compound 79:**

$^1\text{H NMR}$  (250 MHz,  $\text{CDCl}_3$ ):  $\delta$  0.90 (s, 3H,  $\text{CH}_3$ ), 1.39 (s, 3H,  $\text{CH}_3$ ), 1.42 (s, 9H,  $t\text{Bu}$ ), 1.65-2.01 (m, 1H,  $\text{H}_4$ ), 2.03 (s, 3H,  $\text{COCH}_3$ ), 2.48-2.69 (m, 2H,  $\text{H}_1, \text{H}_4'$ ), 2.81 (m, 1H,  $\text{H}_3$ ).

Spectroscopic data are consistent with those reported in reference:

Rouge, P.; Monglioni, A.; Moltrasio, G.; Ortuño, R., M., *Tetrahedron: Asymmetry* **2003**, *142*, 193-195

**(1*R*,3*S*)-3-(*tert*-Butoxycarbonyl)-2,2-dimethylcyclobutane-1-carboxylic acid, **80****



To an ice cooled solution of ketone **79** (0.410 g, 1.8 mmol) in dioxane-water (7:2, 13 mL) was added a sodium hypobromite solution, prepared from bromine (0.33 mL, 6.5 mmol, 3.6 eq) and sodium hydroxide (0.50 g, 12.6 mmol, 7 eq) in 3:1 mixture of water-dioxane (24 mL). The resulting mixture was stirred for 6 hours at 0 °C. Then, sodium bisulphite was added (7 mL) and the mixture was brought to acidic pH by adding 5% hydrochloric acid. The acid solution was extracted with dichloromethane (4 x 30 mL) and the organic phases were dried over magnesium sulphate and the solvent was evaporated under to dryness to afford carboxylic acid **80** as a white powder (0.383 g, 93% yield).

## 7. Experimental Methodologies

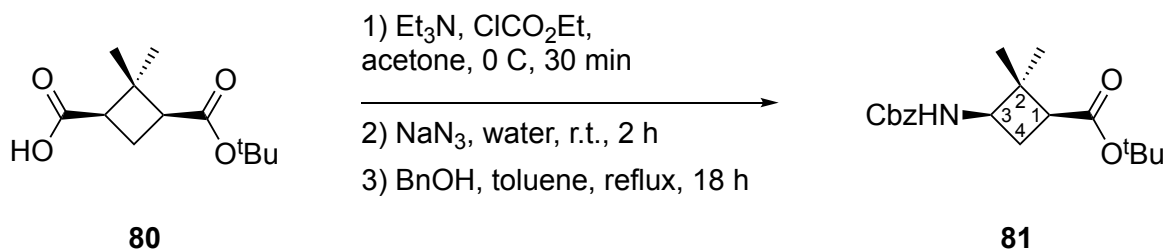
### Spectroscopic data for compound **80**:

$^1\text{H NMR}$  (250 MHz,  $\text{CDCl}_3$ ):  $\delta$  1.01 (s, 3H,  $\text{CH}_3$ ), 1.30 (s, 3H,  $\text{CH}_3$ ), 1.41 (s, 9H,  $t\text{Bu}$ ), 1.90-2.05 (m, 1H,  $\text{H}_4$ ), 2.39-2.55 (m, 1H,  $\text{H}_4'$ ), 2.59-2.86 (m, 2H,  $\text{H}_1$ ,  $\text{H}_3$ ).

Spectroscopic data are consistent with those reported in reference:

Aguado, G. P.; Moglioni, A. G.; Brousse, B. N.; Ortuño, R. M. *Tetrahedron: Asymmetry* **2003**, *14*, 2445-2451.

### *tert*-Butyl(1*S*,3*R*)-3-((benzyloxycarbonyl)amino)-2,2-dimethyl cyclobutane-1-carboxylate, **81**



To an ice-cooled solution of acid **80** (0.30 g, 1.3 mmol) in anhydrous acetone (10 mL), triethylamine (0.29 mL, 1.5 mmol, 1.5 eq) and ethyl chloroformate (0.2 mL, 2.0 mmol, 1.5 eq) were subsequently added. The mixture was stirred at 0 °C for 30 minutes. Then, sodium azide (145 mg, 2.2 mmol, 1.7 eq) in 5 mL of water was added and the resultant solution was stirred at room temperature for 2 h. The reaction mixture was extracted with dichloromethane (4 x 20 mL), and the organic extracts were dried over magnesium sulphate and the solvents were removed under reduced pressure. The crude was dissolved in toluene (13 mL) and benzyl alcohol (0.17 mL, 1.95 mmol, 1.5 eq) was added. Then, the mixture was heated to reflux for 18 hours. Toluene was removed under reduced pressure and then the excess of benzyl alcohol was eliminated by lyophilisation. The residue was chromatographed on silica gel (1:2 ethyl EtOAc-hexane as eluent) to afford carbamate **81** as an oil (0.307 g, 0.92 mmol, 71% yield).

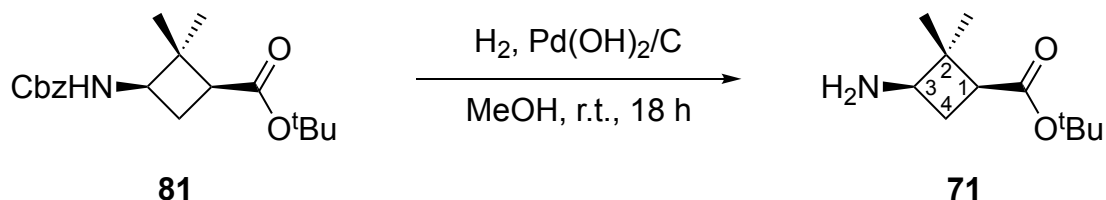
**Spectroscopic data for compound 81:**

$^1\text{H NMR}$  (250 MHz,  $\text{CDCl}_3$ ):  $\delta$  0.95 (s, 3H,  $\text{CH}_3$ ), 1.30 (s, 3H,  $\text{CH}_3$ ), 1.46 (s, 9H,  $t\text{Bu}$ ), 2.02 (m, 1H,  $\text{H}_4$ ), 2.25-2.36 (m, 1H,  $\text{H}_4'$ ), 2.51 (m, 1H,  $\text{H}_1$ ), 3.90 (m, 1H,  $\text{H}_3$ ), 5.13 (m, 2H,  $\text{CH}_2\text{-Ph}$ ), 7.36 (m, 5H,  $\text{H}_{\text{ar}}$ ).

Spectroscopic data are consistent with those reported in reference:

Aguilera, J.; Moglioni, A. G.; Moltrasio, G. Y.; Ortuño, R. M. *Tetrahedron: Asymmetry* **2008**, *19*, 302-308.

***tert*-Butyl(1*S*,3*R*)-3-amino-2,2-dimethylcyclobutane-1-carboxylate,  
71**



Carbamate **81** (0.50 g, 1.75 mmol) in methanol (5 mL) was hydrogenated under 7 atmospheres of pressure in the presence  $\text{Pd(OH)}_2/\text{C}$  (0.1 g, 20% weight) at r.t. overnight. The reaction mixture was filtered through Celite and solvent was removed under vacuum to provide amine **71** as an oil (0.330 g, 1.66 mmol, 95% yield), which is used without further purification.

**Spectroscopic data for compound 71:**

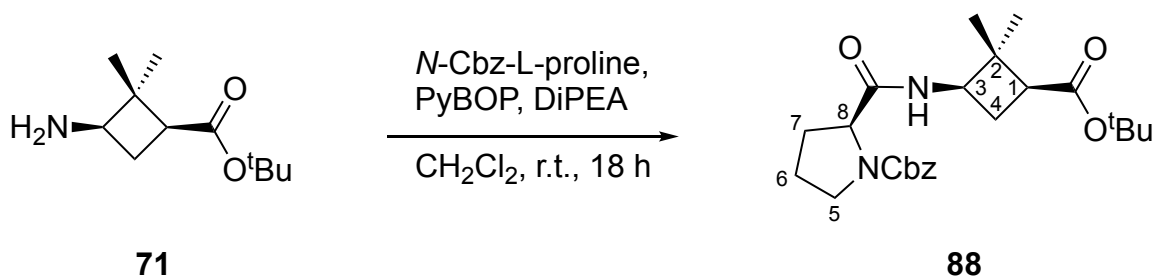
$^1\text{H NMR}$  (250 MHz,  $\text{CDCl}_3$ ):  $\delta$  1.08 (s, 3H,  $\text{CH}_3$ ), 1.24 (s, 3H,  $\text{CH}_3$ ), 1.42 (s, 9H,  $t\text{Bu}$ ), 1.95-2.34 (m, 2H,  $\text{H}_4$ ,  $\text{H}_1$ ), 2.46 (m, 1H,  $\text{H}_4'$ ), 3.21 (m, 1H,  $\text{H}_3$ ), 5.76 (m, 2H,  $\text{NH}_2$ ).

Spectroscopic data are consistent with those reported in reference:

Aguilera, J.; Moglioni, A. G.; Moltrasio, G. Y.; Ortuño, R. M. *Tetrahedron: Asymmetry* **2008**, *19*, 302-308.

## 7. Experimental Methodologies

### Benzyl(*S*)-2-(((1*R*,3*S*)-3-(*tert*-butoxycarbonyl)-2,2-dimethylcyclobutyl)carbamoyl)pyrrolidine-1-carboxylate, **88**



*N*-Cbz-L-proline (1.13 g, 4.5 mmol, 1 eq) and PyBOP (3.51 g, 6.8 mmol, 1.5 eq) were dissolved in CH<sub>2</sub>Cl<sub>2</sub> (30 mL) and DiPEA (3.2 mL, 18 mmol, 4 eq) was added under nitrogen atmosphere. After stirring for 10 min amine **71** (0.90 g, 4.5 mmol) and CH<sub>2</sub>Cl<sub>2</sub> (16 mL) were added. The reaction was stirred at room temperature overnight. Then, the solution was washed with saturated NaHCO<sub>3</sub> (3 x 20 mL) and brine (20 mL). The organic phase was dried over MgSO<sub>4</sub>, filtered and evaporated under reduced pressure. The residue was purified by column chromatography (EtOAc/hexane, 2:3) to afford **88** (1.21 g, 2.8 mmol, 62%) as a white solid.

#### Spectroscopic data and physical constants for compound **88**:

**Mp**: 47-48 °C (CH<sub>3</sub>OH)

**[α]<sub>D</sub><sup>20</sup>**: -4 (c = 1.0, CH<sub>3</sub>OH)

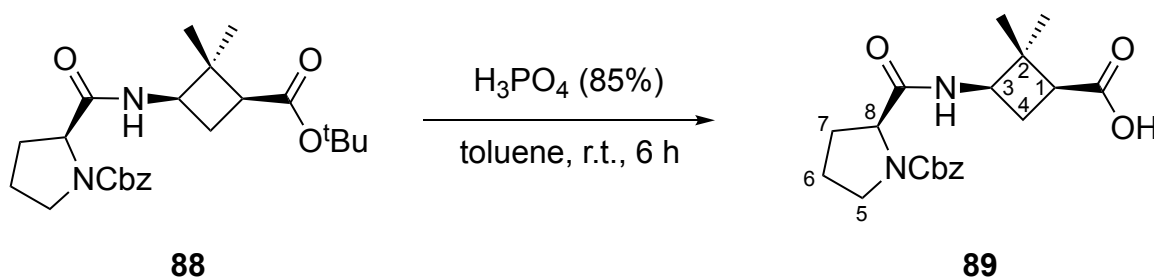
**IR** (ATR): 3310, 2958, 1703, 1534.

**<sup>1</sup>H NMR** (CDCl<sub>3</sub>, 400 MHz): δ 0.81 (s, 3H, CH<sub>3</sub>), 1.25 (s, 3H, CH<sub>3</sub>), 1.44 (s, 9H, *t*Bu), 1.90-2.33 (m, 6H, H<sub>4</sub>, H<sub>6</sub>, H<sub>7</sub>), 2.49 (dd, 1H, *J* = 9.7, 7.9 Hz, H<sub>1</sub>), 3.50 (m, 2H, H<sub>5</sub>), 3.99 (m, 1H, H<sub>3</sub>), 4.32 (m, 1H, H<sub>8</sub>), 5.16 (m, 2H, CH<sub>2</sub>-Ph), 7.35 (m, 5H, H<sub>ar</sub>).

**<sup>13</sup>C NMR** (CDCl<sub>3</sub>, 100 MHz): δ 16.8, 17.0, 24.5, 25.7, 28.2, 29.0, 43.9, 45.7, 48.6, 50.0, 60.3, 67.2, 80.5, 127.8, 128.5, 136.5, 161.1, 172.1.

**HRMS** (ESI) calculated for C<sub>24</sub>H<sub>34</sub>N<sub>2</sub>O<sub>5</sub>Na (M+Na<sup>+</sup>): 453.2360. Found: 453.2369.

**(1*S*,3*R*)-3-((*S*)-1-((Benzyloxy)carbonyl)pyrrolidine-2-carboxamido)-2,2-dimethylcyclobutane-1-carboxylic acid, **89****



To a solution of dipeptide **88** (0.11 g, 0.26 mmol) in toluene (0.2 mL) was added aqueous phosphoric acid (0.25 mL, 3.8 mmol, 15 eq, 85% weight) dropwise and the resulting mixture was stirred for 6 h at room temperature. Water (5 mL) was added, and the mixture was extracted with EtOAc (3 x 10 mL). The organic phases were dried over MgSO<sub>4</sub>, filtered and evaporated under reduced pressure to give the compound **89** (96 mg, 0.26 mmol, 99%) as a white solid.

**Spectroscopic data and physical constants for compound 89:**

**Mp:** 65-66 °C (CH<sub>3</sub>OH)

**[α]<sub>D</sub><sup>20</sup>:** +4 (c = 0.8, CH<sub>3</sub>OH)

**IR (ATR):** 3338, 2956, 1701, 1648, 1533.

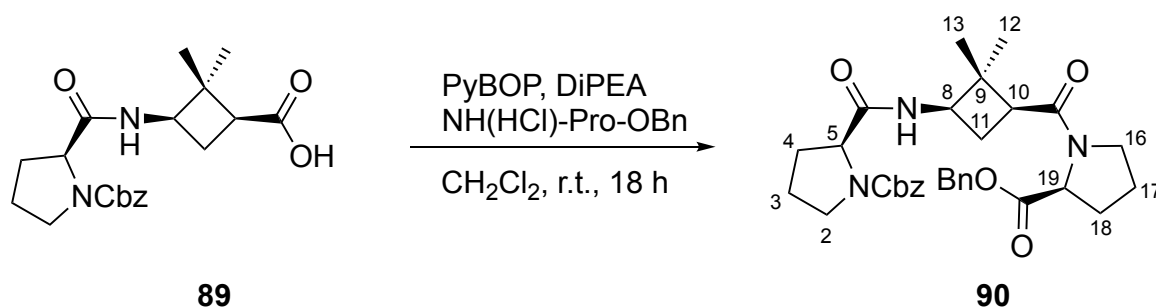
**<sup>1</sup>H NMR** (CD<sub>3</sub>OD, 400 MHz): δ 0.96 (s, 3H, Me), 1.28 (s, 3H, Me), 1.92-2.20 (m, 6H, H<sub>4</sub>, H<sub>6</sub>, H<sub>7</sub>), 2.59 (m, 1H, H<sub>1</sub>), 3.51 (m, 1H, H<sub>5</sub>), 3.58 (m, 1H, H<sub>5</sub>), 3.91 (m, 1H, H<sub>3</sub>), 4.25 (m, 1H, H<sub>8</sub>), 5.09 (m, 2H, CH<sub>2</sub>-Ph), 7.31 (m, 5H, H<sub>ar</sub>).

**<sup>13</sup>C NMR** (CD<sub>3</sub>OD, 100 MHz): δ 16.0, 23.1, 24.2, 26.2, 28.0, 31.5, 42.6, 45.7, 50.0, 59.8, 66.7, 127.6, 128.1, 136.5, 154.9, 173.7, 174.5.

**HRMS** (ESI) calculated for C<sub>20</sub>H<sub>26</sub>N<sub>2</sub>O<sub>5</sub>Na (M+Na<sup>+</sup>): 397.1734. Found: 397.1735.

## 7. Experimental Methodologies

### Protected tripeptide **90**



Acid **89** (0.36 g, 0.96 mmol) and PyBOP (0.76 g, 1.45 mmol, 1.5 eq) were dissolved in  $\text{CH}_2\text{Cl}_2$  (12 mL) and DiPEA (0.26 mL, 3.84 mmol, 4 eq) was added under nitrogen atmosphere. After stirring for 10 min  $\text{NH}(\text{HCl})\text{-Pro-OBn}$  (0.23 g, 0.96 mmol, 1 eq) in  $\text{CH}_2\text{Cl}_2$  (5 mL) were added and the reaction was stirred at room temperature overnight. Then, the solution was washed with saturated  $\text{NaHCO}_3$  (3 x 10 mL) and brine (10 mL). The organic phase was dried over  $\text{MgSO}_4$ , filtered and evaporated under reduced pressure. The crude was purified by column chromatography (EtOAc /hexane, from 1:1 to 1:0) to give **90** (0.37 g, 0.66 mmol, 68%) as a white solid.

#### Spectroscopic data and physical constants for compound **90**:

**Mp**: 91-92 °C ( $\text{CH}_3\text{OH}$ )

$[\alpha]_D^{20}$ : -40 ( $c = 1.0$ ,  $\text{CH}_3\text{OH}$ )

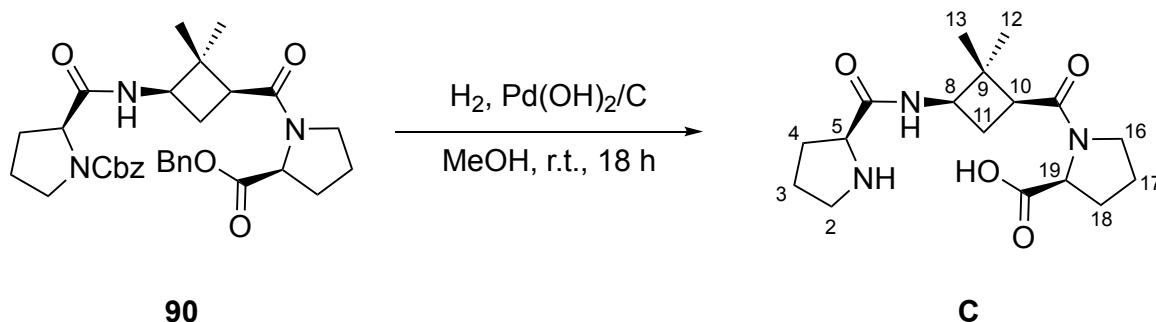
**IR** (ATR): 2957, 1686, 1625, 1529.

**$^1\text{H NMR}$**  ( $\text{CDCl}_3$ , 400 MHz):  $\delta$  0.88 (s, 3H, Me), 1.37 (s, 3H, Me), 1.92-2.16 (m, 10H,  $\text{H}_3$ ,  $\text{H}_4$ ,  $\text{H}_{11}$ ,  $\text{H}_{17}$ ,  $\text{H}_{18}$ ), 2.77 (t, 1H,  $J = 7.9$  Hz,  $\text{H}_{10}$ ), 3.54 (m, 4H,  $\text{H}_2$ ,  $\text{H}_{16}$ ), 4.06 (m, 1H,  $\text{H}_8$ ), 4.33 (m, 1H,  $\text{H}_5$ ), 4.55 (m, 1H,  $\text{H}_{19}$ ), 5.16 (m, 4H,  $\text{CH}_2\text{-Ph}$ ), 7.34 (m, 10H,  $\text{H}_{ar}$ ).

**$^{13}\text{C NMR}$**  ( $\text{CDCl}_3$ , 100 MHz):  $\delta$  17.5, 24.9, 25.5, 29.0, 30.0, 31.3, 43.4, 47.1, 50.2, 58.9, 60.8, 66.7, 67.3, 127.9, 128.1, 128.6, 135.7, 136.5, 171.1, 172.1.

**HRMS** (ESI) calculated for  $\text{C}_{32}\text{H}_{39}\text{N}_3\text{O}_6\text{Na}$  ( $\text{M}+\text{Na}^+$ ): 584.2731. Found: 584.2737.

## Tripeptide C



Protected tripeptide **90** (0.18 g, 0.32 mmol) was dissolved in CH<sub>3</sub>OH (10 mL) and Pd(OH)<sub>2</sub>/C (0.018 g, 10% weight) was added. The mixture was stirred under 7 atm of H<sub>2</sub> at room temperature overnight. After this period, the crude was filtered through Celite and washed with CH<sub>3</sub>OH. The collected solvent was evaporated to provide tripeptide **C** (0.11 g, 0.32 mmol, 99%) as a white solid without need for further purification.

**Spectroscopic data and physical constants for C:**

**Mp:** 154-156 °C (CH<sub>3</sub>OH)

**[α]<sub>D</sub><sup>20</sup>:** -10 (c = 0.5, CH<sub>3</sub>OH)

**IR (ATR):** 2956, 1671, 1608, 1552, 1448.

**<sup>1</sup>H NMR** (CD<sub>3</sub>OD, 400 MHz): δ 0.98 (s, 3H, Me), 1.40 (s, 3H, Me), 2.04 (m, 9H, H<sub>3</sub>, H<sub>3'</sub>, H<sub>4</sub>, H<sub>11</sub>, H<sub>11'</sub>, H<sub>17</sub>, H<sub>17'</sub>, H<sub>18</sub>, H<sub>18'</sub>), 2.44 (m, 2H, H<sub>4'</sub>, H<sub>10</sub>), 2.99 (m, 1H, H<sub>2</sub>), 3.38 (m, 2H, H<sub>2'</sub>, H<sub>16</sub>), 3.59 (m, 1H, H<sub>16'</sub>), 3.71 (m, 1H, H<sub>8</sub>), 4.06 (m, 1H, H<sub>5</sub>), 4.22 (m, 1H, H<sub>19</sub>).

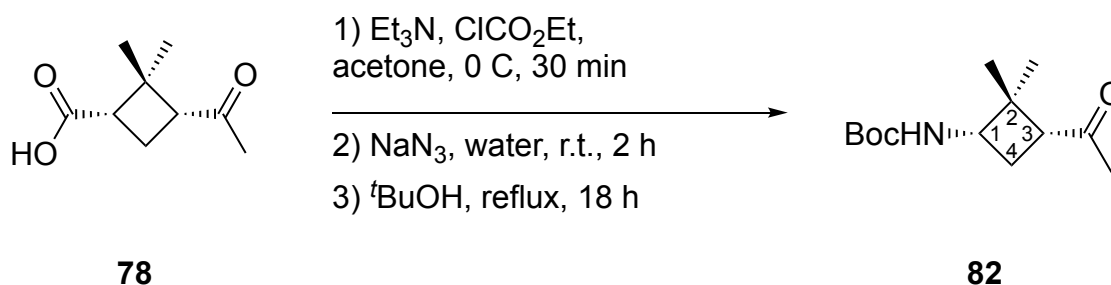
**<sup>13</sup>C NMR** (CD<sub>3</sub>OD, 100 MHz): δ 16.2, 16.5, 22.1, 23.6, 23.9, 24.4, 28.8, 29.8, 42.0, 45.9, 50.4, 59.6, 168.1

**HRMS** (ESI) calculated for C<sub>17</sub>H<sub>28</sub>N<sub>3</sub>O<sub>4</sub>Na (M+H<sup>+</sup>): 338.2074. Found: 338.2085.



## 7. Experimental Methodologies

### ***tert*-Butyl ((1*S*,3*R*)-3-acetyl-2,2-dimethylcyclobutyl)carbamate, **82****



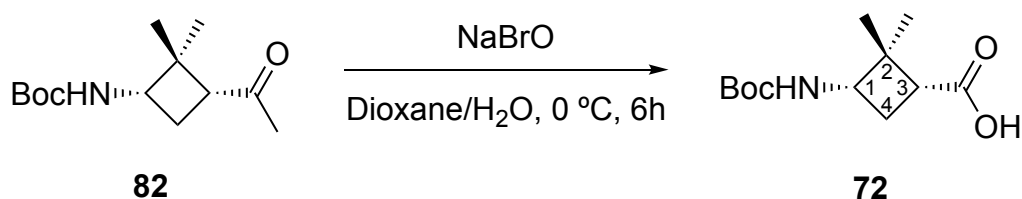
To an ice-cooled solution of acid **78** (3.01 g, 17.7 mmol) in anhydrous acetone (80 mL), triethylamine (2.96 mL, 21.2 mmol, 1.2 eq) and ethyl chloroformate (2.02 mL, 21.2 mmol, 1.2 eq) were subsequently added. The mixture was stirred at 0 °C for 30 minutes. Then, sodium azide (1.84 g, 28.3 mmol, 1.6 eq) in 25 mL of water was added and the resultant solution was stirred at room temperature for 2 h. The reaction mixture was extracted with dichloromethane (4 x 30 mL), and the organic extracts were dried over magnesium sulphate and the solvents were removed under reduced pressure. The crude was dissolved in *tert*-butanol (80 mL) and the mixture was heated to reflux for 18 hours. The solvent was evaporated under reduced pressure and the residue was chromatographed on silica gel (1:3 ethyl acetate-hexane as eluent) to afford carbamate **82** as a white solid (2.21 g, 9.20 mmol, 52% yield).

#### **Spectroscopic data for compound **82**:**

**<sup>1</sup>H NMR** (250 MHz, CDCl<sub>3</sub>): δ 0.70 (s, 3H, Me), 1.26 (s, 3H, Me), 1.30 (s, 9H, *t*Bu), 1.94 (s, 3H, COCH<sub>3</sub>), 2.00 (m, 2H, H<sub>4</sub>), 2.60 (m, 1H, H<sub>3</sub>), 3.70 (m, 1H, H<sub>1</sub>), 4.85 (brs, 1H, NH).

Spectroscopic data are consistent with those reported in reference:

Aguilera, J.; Moglioni, A. G.; Moltrasio, G. Y.; Ortuño, R. M. *Tetrahedron: Asymmetry* **2008**, *19*, 302-308.

**(1*R*,3*S*)-3-((*tert*-Butoxycarbonyl)amino)-2,2-dimethylcyclobutane-1-carboxylic acid, 72**

To an ice cooled solution of ketone **82** (1.0 g, 4.14 mmol) in dioxane-water (7:2, 30 mL) was added a sodium hypobromite solution, prepared from bromine (0.76 mL, 14.9 mmol, 3.6 eq) and sodium hydroxide (1.15g, 29.0 mmol, 7 eq) in 3:1 mixture of water-dioxane (55 mL). The resulting mixture was stirred for 6 hours at 0 °C. Then, sodium bisulphite was added (16 mL) and the mixture was brought to acidic pH by adding 5% hydrochloric acid. The acid solution was extracted with dichloromethane (4 x 40 mL) and the organic phases were dried over magnesium sulphate and the solvent was evaporated under to dryness to afford carboxylic acid **72** as a white solid (0.907 g, 3.73 mmol, 90% yield).

**Spectroscopic data for compound 72:**

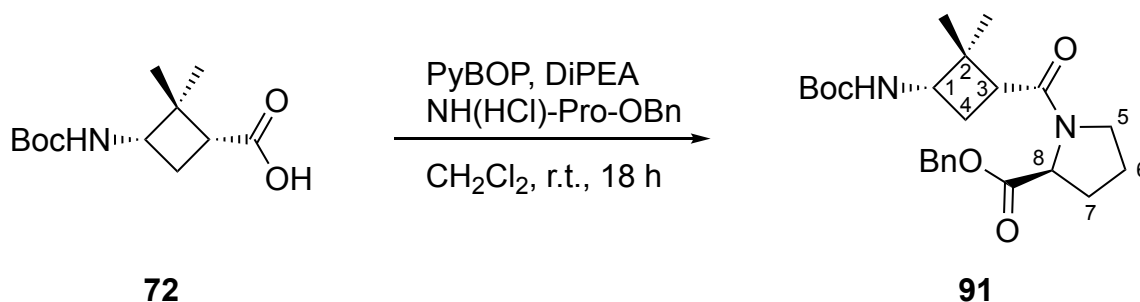
**<sup>1</sup>H NMR** (250 MHz, CDCl<sub>3</sub>): δ 0.99 (s, 3H, Me), 1.30 (s, 3H, Me), 1.45 (s, 9H, *t*Bu), 2.17 (m, 2H, H<sub>4</sub>), 2.59 (m, 1H, H<sub>3</sub>), 3.83 (m, 1H, H<sub>1</sub>), 4.70 (brs, 1H, NH).

Spectroscopic data are consistent with those reported in reference:

Aguilera, J.; Moglioni, A. G.; Moltrasio, G. Y.; Ortuño, R. M. *Tetrahedron: Asymmetry* **2008**, *19*, 302-308.

## 7. Experimental Methodologies

### Benzyl((1*R*,3*S*)-3-((*tert*-butoxycarbonyl)amino)-2,2-dimethylcyclobutane-1-carbonyl)-*L*-prolinate, **91**



Acid **72** (1.00 g, 4.1 mmol) and PyBOP (3.21 g, 6.2 mmol, 1.5 eq) were dissolved in CH<sub>2</sub>Cl<sub>2</sub> (50 mL) and DiPEA (2.83 mL, 16.4 mmol, 4 eq) was added under nitrogen atmosphere. After stirring for 10 min NH(HCl)-Pro-OBn (1.0 g, 4.1 mmol, 1 eq) in CH<sub>2</sub>Cl<sub>2</sub> (20 mL) were added and the reaction was stirred at room temperature overnight. Then, the solution was washed with saturated NaHCO<sub>3</sub> (3 x 20 mL) and brine (20 mL). The organic phase was dried over MgSO<sub>4</sub>, filtered and evaporated under reduced pressure to give crude compound. The crude was purified by column chromatography (EtOAc/hexane, 1:1) to afford **91** (0.94 g, 2.2 mmol, 53%) as a white solid.

#### Spectroscopic data and physical constants for compound **91**:

**Mp**: 95-98 °C (EtOAc).

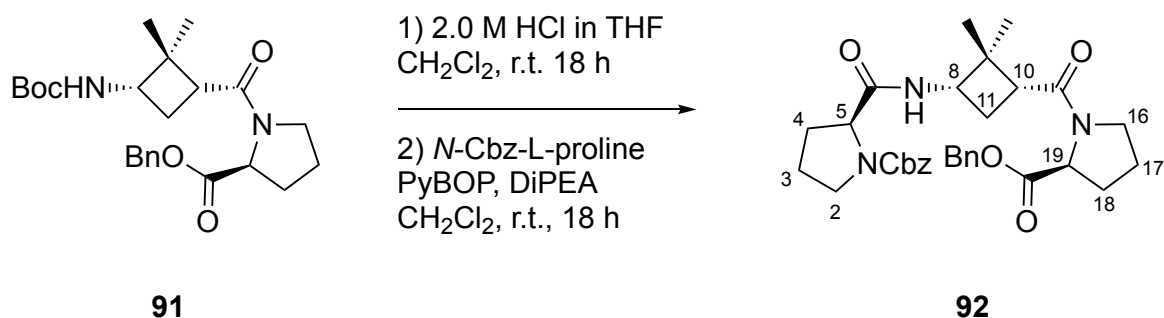
**[α]<sub>D</sub><sup>20</sup>**: -50 (c = 0.8, CH<sub>3</sub>OH)

**IR** (ATR): 3391, 2971, 2863, 1749, 1705, 1634, 1507.

**<sup>1</sup>H NMR** (CDCl<sub>3</sub>, 400 MHz): δ 0.88 (s, 3H, Me), 1.36 (s, 3H, Me), 1.43 (s, 9H, *t*Bu), 1.95-2.25 (m, 6H, H<sub>4</sub>, H<sub>6</sub>, H<sub>7</sub>), 2.78 (t, 1H, *J* = 8.0 Hz, H<sub>3</sub>), 3.46 (m, 1H, H<sub>5</sub>), 3.64 (m, 1H, H<sub>5'</sub>), 3.80 (m, 1H, H<sub>1</sub>), 4.52 (d, 1H, *J* = 7.2 Hz, H<sub>8</sub>), 5.11 (m, 2H, CH<sub>2</sub>-Ph), 7.33 (m, 5H, H<sub>ar</sub>).

**<sup>13</sup>C NMR** (CDCl<sub>3</sub>, 100 MHz): δ 17.9, 25.2, 26.3, 28.8, 29.6, 30.3, 43.8, 45.8, 47.6, 51.9, 59.3, 67.2, 128.5, 128.9, 136.2, 155.9, 171.5, 172.6.

**HRMS** (ESI) calculated for C<sub>24</sub>H<sub>34</sub>N<sub>2</sub>O<sub>5</sub>Na (M+Na<sup>+</sup>): 453.2523. Found: 453.2528.

**Protected tripeptide, 92**

Protected dipeptide **91** (0.65 g, 1.5 mmol) was dissolved in CH<sub>2</sub>Cl<sub>2</sub> (40 mL). A solution 2M of HCl in THF (10 mL, 20 mmol, 13 eq) was added and the mixture was stirred at room temperature overnight. The evaporation of the solvent under reduced pressure affords the half-protected dipeptide. This product dissolved in CH<sub>2</sub>Cl<sub>2</sub> (16 mL) was added to a solution of *N*-Cbz-L-proline (0.37 g, 1.5 mmol, 1 eq), PyBOP (1.19 g, 2.3 mmol, 1.5 eq) and DiPEA (1.0 mL, 6 mmol, 4 eq) in CH<sub>2</sub>Cl<sub>2</sub> (33 mL), which was stirred beforehand for 10 min under nitrogen atmosphere. The reaction mixture was stirred overnight at room temperature. The solution was washed with saturated NaHCO<sub>3</sub> (3 x 25 mL) and brine (25 mL). The organic phase was dried over MgSO<sub>4</sub>, filtered and evaporated under reduced pressure. Purification by column chromatography (EtOAc/hexane, from 1:2 to 1:0) gives **92** (0.51 g, 0.91 mmol, 61%) as a white solid.

**Spectroscopic data and physical constants for compound 92:**

**Mp:** 54-55 °C (EtOAc).

**[α]<sub>D</sub><sup>20</sup>:** -113 (c = 1.1, CH<sub>3</sub>OH).

**IR (ATR):** 3312, 2952, 1702, 1677, 1636, 1529.

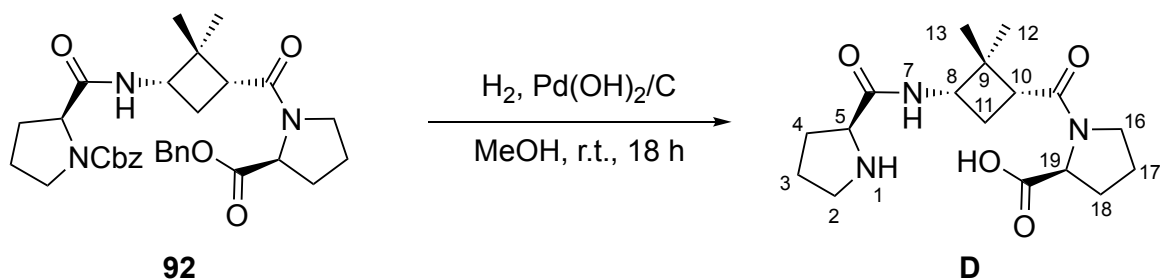
**<sup>1</sup>H NMR** (CDCl<sub>3</sub>, 400 MHz): δ 0.90 (s, 3H, Me), 1.40 (s, 3H, Me), 1.94-2.34 (m, 10H, H<sub>3</sub>, H<sub>4</sub>, H<sub>11</sub>, H<sub>17</sub>, H<sub>18</sub>), 2.85 (t, 1H, *J* = 7.1 Hz, H<sub>10</sub>), 3.49-3.65 (m, 4H, H<sub>2</sub>, H<sub>16</sub>), 4.09 (m, 1H, H<sub>8</sub>), 4.36 (m, 1H, H<sub>5</sub>), 4.55 (m, 1H, H<sub>19</sub>), 5.16 (m, 4H, CH<sub>2</sub>-Ph), 7.36 (m, 10H, H<sub>ar</sub>).

**<sup>13</sup>C NMR** (CDCl<sub>3</sub>, 100 MHz): δ 17.8, 24.7, 25.5, 29.2, 29.8, 43.9, 47.1, 50.4, 58.8, 60.7, 66.6, 67.2, 128.0, 128.4, 135.7, 171.2, 172.2.

**HRMS** (ESI) calculated for C<sub>32</sub>H<sub>39</sub>N<sub>3</sub>O<sub>6</sub>Na (M+Na<sup>+</sup>): 584.2731. Found: 584.2732

## 7. Experimental Methodologies

### Tripeptide D



Protected tripeptide **92** (0.25 g, 0.45 mmol) was dissolved in CH<sub>3</sub>OH (12 mL) and Pd(OH)<sub>2</sub>/C (10% weight) was added. The mixture was stirred under 7 atm of H<sub>2</sub> at room temperature overnight. After this period, the crude was filtered through Celite and washed with CH<sub>3</sub>OH. The collected solvent was evaporated to provide tripeptide **D** (0.15 g, 0.45 mmol, 99%) as a white solid.

#### Spectroscopic data and physical constants for **D**:

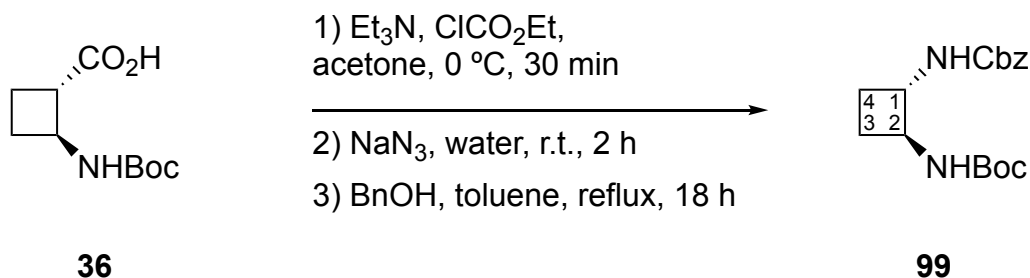
**Mp**: 137-140 °C (CH<sub>3</sub>OH).  $[\alpha]_D^{20}$ : -110 (c = 0.90, CH<sub>3</sub>OH).

**IR** (ATR): 3383, 3067, 2956, 1721, 1671, 1609, 1562, 1447.

**<sup>1</sup>H NMR** (CD<sub>3</sub>OD, 600 MHz): major conformation: δ 0.92 (s, 3H, Me<sub>12</sub>), 1.40 (s, 3H, Me<sub>13</sub>), 1.96-2.09 (m, 6H, H<sub>3</sub>, H<sub>3'</sub>, H<sub>4</sub>, H<sub>17</sub>, H<sub>17'</sub>, H<sub>18</sub>), 2.21-2.26 (m, 2H, H<sub>11</sub>, H<sub>18'</sub>), 2.42 (m, 1H, H<sub>11'</sub>), 2.49 (m, 1H, H<sub>4'</sub>), 3.04 (t, 1H, *J* = 8.6 Hz, H<sub>10</sub>), 3.41 (m, 2H, H<sub>2</sub>, H<sub>2'</sub>), 3.54 (m, 1H, H<sub>16</sub>), 3.74 (m, 1H, H<sub>16'</sub>), 4.13 (t, 1H, *J* = 9.1 Hz, H<sub>8</sub>), 4.31 (m, 1H, H<sub>5</sub>), 4.38 (m, 1H, H<sub>19</sub>). minor conformation: δ 0.99 (s, 3H, Me<sub>12</sub>), 1.31 (s, 3H, Me<sub>13</sub>), 1.96-2.09 (m, 5H, H<sub>3</sub>, H<sub>3'</sub>, H<sub>4</sub>, H<sub>17</sub>, H<sub>17'</sub>), 2.17-2.25 (m, 3H, H<sub>11</sub>, H<sub>18</sub>, H<sub>18'</sub>), 2.42 (m, 1H, H<sub>11'</sub>), 2.49 (m, 1H, H<sub>4'</sub>), 2.87 (t, 1H, *J* = 8.6 Hz, H<sub>10</sub>), 3.41 (m, 2H, H<sub>2</sub>, H<sub>2'</sub>), 3.61 (m, 1H, H<sub>16</sub>), 3.74 (m, 1H, H<sub>16'</sub>), 4.05 (t, 1H, *J* = 8.9 Hz, H<sub>8</sub>), 4.31 (m, 1H, H<sub>5</sub>), 4.50 (m, 1H, H<sub>19</sub>).

**<sup>13</sup>C NMR** (CD<sub>3</sub>OD, 150 MHz): major conformation: δ 16.5 (C<sub>12</sub>), 23.8 (C<sub>3</sub>), 24.3 (C<sub>11</sub>, C<sub>17</sub>), 29.0 (C<sub>13</sub>), 29.3 (C<sub>18</sub>), 30.3 (C<sub>4</sub>), 42.7 (C<sub>10</sub>), 45.9 (C<sub>2</sub>, C<sub>9</sub>), 47.3 (C<sub>16</sub>), 50.0 (C<sub>8</sub>), 59.5 (C<sub>5</sub>), 60.2 (C<sub>19</sub>), 168.3 (C<sub>6</sub>), 170.9 (C<sub>14</sub>), 176.3 (C<sub>20</sub>). minor conformation: δ 16.1 (C<sub>12</sub>), 21.8 (C<sub>17</sub>), 23.7 (C<sub>3</sub>), 25.2 (C<sub>11</sub>), 28.5 (C<sub>13</sub>), 30.2 (C<sub>4</sub>), 31.3 (C<sub>18</sub>), 42.2 (C<sub>10</sub>), 46.1 (C<sub>2</sub>), 46.4 (C<sub>9</sub>), 47.3 (C<sub>16</sub>), 50.4 (C<sub>8</sub>), 60.2 (C<sub>5</sub>), 61.1 (C<sub>19</sub>), 168.1 (C<sub>6</sub>), 171.5 (C<sub>14</sub>), 176.5 (C<sub>20</sub>).

**HRMS** (ESI) calculated for C<sub>17</sub>H<sub>27</sub>N<sub>3</sub>O<sub>4</sub> (M<sup>+</sup>): 337.2001. Found: 337.2002.

**Benzyl *tert*-butyl ((1*S*,2*S*)-cyclobutane-1,2-diyl)dicarbamate, 99**

Carboxylic acid **36** (400 mg, 1.9 mmol) was dissolved in anhydrous acetone (40 mL) and ethyl chloroformate (0.2 mL, 2.1 mmol) and triethylamine (0.26 mL, 1.9 mmol) were added at 0 °C under nitrogen atmosphere and the reaction mixture was stirred for 30 minutes. Then, NaN<sub>3</sub> (0.19 g, 1.6 eq, 3.0 mmol) dissolved in water (5 mL) was added and the mixture was stirred at room temperature for 2 hours. After that, the reaction mixture was extracted with CH<sub>2</sub>Cl<sub>2</sub> (3 x 30 mL) and the organic layer was dried with MgSO<sub>4</sub> and the solvent was evaporated. 0.36 g (1.5 mmol, 80 % yield) of the acyl azide were obtained as a yellow oil, which was used directly in the following step. Acyl azide (0.36 g, 1.5 mmol) was dissolved in anhydrous toluene (80 mL) and 0.4 mL (3.9 mmol) of benzyl alcohol were added. The mixture was refluxed for 18 hours. After that, the solvent was evaporated under vacuum and the excess of benzyl alcohol was lyophilised. The reaction crude was purified by column chromatography using silica gel (EtOAc-hexane; 1:3) to obtain **9** (410 mg, 1.3 mmol, 70 % yield) as a yellow oil. **WARNING:** Acyl azide intermediate should be carefully manipulated because of its explosive nature.

**Spectroscopic data for compound 99:**

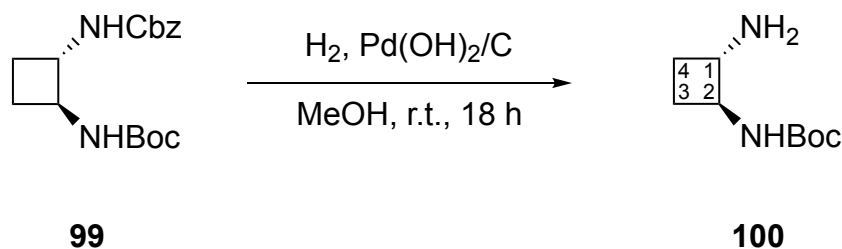
**<sup>1</sup>H NMR** (250 MHz, CDCl<sub>3</sub>): δ 1.45 (s, 9H, *t*Bu), 1.50 (m, 2H), 2.16 (m, 2H), 3.88 (m, 2H, H<sub>1</sub>, H<sub>2</sub>), 4.93 (broad s, 1H, NH), 5.10 (m, 2H, CH<sub>2</sub>-Ph), 5.83 (broad s, 1H, NH), 7.37 (m, 5H, H<sub>ar</sub>).

Spectroscopic data are consistent with those reported in reference:

Sans, M.; Illa, O.; Ortuño, R. M. *Org. Letters* **2012**, *14*, 10, 2431-2433

## 7. Experimental Methodologies

### ***tert*-Butyl ((1*S*,2*S*)-2-aminocyclobutyl)carbamate, **100****



Protected diamine **99** (0.3 g, 0.93 mmol) was dissolved in MeOH (15 mL) and Pd(OH)<sub>2</sub> (0.09 g, 30% weight) was added. The reaction mixture was stirred at room temperature under 7 atm of pressure for 18 h. Then, the crude was filtered through Celite and washed with MeOH (3 x 15 mL). The solvent was evaporated under reduced pressure to afford **100** (0.15 g, 0.73 mmol, 84% yield) as a colourless oil.

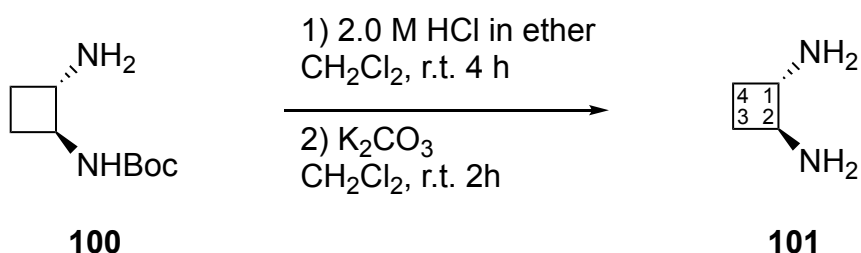
#### **Spectroscopic data for compound 100:**

**<sup>1</sup>H NMR** (250 MHz, CD<sub>3</sub>OD): δ 1.43 (s, 9H, *t*Bu), 1.6 (m, 2H), 2.01 (m, 2H), 3.12 (m, 1H, H<sub>1</sub>), 3.61 (m, 1H, H<sub>2</sub>).

Spectroscopic data are consistent with those reported in reference:

Sans, M.; Illa, O.; Ortuño, R. M. *Org. Letters* **2012**, *14*, 10, 2431-2433.

### **(1*S*,2*S*)-Cyclobutane-1,2-diamine, **101****



Half protected diamine **100** (0.07 g, 0.38 mmol) was dissolved in DCM (5 mL). Then, a solution of 2 M HCl in ether (2.8 mL, 5.63 mmol, 15 eq) was added. The reaction was stirred at room temperature for 4 h. After this period, the solvent was evaporated under reduced pressure. Then, the crude product was dissolved in DCM (10 mL) and stirred over an excess of K<sub>2</sub>CO<sub>3</sub> (0.41 g, 3 mmol). After 2 h, the

solution was filtered and evaporated to reduced pressure to afford **101** (0.25 g, 0.3 mmol, 80% yield) as a yellow oil. It should be noted that the filtrate often contained very little product when the reaction was performed on a larger scale. When this occurred, the slurry containing product and  $K_2CO_3$  could be carried directly through to the next step (assuming 100% product) and afforded excellent yields.

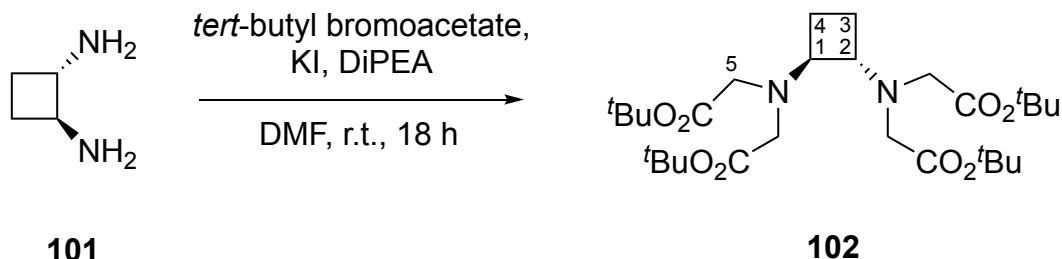
**Spectroscopic data for compound 101:**

$^1H$  NMR (250 MHz,  $CD_3OD$ ):  $\delta$  1.61 (m, 2H), 2.14 (m, 2H), 3.30 (m, 2H,  $H_1$ ,  $H_2$ )

Spectroscopic data are consistent with those reported in reference:

Sans, M.; Illa, O.; Ortuño, R. M. *Tetrahedron* **2016**, *72*, 2913-2919.

**Tetra-*tert*-butyl 2,2',2'',2'''-(((1*S*,2*S*)-cyclobutane-1,2-diyl)bis(azanetriyl))tetraacetate, 102**



To a solution of **101** (65.6 mg, 0.75 mmol), potassium iodide (480 mg, 2.89 mmol, 3.85 eq), and DiPEA (1.08 mL, 6.2 mmol, 8.3 eq) in DMF (2 mL) was added *tert*-butyl bromoacetate (0.49 mL, 3.3 mmol, 4.4 eq) and the reaction mixture was stirred at room temperature for 18 h under  $N_2$  atmosphere. Then, the solution was diluted with  $CH_2Cl_2$  (20 mL) and washed with satd  $K_2CO_3$  (2 x 5 mL), and brine (1 x 5 mL). The organic layer was dried over  $MgSO_4$ , filtered and evaporated under reduced pressure. Purification by column chromatography (EtOAc/hexane, 1:3) affords **102** (288 mg, 0.53 mmol, 70% yield) as a yellow oil.



## 7. Experimental Methodologies

### Spectroscopic data and physical constants for compound **102**:

$[\alpha]_D^{20}$ : +8 (c = 1.0, CH<sub>3</sub>OH).

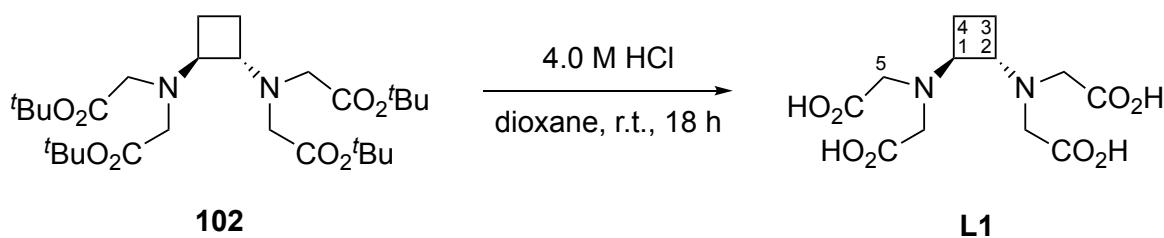
IR (ATR): 2978, 2931, 1729.

<sup>1</sup>H NMR (CDCl<sub>3</sub>, 360 MHz): δ 1.44 (s, 28H, *t*Bu, H<sub>3</sub>, H<sub>4</sub>), 1.79 (m, 2H, H<sub>3'</sub>, H<sub>4'</sub>), 3.32 (m, 2H, H<sub>1</sub>, H<sub>2</sub>), 3.41 (m, 1H, H<sub>5</sub>), 3.46 (m, 3H, H<sub>5</sub>), 3.49 (m, 3H, H<sub>5</sub>), 3.54 (m, 1H, H<sub>5</sub>).

<sup>13</sup>C NMR (CDCl<sub>3</sub>, 90 MHz): δ 20.3 (C<sub>3</sub>, C<sub>4</sub>), 28.1 (*t*Bu), 52.9 (C<sub>5</sub>), 62.9 (C<sub>1</sub>, C<sub>2</sub>), 80.6 (C-*t*Bu), 171.1 (CO).

HRMS (ESI) calculated for C<sub>28</sub>H<sub>51</sub>N<sub>2</sub>O<sub>8</sub> (M+H<sup>+</sup>): 543.3640. Found: 543.3647

### Ligand **L1**



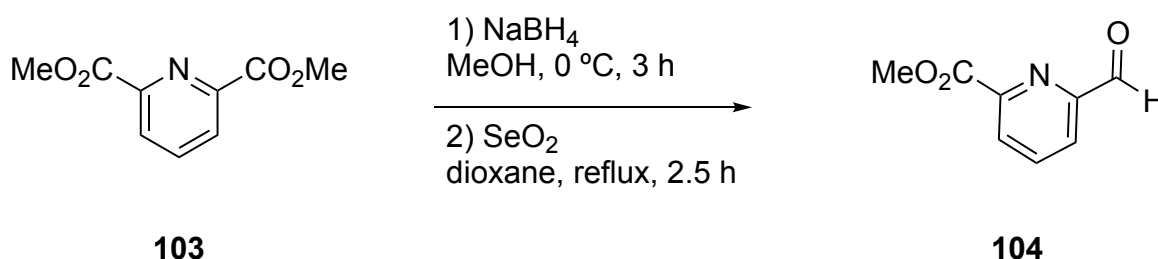
A solution of compound **102** (0.18 g, 0.33 mmol) in 4 M HCl in dioxane (12 mL) was stirred at room temperature for 18 h. Then, the solvent was evaporated under reduced pressure, and after a small amount of water (2 mL) was added and the mixture was evaporated to dryness. This process was repeated once with the addition of water and twice with an addition of diethyl ether (2 mL) to afford **L1** · **2 HCl** (0.11 g, 0.25 mmol, 77% yield) as a yellow solid without need for further purification.

**Spectroscopic data and physical constants for L1 · 2HCl:**

**<sup>1</sup>H NMR** (D<sub>2</sub>O, 600 MHz): δ 1.67 (m, 2H, H<sub>3</sub>, H<sub>4</sub>), 1.97 (m, 2H, H<sub>3</sub>, H<sub>4</sub>), 3.88 (m, 8H, H<sub>5</sub>), 3.94 (m, 2H, H<sub>1</sub>, H<sub>2</sub>).

**<sup>13</sup>C NMR** (D<sub>2</sub>O, 150 MHz): δ 18.1 (C<sub>3</sub>, C<sub>4</sub>), 52.5 (C<sub>5</sub>), 61.7 (C<sub>1</sub>, C<sub>2</sub>), 171.2 (CO).

**MS** (ESI) calculated for C<sub>12</sub>H<sub>18</sub>N<sub>2</sub>O<sub>8</sub> (M+H<sup>+</sup>): 319.1. Found: 319.1

**Methyl 6-formylpicolinate, 104**

To a stirred solution of **103** (5 g, 25.5 mmol) in CH<sub>3</sub>OH (200 mL), was added NaBH<sub>4</sub> (3.65 g, 96.5 mmol) at 0 °C. The solution was stirred 3 h at 0 °C and then poured into a saturated NaHCO<sub>3</sub> aqueous solution (100 mL). The methanol was evaporated, and the resulting aqueous solution was extracted with CHCl<sub>3</sub> (4 x 50 mL). The organic phase was dried over MgSO<sub>4</sub>, filtered and evaporated under reduced pressure. The resulting residue was dissolved in dioxane (100 mL) and SeO<sub>2</sub> (1.4 g, 12.5 mmol) was added. The solution was heated to reflux for 2.5 h, filtered while hot, and evaporated to dryness. The crude residue was purified by column chromatography (CH<sub>2</sub>Cl<sub>2</sub>) to afford **104** (2.88 g, 17.4 mmol, 68% yield) as a yellow oil.

**Spectroscopic data for compound 104:**

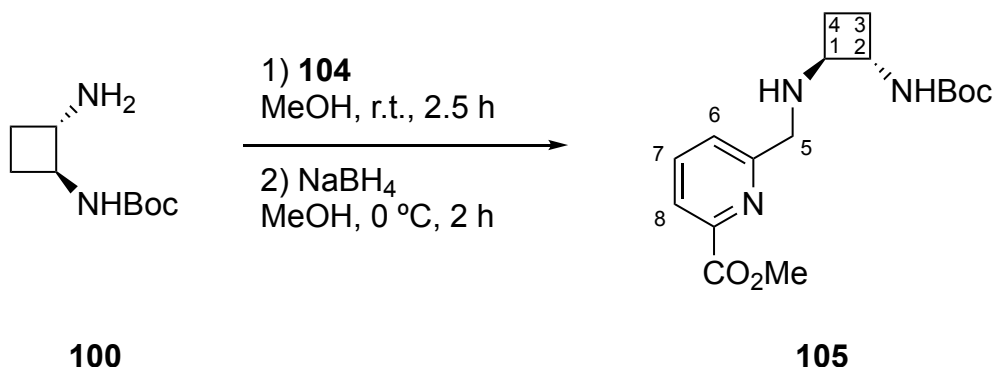
**<sup>1</sup>H NMR** (250 MHz, CDCl<sub>3</sub>): δ 4.07 (s, 3H, Me), 8.06 (m, 1H), 8.15 (m, 1H), 8.36 (dd, 1H, *J* = 7.6 Hz, *J* = 1.5 Hz), 10.19 (s, 1H, CHO).

Spectroscopic data are consistent with those reported in reference:

Platas-Iglesias, C.; Mato-Iglesias, M.; Djanashvili, K.; Muller, R. N.; Vander Elst, L.; Peters, J. A.; de Blas, A.; Rodriguez-Blas, T. *Chem. Eur. J.* **2004**, 10, 2579.

## 7. Experimental Methodologies

### Methyl 6-((((1*S*,2*S*)-2-((*tert*-butoxycarbonyl)amino)cyclobutyl)amino)methyl)picolinate, **105**



To a solution of **100** (0.140 g, 0.75 mmol) in CH<sub>3</sub>OH (5 mL) was added **104** (0.124 g, 0.75 mmol, 1 eq) and the reaction mixture was stirred at room temperature for 2.5 h. Small aliquots of this reaction were removed and concentrated to dryness for NMR analysis to confirm full Schiff base formation. Then, the reaction diluted with CH<sub>3</sub>OH (5 mL), cooled to 0 °C and NaBH<sub>4</sub> (31 mg, 0.81 mmol) was added. After 2 h of stirring at 0 °C, the reaction was quenched with satd. NaHCO<sub>3</sub> and extracted with CH<sub>2</sub>Cl<sub>2</sub>. The organic layer was dried over MgSO<sub>4</sub>, filtered and evaporated under reduced pressure to afford **105** (0.218 g, 0.65 mmol, 87% yield) as a yellow oil.

#### Spectroscopic data and physical constants for compound **105**:

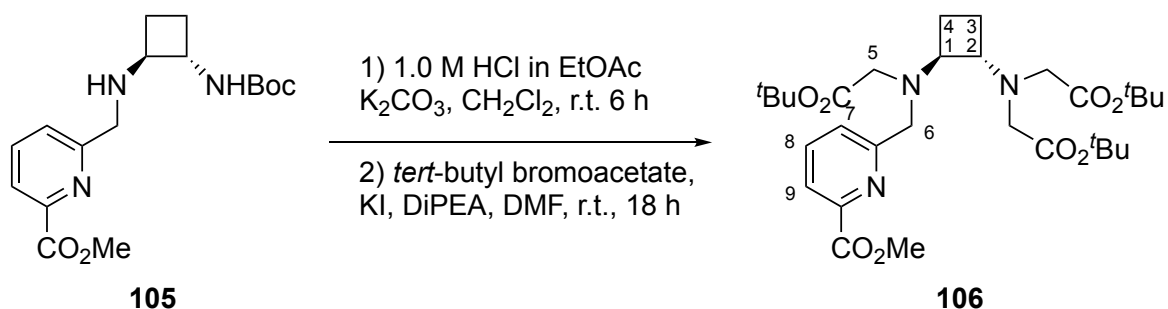
$[\alpha]_D^{20}$ : +5 (c = 1.0, CH<sub>3</sub>OH).

IR (ATR): 3117, 2975, 1687.

<sup>1</sup>H NMR (CDCl<sub>3</sub>, 400 MHz): δ 1.42 (s, 11H, *t*Bu, H<sub>3</sub>, H<sub>4</sub>), 1.95 (m, 1H), 2.12 (m, 1H), 2.87 (br s, 2H, NH), 3.15 (m, 1H), 3.79 (m, 1H), 3.98 (s, 3H, Me), 4.01 (m, 2H, H<sub>5</sub>), 7.55 (m, 1H), 7.78 (m, 1H), 7.97 (m, 1H).

<sup>13</sup>C NMR (CDCl<sub>3</sub>, 90 MHz): δ 23.3, 23.5, 28.3, 52.2, 52.8, 61.5, 64.5, 77.2, 123.7, 125.7, 137.6, 146.9, 154.9, 160.3, 165.5.

HRMS (ESI) calculated for C<sub>17</sub>H<sub>25</sub>N<sub>3</sub>O<sub>4</sub>Na (M+Na<sup>+</sup>): 358.1737. Found: 358.1724

Protected Ligand **106**

Half protected diamine **105** (0.218 g, 0.65 mmol) was dissolved in CH<sub>2</sub>Cl<sub>2</sub> (5 mL). Then, a solution of 1 M HCl in EtOAc (11.25 mL, 11.25 mmol, 15 eq) was added and the reaction was stirred at r.t. for 4 h. After this period, the solvent was evaporated under reduced pressure. Then, the crude product was dissolved in CH<sub>2</sub>Cl<sub>2</sub> (20 mL) and stirred over an excess of K<sub>2</sub>CO<sub>3</sub> (0.83 g, 6 mmol). After 2 h, the solution was filtered and evaporated. The slurry containing product and K<sub>2</sub>CO<sub>3</sub> could be carried directly through to the next step (assuming 100% product). Then, the mixture was dissolved in DMF (2 mL) under N<sub>2</sub> atmosphere. KI (0.312 g, 1.88 mmol, 2.89 eq), DiPEA (0.71 mL, 4.10 mmol, 6.3 eq) and *tert*-butyl bromoacetate (0.315 mL, 2.14 mmol, 3.3 eq) were added and the reaction mixture was stirred at r.t. for 18 h. Then, the solution was diluted with CH<sub>2</sub>Cl<sub>2</sub> (20 mL) and washed with satd K<sub>2</sub>CO<sub>3</sub> (2 x 5 mL), and brine (1 x 5 mL). The organic layer was dried over MgSO<sub>4</sub>, filtered and evaporated under reduced pressure. Purification by column chromatography (EtOAc/hexane, 1:3 to 1:1) affords **106** (0.263 g, 0.455 mmol, 74% yield) as a yellow oil.

## 7. Experimental Methodologies

### Spectroscopic data and physical constants for compound **106**:

$[\alpha]_D^{20}$ : +17 (c = 1.0, CH<sub>3</sub>OH).

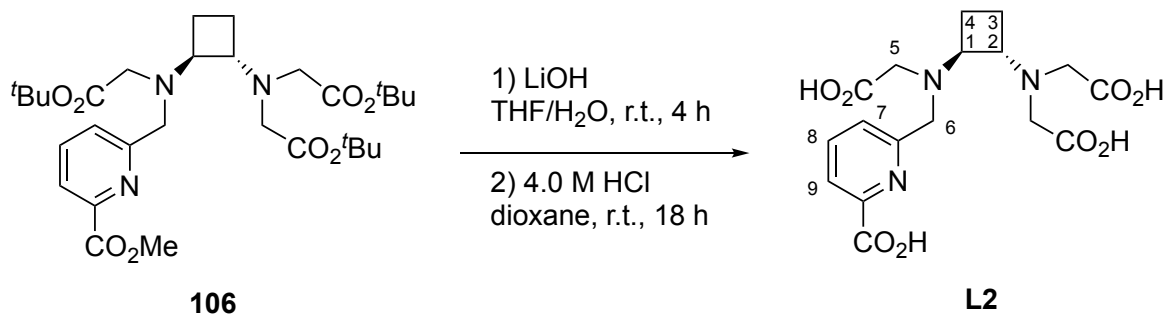
IR (ATR): 2978, 1722.

<sup>1</sup>H NMR (CDCl<sub>3</sub>, 400 MHz): δ 1.43 (m, 29H, tBu, H<sub>3</sub>, H<sub>4</sub>), 1.82 (m, 2H, H<sub>3</sub>, H<sub>4</sub>), 3.32 (m, 3H), 3.48 (m, 5H), 3.99 (s, 3H, Me), 4.02 (m, 1H, H<sub>6</sub>), 4.09 (m, 1H, H<sub>6</sub>'), 7.80 (t, 1H, J = 7.6 Hz, H<sub>8</sub>), 7.91 (d, 1H, J = 7.6 Hz), 7.98 (d, 1H, J = 7.5 Hz).

<sup>13</sup>C NMR (CDCl<sub>3</sub>, 100 MHz): δ 18.6, 20.5, 28.0, 28.1, 52.7, 54.1, 56.8, 61.8, 63.3, 80.6, 123.4, 126.1, 137.2, 147.0, 161.2, 165.9, 170.9.

HRMS (ESI) calculated for C<sub>30</sub>H<sub>47</sub>N<sub>3</sub>O<sub>8</sub>Na (M+Na<sup>+</sup>): 600.3255. Found: 600.3267

### Lligand **L2**



A solution of compound **106** (0.18 g, 0.31 mmol) was dissolved in THF/H<sub>2</sub>O (1:1, 5 mL), LiOH (0.052 g, 1.25 mmol, 4 eq) was added and the reaction mixture was stirred at room temperature for 4 h. Then, the mixture was concentrated to dryness under reduced pressure and the resultant residue was dissolved in 4 M HCl in dioxane (8 mL) and stirred at room temperature for 18 h. Then, the solvent was evaporated under reduced pressure. A small amount of water (2 mL) was added and the mixture was evaporated to dryness. This process was repeated once with the addition of water and twice with an addition of diethyl ether (2 mL) to afford **L2 · 2HCl** (0.11 g, 0.25 mmol, 77% yield) as a yellow solid without need for further purification.

**Spectroscopic data and physical constants for compound L2 · 2HCl:**

**<sup>1</sup>H NMR** (D<sub>2</sub>O, 600 MHz): δ 1.75 (m, 2H, H<sub>3</sub>, H<sub>4</sub>), 2.06 (m, 2H, H<sub>3</sub>', H<sub>4</sub>'), 3.76 (m, 1H), 3.75 (m, 1H), 3.83 (m, 1H), 4.00 (m, 4H), 4.16 (m, 1H), 4.32 (m, 2H, H<sub>6</sub>), 8.01 (d, 1H, *J* = 7.7 Hz), 8.28 (d, 1H, *J* = 6.2 Hz), 8.46 (t, 1H, *J* = 7.6 Hz, H<sub>8</sub>).

**<sup>13</sup>C NMR** (D<sub>2</sub>O, 150 MHz): δ 17.3, 18.2, 52.0, 53.1, 53.4, 60.6, 62.3, 126.2, 129.0, 146.6, 154.0, 163.0, 168.7, 174.25.

**MS** (ESI) calculated for C<sub>17</sub>H<sub>21</sub>N<sub>3</sub>O<sub>8</sub> (M+H<sup>+</sup>): 396.1. Found: 396.1

## 7.19 Details for the catalysis presented in chapter 3

### 7.19.1 General epoxidation for uncatalyzed reactions

In a 50 mL flask containing 3.8 mmol of the desired olefin dissolved in 4 mL of CH<sub>2</sub>Cl<sub>2</sub>, a solution of 4.2 mmol (1.1 eq) of *m*-chloroperbenzoic acid in 9 mL of CH<sub>2</sub>Cl<sub>2</sub> was added dropwise at r.t. under stirring. After 2 hours, an additional 0.38 mmol (0.1 eq) of *m*-chloroperbenzoic acid in 1 mL of CH<sub>2</sub>Cl<sub>2</sub> was added to the resulting suspension. After stirring for an additional 2 h, the suspension was washed successively with aqueous solutions of NaHCO<sub>3</sub> and brine. Then, it was dried over MgSO<sub>4</sub>, and the solvent was removed under reduced pressure. The resulting products were analysed by <sup>1</sup>H NMR and GC.

### 7.19.2 General epoxidation for catalyzed reactions

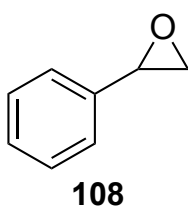
In a 25 mL flash, the catalyst (0.005 mmol, 0.005 eq) was sonicated in 10 mL of CH<sub>2</sub>Cl<sub>2</sub>/MeOH, 9:1 (v/v). Then, the desired olefin (1 mmol, 1 eq) and undecane (GC internal standard, 100 μL) were added. After, urea hydrogen peroxide complex (188 mg, 2 mmol, 2 eq) was added in three portions at 0, 1 and 2 h. The reaction mixture was stirred at r.t. and aliquots were taken from the reaction

## 7. Experimental Methodologies

mixture and subjected to GC analysis for the determination of yield and conversion data. When the reaction was finished, the suspension was washed successively with aqueous solutions of NaHCO<sub>3</sub> and brine. Then, it was dried over MgSO<sub>4</sub>, and the solvent was removed under reduced pressure. The resulting products were analysed chiral HPLC for the determination of the enantiomeric ratio.

### 7.19.3 Experimental data of the catalyzed reaction products

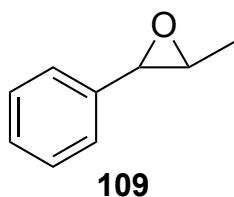
#### Styrene oxide, **108**:



<sup>1</sup>H NMR (CDCl<sub>3</sub>, 250 MHz): δ 2.84 (dd, 1H, *J* = 5.5, 2.6 Hz), 3.18 (dd, 1H, *J* = 5.5, 4.1 Hz), 3.90 (dd, 1H, *J* = 4.1, 2.6 Hz), 7.35 (m, 5H).

Yields of the epoxidation of styrene to obtain styrene oxide were determined using GC analysis. Calibration using 5 standard samples containing different ratios of concentrations of **108** and undecane (internal standard) was performed. Then, the fraction of the relative areas of **108** and undecane versus the amount of **108** was plotted. Then the experimental data was fitted and the following linear function was obtained:  $y = 0.003x + 0.0334$ ; *x* in mg ( $R^2 = 0.98$ ). Yields of the catalyzed reactions were calculated from the linear interpolation of the previous function. Detector: FID; column: Agilent HP-5MS; Temp program: 80 °C -0 min-5 °C/min-175 °C-5 min; Inlet: 200 °C; Detector: 300 °C; flow: 3.2 mL/min.  $t_R = 6.875$  min for styrene oxide;  $t_R = 7.398$  min for undecane.

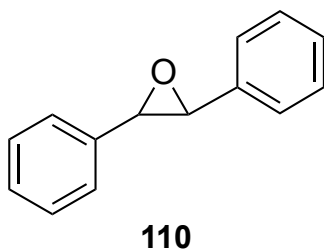
Enantiomeric ratio determined by chiral HPLC analysis. Chiralpak AS column, hexane/2-propanol 98/2, 0.5 mL/min  $t_R = 13.45$  and 15.66 min.

***trans*-2-Methyl-3-phenyloxirane, 109**

$^1\text{H}$  NMR ( $\text{CDCl}_3$ , 250 MHz):  $\delta$  1.37 (d, 3H,  $J = 5.1$  Hz), 2.98 (m, 1H), 3.55 (m, 1H), 7.38 (m, 5H).

Yields of the epoxidation of (*trans*)-prop-1-en-1-ylbenzene to obtain (*trans*)-2-methyl-3-phenyloxirane were determined using GC analysis. Calibration using 5 standard samples containing different ratios of concentrations of **109** and undecane (internal standard) was performed. Then, the fraction of the relative areas of **109** and undecane versus the amount of **109** was plotted. Then the experimental data was fitted and the following linear function was obtained:  $y = 0.0032x + 0.0165$ ;  $x$  in mg ( $R^2 = 0.996$ ). Yields of the catalyzed reactions were calculated from the linear interpolation of the previous function. Detector: FID; column: Agilent HP-5MS; Temp program: 100 °C -0 min-5 °C/min-175 °C-5 min; Inlet: 200 °C; Detector: 300 °C; flow: 3.2 mL/min.  $t_R = 5.459$  min for **109**;  $t_R = 5.069$  min for undecane.

Enantiomeric ratio determined by chiral HPLC analysis. Chiralpak AD-H column, hexane/2-propanol 98/2, 0.3 mL/min  $t_R = 18.45$  and 23.27 min.

***trans*-2,3-Diphenyloxirane:**

$^1\text{H}$  NMR ( $\text{CDCl}_3$ , 250 MHz):  $\delta$  3.94 (s, 2H), 7.43 (m, 10H).  $^{13}\text{C}$  NMR ( $\text{CDCl}_3$ , 62.5 MHz):  $\delta$  63.3, 126.0, 129.0, 137.6.

Yields of the epoxidation of (*trans*)-1,2-diphenylethene to obtain (*trans*)-2,3-diphenyloxirane were determined using GC analysis. Calibration using 5 standard



## 7. Experimental Methodologies

samples containing different ratios of concentrations of **110** and undecane (internal standard) was performed. Then, the fraction of the relative areas of **110** and undecane versus the amount of **110** was plotted. Then the experimental data was fitted and the following linear function was obtained:  $y = 0.0083x + 0.0053$ ; x in mg ( $R^2 = 0.997$ ). Yields of the catalyzed reactions were calculated from the linear interpolation of the previous function. Detector: FID; column: Agilent HP-5MS; Temp program: 120 °C -0 min-5 °C/min-200 °C-10 min; Inlet: 250 °C; Detector: 300 °C; flow: 3.2 mL/min.  $t_R = 13.845$  min for **110**;  $t_R = 3.651$  min for undecane.

Enantiomeric ratio determined by chiral HPLC analysis. Chiralpak AD-H column, hexane/2-propanol 95/5, 0.5 mL/min  $t_R = 12.34$  and 26.56 min.

## 7.20 Details for the catalysis presented in chapter 4

### 7.20.1 General procedure for catalytic asymmetric aldol reactions

**Water free conditions:** 0.01 to 0.04 mmol (5 to 20%) of the selected catalyst were added to 0.2 mmol of aldehyde and dissolved in 0.75 to 2 mL (0.1 M to 0.3 M) of solvent (acetone or acetone/methanol 10:1) under  $N_2$  atmosphere in the desired temperature. The reaction was stirred for the time indicated. The solvent was evaporated and 5 mL of EtOAc and 5 mL of water were added. The organic phase was washed with 2 x 3 mL of water, dried over  $MgSO_4$ , filtered and evaporated under reduced pressure. Purification by column chromatography (EtOAc/hexane 1:3) yields the desired aldol product.

**Acetone/solvent mixture:** 0.01 to 0.04 mmol (5 to 20% catalyst) of the selected catalyst were added to 0.2 mmol of aldehyde and dissolved in 0.75 to 2 mL (0.1 M to 0.3 M) of acetone/solvent (at desired ratio). The reaction mixture was stirred for the time indicated. The acetone was evaporated and 5 mL of EtOAc and 5 mL of water were added. The organic phase was washed with 2 x 3 mL of water, dried over  $MgSO_4$ , filtered and evaporated under reduced pressure. Purification by column chromatography (EtOAc/hexane 1:3) yields the desired aldol product.

**Catalyst recovery:** The combined water phases were washed with 3 x 5 mL of Et<sub>2</sub>O. The lyophilisation of the water phases allowed the recovery of the catalyst (90 %), which could be reused without any loss of catalytic activity.

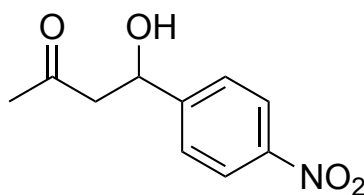
**Reaction between *p*-nitrobenzaldehyde and cyclohexanone:** The catalyst **4** (3.4 mg, 0.01 mmol, 0.05 eq) and *p*-nitrobenzaldehyde (30 mg, 0.2 mmol) were dissolved in 2 mL of cyclohexanone under N<sub>2</sub> atmosphere. The reaction was stirred for 5 h and the solvent was evaporated. 5 mL of EtOAc and 5 mL of water were added and the organic phase was washed with 2 x 3 mL of water, dried over MgSO<sub>4</sub>, filtered and evaporated under reduced pressure. Purification by column chromatography (EtOAc/hexane 1:1) gives the diastereomeric mixture of aldols.

### 7.20.2 General procedure for catalytic asymmetric Michael reactions

**Reaction between ketone and *trans*-β-nitrostyrene:** 0.01 mmol (5% catalyst) of the selected catalyst and *trans*-β-nitrostyrene (30 mg, 0.2 mmol) were dissolved in 2 mL of solvent (acetone, cyclohexanone or acetone/methanol 1:4) under N<sub>2</sub> atmosphere and the reaction mixture was stirred 24 h at room temperature. The solvent was evaporated and 5 mL of EtOAc and 5 mL of water were added. The organic phase was washed with 2 x 3 mL of NaHCO<sub>3</sub> and 3 mL of brine, dried over MgSO<sub>4</sub>, filtered and evaporated under reduced pressure. Purification by column chromatography (EtOAc/hexane 1:2) yields the desired nitro ketone product.

### 7.20.3 Experimental data of the catalyzed reaction products

**4-Hydroxy-4-(4-nitrophenyl)butan-2-one (59a):**



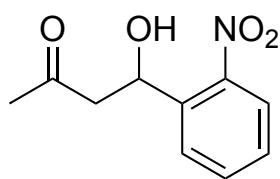
**59a**

## 7. Experimental Methodologies

$^1\text{H}$  NMR ( $\text{CDCl}_3$ , 360 MHz):  $\delta$  2.22 (s, 3H), 2.86 (m, 2H), 3.58 (d, 1H,  $J = 3.2$  Hz), 5.26 (m, 1H), 7.54 (d, 2H,  $J = 8.4$  Hz), 8.21 (d, 2H,  $J = 8.4$  Hz).

Enantiomeric ratio determined by chiral HPLC analysis. Chiralpak AS column, hexane/2-propanol 70/30, 0.5 mL/min  $t_R = 25.37$  min for (*R*)-enantiomer,  $t_R = 34.50$  min for (*S*)-enantiomer. The absolute configuration was assigned by comparison with the values reported in literature.<sup>126</sup>

### 4-Hydroxy-4-(2-nitrophenyl)butan-2-one (59g):

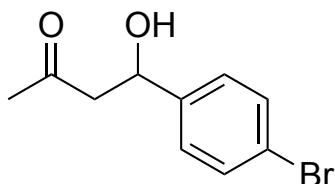


**59g**

$^1\text{H}$  NMR ( $\text{CDCl}_3$ , 250 MHz):  $\delta$  2.25 (s, 3H), 2.76 (m, 1H), 3.14 (m, 1H), 3.78 (br s, 1H), 5.69 (dd, 1H,  $J = 9.4, 2.2$  Hz), 7.45 (m, 1H), 7.68 (m, 1H), 7.95 (m, 2H).

Enantiomeric ratio determined by chiral HPLC analysis. Chiralpak AS column, hexane/2-propanol 70/30, 0.5 mL/min  $t_R = 17.03$  min for (*S*)-enantiomer,  $t_R = 20.68$  min for (*R*)-enantiomer. The absolute configuration was assigned by comparison with the values reported in literature.<sup>126,248</sup>

### 4-(4-Bromophenyl)-4-hydroxybutan-2-one (59c):



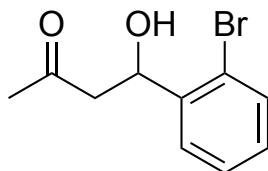
**59c**

$^1\text{H}$  NMR ( $\text{CDCl}_3$ , 250 MHz):  $\delta$  2.22 (s, 3H), 2.82 (m, 2H), 5.13 (m, 1H), 7.27 (m, 2H), 7.48 (m, 2H).

Enantiomeric ratio determined by chiral HPLC analysis. Chiralpak AS column, hexane/2-propanol 90/10, 0.5 mL/min  $t_R = 30.57$  min for (*R*)-enantiomer,

$t_R = 41.62$  min for (*S*)-enantiomer. The absolute configuration was assigned by comparison with the values reported in literature.<sup>249</sup>

**4-(2-Bromophenyl)-4-hydroxybutan-2-one (59h):**

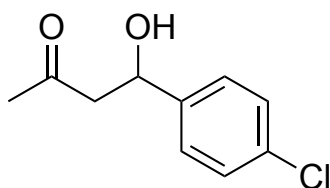


**59h**

<sup>1</sup>H NMR (CDCl<sub>3</sub>, 250 MHz):  $\delta$  2.22 (s, 3H), 2.67 (m, 1H), 3.02 (m, 1H), 5.43 (m, 1H), 7.14 (t, 1H,  $J = 7.6$  Hz), 7.35 (t, 1H,  $J = 7.6$  Hz), 7.51 (d, 1H,  $J = 7.9$  Hz), 7.61 (d, 1H,  $J = 7.7$  Hz).

Enantiomeric ratio determined by chiral HPLC analysis. Chiralpak AS column, hexane/2-propanol 90/10, 0.3 mL/min  $t_R = 37.34$  min for (*S*)-enantiomer,  $t_R = 43.54$  min for (*R*)-enantiomer. The absolute configuration was assigned by comparison with the values reported in literature.<sup>126,250</sup>

**4-(4-Chlorophenyl)-4-hydroxybutan-2-one (59d):**



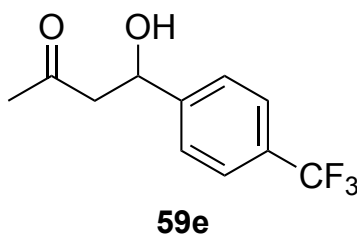
**59d**

<sup>1</sup>H NMR (CDCl<sub>3</sub>, 250 MHz):  $\delta$  2.22 (s, 3H), 2.81 (m, 2H), 5.13 (m, 1H), 7.30 (m, 1H).

Enantiomeric ratio determined by chiral HPLC analysis. Chiralpak AS column, hexane/2-propanol 90/10, 0.5 mL/min  $t_R = 27.64$  min for (*R*)-enantiomer,  $t_R = 35.84$  min for (*S*)-enantiomer. The absolute configuration was assigned by comparison with the values reported in literature.<sup>249</sup>

## 7. Experimental Methodologies

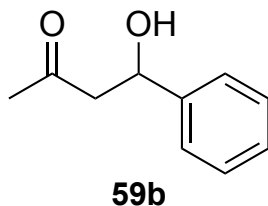
### 4-Hydroxy-4-(4-(trifluoromethyl)phenyl)butan-2-one (59e):



$^1\text{H}$  NMR ( $\text{CDCl}_3$ , 250 MHz):  $\delta$  2.21 (s, 3H), 2.86 (m, 2H); 5.22 (m, 1H), 7.50 (m, 2H), 7.60 (m, 2H).

Enantiomeric ratio determined by chiral HPLC analysis. Chiralpak AS column, hexane/2-propanol 92/8, 0.5 mL/min  $t_R = 22.79$  min for (*R*)-enantiomer,  $t_R = 28.85$  min for (*S*)-enantiomer. The absolute configuration was assigned by comparison with the values reported in literature. <sup>249</sup>

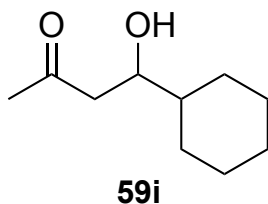
### 4-Hydroxy-4-phenylbutan-2-one (59b):



$^1\text{H}$  NMR ( $\text{CDCl}_3$ , 250 MHz):  $\delta$  2.25 (s, 3H), 2.87 (m, 2H), 4.40 (br s, 1H), 5.23 (m, 2H), 7.47 (m, 5H).

Enantiomeric ratio determined by chiral HPLC analysis. Chiralpak AS column, hexane/2-propanol 90/10, 0.5 mL/min  $t_R = 28.01$  min for (*R*)-enantiomer,  $t_R = 35.76$  min for (*S*)-enantiomer. The absolute configuration was assigned by comparison with the values reported in literature. <sup>249</sup>

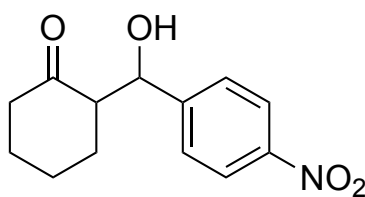
### 4-cyclohexyl-4-hydroxybutan-2-one (59i):



$^1\text{H}$  NMR ( $\text{CDCl}_3$ , 250 MHz):  $\delta$  0.84–1.22 (m, 6H), 1.50–1.74 (m, 5H), 2.06 (s, 3H), 2.45 (m, 2H), 3.28 (br s, 1H), 3.69 (m, 1H).

Enantiomeric ratio determined by chiral HPLC analysis. Chiralpak AS column, hexane/2-propanol 92/8, 0.5 mL/min  $t_R$  = 16.75 min for (*R*)-enantiomer,  $t_R$  = 19.37 min for (*S*)-enantiomer. The absolute configuration was assigned by comparison with the values reported in literature.<sup>249</sup>

**2-(Hydroxy(4-nitrophenyl)methyl)cyclohexan-1-one (95):**

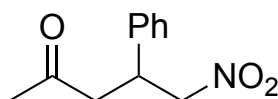


**95**

$^1\text{H}$  NMR ( $\text{CDCl}_3$ , 250 MHz):  $\delta$  1.53–1.83 (m, 5H), 2.10 (m, 1H), 2.35–2.59 (m, 3H), 4.90 (d, 1H,  $J$  = 8.4 Hz), 7.51 (d, 2H,  $J$  = 8.7 Hz), 8.21 (d, 2H,  $J$  = 8.8 Hz).

Enantiomeric and diastereomeric ratio determined by chiral HPLC analysis. Chiralpak AD-H column, hexane/2-propanol 88/12, 0.7 mL/min  $t_R$  = 23.60 min for (*R*)-enantiomer,  $t_R$  = 25.79 min for (*S*)-enantiomer for the *anti* diastereomer.  $t_R$  = 28.73 min for (*R*)-enantiomer,  $t_R$  = 37.65 min for (*S*)-enantiomer for the *syn* diastereomer. The absolute configuration was assigned by comparison with the values reported in literature.<sup>125</sup>

**5-Nitro-4-phenylpentan-2-one (96):**



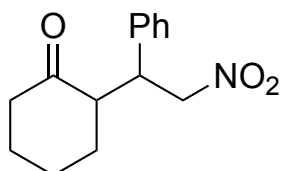
**96**

$^1\text{H}$  NMR ( $\text{CDCl}_3$ , 250 MHz):  $\delta$  2.12 (s, 3H), 2.93 (m, 2H), 3.98 (m, 1H), 4.61 (m, 2H), 7.31 (m, 5H).

## 7. Experimental Methodologies

Enantiomeric ratio determined by chiral HPLC analysis. Chiralpak AS column, hexane/2-propanol 87/13, 1 mL/min  $t_R = 12.09$  min for (*S*)-enantiomer,  $t_R = 14.89$  min for (*R*)-enantiomer. The absolute configuration was assigned by comparison with the values reported in literature.<sup>251</sup>

### 2-(2-nitro-1-phenylethyl)cyclohexan-1-one (97):



**97**

<sup>1</sup>H NMR (CDCl<sub>3</sub>, 250 MHz) syn diastereomer:  $\delta$  1.60–1.75 (m, 5H), 2.08 (m, 1H), 2.44 (m, 2H), 2.68 (m, 1H), 3.75 (m, 1H), 4.63 (dd, 1H,  $J = 12.5, 9.9$  Hz), 4.94 (dd, 1H, 12.4, 4.5 Hz), 7.29 (m, 5H). <sup>1</sup>H NMR (CDCl<sub>3</sub>, 250 MHz) anti diastereomer:  $\delta$  1.60–1.75 (m, 5H), 2.08 (m, 1H), 2.44 (m, 2H), 2.68 (m, 1H), 4.02 (m, 1H), 4.63 (dd, 1H,  $J = 12.5, 9.9$  Hz), 4.94 (dd, 1H, 12.4, 4.5 Hz), 7.29 (m, 5H).

Diastereomeric ratio determined by <sup>1</sup>H NMR and enantiomeric ratio determined by chiral HPLC analysis. Chiralpak AS column, hexane/2-propanol 81/19, 1 mL/min  $t_R = 9.90$  min for (*S*)-enantiomer,  $t_R = 12.57$  min for (*R*)-enantiomer for the *syn* diastereomer. The absolute configuration was assigned by comparison with the values reported in literature.<sup>110,252</sup>

## **8. Bibliography**

---





## 8. Bibliography

- (1) Sorrenti, A.; Illa, O.; Ortuño, R. M.; Pons, R. Chiral Cyclobutane  $\beta$ -Amino Acid-Based Amphiphiles: Influence of Cis/Trans Stereochemistry on Condensed Phase and Monolayer Structure. *Langmuir* **2016**, *32* (27), 6977–6984.
- (2) Fernández, D.; Torres, E.; Avilés, F. X.; Ortuño, R. M.; Vendrell, J. Cyclobutane-Containing Peptides: Evaluation as Novel Metallocoarboxypeptidase Inhibitors and Modelling of Their Mode of Action. *Bioorganic Med. Chem.* **2009**, *17* (11), 3824–3828.
- (3) Aguilera, J.; Favier, I.; Sans, M.; Mor, À.; Álvarez-Larena, Á.; Illa, O.; Gómez, M.; Ortuño, R. M. Synthesis of Chiral Functionalised Cyclobutylpyrrolidines and Cyclobutylamino Alcohols from (-)-(S)-Verbenone - Applications in the Stabilisation of Ruthenium Nanocatalysts. *European J. Org. Chem.* **2015**, *2015* (4), 810–819.
- (4) Celis, S.; Pi-boleda, B.; Nolis, P.; Illa, O. Synthesis, Selectivity and Structural Study of New C3-Symmetric Tripodal Amides as Anion Receptors. An Experimental and Theoretical Approach. *Chem. Sel.* **2016**, 1887–1892.
- (5) Izquierdo, S.; Martín-Vilà, M.; Moglioni, A. G.; Branchadell, V.; Ortuño, R. M. Stereodivergent Syntheses of the First Bis(cyclobutane)  $\beta$ -Dipeptides. *Tetrahedron: Asymmetry* **2002**, *13* (22), 2403–2405.
- (6) Aguilera, J.; Moglioni, A. G.; Moltrasio, G. Y.; Ortuño, R. M. Stereodivergent Synthesis of the First Bis(cyclobutane)  $\gamma$ -Dipeptides and Mixed  $\gamma$ -Oligomers. *Tetrahedron: Asymmetry* **2008**, *19* (3), 302–308.
- (7) Saragovi, H. U.; Greene, M. I.; Chrusciel, R. A.; Kahn, M. Loops and Secondary Structure Mimetics: Development and Applications in Basic Science and Rational Drug Desing. *Nat. Biotechnol.* **1992**, *10*, 773–778.
- (8) Yang, H.; Xiang, J.; Wang, N.; Zhao, Y.; Hyman, J.; Li, S.; Jiang, J.; Chen, J. K.; Yang, Z.; Lin, S. Converse Conformational Control of Smoothened Activity by Structurally Related Small Molecules. *J. Biol. Chem.* **2009**, *284* (31), 20876–20884.
- (9) Lawson, A. D. G. Antibody-Enabled Small-Molecule Drug Discovery. *Nat. Rev. Drug Discov.* **2012**, *11* (7), 519–525.
- (10) *Small Molecule Medicinal Chemistry*; Czechtizky, W., Hamley, P., Eds.; John Wiley & Sons, 2015.
- (11) Izquierdo, S.; Rúa, F.; Sbai, A.; Parella, T.; Álvarez-Larena, Á.; Branchadell, V.; Ortuño, R. M. (+)- and (-)-2-Aminocyclobutane-1-Carboxylic Acids and Their Incorporation into Highly Rigid  $\beta$ -Peptides: Stereoselective Synthesis and a Structural Study. *J. Org. Chem.* **2005**, *70* (20), 7963–7971.
- (12) Ortuño, R. M.; Moglioni, A. G.; Moltrasio, G. Y. Cyclobutane Biomolecules: Synthetic Approaches to Amino Acids, Peptides and Nucleosides. *Curr. Org. Chem.* **2005**, *9*, 237–259.
- (13) Gorrea, E.; Pohl, G.; Nolis, P.; Celis, S.; Burusco, K. K.; Branchadell, V.; Perczel, A.; Ortuño, R. M. Secondary Structure of Short Beta-Peptides as the Chiral Expression of Monomeric Building Units: A Rational and Predictive Model. *J. Org. Chem.* **2012**, *77* (21), 9795–9806.
- (14) Gutiérrez-Abad, R.; Carbajo, D.; Nolis, P.; Acosta-Silva, C.; Cobos, J. A.; Illa, O.; Royo, M.; Ortuño, R. M. Synthesis and Structural Study of Highly Constrained Hybrid Cyclobutane-Proline  $\gamma, \gamma$ -Peptides. *Amino Acids* **2011**, *41* (3), 673–686.

## 8. Bibliography

- (15) Sans, M.; Illa, O.; Ortuño, R. M. Stereoselective Synthesis of All Stereoisomers of Orthogonally Protected Cyclobutane-1,2-Diamine and Some Chemoselective Transformations. *Org. Lett.* **2012**, *14* (10), 2431–2433.
- (16) Okino, T.; Hoashi, Y.; Takemoto, Y. Enantioselective Michael Reaction of Malonates to Nitroolefins Catalyzed by Bifunctional Organocatalysts. *J. Am. Chem. Soc.* **2003**, *125* (42), 12672–12673.
- (17) Mayans, E.; Gargallo, A.; Álvarez-Larena, Á.; Illa, O.; Ortuño, R. M. Diastereodivergent Synthesis of Chiral Vic-Disubstituted-Cyclobutane Scaffolds: 1,3-Amino Alcohol and 1,3-Diamine Derivatives - Preliminary Use in Organocatalysis. *European J. Org. Chem.* **2013**, *8*, 1425–1433.
- (18) Torres, E.; Puigmartí, L. J.; Ortuño, R. M.; Amabilino, D. B. Use of Unnatural Beta-Peptides as a Self-Assembling Component in Functional Organic Fibers. *Org. Biomol. Chem.* **2010**, *8* (7), 1661–1665.
- (19) Sans, M.; Illa, O.; Ortuño, R. M. Organobridged Silsesquioxanes Based on Cyclobutane Diamines: Influence of the Stereochemistry on the Morphology of the Materials. *Tetrahedron* **2016**, *72* (22), 2913–2919.
- (20) Ospina, J.; Sorrenti, A.; Illa, O.; Pons, R.; Ortuño, R. M. New Chiral Polyfunctional Cyclobutane Derivatives from (-)-Verbenone: Possible Surfactant Behaviour. *Tetrahedron: Asymmetry* **2013**, *24* (12), 713–718.
- (21) Gorrea, E.; Carbajo, D.; Gutiérrez-Abad, R.; Illa, O.; Branchadell, V.; Royo, M.; Ortuño, R. M. Searching for New Cell-Penetrating Agents: Hybrid Cyclobutane–proline  $\gamma$ ,  $\gamma$ -Peptides. *Org. Biomol. Chem.* **2012**, *10* (20), 4050.
- (22) Gutiérrez-Abad, R.; Illa, O.; Ortuño, R. M. Synthesis of Chiral Cyclobutane Containing C3-Symmetric Peptide Dendrimers. *Org. Lett.* **2010**, *12* (14), 3148–3151.
- (23) *Gels: Structures, Properties, and Functions*; Tokita, M., Nishinari, K., Eds.; Springer: New York, 2009.
- (24) Jordan Lloyd, D. *Colloid Chemistry*; The Chemical Catalog Co.: New York, 1926.
- (25) *Functional Molecular Gels*; Escuder, B., Miravet, J. M., Eds.; RSC Soft Matter Series: Cambridge, 2014.
- (26) *Molecular Gels. Materials with Self-Assembled Fibrillar Networks*; Weiss, R. G., Terech, P., Eds.; Springer: Dordrecht, 2006.
- (27) Lan, Y.; Corradini, M. G.; Weiss, R. G.; Raghavan, S. R.; Rogers, M. A. To Gel or Not to Gel: Correlating Molecular Gelation with Solvent Parameters. *Chem. Soc. Rev.* **2015**, *44* (17), 6035–6058.
- (28) Segarra-Maset, M. D.; Nebot, V. J.; Miravet, J. F.; Escuder, B. Control of Molecular Gelation by Chemical Stimuli. *Chem. Soc. Rev.* **2013**, *42* (17), 7086–7098.
- (29) Vintiloiu, A.; Leroux, J.-C. Organogels and Their Use in Drug Delivery - A Review. *J. Control. Release* **2008**, *125* (3), 179–192.
- (30) *Organic Nanostructures*; Atwood, J. L., Steed, J. W., Eds.; Wiley-VCH: Weinheim, 2000.
- (31) Hanabusa, K.; Tange, J.; Taguchi, Y.; Koyoma, T.; Shirai, H. Small Molecular Gelling Agents to Harden Organic Liquids: Alkylamide of N-Benzoyloxycarbonyl-L-Valyl-L-Valine. *J. Chem. Soc., Chem. Commun.* **1993**, *0* (4), 390–392.
- (32) Menger, F. M.; Yamasaki, Y.; Catlin, K. K.; Nishimi, T. X-Ray Structure of a Self-Assembled Gelating Fiber. *Angew. Chem. - Int. Ed.* **1995**, *34* (5), 585–586.

## 8. Bibliography

- (33) Brotin, T.; Utermöhlen, R.; Fages, F.; Bouas-Laurent, H.; Desvergne, J.-P. A Novel Small Molecular Luminescent Gelling Agent for Alcohols. *J. Chem. Soc., Chem. Commun.* **1991**, 0 (6), 416–418.
- (34) Pi-Boleda, B.; Sans, M.; Campos, M.; Nolis, P.; Illa, O.; Estévez, J. C.; Branchadell, V.; Ortuño, R. M. Studies on Cycloalkane-Based Bisamide Organogelators: A New Example of Stochastic Chiral Symmetry Breaking Induced by Sonication. *Chem. - A Eur. J.* **2017**, 23, 3357–3365.
- (35) Camiolo, S.; Gale, P. A.; Hursthouse, M. B.; Light, M. E. Nitrophenyl Derivatives of Pyrrole 2,5- Diamides: Structural Behaviour, Anion Binding and Colour Change Signalled Deprotonation. *Org. Biomol. Chem.* **2003**, 1 (4), 741–744.
- (36) Díaz-Oltra, S.; Berdugo, C.; Miravet, J. F.; Escuder, B. Study of the Effect of Polymorphism on the Self-Assembly and Catalytic Performance of an L -Proline Based Molecular Hydrogelator. *New J. Chem.* **2015**, 39 (5), 3785–3791.
- (37) Smith, D. K. Lost in Translation? Chirality Effects in the Self-Assembly of Nanostructured Gel-Phase Materials. *Chem. Soc. Rev.* **2009**, 38 (3), 684–694.
- (38) Duan, P.; Cao, H.; Zhang, L.; Liu, M. Gelation Induced Supramolecular Chirality: Chirality Transfer, Amplification and Application. *Soft Matter* **2014**, 10 (30), 5428.
- (39) Takafuji, M.; Kira, Y.; Tsuji, H.; Sawada, S.; Hachisako, H.; Ihara, H. Optically Active Polymer Film Tuned by a Chirally Self-Assembled Molecular Organogel. *TetrahedronTetrahedron* **2007**, 63 (31), 7489–7494.
- (40) Gorrea, E.; Nolis, P.; Torres, E.; Da Silva, E.; Amabilino, D. B.; Branchadell, V.; Ortuño, R. M. Self-Assembly of Chiral Trans-Cyclobutane-Containing  $\beta$ -Dipeptides into Ordered Aggregates. *Chem. - A Eur. J.* **2011**, 17, 4588–4597.
- (41) Celis, S.; Nolis, P.; Illa, O.; Branchadell, V.; Ortuño, R. M. Low-Molecular-Weight Gelators Consisting of Hybrid Cyclobutane-Based Peptides. *Org. Biomol. Chem.* **2013**, 11, 2839–2846.
- (42) Li, S.; John, V. T.; Irvin, G. C.; Rachakonda, S. H.; McPherson, G. L.; O'Connor, C. J. Synthesis and Magnetic Properties of a Novel Ferrite Organogel. *J. Appl. Phys.* **1999**, 85 (8), 5965.
- (43) Rodríguez-Llansola, F.; Escuder, B.; Miravet, J. F. Switchable Performance of an L-Proline-Derived Basic Catalyst Controlled by Supramolecular Gelation. *J. Am. Chem. Soc.* **2009**, 131 (32), 11478–11484.
- (44) Puigmartí, L. J.; Laukhin, V.; Perez del Pino, Á.; Vidal-Gancedo, J.; Rovira, C.; Laukhina, E.; Amabilino, D. B. Supramolecular Conducting Nanowires from Organogels. *Angew. Chem. - Int. Ed.* **2007**, 46 (1–2), 238–241.
- (45) Wang, C.; Chen, Q.; Sun, F.; Zhang, D.; Zhang, G.; Huang, Y.; Zhao, R.; Zhu, D. Multistimuli Responsive Organogels Based on a New Gelator Featuring Tetrathiafulvalene and Azobenzene Groups: Reversible Tuning of the Gel-Sol Transition by Redox Reactions and Light Irradiation. *J. Am. Chem. Soc.* **2010**, 132 (9), 3092–3096.
- (46) Tam, A. Y.-Y.; Yam, V. W.-W. Recent Advances in Metallogels. *Chem. Soc. Rev.* **2013**, 42 (4), 1540–1567.
- (47) Svobodová, H.; Noponen, V.; Kolehmainen, E.; Sievänen, E. Recent Advances in Steroidal Supramolecular Gels. *RSC Adv.* **2012**, 2, 4985–5007.
- (48) Yang, L.; Luo, L.; Zhang, S.; Su, X.; Lan, J.; Chen, C.-T.; You, J. Self-Assembly from Metal-Organic Vesicles to Globular Networks: Metallogel-Mediated Phenylation of

## 8. Bibliography

- Indole with Phenyl Boronic Acid. *Chem. Commun.* **2010**, *46*, 3938–3940.
- (49) Zhang, J.; Su, C. Y. Metal-Organic Gels: From Discrete Metallogelators to Coordination Polymers. *Coord. Chem. Rev.* **2013**, *257* (7–8), 1373–1408.
- (50) Fages, F. Metal Coordination to Assist Molecular Gelation. *Angew. Chem. - Int. Ed.* **2006**, *45* (11), 1680–1682.
- (51) Martínez-Calvo, M.; Kotova, O.; Möbius, M. E.; Bell, A. P.; McCabe, T.; Boland, J. J.; Gunnlaugsson, T. Healable Luminescent Self-Assembly Supramolecular Metallogels Possessing Lanthanide (Eu/Tb) Dependent Rheological and Morphological Properties. *J. Am. Chem. Soc.* **2015**, *137* (5), 1983–1992.
- (52) Escuder, B.; Rodríguez-Llansola, F.; Miravet, J. F. Supramolecular Gels as Active Media for Organic Reactions and Catalysis. *New J. Chem.* **2010**, *34* (6), 1044.
- (53) Tu, T.; Assenmacher, W.; Peterlik, H.; Weisbarth, R.; Nieger, M.; Dötz, K. H. An Air-Stable Organometallic Low-Molecular-Mass Gelator: Synthesis, Aggregation, and Catalytic Application of a Palladium Pincer Complex. *Angew. Chem. - Int. Ed.* **2007**, *46* (33), 6368–6371.
- (54) Bühler, G.; Feiters, M. C.; Nolte, R. J. M.; Dötz, K. H. A Metal-Carbene Carbohydrate Amphiphile as a Low-Molecular-Mass Organometallic Gelator. *Angew. Chem. - Int. Ed.* **2003**, *42* (22), 2494–2497.
- (55) Celis, S.; Nolis, P.; Illa, O.; Branchadell, V.; Ortuño, R. M. Low-Molecular-Weight Gelators Consisting of Hybrid Cyclobutane-Based Peptides. *Org. Biomol. Chem.* **2013**, *11*, 2839–2846.
- (56) Izquierdo, S.; Kogan, M. J.; Parella, T.; Moglioni, A. G.; Branchadell, V.; Giralt, E.; Ortuño, R. M. 14-Helical Folding in a Cyclobutane-Containing  $\beta$ -Tetrapeptide. *J. Org. Chem.* **2004**, *69*, 5093–5099.
- (57) Fernandes, C.; Pereira, E.; Faure, S.; Aitken, D. J. Expedient Preparation of All Isomers of 2-Aminocyclobutanecarboxylic Acid in Enantiomerically Pure Form. *J. Org. Chem.* **2009**, *74* (8), 3217–3220.
- (58) Fernandes, C.; Gauzy, C.; Yang, Y.; Roy, O.; Pereira, E.; Faure, S.; Aitken, D. J. [2+2] Photocycloadditions with Chiral Uracil Derivatives: Access to All Four Stereoisomers of 2-Aminocyclobutanecarboxylic Acid. *Synthesis* **2007**, *14*, 2222–2232.
- (59) Terech, P. Metastability and Sol Phases: Two Keys for the Future of Molecular Gels? *Langmuir* **2009**, *25* (15), 8370–8372.
- (60) de Loos, M.; van Esch, J.; Stokroos, I.; Kellogg, R. M.; Feringa, B. L. Remarkable Stabilization of Self-Assembled Organogels by Polymerization. *J. Am. Chem. Soc.* **1997**, *119* (51), 12675–12676.
- (61) Grigoriev, H.; Chmielewska, D.; Gronkowski, J. SAXS Structural Study of Xerogels and Aerogels Formed from Small-Molecule Organic Gelators. **2008**, *100* (2), 1–4.
- (62) Shalley, C. A. *Analytical Methods in Supramolecular Chemistry*; Wiley-VCH: Weinheim, 2012.
- (63) Kim, K. H.; Akase, Z.; Suzuki, T.; Shindo, D. Charging Effects on SEM/SIM Contrast of Metal/Insulator System in Various Metallic Coating Conditions. *Mater. Trans.* **2010**, *51* (6), 1080–1083.
- (64) Aggeli, A.; Nyrkova, I. A.; Bell, M.; Harding, R.; Carrick, L.; McLeish, T. C. B.; Semenov, A. N.; Boden, N. Hierarchical Self-Assembly of Chiral Rod-like Molecules as a Model for Peptide  $\beta$ -Sheet Tapes, Ribbons, Fibrils, and Fibers. *Proc. Natl.*

- Acad. Sci.* **2001**, *98* (21), 11857–11862.
- (65) Kawata, Y.; Yamamoto, T.; Kihara, H.; Yamamura, Y.; Saito, K.; Ohno, K. Three Gel States of Colloidal Composites Consisting of Polymer-Brush-Afforded Silica Particles and a Nematic Liquid Crystal with Distinct Viscoelastic and Optical Properties. *ACS Appl. Mater. Interfaces* **2016**, *8* (43), 29649–29657.
- (66) Ikeda, S. Heat-Induced Gelation of Whey Proteins Observed by Rheology, Atomic Force Microscopy, and Raman Scattering Spectroscopy. *Food Hydrocoll.* **2003**, *17* (4), 399–406.
- (67) Celis, S.; Gorrea, E.; Nolis, P.; Illa, O.; Ortuño, R. M. Designing Hybrid Foldamers: The Effect on the Peptide Conformational Bias of  $\beta$ - Versus  $\alpha$ - and  $\gamma$ -Linear Residues in Alternation with (1R,2S)-2-Aminocyclobutane-1-Carboxylic Acid. *Org. Biomol. Chem.* **2012**, *10* (4), 861–868.
- (68) de Loos, M.; van Esch, J.; Kellogg, R. M.; Feringa, B. L. Chiral Recognition in Bis-Urea-Aggregates and Organogels through Cooperative Interactions. *Angew. Chemie* **2001**, *113*, 633–636.
- (69) Hunter, C. A.; Anderson, H. L. Whats Is Cooperativity? *Angew. Chem. - Int. Ed.* **2009**, *48* (41), 7488–7499.
- (70) Hirst, A. R.; Coates, I. A.; Boucheteau, T. R.; Miravet, J. F.; Escuder, B.; Castelletto, V.; Hamley, I. W.; Smith, D. K. Low-Molecular-Weight Gelators: Elucidating the Principles of Gelation Based on Gelator Solubility and a Cooperative Self-Assembly Model. *J. Am. Chem. Soc.* **2008**, *130* (28), 9113–9121.
- (71) Mahadevi, A. S.; Sastry, G. N. Cooperativity in Noncovalent Interactions. *Chem. Rev.* **2016**, *116*, 2775–2825.
- (72) Minguet, M.; Amabilino, D. B.; Wurst, K.; Veciana, J. Circular Dichroism Studies of Crystalline Chiral and Achiral  $\alpha$ -Nitronyl Nitroxide Radicals in a KBr Matrix. *J. Chem. Soc. Perkin Trans. 2* **2001**, *39* (5), 670–676.
- (73) Berova, N.; Di Bari, L.; Pescitelli, G. Application of Electronic Circular Dichroism in Configurational and Conformational Analysis of Organic Compounds. *Chem. Soc. Rev.* **2007**, *36* (6), 914–931.
- (74) Iavicoli, P.; Xu, H.; Feldborg, L. N.; Linares, M.; Paradinas, M.; Stafström, S.; Ocal, C.; Nieto-Ortega, B.; Casado, J.; Navarrete, J. T. L.; et al. Tuning the Supramolecular Chirality of One- and Two-Dimensional Aggregates with the Number of Stereogenic Centers in the Component Porphyrins. *J. Am. Chem. Soc.* **2010**, *132* (27), 9350–9362.
- (75) Würthner, F.; Kaiser, T. E.; Saha-Möller, C. R. J-Aggregates: From Serendipitous Discovery to Supramolecular Engineering of Functional Dye Materials. *Angew. Chem. - Int. Ed.* **2011**, *50* (15), 3376–3410.
- (76) Bauernshmitt, R.; Ahlrichs, R. Treatment of Electronic Excitations within the Adiabatic Approximation of Time Dependent Density Functional Theory. *Chem. Phys. Lett.* **1996**, *156*, 454–464.
- (77) Autschbach, J.; Ziegler, T.; van Gisbergen, S. J. A.; Baerends, E. J. Chiroptical Properties from Time-Dependent Density Functional Theory. I. Circular Dichroism Spectra of Organic Molecules. *J. Chem. Phys.* **2002**, *116* (16), 6930.
- (78) Stratmann, R. R.; Scuseria, G. E.; Frisch, M. J. An Efficient Implementation of Time-Dependent Density-Functional Theory for the Calculation of Excitation Energies of Large Molecules. *J. Chem. Phys.* **1998**, *109* (19), 8218–8224.

## 8. Bibliography

- (79) Yanai, T.; Tew, D. P.; Handy, N. C. A New Hybrid Exchange–correlation Functional Using the Coulomb-Attenuating Method (CAM-B3LYP). *Chem. Phys. Lett.* **2004**, *393* (1–3), 51–57.
- (80) O’Boyle, N. M.; Tenderholt, A. L.; Langner, K. M. Cclib: A Library for Package-Independent Computational Chemistry Algorithms. *J. Comput. Chem.* **2008**, *29* (5), 839–845.
- (81) Norrby, T.; Börje, A.; Åkermark, B.; Hammarström, L.; Alsins, J.; Lashgari, K.; Norrestam, R.; Mårtensson, J.; Stenhagen, G. Synthesis, Structure, and Photophysical Properties of Novel Ruthenium(II) Carboxypyridine Type Complexes. *Inorg. Chem.* **1997**, *36* (25), 5850–5858.
- (82) Tse, M. K.; Jiao, H.; Anilkumar, G.; Bitterlich, B.; Gelalcha, F. G.; Beller, M. Synthetic, Spectral and Catalytic Activity Studies of Ruthenium Bipyridine and Terpyridine Complexes: Implications in the Mechanism of the Ruthenium(pyridine-2,6-Bisoxazoline)(pyridine-2,6-Dicarboxylate)-Catalyzed Asymmetric Epoxidation of Olefins Utilized. *J. Organomet. Chem.* **2006**, *691* (21), 4419–4433.
- (83) Delgado, J.; Zhang, Y.; Xu, B.; Epstein, I. R. Terpyridine- and Bipyridine-Based Ruthenium Complexes as Catalysts for the Belousov-Zhabotinsky Reaction. *J. Phys. Chem. A* **2011**, *115*, 2208–2215.
- (84) Klawonn, M.; Tse, M. K.; Bhor, S.; Döbler, C.; Beller, M. A Convenient Ruthenium-Catalyzed Alkene Epoxidation with Hydrogen Peroxide as Oxidant. *J. Mol. Catal. A Chem.* **2004**, *218* (1), 13–19.
- (85) Bhor, S.; Anilkumar, G.; Man, K. T.; Klawonn, M.; Döbler, C.; Bitterlich, B.; Grotevendt, A.; Beller, M. Synthesis of a New Chiral N,N,N-Tridentate Pyridinebisimidazole Ligand Library and Its Application in Ru-Catalyzed Asymmetric Epoxidation. *Org. Lett.* **2005**, *7* (16), 3393–3396.
- (86) Sinha, P.; Raghuvanshi, D. S.; Singh, K. N.; Mishra, L. Synthesis, Characterization and Catalytic Property of Ruthenium-Terpyridyl Complexes. *Polyhedron* **2012**, *31* (1), 227–234.
- (87) Tse, M. K.; Klawonn, M.; Bhor, S.; Do, C.; Anilkumar, G.; Hugl, H.; Ma, W.; Beller, M. Convenient Method for Epoxidation of Alkenes Using Aqueous Hydrogen Peroxide. *Org. Lett.* **2005**, *7* (6), 9987–9990.
- (88) Rouhi, M. Thalidomide. *Chem. Eng. News* **2005**, *85* (25), 122–123.
- (89) Lasagna, L. Thalidomide—A New Nonbarbiturate Sleep-Inducing Drug. *J. Chronic Dis.* **1960**, *11* (6), 627–631.
- (90) *Organometallics*; Elschenbroich, C., Ed.; Wiley-VCH: Weinheim, 2006.
- (91) *Transition Metal Reagents and Catalysts*; Tsuji, J., Ed.; John Wiley & Sons: Chichester, 2000.
- (92) *Transition Metals for Organic Synthesis*; Beller, M., Bolm, C., Eds.; Wiley-VCH: Weinheim, 2004.
- (93) Knowles, W. S. *Chapter 1. Asymmetric Hydrogenations - The Monsanto L-Dopa Process*; Blaser, H.-U., Schmidt, E., Eds.; Wiley-VCH: Weinheim, 2004.
- (94) *Enzymes as Catalysts in Organic Synthesis*; Schneider, M. P., Ed.; D. Reidel Publishing Company: Dordrecht, 1986.
- (95) *Comprehensive Enantioselective Organocatalysis*; Dalko, P. I., Ed.; Wiley-VCH: Weinheim, 2013.

## 8. Bibliography

- (96) *Asymmetric Organocatalysis - From Biomimetic Concepts to Applications in Asymmetric Synthesis*; Berkessel, A., Gröger, H., Eds.; Wiley-VCH: Weinheim, 2005.
- (97) *Organocatalysis*; Reetz, M. T., List, B., Jaroch, S., Weinmann, H., Eds.; Springer-Verlag: Heidelberg, 2007.
- (98) MacMillan, D. W. C. The Advent and Development of Organocatalysis. *Nature* **2008**, *455*, 304–308.
- (99) Bredig, G.; Fiske, W. S. No Title. *Biochem. Z.* **1912**, *7*.
- (100) Pracejus, H. Organische Katalysatoren, LXI. Asymmetrische Synthesen Mit Ketenen, I. Alkaloid-Katalysierte Asymmetrische Synthesen von  $\alpha$ -Phenyl-Propionsäureestern. *Justus Liebigs Ann. Chem.* **1960**, *634*, 9–22.
- (101) Eder, U.; Sauer, G.; Wiechert, R. New Type of Asymmetric Cyclization to Optically Active Steroid CD Partial Structures. *Angew. Chem. - Int. Ed.* **1971**, *10* (7), 496–497.
- (102) Hajos, Z. G.; Parrish, D. R. Asymmetric Synthesis of Bicyclic Intermediates of Natural Product Chemistry. *J. Org. Chem.* **1974**, *39* (12), 1615–1621.
- (103) Ahrendt, K. A.; Borths, C. J.; Macmillan, D. W. C. New Strategies for Organic Catalysis: The First Highly Enantioselective Organocatalytic Diels - Alder Reaction. *J. Am. Chem. Soc.* **2000**, *122* (6), 4243–4244.
- (104) List, B.; Lerner, R. a; Barbas III, C. F. Proline-Catalyzed Direct Asymmetric Aldol Reactions. *J. Am. Chem. Soc.* **2000**, *122* (13), 2395–2396.
- (105) Agami, C.; Puchot, C. Kinetic Analysis of the Dual Catalysis by Proline in the Asymmetric Intramolecular Aldol Reaction. *J. Mol. Cat.* **1986**, *38*, 341.
- (106) Sakthivel, K.; Notz, W.; Bui, T.; Barbas, C. F. Amino Acid Catalyzed Direct Asymmetric Aldol Reactions: A Bioorganic Approach to Catalytic Asymmetric Carbon-Carbon Bond-Forming Reactions. *J. Am. Chem. Soc.* **2001**, *123* (22), 5260–5267.
- (107) Hoang, L.; Bahmanyar, S.; Houk, K. N.; List, B. Kinetic and Stereochemical Evidence for the Involvement of Only One Proline Molecule in the Transition States of Proline-Catalyzed Intra- and Intermolecular Aldol Reactions. *J. Am. Chem. Soc.* **2003**, *125* (1), 16–17.
- (108) Allemann, C.; Gordillo, R.; Clemente, F. R.; Cheong, P. H. Y.; Houk, K. N. Theory of Asymmetric Organocatalysis of Aldol and Related Reactions: Rationalizations and Predictions. *Acc. Chem. Res.* **2004**, *37* (8), 558–569.
- (109) Notz, W.; List, B. Catalytic Asymmetric Synthesis of Anti-1,2-Diols. *J. Am. Chem. Soc.* **2000**, *122* (30), 7386–7387.
- (110) List, B.; Pojarliev, P.; Martin, H. J. Efficient Proline-Catalyzed Michael Additions of Unmodified Ketones to Nitro Olefins. *Org. Lett.* **2001**, *3* (16), 2423–2425.
- (111) List, B.; Pojarliev, P.; Biller, W. T.; Martin, H. J. The Proline-Catalyzed Direct Asymmetric Three-Component Mannich Reaction: Scope, Optimization, and Application to the Highly Enantioselective Synthesis of 1,2-Amino Alcohols. *J. Am. Chem. Soc.* **2002**, *124* (5), 827–833.
- (112) Gröger, H.; Wilken, J. The Application of L-Proline as an Enzyme Mimic and Further New Asymmetric Syntheses Using Small Organic Molecules as Chiral Catalysts. *Angew. Chem. - Int. Ed.* **2001**, *40* (3), 529–532.



## 8. Bibliography

- (113) Notz, W.; Tanaka, F.; Barbas, C. F. Enamine-Based Organocatalysis with Proline and Diamines: The Development of Direct Catalytic Asymmetric Aldol, Mannich, Michael, and Diels-Alder Reactions. *Acc. Chem. Res.* **2004**, *37* (8), 580–591.
- (114) Nakadai, M.; Saito, S.; Yamamoto, H. Diversity-Based Strategy for Discovery of Environmentally Benign Organocatalyst: Diamine – Protonic Acid Catalysts for Asymmetric Direct Aldol Reaction. *Tetrahedron* **2002**, *58*, 8167–8177.
- (115) Cobb, A. J. a; Shaw, D. M.; Longbottom, D. a; Gold, J. B.; Ley, S. V. Organocatalysis with Proline Derivatives: Improved Catalysts for the Asymmetric Mannich, Nitro-Michael and Aldol Reactions. *Org. Biomol. Chem.* **2005**, *3* (1), 84–96.
- (116) Torii, H.; Nakadai, M.; Ishihara, K.; Saito, S.; Yamamoto, H. Asymmetric Direct Aldol Reaction Assisted by Water and a Proline-Derived Tetrazole Catalyst. *Angew. Chem. - Int. Ed.* **2004**, *43* (15), 1983–1986.
- (117) Wiesner, M.; Upert, G.; Angelici, G.; Wennemers, H. Enamine Catalysis with Low Catalyst Loadings - High Efficiency via Kinetic Studies. *J. Am. Chem. Soc.* **2010**, *132* (1), 6–7.
- (118) Palomo, C.; Oiarbide, M.; Lopez, R. Asymmetric Organocatalysis by Chiral Bronsted Bases: Implications and Applications. *Chem. Soc. Rev.* **2009**, *38* (2), 632–653.
- (119) Davie, E. A. C.; Mennen, S. M.; Xu, Y.; Miller, S. J. Asymmetric Catalysis Mediated by Synthetic Peptides Bond-Forming Reactions Catalyzed by Synthetic. *Chem. Rev.* **2007**, *107*, 5759–5812.
- (120) Wennemers, H. Asymmetric Catalysis with Peptides. *Chem. Comm.* **2011**, *47*, 12036–12041.
- (121) Oku, J.; Ito, N.; Inoue, S. Asymmetric Cyanohydrin Synthesis Catalyzed by Synthetic Dipeptides , 1. *Makromol. Chem.* **1979**, *180*, 1089–1091.
- (122) Juliá, S.; Masana, J.; Vega, J. C. “Synthetic Enzymes”. Highly Stereoselective Epoxidation of Chalcone in a Triphasic Toluene- Water-Poly[(S)-Alanine] System. *Angew. Chem. - Int. Ed.* **1980**, *19*, 929–931.
- (123) Ueoka, R.; Matsumoto, Y.; Ihara, Y. Dramatically Enhanced Enantioselectivity Hydrolysis of Amino Acid Esters with Tripeptide Nucleophile by Controlling the Reaction Field at Room Temperature. *Chem. Lett.* **1984**, 1807–1984.
- (124) Miller, S. J.; Copeland, G. T.; Papaioannou, N.; Horstmann, T. E.; Ruel, E. M. Kinetic Resolution of Alcohols Catalyzed by Tripeptides Containing the N -Alkylimidazole Substructure. *J. Am. Chem. Soc.* **1998**, *120* (7), 1629–1630.
- (125) Messerer, M.; Wennemers, H. Reversing the Enantioselectivity of a Peptidic Catalyst by Changing the Solvent. *Synlett* **2011**, No. 4, 499–502.
- (126) Elia, V. D.; Zwicknagl, H.; Reiser, O. Short  $\alpha$  / $\beta$  Peptides as Catalysts for Intra- and Intermolecular Aldol Reactions. *J. Org. Chem.* **2008**, *73*, 3262–3265.
- (127) Burgess, K.; Li, S.; Rebenspies, J. Chiral 1,3-Cyclobutane Amino Acids: Synthesis and Extended Conformations. *Tetrahedron Lett.* **1997**, *38* (10), 1681–1684.
- (128) Milbeo, P.; Maurent, K.; Moulat, L.; Lebrun, A.; Didierjean, C.; Aubert, E.; Martinez, J.; Calmès, M. N-Pyrrolidine-Based  $\alpha$  / $\beta$ -Peptides Incorporating ABOC, a Constrained Bicyclic  $\beta$ -Amino Acid, for Asymmetric Aldol Reaction Catalysis. *Tetrahedron* **2016**, *72* (13), 1706–1715.
- (129) Flores-Ferrándiz, J.; Fiser, B.; Gómez-Bengoa, E.; Chinchilla, R. Solvent-Induced Reversal of Enantioselectivity in the Synthesis of Succinimides by the Addition of Aldehydes to Maleimides Catalysed by Carbamate-Monoprotected 1,2-Diamines.

## 8. Bibliography

*European J. Org. Chem.* **2015**, 2015 (6), 1218–1225.

- (130) Sohtome, Y.; Yamaguchi, T.; Tanaka, S.; Nagasawa, K. Sequential Enantiodivergent Organocatalysis: Reversibility in Enantioswitching Controlled by a Conformationally Flexible Guanidine/bisthiourea Organocatalyst. *Org. Biomol. Chem.* **2013**, 11 (17), 2780–2786.
- (131) Sohtome, Y.; Nagasawa, K. Sequential Stereodivergent Organocatalysis and Programmed Organocascades. *Org. Biomol. Chem.* **2014**, 12 (11), 1681–1685.
- (132) Bahmanyar, S.; Houk, K. N.; Martin, H. J.; List, B. Quantum Mechanical Predictions of the Stereoselectivities of Proline-Catalyzed Asymmetric Intermolecular Aldol Reactions. *J. Am. Chem. Soc.* **2003**, 125 (9), 2475–2479.
- (133) *The Chemistry of Contrast Agents in Medical Magnetic Resonance Imaging*, second Ed.; Merbach, A., Helm, L., Tóth, É., Eds.; Wiley, 2013.
- (134) Ojha, T.; Rizzo, L.; Storm, G.; Kiessling, F.; Lammers, T. Image-Guided Drug Delivery: Preclinical Applications and Clinical Translation. *Expert opin. Drug deliv.* **2015**, 12 (8), 1–5.
- (135) Lauterbur, P. C. Image Formation by Induced Local Interactions: Examples Employing Nuclear Magnetic Resonance. *Nature* **1973**, 242, 190–191.
- (136) Bloch, F.; Hansen, W. W.; Packard, M. Nuclear Induction. *Phys. Rev.* **1946**, 69 (3–4), 127.
- (137) Bloembergen, N.; Purcell, E. M.; Pound, R. V. Relaxation Effects in Nuclear Magnetic Resonance Absorption. *Phys. Rev.* **1948**, 73, 679.
- (138) *An Introduction to Biomedical Nuclear Magnetic Resonance*; Petersen, S. B., Muller, R. N., van As, H., Rinck, P. A., Eds.; Georg Thieme Verlag, 1985.
- (139) Steele, J.; Ilinsky, N. *Beautiful Visualization*; O'Reilly Media, 2010.
- (140) *Lanthanide and Actinide Chemistry*; Cotton, Si., Ed.; John Wiley & Sons: Uppingham, Rutland, UK, 2006.
- (141) *Principles of Neural Science*; Kandel, E. R., Schwartz, J. H., Jessell, T. M., Eds.; McGraw-Hill: New York, 2000.
- (142) *Lanthanide Probes in Life, Chemical and Earth Science: Theory and Practice*; Bünzli, J.-C. G., Choppin, G. R., Eds.; Elsevier: Amsterdam, 1989.
- (143) Weinmann, H. J.; Brasch, R. C.; Press, W. R. Characteristics of Gadolinium-DTPA Complex: A Potential NMR Contrast Agent. *Am. J. Roentgenol.* **1984**, 142, 619–624.
- (144) Brasch, R. C.; Weinmann, H. J.; Wesbey, G. E. Contrast-Enhanced NMR Imaging: Animal Studies Using Gadolinium-DTPA Complex. *Am. J. Roentgenol.* **1984**, 142, 625–630.
- (145) Carr, D. H.; Brown, J.; Bydder, G. M.; Steiner, R. E.; Weinmann, H. J.; Speck, U.; Hall, A. S.; Young, I. R. Gadolinium-DTPA as a Contrast Agent in MRI: Initial Clinical Experience in 20 Patients. *Am. J. Roentgenol.* **1984**, 143, 215–224.
- (146) Pierre, V. C.; Allen, M. J.; Caravan, P. Contrast Agents for MRI: 30+ Years and Where Are We Going? *J. Biol. Inorg. Chem.* **2014**, 19 (2), 127–131.
- (147) Caravan, P.; Ellison, J. J.; McMurry, T. J.; Lauffer, R. B. Gadolinium(III) Chelates as MRI Contrast Agents: Structure, Dynamics, and Applications. *Chem. Rev.* **1999**, 99 (9), 2293–2352.
- (148) Werner, E. J.; Datta, A.; Jocher, C. J.; Raymond, K. N. High Relaxivity MRI Contrast

## 8. Bibliography

- Agents: Where Coordination Chemistry Meets Medical Imaging. *Angew. Chem. - Int. Ed.* **2008**, *47* (45), 8568–8580.
- (149) Aime, S.; Caravan, P. Biodistribution of Gadolinium-Based Contrast Agents, Including Gadolinium Deposition. *J. Magn. Reson. Imaging.* **2009**, *30* (6), 1259–1267.
- (150) *Lanthanide Probes in Life, Chemical and Earth Science: Theory and Practice*; Bünzli, J., Choppin, G. R., Eds.; Elsevier: Amsterdam, 1989.
- (151) Uggeri, F.; Aime, S.; Anelli, P. L.; Botta, M.; Brocchetta, M.; de Haen, C.; Ermondi, G.; Grandi, M.; Paoli, P. Novel Contrast Agents for Magnetic Resonance Imaging. Synthesis and Characterization of the Ligand BOPTA and Its Ln(III) Complexes (Ln = Gd, La, Lu). *Inorg. Chem.* **1995**, *34*, 633–643.
- (152) Caravan, P. Protein-Targeted Gadolinium-Based Magnetic Resonance Imaging (MRI) Contrast Agents: Design and Mechanism of Action. *Acc. Chem. Res.* **2009**, *42* (7), 851–862.
- (153) Strijkers, G. J.; Mulder, W. J. M.; Tilborg, G. A. F. Van; Nicolay, K. MRI Contrast Agents: Current Status and Future Perspectives. *Anticancer. Agents Med. Chem.* **2007**, *7*, 291–305.
- (154) Lee, S.; Xie, J.; Chen, X. Peptides and Peptide Hormones for Molecular Imaging and Disease Diagnosis. *Chem. Rev.* **2010**, *110* (5), 3087–3111.
- (155) Gale, E. M.; Atanasova, I. P.; Blasi, F.; Ay, I.; Caravan, P. A Manganese Alternative to Gadolinium for MRI Contrast. *J. Am. Chem. Soc.* **2015**, *137* (49), 15548–15557.
- (156) Troughton, J. S.; Greenfield, M. T.; Greenwood, J. M.; Dumas, S.; Wiethoff, A. J.; Wang, J.; Spiller, M.; McMurry, T. J.; Caravan, P. Synthesis and Evaluation of a High Relaxivity Manganese(II)-Based MRI Contrast Agent. *Inorg. Chem.* **2004**, *43* (20), 6313–6323.
- (157) Gallez, B.; Baudalet, C.; Adline, J.; Geurts, M.; Delzenne, N. Accumulation of Manganese in the Brain of Mice after Intravenous Injection of Manganese-Based Contrast Agents. *Chem. Res. Toxicol.* **1997**, *10* (4), 360–363.
- (158) Grobner, T. Gadolinium-- a Specific Trigger for the Development of Nephrogenic Fibrosing Dermopathy and Nephrogenic Systemic Fibrosis? *Nephrol. Dial. Transplant.* **2006**, *21* (4), 1104–1108.
- (159) Prchal, D.; Holmes, D.; Levin, A. Nephrogenic Systemic Fibrosis: The Story Unfolds. *Kidney Int.* **2008**, *73* (12), 1335–1337.
- (160) Frenzel, T.; Lengsfeld, P.; Schirmer, H.; Hütter, J.; Weinmann, H. J. Stability of Gadolinium-Based Magnetic Resonance Imaging Contrast Agents in Human Serum at 37 Degrees C. *Invest Radiol.* **2008**, *43* (12), 817–828.
- (161) Yang, L.; Krefting, I.; Gorovets, A.; Marzella, L.; Kaiser, J.; Boucher, R.; Rieves, D. Nephrogenic Systemic Fibrosis and Class Labeling of Gadolinium-Based Contrast Agents by the Food and Drug Administration. *Radiology* **2012**, *265* (248–253).
- (162) Sarka, L.; Burai, L.; Brücher, E. The Rates of the Exchange Reactions between [Gd(DTPA)]<sup>2-</sup> and the Endogenous Ions Cu<sup>2+</sup> and Zn<sup>2+</sup>: A Kinetic Model for the Prediction of the Magnetic Resonance Imaging. *Chem. Eur. J.* **2000**, *6* (4), 719–724.
- (163) Pasha, A.; Tircsó, G.; Benyó, E. T.; Brücher, E.; Sherry, A. D. Synthesis and Characterization of DOTA-(amide)<sub>4</sub> Derivatives: Equilibrium and Kinetic Behavior of Their Lanthanide(III) Complexes. *Eur. J. Inorg. Chem.* **2007**, No. 27, 4340–4349.
- (164) Pálinkás, Z.; Roca-Sabio, A.; Mato-Iglesias, M.; Esteban-Gómez, D.; Platas-Iglesias,

## 8. Bibliography

- C.; De Blas, A.; Rodríguez-Blas, T.; Tóth, E. Stability, Water Exchange, and Anion Binding Studies on Lanthanide(III) Complexes with a Macrocyclic Ligand Based on 1.7-Diaza-12-Crown-4: Extremely Fast Water Exchange on the Gd<sup>3+</sup> Complex. *Inorg. Chem.* **2009**, *48* (18), 8878–8889.
- (165) McMurry, T. J.; Pippin, C. G.; Wu, C.; Deal, K. A.; Brechbiel, M. W.; Mirzadeh, S.; Gansow, O. A. Physical Parameters and Biological Stability of Yttrium(III) Diethylenetriaminepentaacetic Acid Derivative Conjugates. *J. Med. Chem.* **1998**, *41* (18), 3546–3549.
- (166) Farkas, E.; Fodor, T.; Kálmán, F. K.; Tircsó, G.; Tóth, I. Equilibrium and Dissociation Kinetics of the [Al(NOTA)] Complex (NOTA = 1,4,7-Triazacyclononane-1,4,7-Triacetate). In *Reaction Kinetics, Mechanisms and Catalysis*; 2015.
- (167) Tircsó, G.; Kálmán, F. K.; Pál, R.; Varga, T. R.; Király, R.; Lázár, I.; Québatte, L.; Merbach, A. E.; Tóth, É.; Brücher, E. Lanthanide Complexes Formed with the Tri- and Tetraacetate Derivatives of Bis(aminomethyl)phosphinic Acid: Equilibrium, Kinetic and NMR Spectroscopic Studies. *Eur. J. Inorg. Chem.* **2012**, 2062–2073.
- (168) Rodríguez-Rodríguez, A.; Esteban-Gómez, D.; Tripier, R.; Tircsó, G.; Garda, Z.; Tóth, I.; De Blas, A.; Rodríguez-Blas, T.; Platas-Iglesias, C. Lanthanide(III) Complexes with a Reinforced Cyclam Ligand Show Unprecedented Kinetic Inertness. *J. Am. Chem. Soc.* **2014**, *136* (52), 17954–17957.
- (169) Kálmán, F. K.; Végh, A.; Regueiro-Figueroa, M.; Tóth, É.; Platas-Iglesias, C.; Tircsó, G. H<sub>4</sub>octapa: Highly Stable Complexation of Lanthanide(III) Ions and Copper(II). *Inorg. Chem.* **2015**, *54* (5), 2345–2356.
- (170) Platas-Iglesias, C.; Mato-Iglesias, M.; Djanashvili, K.; Muller, R. N.; Vander Elst, L.; Peters, J. A.; De Blas, A.; Rodríguez-Blas, T. Lanthanide Chelates Containing Pyridine Units with Potential Application as Contrast Agents in Magnetic Resonance Imaging. *Chem. - A Eur. J.* **2004**, *10* (14), 3579–3590.
- (171) Molnár, E.; Camus, N.; Patinec, V.; Rolla, G. A.; Botta, M.; Tircsó, G.; Kálmán, F. K.; Fodor, T.; Tripier, R.; Platas-Iglesias, C. Picolinate-Containing Macrocyclic Mn<sup>2+</sup> Complexes as Potential MRI Contrast Agents. *Inorg. Chem.* **2014**, *53* (10), 5136–5149.
- (172) Tircsó, G.; Regueiro-Figueroa, M.; Nagy, V.; Garda, Z.; Garai, T.; Kálmán, F. K.; Esteban-Gómez, D.; Tóth, É.; Platas-Iglesias, C. Approaching the Kinetic Inertness of Macrocyclic Gadolinium(III)-Based MRI Contrast Agents with Highly Rigid Open-Chain Derivatives. *Chem. - A Eur. J.* **2016**, *22* (3), 896–901.
- (173) Pellegatti, L.; Zhang, J.; Drahos, B.; Villette, S.; Suzenet, F.; Guillaumet, G.; Petoud, S.; Tóth, E. Pyridine-Based Lanthanide Complexes: Towards Bimodal Agents Operating as near Infrared Luminescent and MRI Reporters. *Chem. Commun. (Camb)*. **2008**, *60* (48), 6591–6593.
- (174) Gale, E. M.; Kenton, N.; Caravan, P. [Gd(CyPic3A)(H<sub>2</sub>O)<sub>2</sub>]<sup>-</sup>: A Stable, Bis(aquated) and High-Relaxivity Gd(III) Complex. *Chem. Commun.* **2013**, *49* (73), 8060–8062.
- (175) Bonnet, C. S.; Laine, S.; Buron, F.; Tircsó, G.; Pallier, A.; Helm, L.; Suzenet, F.; Toth, E. A Pyridine-Based Ligand with Two Hydrazine Functions for Lanthanide Chelation: Remarkable Kinetic Inertness for a Linear, Bishydrated Complex. *Inorg. Chem.* **2015**, *54* (12), 5991–6003.
- (176) Bloembergen, N.; Morgan, L. O. Proton Relaxation Times in Paramagnetic Solutions. Effects of Electron Spin Relaxation. *J. Chem. Phys.* **1961**, *34*, 842.
- (177) Micskei, K.; Helm, L.; Brücher, E.; Merbach, A. E. Oxygen-17 NMR Study of Water

## 8. Bibliography

- Exchange on Gadolinium Polyaminopolyacetates [Gd(DTPA)(H<sub>2</sub>O)]<sup>2-</sup> and [Gd(DOTA)(H<sub>2</sub>O)]<sup>-</sup> Related to NMR Imaging. *Inorg. Chem.* **1993**, *32*, 3844–3850.
- (178) Fries, P. H.; Belorizky, E. Electronic Relaxation of Paramagnetic Metal Ions and NMR Relaxivity in Solution: Critical Analysis of Various Approaches and Application to a Gd(III)-Based Contrast Agent. *J. Chem. Phys.* **2005**, *123* (12), 124510–124515.
- (179) Bonnet, C. S.; Fries, P. H.; Crouzy, S.; Delangle, P. Outer-Sphere Investigation of MRI Relaxation Contrast Agents. Example of a Cyclodecapeptide Gadolinium Complex with Second-Sphere Water. *J. Phys. Chem. B* **2010**, *114*, 8770–8781.
- (180) Botta, M. Second Coordination Sphere Water Molecules and Relaxivity of Gadolinium(III) Complexes: Implications for MRI Contrast Agents. *Eur. J. Inorg. Chem.* **2000**, *2000* (3), 399–407.
- (181) Aime, S.; Calabi, L.; Cavallotti, C.; Gianolio, E.; Giovenzana, G. B.; Losi, P.; Maiocchi, A.; Palmisano, G.; Sisti, M. [Gd-AAZTA]<sup>-</sup>: A New Structural Entry for an Improved Generation of MRI Contrast Agents. *Inorg. Chem.* **2004**, *43*, 7588–7590.
- (182) Datta, A.; Raymond, K. N. Gd-HOPO Based High Relaxivity MRI Contrast Agents. *Acc. Chem. Res.* **2009**, *42*, 938–947.
- (183) Baranyai, Z.; Botta, M.; Fekete, M.; Giovenzana, G. B.; Negri, R.; Tei, L.; Plasas-Iglesias, C. Ligand Denticity Leading to Improved Thermodynamic and Kinetic Stability of the Gd<sup>3+</sup> Complex: The Strange Case of OBETA. *Chem. - A Eur. J.* **2012**, *18*, 7680–7685.
- (184) Boros, E.; Caravan, P. Probing the Structure-Relaxivity Relationship of Bis-Hydrated Gd(DOTA) Derivatives. *Inorg. Chem.* **2015**, *54* (5), 2403–2410.
- (185) Boros, E.; Karimi, S.; Kenton, N.; Helm, L.; Caravan, P. Gd(DOTA)P: Exploring the Boundaries of Fast Water Exchange in Gadolinium-Based Magnetic Resonance Imaging Contrast Agents. *Inorg. Chem.* **2014**, *53* (13), 6985–6994.
- (186) Viswanathan, S.; Kovacs, Z.; Green, K. N.; Ratnakar, S. J.; Sherry, A. D. Alternatives to Gadolinium-Based Metal Chelates for Magnetic Resonance Imaging. *Chem. Rev.* **2010**, *110* (5), 2960–3018.
- (187) Villaraza, A.J.L.; Bumb, A.; Brechbiel, M. W. Macromolecules, Dendrimers, and Nanomaterials in Magnetic Resonance Imaging: The Interplay between Size, Function, and Pharmacokinetics. *Chem. Rev.* **2010**, *110* (5), 2921–2959.
- (188) Ospina, J.; Gutiérrez-Abad, R.; Lope-Piedrafita, S.; Illa, O.; Branchadell, V.; Ortuño, R. M. Stereoselective Synthesis of Highly Branched Chiral Cyclobutane-Cored Triamines and Their Conjugation to Gd-DOTA. *Tetrahedron* **2015**, *71* (42), 8085–8095.
- (189) Kálmán, F. K.; Tircsó, G. Kinetic Inertness of the Mn<sup>2+</sup> Complexes Formed with AAZTA and Some Open-Chain EDTA Derivatives. *Inorg. Chem.* **2012**, *51* (19), 10065–10067.
- (190) Bonnet, C. S.; Laine, S.; Buron, F.; Tircsó, G.; Pallier, A.; Helm, L.; Suzenet, F.; Tóth, É. A Pyridine-Based Ligand with Two Hydrazine Functions for Lanthanide Chelation: Remarkable Kinetic Inertness for a Linear, Bishydrated Complex. *Inorg. Chem.* **2015**, *54* (12), 5991–6003.
- (191) Takács, A.; Napolitano, R.; Purgel, M.; Bényei, A. C.; Zékány, L.; Brücher, E.; Tóth, I.; Baranyai, Z.; Aime, S. Solution Structures, Stabilities, Kinetics, and Dynamics of DO3A and DO3A-Sulphonamide Complexes. *Inorg. Chem.* **2014**, *53* (6), 2858–2872.

## 8. Bibliography

- (192) Garw, P.; Sabatini, A.; Vacca, A. Investigation of Equilibria in Solution. Determination of Equilibrium Constant with the HYPERQUAD Suite of Programs. *Talanta* **1996**, *43*, 1739–1753.
- (193) *Biochemistry of the Lanthanides*; Evans, C. H., Ed.; Springer US, 1990.
- (194) Cacheris, W. P.; Quay, S. C.; Rocklage, S. M. The Relationship between Thermodynamics and the Toxicity of Gadolinium Complexes. *Magn. Reson. Imaging* **1990**, *8* (4), 467–481.
- (195) Alderighi, L.; Gans, P.; Ienco, A.; Peters, D.; Sabatini, A.; Vacca, A. Hyperquad Simulation and Speciation (HySS): A Utility Program for the Investigation of Equilibria Involving Soluble and Partially Soluble Species. *Coord. Chem. Rev.* **1999**, *184*, 311–318.
- (196) Baranyai, Z.; Brücher, E.; Uggeri, F.; Maiocchi, A.; Tóth, I.; Andrási, M.; Gáspár, A.; Zékány, L.; Aime, S. The Role of Equilibrium and Kinetic Properties in the Dissociation of Gd[DTPA-Bis(methylamide)] (Omniscan) at near to Physiological Conditions. *Chem. - A Eur. J.* **2015**, *21* (12), 4789–4799.
- (197) Kálmán, F. K.; Tircso, G. Kinetic Inertness of the Mn 2+ Complexes Formed with AAZTA and Some Open-Chain EDTA Derivatives. *Inorg. Chem.* **2012**, *51*, 10065–10067.
- (198) Baranyai, Z.; Uggeri, F.; Giovenzana, G. B.; Bényei, A.; Brücher, E.; Aime, S. Equilibrium and Kinetic Properties of the Lanthanoids(III) and Various Divalent Metal Complexes of the Heptadentate Ligand AAZTA. *Chem. - A Eur. J.* **2009**, *15* (7), 1696–1705.
- (199) Jung, K. H.; Kim, H. K.; Lee, G. H.; Kang, D. S.; Park, J. A.; Kim, K. M.; Chang, Y.; Kim, T. J. Gd Complexes of Macrocyclic Diethylenetriaminepentaacetic Acid (DTPA) Biphenyl-2,2'-bisamides as Strong Blood-Pool Magnetic Resonance Imaging Contrast Agents. *J. Med. Chem.* **2011**, *54* (15), 5385–5394.
- (200) Wang, X.; Jin, T.; Comblin, V.; Lopez-Mut, A.; Merciny, E.; Desreux, J. F. A Kinetic Investigation of the Lanthanide DOTA Chelates. Stability and Rates of Formation and of Dissociation of a Macrocyclic Gadolinium (III) Polyaza Polycarboxylic MRI Contrast Agent. *Inorg. Chem.* **1992**, No. 31, 1095–1099.
- (201) Tóth, É.; Brücher, E.; Lázár, I.; Tóth, I. Kinetics of Formation and Dissociation of Lanthanide(III) -DOTA Complexes. *Inorg. Chem.* **1994**, *33*, 4070–4076.
- (202) Port, M.; Idée, J.-M.; Medina, C.; Robic, C.; Sabatou, M.; Corot, C. Efficiency, Thermodynamic and Kinetic Stability of Marketed Gadolinium Chelates and Their Possible Clinical Consequences: A Critical Review. *Biometals* **2008**, *21*, 469–490.
- (203) Port, M.; Robic, C.; Medina, C.; Sabatou, M.; Corot, C. Role of Thermodynamic and Kinetic Parameters in Gadolinium Chelate Stability. *J. Magn. Reson. imaging* **2009**, *30*, 1249–1258.
- (204) Broome, D. R. Nephrogenic Systemic Fibrosis Associated with Gadolinium Based Contrast Agents: A Summary of the Medical Literature Reporting. *Eur. J. Radiol.* **2008**, *66*, 230–234.
- (205) Faulkner, S.; Pope, S. J. A.; Burton-Pye, B. P. Lanthanide Complexes for Luminescence Imaging Applications. *Appl. Spectrosc. Rev.* **2005**, *40* (1), 1–31.
- (206) Haas, Y.; Stein, G. Pathways of Radiative and Radiationless Transitions in Europium (III) Solutions. Role of Solvents and Anions. *J. Phys. Chem.* **1971**, *75* (24), 3668–3677.

## 8. Bibliography

- (207) Horrocks, W. D.; Sudnick, D. R. Lanthanide Ion Luminescence Probes of the Structure of Biological Macromolecules. *Acc. Chem. Res.* **1981**, *14* (12), 384–392.
- (208) William De, W. H.; Sudnick, D. R. Lanthanide Ion Probes of Structure in Biology. Laser-Induced Luminescence Decay Constants Provide a Direct Measure of the Number of Metal-Coordinated Water Molecules. *J. Am. Chem. Soc.* **1979**, *101* (2), 334–340.
- (209) Beeby, A.; Clarkson, I. M.; Dickins, R. S.; Faulkner, S.; Parker, D.; Royle, L.; de Sousa, A. S.; Williams, J. a. G.; Woods, M. Non-Radiative Deactivation of the Excited States of Europium, Terbium and Ytterbium Complexes by Proximate Energy-Matched OH, NH and CH Oscillators: An Improved Luminescence Method for Establishing Solution Hydration States. *J. Chem. Soc. Perkin Trans. 2* **1999**, *2* (3), 493–504.
- (210) Supkowski, R. M.; Horrocks, W. D. On the Determination of the Number of Water Molecules, Q, Coordinated to Europium(III) Ions in Solution from Luminescence Decay Lifetimes. *Inorganica Chim. Acta* **2002**, *340*, 44–48.
- (211) Botta, M.; Aime, S.; Barge, A.; Bobba, G.; Dickins, R. S.; Parker, D.; Terreno, E. Ternary Complexes between Cationic Gd(III) Chelates and Anionic Metabolites in Aqueous Solution: An NMR Relaxometric Study. *Chem. - A Eur. J.* **2003**, *9* (9), 2102–2109.
- (212) Aime, S.; Barge, A.; Botta, M.; Howard, J. a. K.; Katakay, R.; Lowe, M. P.; Moloney, J. M.; Parker, D.; de Sousa, A. S. Dependence of the Relaxivity and Luminescence of Gadolinium and Europium Amino-Acid Complexes on Hydrogencarbonate and pH. *Chem. Commun.* **1999**, *2* (11), 1047–1048.
- (213) Aime, S.; Gianolio, E.; Terreno, E.; Giovenzana, G. B.; Pagliarin, R.; Sisti, M.; Palmisano, G.; Botta, M.; Lowe, M. P.; Parker, D. Ternary Gd(III)L-HSA Adducts: Evidence for the Replacement of Inner-Sphere Water Molecules by Coordinating Groups of the Protein. Implications for the Design of Contrast Agents for MRI. *J. Biol. Inorg. Chem.* **2000**, *5*, 488–497.
- (214) Aime, S.; Terreno, E.; Botta, M.; Bruce, J. I.; Parker, D.; Mainero, V. Modulation of the Water Exchange Rates in [Gd–DO3A] Complex by Formation of Ternary Complexes with Carboxylate Ligands. *Chem. Commun.* **2001**, No. 1, 115–116.
- (215) de Sousa, P. L.; Livramento, J. B.; Helm, L.; Merbach, A. E.; Mème, W.; Doan, B.-T.; Beloeil, J.-C.; Prata, M. I. M.; Santos, A. C.; C. Geraldés, C. F. G.; et al. In Vivo MRI Assessment of a Novel Gd(III)-Based Contrast Agent Designed for High Magnetic Field Applications. *Contrast Media Mol. Imaging* **2008**, *3* (2), 78–85.
- (216) Mato-Iglesias, M.; Roca-Sabio, A.; Pálinkás, Z.; Esteban-Gomez, D.; Platas-Iglesias, C.; Tóth, É.; De Blas, A.; Rodríguez-Blas, T. Complexes Based on a 1, 7-Diaza-12-Crown-4 Platform Containing Picolinate Pendants: A New Structural Entry for the Design of Magnetic Resonance Imaging Contrast. *Inorg. Chem.* **2008**, *47* (17), 7840–7851.
- (217) Anderegg, G.; Malik, S. Komplexe XLIII Die Komplexe Des Dreiwertigen Antimons Mit Polyaminocarboxylaten. *Helv. Chim. Acta* **1970**, *53* (564).
- (218) Caravan, P.; Astashkin, A. V.; Raitsimring, A. M. The Gadolinium(III)-Water Hydrogen Distance in MRI Contrast Agents. *Inorg. Chem.* **2003**, *42* (13), 3972–3974.
- (219) Halle, B.; Wennerström, H. Interpretation of Magnetic Resonance Data from Water Nuclei in Heterogeneous Systems. *J. Phys. Chem.* **1981**, *75*, 1928.

## 8. Bibliography

- (220) Powell, D. H.; Dhubhghaill, O. M. N.; Pubanz, D.; Helm, L.; Lebedev, Y. S.; Schlaepfer, W. Structural and Dynamic Parameters Obtained from  $^{17}\text{O}$  NMR, EPR, and NMRD Studies of Monomeric and Dimeric  $\text{Gd}^{3+}$  Complexes of Interest in Magnetic Resonance Imaging: An Integrated and Theoretically Self-Consistent Approach. *J. Am. Chem. Soc.* **1996**, *7863* (3), 9333–9346.
- (221) Castiglioni, E.; Biscarini, P.; Abbate, S. Experimental Aspects of Solid State Circular Dichroism. *Chirality* **2009**, *21* (1), 28–36.
- (222) *ELECTROCHEMICAL METHODS Fundamentals and Applications*, 2nd ed.; Bard, A. J., Faulkner, L. R., Eds.; Wiley, 2001.
- (223) Corsi, D. M.; Platas-Iglesias, C.; Van Bekkum, H.; Peters, J. A. Determination of Paramagnetic lanthanide(III) Concentrations from Bulk Magnetic Susceptibility Shifts in NMR Spectra. *Magn. Reson. Chem.* **2001**, *39* (11), 723–726.
- (224) *Determination and Use of Stability Constants*; Martell, A. E., Motekaitis, R. J., Eds.; VCH: New York, 1992.
- (225) Gans, P.; O'Sullivan, B. Glee, a New Computer Program for Glass Electrode Calibration. *Talanta* **2000**, *51*, 33.
- (226) Smith, R. M.; Motekaitis, R. J.; Martell, A. E. NIST Standard Reference Database. *Natl. Inst. Stand. Technol.* **1997**.
- (227) Yerly, F. *VISUALISEUR 2.3.5*; Lausanne, Switzerland, 1999.
- (228) Yerly, F. *OPTIMISEUR 2.3.5*; Lausanne, Switzerland, 1999.
- (229) Solomon, I. Relaxation Processes in a System of Two Spins. *Phys. Rev.* **1955**, *99*, 559.
- (230) Solomon, I.; Bloembergen, N. Nuclear Magnetic Interactions in the HF Molecule. *J. Chem. Phys.* **1956**, *25*, 261.
- (231) Bloembergen, N. Proton Relaxation Times in Paramagnetic Solutions. *J. Chem. Phys.* **1957**, *27*, 572.
- (232) Luz, Z.; Meiboom, S. Proton Relaxation in Dilute Solutions of Cobalt (II) and Nickel (II) Ions in Methanol and the Rate of Methanol Exchange of the Solvation Sphere. *J. Chem. Phys.* **1964**, *40*, 2686.
- (233) Fries, P. H.; Gateau, C.; Mazzanti, M. Practical Route to Relative Diffusion Coefficients and Electronic Relaxation Rates of Paramagnetic Metal Complexes in Solution by Model-Independent Outer-Sphere NMRD. Potentiality for MRI Contrast Agents. *J. Am. Chem. Soc.* **2005**, *127*, 15801–15814.
- (234) Borel, A.; Laus, S.; Ozarowski, A.; Gateau, C.; Nonat, A.; Mazzanti, M.; Helm, L. Multiple-Frequency EPR Spectra of Two Aqueous  $\text{Gd}^{3+}$  Polyamino Polypyridine Carboxylate Complexes: A Study of High Field Effects. *J. Chem. Phys.* **2007**, *111*, 5399–5407.
- (235) Freed, J. H. Dynamic Effects of Pair Correlation Functions on Spin Relaxation by Translational Diffusion in Liquids. Finite Jumps and Independent T<sub>1</sub> Processes. *J. Chem. Phys.* **1978**, *68*, 4034–4037.
- (236) Koenig, S. H.; Brown III, R. D. Field-Cycling Relaxometry of Protein Solutions and Tissue: Implications for MRI. *Prog. Nucl. Magn. Reson. Spectrosc.* **1990**, *22*, 487–567.
- (237) Raiford, D. S.; Fisk, C. L.; Becker, E. D. Calibration of Methanol and Ethylene Glycol Nuclear Magnetic Resonance Thermometers. *Anal. Chem.* **1979**, *51* (12), 2050–



## 8. Bibliography

2051.

- (238) Meiboom, S.; Gill, D. Modified Spin-Echo Method for Measuring Nuclear Relaxation Times. *Rev. Sci. Instrum.* **1958**, *29* (8), 688–691.
- (239) Hugi, A. D.; Helm, L.; Merbach, A. E. Water Exchange on Hexaaquavanadium(III): A Variable-Temperature and Variable-Pressure <sup>17</sup>O-NMR Study at 1.4 and 4.7 Tesla. *Helv. Chim. Acta* **1985**, *68* (2), 508–521.
- (240) Brittain, H. G.; Desreux, J. F. Luminescence and NMR Studies of the Conformational Isomers of Lanthanide Complexes with an Optically Active Polyaza Polycarboxylic Macrocyclic. *Inorg. Chem.* **1984**, *23* (1), 4459–4466.
- (241) *Textbook of Practical Organic Chemistry*; Vogel, A., Ed.; Logman Scientific and Technical: UK, 1989.
- (242) Kolossváry, I.; Guida, W. C. Low Mode Search. An Efficient, Automated Computational Method for Conformational Analysis: Applications to Cyclic and Acyclic Alkanes and Cyclic Peptides. *J. Am. Chem. Soc.* **1996**, *118* (21), 5011–5019.
- (243) Kaminski, G. A.; Friesner, R. A.; Tirado-Rives, J.; Jorgensen, W. L. Evaluation and Reparametrization of the OPLS-AA Force Field for Proteins via Comparison with Accurate Quantum Chemical Calculations on Peptides. *J. Phys. Chem. B* **105** (28), 6474–6487.
- (244) Mohamadi, F.; Richards, N. G. J.; Guida, W. C.; Liskamp, R.; Lipton, M.; Caufield, C.; Chang, G.; Hendrickson, T.; Still, W. C. MacroModel: An Integrated Software System for Modeling Organic and Bioorganic Molecules Using Molecular Mechanics. *J. Comput. Chem.* **1990**, *11* (4), 440–467.
- (245) Zhao, Y.; Truhlar, D. G. Density Functional for Spectroscopy: No Long-Range Self-Interaction Error, Good Performance for Rydberg and Charge-Transfer States, and Better Performance on Average than B3LYP for Ground States. *J. Phys. Chem. A* **2006**, *110* (49), 13126–13130.
- (246) Zhao, Y.; Truhlar, D. G. The M06 Suite of Density Functionals for Main Group Thermochemistry, Thermochemical Kinetics, Noncovalent Interactions, Excited States, and Transition Elements: Two New Functionals and Systematic Testing of Four M06-Class Functionals and 12 Other Functionals. *Theor. Chem. Acc.* **2007**, *120*, 215–241.
- (247) Zhao, Y.; Truhlar, D. G. A New Local Density Functional for Main-Group Thermochemistry, Transition Metal Bonding, Thermochemical Kinetics, and Noncovalent Interactions. *J. Chem. Phys.* **2006**, *125* (19), 194101, 1–18.
- (248) Kanger, T.; Kriis, K.; Laars, M.; Kailas, T.; Müürisepp, A. M.; Pehk, T.; Lopp, M. Bimorpholine-Mediated Enantioselective Intramolecular and Intermolecular Aldol Condensation. *J. Org. Chem.* **2007**, *72* (14), 5168–5173.
- (249) Tang, Z.; Yang, Z. H.; Chen, X. H.; Cun, L. F.; Mi, A. Q.; Jiang, Y. Z.; Gong, L. Z. A Highly Efficient Organocatalyst for Direct Aldol Reactions of Ketones with Aldehydes. *J. Am. Chem. Soc.* **2005**, *127* (25), 9285–9289.
- (250) Zhou, Y.; Shan, Z. (R)- or (S)-Bi-2-Naphthol Assisted, L-Proline Catalyzed Direct Aldol Reaction. *Tetrahedron: Asymmetry* **2006**, *17* (11), 1671–1677.
- (251) McCooey, S. H.; Connon, S. J. Readily Accessible 9-Epi-Amino Cinchona Alkaloid Derivatives Promote Efficient, Highly Enantioselective Additions of Aldehydes and Ketones to Nitroolefins. *Org. Lett.* **2007**, *9* (4), 599–602.
- (252) Juaristi, E.; Beck, A. K.; Hansen, J.; Matt, T.; Mukhopadhyay, T.; Simson, M.;

## 8. Bibliography

Seebach, D. Enantioselective Aldol and Michael Additions of Achiral Enolates in the Presence of Chiral Lithium Amides and Amines. *Synthesis* **1993**, 1271–1290.

